DISSERTATION / DOCTORAL THESIS

Titel der Dissertation /Title of the Doctoral Thesis

Low scaling *GW* method: implementation and applications

verfasst von / submitted by

Peitao Liu

angestrebter akademischer Grad / in partial fulfilment of the requirements for the degree of

Doktor der Naturwissenschaften (Dr. rer. nat.)

Wien, 2017 / Vienna, 2017

Studienkennzahl lt. Studienblatt / degree programme code as it appears on the student record sheet:	A 796 605 411
Dissertationsgebiet lt. Studienblatt / field of study as it appears on the student record sheet:	Physik
Betreut von / Supervisor:	Univ.-Prof. Dipl.-Ing. Dr. Georg Kresse Univ.- Assoz. Prof. Dipl.-Ing. Dr. Cesare Franchini

Vorwort

Die vorliegende Arbeit setzt sich aus drei Teilen zusammen. Der erste Teil deckt die Grundlagen zum elektronischen Vielteilchenproblem in der Physik der kondensierten Materie ab und stellt den theoretischen Hintergrund der *GW* Methode vor. Nach einer Einführung zur Dichtefunktionaltheorie (DFT) werden später Methoden welche über konventionelle DFT hinausgehen, wie DFT+U und Hybridfunktionale vorgestellt. Dabei werden auch die jeweiligen Grenzen der Anwendbarkeit dieser Methoden diskutiert. Anschließend wird ein Überblick über die *GW* Approximation gegeben, beginnend mit dem Bandlückenproblem und experimenteller Photoemissionsspektroskopie. Die Herleitung der *GW* Approximation aus der Vielkörper-Störungstheorie wird danach ausführlich behandelt. Insbesondere werden die Ein-Teilchen-Green's-Funktionen, die Dyson-Gleichung und die Hedin-Gleichungen eingeführt. Zuletzt wird die praktische Umsetzung der *GW* Approximation besprochen, einschließlich der konventionellen *GW* Implementierungen sowie der Space-Time-Methode. Hierbei werden auch die Nachteile der bestehenden *GW* Implementierungen aufgezeigt, wodurch die Notwendigkeit für einen niedrig skalierenden *GW* Algorithmus deutlich wird. Aus dieser Überlegung stammt die Motivation zu dieser Arbeit. Abschließend kann gesagt werden, dass dieser Teil eine solide Grundlage bildet und eine konsequente Terminologie für den zweiten Teil der Arbeit einführt.

Der zweite Teil präsentiert unsere kürzlich entwickelte Low-Scaling-*GW* Methode, die im "Vienna *ab-initio* Simulation Package" (VASP), einem weit verbreiteten Programm zur Berechnung der elektronischen Struktur, implementiert wurde. Diese neue Methode ermöglicht schnelle Quasiteilchenberechnungen mit einer Skalierung, die sich in der Systemgröße kubisch verhält und linear in der Anzahl der k-Punkte, die verwendet werden um die Brillouin-Zone zu sampeln. Dadurch werden sowohl die Nachteile der konventionellen *GW* Implementierungen, welche in der Regel auf kleine Systeme beschränkt sind, als auch jene der speicherintensiven Space-Time-Methode überwunden. Es wird ausführlich erläutert, wie eine so günstige Skalierung erreicht werden kann. Danach wird der Erfolg der Methode bei der Berechnung von Quasiteilchen-Energien und Spektralfunktionen typischer Isolatoren, Halbleiter und Metalle diskutiert. Die Ergebnisse werden mit konventionellen *GW* Berechnungen verglichen und es zeigt sich eine sehr hohe Übereinstimmung. Darüber hinaus wurde die neue Methode auch erfolgreich zur Bestimmung der Ionisierungspotentiale und der Elektronenaffinitäten von hundert Closed-Shell-Molekülen angewandt. Die Ergebnisse werden mit experimentellen Daten sowie Ergebnissen aus anderen elektronischen Strukturpaketen verglichen. Insgesamt wurde eine gute Übereinstimmung erzielt. Um diese Übereinstimmung zu erreichen, korrigieren wir die Fehler für endliche Basissätze sowie Fehler, die durch periodisch wiederholte Bilder entstehen. Für die etwas größeren Abweichungen der Elektronenaffinitäten werden mögliche Erklärungen diskutiert. Wegen der geringen Skalierung unserer neuen Methode glauben wir, dass sie ein großes Anwendungspotenzial besitzt, insbesondere für große Einheitszellen. Dies wird im Bereich der Materialmodellierung dazu beitragen, Methoden welche über DFT hinaus gehen zu etablieren.

Die vorgestellte Low-Scaling-GW stellt zwar einen großen Fortschritt gegenüber älterer GW Methoden dar, jedoch wird in der aktuellen Implementierung die Spin-Orbit-Kopplung (SOC) nicht berücksichtigt, während dies bei der herkömmlichen GW Implementierung in VASP möglich ist. In diesem Abschnitt werden daher einige Änderungen an der herkömmlichen Implementierung der GW besprochen, welche es erlauben mäßig große Systeme zu behandeln, bei denen SOC nicht vernachlässigt werden darf. Dies wird durch optimierte imaginäre Zeit/Frequenz Gitter sowie äußerst effiziente diskrete Fourier-Transformationen erreicht, beides Hauptmerkmale der neuen Low-Scaling-GW Methode. Die modifizierte GW Methode wurde für ZnO und CdTe getestet und es zeigt sich eine ausgezeichnete Übereinstimmung mit der herkömmlichen, unmodifizierten GW Implementierung.

Darüber hinaus wird eine teilweise selbst-konsistente Low-Scaling-GW_0r Methode vorgestellt und vorläufige Testergebnisse für Si werden präsentiert. Die Auswirkungen der Selbstkonsistenz werden in Bezug auf Teilchenzahlerhaltung und Bandlücken diskutiert. Abschließend wird noch eine praktikable Möglichkeit zur Kombination unserer Low-Scaling-GW Methode mit der Dynamical-Mean-Field-Theorie (DMFT), d.h. GW+DMFT, vorgestellt. Besonders hervorgehoben und ausführlich besprochen wird die frequenzabhängige, partiell abgeschirmte Wechselwirkung $U(\mathrm{i}\omega)$, welche mittels der Constrained-Random-Phase-Approximation (cRPA) berechnet wird sowie das Double-Counting, das bei GW+DMFT auftritt. Vorläufige Ergebnisse von GW+DMFT für $\mathrm{SrVO_3}$ werden präsentiert. Am Ende der Arbeit befindet sich eine Conclusio in welcher die Ergebnisse und Schlussfolgerungen zusammengefasst werden und ein Ausblick über die weitere Entwicklung skizziert ist.

Es sei noch angemerkt, dass einige Gleichungen und Herleitungen separat in den Anhängen platziert wurden. Obwohl viele dieser Gleichungen zum besseren Verständnis des Haupttextes beitragen, wurde zum Zwecke der besseren Lesbarkeit und Übersicht diese Aufteilung gewählt. Der interessierte Leser wird daher in den Anhängen nützliche und ausführliche Details finden.

Preface

The thesis is divided into three main parts. The first part covers basic textbook and literature knowledge about the electronic structure problem in condensed matter physics. It introduces the theoretical background of the GW method. Starting from density functional theory (DFT), methods beyond DFT, such as DFT+U and hybrid functionals are then introduced, followed by a discussion of their limitations. Afterwards, an overview of the GW approximation is given, setting out from the band gap problem and experimental photoemission spectroscopy. Then, the GW approximation is established starting from many-body perturbation theory. In particular, the one-particle Green's functions, Dyson equation, and Hedin's equations are introduced. At the end, practical implementations of the GW approximation including the conventional GW implementations and the space-time method are discussed. Also, the drawbacks of existing GW implementations are raised, highlighting the need for a low-scaling GW scheme. This provides the motivation for the thesis. The first part lays a solid foundation and builds a consistent terminology for the second part of the thesis.

The second part presents our recently developed low-scaling GW method, which is implemented in the widely used electronic structure code Vienna *ab-initio* simulation package (VASP). This new implementation allows for fast quasiparticle calculations with a scaling that is cubic in the system size and linear in the number of k-points used to sample the Brillouin zone. This overcomes the shortcomings of conventional GW implementations that are usually restricted to small systems. It also addresses some of the drawbacks of the first implementations of the space-time method such as the large memory requirements. An exhaustive explanation regarding how such low scaling can be achieved is given. Then, the success of this method in predicting the quasiparticle energies and spectral functions of typical insulators, semiconductors and metals is discussed. The results are compared to conventional GW calculations, showing very good agreement. In addition, the new method is also successfully applied to predict the ionization potentials and electron affinities of 100 closed shell molecules. The results are compared with the ones from experiments and other electronic structure packages. Overall, good agreement is obtained. In order to achieve this agreement, we correct for finite basis set errors as well as errors introduced by periodically repeated images. For the slightly larger deviations on the electron affinities, tentative explanations are given. Due to the low scaling of our new method, we believe that this method has great potential for applications, in particular for large unit cells. This will greatly help to establish methods beyond DFT in the realm of materials modeling.

However, the spin-orbit coupling (SOC) has not yet been implemented in our low-scaling GW method, which is instead covered by the conventional GW implementation in the VASP code. Hence, some modifications are made to the conventional GW implementation. This makes possible the applications of the conventional GW method to moderately large systems where SOC is non-negligible. This is achieved by employing the optimized imaginary time/frequency grids and efficient discrete Fourier transformations which are the key features used in the low-scaling GW method. Tests of this modified GW implementation on ZnO and CdTe are shown and very good agreement is found compared to the conventional original GW implementation.

Moreover, partially self-consistent low-scaling GW_0r is formulated and preliminary test results on Si are shown. The effects of self-consistency are discussed in terms of particle number conservation and the band gap. Finally, a feasible combination of our low-scaling GW method with dynamical mean field theory (DMFT), i.e., GW+DMFT, is given. Particular emphasis is devoted to the frequency-dependent partially screened interaction $U(\mathrm{i}\omega)$ calculated from the constrained random phase approximation (cRPA) and the double counting that occurs in GW+DMFT. Preliminary results of GW+DMFT calculations on $\mathrm{SrVO_3}$ are given. At the end, the conclusions of the thesis are drawn.

It should be stressed that, in order to keep the thesis more readable, some equations and their derivations used in the main text of the thesis are placed in the appendices. There the readers can find useful additional details.

Contents

II. Methodological Developments 68

6. Low scaling *GW* method: implementation 69

III. Appendix 157

Part I.

Theoretical Background

1. Density functional theory

Density functional theory (DFT) is one of the most successful quantum mechanical approaches to condensed matter of physics. Nowadays, it is routinely applied for calculating the electronic structure, the total energy, forces of solids, and so on. In this section, a detailed overview of DFT is given. First, we start from the total Hamiltonian of the many-atom system and the Born-Oppenheimer approximation. Then, the Hartree and Hartree-Fock approximation are introduced. After that, the DFT based on the Hohenberg-Kohn theorem is built and thereby the Kohn-Sham equation is given. We close this section by the introduction of some practical exchange-correlation functionals.

1.1. The many-body Schrödinger equation and the Born-Oppenheimer approximation

In quantum mechanics, particles' behaviors are described by an equation of states, where a wave function is used to characterize the probability of finding particles in a certain quantum mechanic state. For a stationary system, this quantum mechanic equation is given by the time-independent Schrödinger equation [1,2]

$$\mathrm{H}_{\mathrm{tot}}\Phi = E_{\mathrm{tot}}\Phi, \tag{1}$$

where E_{tot} and Φ are the energy eigenvalues and many-body wave functions of the Hamiltonian $\mathrm{H}_{\mathrm{tot}}$ of the system, respectively. Most physical properties can be associated with energies or differences between energies. The Hamilton operator of a non-relativistic system of N nuclei with coordinates $\mathbf{R}_\alpha$ and charges Z_α, and N_e electrons with coordinates $\mathbf{r}_i$ reads

$$\mathrm{H}_{\mathrm{tot}} = \mathrm{T}_\mathrm{e} + \mathrm{V}_{\mathrm{ee}}(\mathbf{r}) + \mathrm{T}_N + \mathrm{V}_{NN}(\mathbf{R}) + \mathrm{V}_{\mathrm{e}N}(\mathbf{r},\mathbf{R}). \tag{2}$$

Here, T_e and T_N are kinetic energy operators of electrons and nuclei, respectively. V_{ee}, V_{NN} and $\mathrm{V}_{\mathrm{e}N}$ are the Coulomb interactions between electrons and electrons, nuclei and nuclei, and electrons and nuclei. The explicit expressions of them are given by

$$\begin{aligned}
\mathrm{T_e} &= \sum_{i}^{N_\mathrm{e}} -\frac{1}{2}\nabla_i^2 && (3)\\
\mathrm{V_{ee}}(\mathbf{r}) &= \frac{1}{2}\sum_{i}^{N_\mathrm{e}}\sum_{j\neq i}^{N_\mathrm{e}} \frac{1}{|\mathbf{r}_i - \mathbf{r}_j|} && (4)\\
\mathrm{T}_N &= \sum_{\alpha}^{N} -\frac{1}{2}\nabla_\alpha^2 && (5)\\
\mathrm{V}_{NN}(\mathbf{R}) &= \frac{1}{2}\sum_{\alpha}^{N}\sum_{\beta\neq\alpha}^{N} \frac{Z_\alpha Z_\beta}{|\mathbf{R}_\alpha - \mathbf{R}_\beta|} && (6)\\
\mathrm{V}_{\mathrm{e}N}(\mathbf{r},\mathbf{R}) &= \sum_{i}^{N_\mathrm{e}} \underbrace{\Big(\sum_{\alpha}^{N} \frac{-Z_\alpha}{|\mathbf{r}_i - \mathbf{R}_\alpha|}\Big)}_{V_\mathrm{ext}(\mathbf{r}_i)}. && (7)
\end{aligned}$$

Here, Z represents the proton number of a nucleus and $V_\mathrm{ext}(\mathbf{r}_i)$ is the external potential caused by the nuclei, which would be used hereafter. Note that throughout the thesis Hartree atomic units are employed unless otherwise explicitly stated.

With Eq. (2), the Schrödinger equation Eq. (1) becomes

$$\{\mathrm{T_e} + \mathrm{V_{ee}}(\mathbf{r}) + \mathrm{T}_N + \mathrm{V}_{NN}(\mathbf{R}) + \mathrm{V}_{\mathrm{e}N}(\mathbf{r},\mathbf{R})\}\,\Phi(\mathbf{x},\mathbf{R}) = E\Phi(\mathbf{x},\mathbf{R}), \tag{8}$$

where $\mathbf{x} = [(\mathbf{r}_1,\sigma_1),\ldots,(\mathbf{r}_{N_\mathrm{e}},\sigma_{N_\mathrm{e}})]$ combines all translational and spin degrees of freedom of all the electrons and $\mathbf{R} = (\mathbf{R}_1,\ldots,\mathbf{R}_N)$ signifies the nuclear coordinates.

Considering that the nuclear mass exceeds the electron mass by more than three orders of magnitude [3] and thus the time scales also differ, the wave function $\Phi(\mathbf{x},\mathbf{R})$ can be separated into an electronic part $\Psi(\mathbf{x},\mathbf{R})$ and a nuclear wave function $\Pi(\mathbf{R})$. The nuclear wave function is much more localized since $\nabla_\alpha\Pi(\mathbf{R}) \gg \nabla_\alpha\Psi(\mathbf{x},\mathbf{R})$, which allows to separate the Schrödinger equation into two parts:

$$\begin{aligned}
\{\mathrm{T_e} + \mathrm{V_{ee}}(\mathbf{r}) + \mathrm{V}_{\mathrm{e}N}(\mathbf{r},\mathbf{R})\}\,\Psi(\mathbf{x},\mathbf{R}) &= E_0(\mathbf{R})\Psi(\mathbf{x},\mathbf{R}) && (9)\\
\{T_N + V_{NN}(\mathbf{R}) + E_0(\mathbf{R})\}\,\Pi(\mathbf{R}) &= E_\mathrm{tot}\Pi(\mathbf{R}). && (10)
\end{aligned}$$

Note that the nuclear positions $\mathbf{R}$ enter the electronic equation (9) only as parameters and it is possible to use the Born-Oppenheimer approximation, which states that on the timescale of the nuclear motion, the electronic system is always in the instantaneous ground state; the electrons follow the ions adiabatically. Therefore, in the Born-Oppenheimer approximation, the electronic part and nuclear part can be treated separately. For the electronic part, Eq. (9) can be solved with fixed positions of nuclei. After the ground state energy of the electron system $E_0(\mathbf{R})$ has been obtained, the nuclear part Eq. (10) reduces to the Newtons equations of motion if the quantum effects on the motion of the nuclei are neglected. This leads to the so-called *ab initio* molecular dynamics, where the forces that act on the nuclei are calculated from the electronic ground state. Ions are moved according to those forces and for every new ionic configuration, the electronic ground state is re-calculated. In this thesis, however, we restrict ourselves to the electronic part only.

1.2. The Schrödinger equation of electrons

As discussed above, in the Born-Oppenheimer approximation, the electronic Hamiltonian can be solved with fixed positions of nuclei. The Schrödinger equation of electrons then becomes

$$\{\mathrm{T_e} + \mathrm{V_{ee}}(\mathbf{r}) + \mathrm{V}_{\mathrm{e}N}(\mathbf{r}, \mathbf{R})\}\,\Psi(\mathbf{r}) \quad = \quad E\Psi(\mathbf{r}), \tag{11}$$

where E and $\Psi(\mathbf{r})$ are the eigenvalue and eigenfunctions of system of many electrons. Note that without loss of generality, we have suppressed the spin degree of freedom for the sake of brevity. The Hamilton operator $\mathrm{H} = \mathrm{T_e} + \mathrm{V_{ee}}(\mathbf{r}) + \mathrm{V}_{\mathrm{e}N}(\mathbf{r}, \mathbf{R})$ of the Schrödinger equation of many electrons is linear and Hermitian, and hence the eigenfunctions form an orthogonal set satisfying [2]

$$\int d\mathbf{r}_1 \cdots d\mathbf{r}_{N_\mathrm{e}}\, \Psi_k^*(\mathbf{r}_1, \ldots, \mathbf{r}_{N_\mathrm{e}})\Psi_l(\mathbf{r}_1, \ldots, \mathbf{r}_{N_\mathrm{e}}) = \langle\Psi_k|\Psi_l\rangle = \delta_{kl}. \tag{12}$$

By means of an orthogonal basis set, the expectation value of the Hamilton operator H can be expressed by [2]

$$E = \langle H \rangle = \frac{\langle\Psi|\mathrm{H}|\Psi\rangle}{\langle\Psi|\Psi\rangle}. \tag{13}$$

Supposing that the wave function Ψ is normalized, the general energy functional of the many electron system is given by [2]

$$E[\Psi] = \langle\Psi|\mathrm{H}|\Psi\rangle. \tag{14}$$

The ground state of the system is thus obtained by minimizing the energy functional with respect to Ψ [2]

$$E_0 = E[\Psi_0] = \mathrm{Min}\{E[\Psi]\} \quad \text{with respect to } \Psi. \tag{15}$$

All eigenstates can be calculated by finding the solutions of the variational principle $\delta E[\Psi] = 0$.

1.3. Hartree approximation

In the Hartree approximation, the wave function of many electrons $\Psi(\mathbf{r}_1, \ldots, \mathbf{r}_{N_\mathrm{e}})$ is approximated by the multiplication of independent one-electron orbitals

$$\Psi(\mathbf{r}_1, \mathbf{r}_2, \ldots, \mathbf{r}_{N_\mathrm{e}}) = \psi_1(\mathbf{r}_1)\psi_2(\mathbf{r}_2)\ldots\psi_{N_\mathrm{e}}(\mathbf{r}_{N_\mathrm{e}}), \tag{16}$$

where $\psi_1(\mathbf{r}_1)$ is the one-electron orbital of the electron at the position of $\mathbf{r}_1$, and orthogonality of the one-electron orbitals $\int d\mathbf{r}\psi_i^*(\mathbf{r})\psi_j(\mathbf{r}) = \delta_{ij}$ is implicitly assumed. The energy functional $E[\Psi] = \langle\Psi|\mathrm{H}|\Psi\rangle$ in the Hartree approximation can thus be obtained by

$$E[\Psi] = \sum_i \int d\mathbf{r}_i\psi_i^*(\mathbf{r}_i)[-\frac{1}{2}\nabla_i^2 + V_\mathrm{ext}(\mathbf{r}_i)]\psi_i(\mathbf{r}_i) + \frac{1}{2}\sum_i^{N_\mathrm{e}}\sum_{j\neq i}^{N_\mathrm{e}} \int d\mathbf{r}_i d\mathbf{r}_j |\psi_i(\mathbf{r}_i)|^2 \frac{1}{|\mathbf{r}_i - \mathbf{r}_j|} |\psi_j(\mathbf{r}_j)|^2. \tag{17}$$

Ground state are obtained by minimizing the $E[\Psi]$ with respect to Ψ under the constraint of $\int d\mathbf{r}_i|\psi_i(\mathbf{r}_i)|^2 = 1$, yielding

$$\delta\left[E[\Psi] - \sum_i \varepsilon_i(\int d\mathbf{r}_i|\psi_i(\mathbf{r}_i)|^2 - 1)\right] = 0, \tag{18}$$

where $\delta E[\Psi]$ is the variation of functional $E[\Psi]$ and ε_i is just a Lagrange multiplier. Finally, we obtain the following equation

$$[-\frac{1}{2}\nabla_i^2 + V_\mathrm{ext}(\mathbf{r}_i) + \frac{1}{2}\sum_{j\neq i}^{N_\mathrm{e}} \int d\mathbf{r}_j \frac{1}{|\mathbf{r}_i - \mathbf{r}_j|}|\psi_j(\mathbf{r}_j)|^2]\psi_i(\mathbf{r}_i) = \varepsilon_i\psi_i(\mathbf{r}_i). \tag{19}$$

With Eq. (19), the total energy in the Hartree approximation is given by

$$E_\mathrm{H} = \sum_i \varepsilon_i - \frac{1}{2}\sum_i^{N_\mathrm{e}}\sum_{j\neq i}^{N_\mathrm{e}} \int d\mathbf{r}_i d\mathbf{r}_j |\psi_i(\mathbf{r}_i)|^2 \frac{1}{|\mathbf{r}_i - \mathbf{r}_j|} |\psi_j(\mathbf{r}_j)|^2, \tag{20}$$

where the second term is included to avoid double counting.

Defining a charge density operator

$$\hat{\rho}(\mathbf{r}) = \sum_i^{N_e} \delta(\mathbf{r} - \mathbf{r}_i), \tag{21}$$

the density is then obtained by

$$\begin{aligned} n(\mathbf{r}) =& \langle\Psi(\mathbf{r}_1, \mathbf{r}_2, \ldots, \mathbf{r}_{N_e})|\hat{\rho}(\mathbf{r})|\Psi(\mathbf{r}_1, \mathbf{r}_2, \ldots \mathbf{r}_{N_e})\rangle \\ =& \sum_i^{\mathrm{occ}} |\psi_i(\mathbf{r})|^2. \end{aligned} \tag{22}$$

With the density, the Hartree potential is defined by

$$V_{\mathrm{H}}(\mathbf{r}) = \int d\mathbf{r}' \frac{1}{|\mathbf{r}-\mathbf{r}'|} n(\mathbf{r}'). \tag{23}$$

By defining an effective mean-field potential $V_{\mathrm{eff}}(\mathbf{r}) = V_{\mathrm{ext}}(\mathbf{r}) + V_{\mathrm{H}}(\mathbf{r})$, Eq. (19) reduces to

$$[-\frac{1}{2}\nabla_i^2 + V_{\mathrm{eff}}(\mathbf{r})]\psi_i(\mathbf{r}) = \varepsilon_i \psi_i(\mathbf{r}). \tag{24}$$

From Eq. (24) one can deduce that the interactions felt by one electron from all other electrons is described by a mean-field Hartree potential $V_{\mathrm{H}}(\mathbf{r})$, which is further absorbed in an effective potential $V_{\mathrm{eff}}(\mathbf{r})$. This equation should be solved self-consistently because $V_{\mathrm{eff}}(\mathbf{r})$ depends on the charge density $n(\mathbf{r})$, which further depends on the one-electron orbital $\psi_i(\mathbf{r})$. It should be noted that the Hartree approximation considers the electron-electron mean-field electrostatic interactions only, whereas the exchange and correlation effects are completely neglected.

1.4. Hartree-Fock approximation

Because electrons are fermions, Pauli's exclusion principle [3] and the antisymmetry of the many-body wave function, when two electrons exchange, should be satisfied. However, this is not true in the Hartree approximation. To overcome the drawbacks of the Hartree approximation, Slater-determinant [2,4] is better suited to describe the wave function of the many-electron system. This is the so-called Hartree-Fock (HF) approximation. The Slater-determinant is constructed by a sum of products of one-electron orbitals $\psi_i(\mathbf{r}_i)$

$$\Psi_{\mathrm{HF}} = \frac{1}{\sqrt{N_{\mathrm{e}}!}} \begin{vmatrix} \psi_1(\mathbf{r}_1) & \psi_2(\mathbf{r}_1) & \cdots & \psi_{N_{\mathrm{e}}}(\mathbf{r}_1) \\ \psi_1(\mathbf{r}_2) & \psi_2(\mathbf{r}_2) & \cdots & \psi_{N_{\mathrm{e}}}(\mathbf{r}_2) \\ \vdots & \vdots & \ddots & \vdots \\ \psi_1(\mathbf{r}_{N_{\mathrm{e}}}) & \psi_2(\mathbf{r}_{N_{\mathrm{e}}}) & \cdots & \psi_{N_{\mathrm{e}}}(\mathbf{r}_{N_{\mathrm{e}}}). \end{vmatrix} \tag{25}$$

The prefactor $\frac{1}{\sqrt{N_{\mathrm{e}}!}}$ normalizes the many-electron wave function. It is trivial to show that the following two equations hold in the HF approximation

$$\Psi_{\mathrm{HF}}(\mathbf{r}_1, \ldots, \mathbf{r}_i, \ldots, \mathbf{r}_j, \ldots, \mathbf{r}_{N_{\mathrm{e}}}) = -\Psi_{\mathrm{HF}}(\mathbf{r}_1, \ldots, \mathbf{r}_j, \ldots, \mathbf{r}_i, \ldots, \mathbf{r}_{N_{\mathrm{e}}}) \tag{26}$$

$$\Psi_{\mathrm{HF}}(\mathbf{r}_1, \ldots, \mathbf{r}_i, \ldots, \mathbf{r}_j, \ldots, \mathbf{r}_{N_{\mathrm{e}}}) = 0, \quad \text{if } \mathbf{r}_i = \mathbf{r}_j. \tag{27}$$

This indicates that the Slater-determinant as a wave function of the many-electron system automatically satisfies the antisymmetry and Pauli's exclusion principle.

After the Slater-determinant is inserted in Eq. (14), the total energy of the many-electron system in the HF approximation is given by [2]

$$E_{\mathrm{HF}}[\psi] = \langle \Psi_{\mathrm{HF}} | \mathrm{H} | \Psi_{\mathrm{HF}} \rangle = \sum_{i=1}^{N_\mathrm{e}} H_i + \frac{1}{2} \sum_{i=1}^{N_\mathrm{e}} \sum_{j=1}^{N_\mathrm{e}} (J_{ij} - K_{ij}), \tag{28}$$

where

$$H_i = \int d\mathbf{r}\, \psi_i^*(\mathbf{r}) \Big[-\frac{1}{2}\nabla_i^2 + V_{\mathrm{ext}}(\mathbf{r}) \Big] \psi_i(\mathbf{r}) \tag{29}$$

$$J_{ij} = \int d\mathbf{r}\, d\mathbf{r}'\, \psi_i^*(\mathbf{r}) \psi_i(\mathbf{r}) \frac{1}{|\mathbf{r} - \mathbf{r}'|} \psi_j^*(\mathbf{r}') \psi_j(\mathbf{r}') \tag{30}$$

$$K_{ij} = \int d\mathbf{r}\, d\mathbf{r}'\, \psi_i^*(\mathbf{r}) \psi_j(\mathbf{r}) \frac{1}{|\mathbf{r} - \mathbf{r}'|} \psi_j^*(\mathbf{r}') \psi_i(\mathbf{r}'). \tag{31}$$

It should be noted that H_i are one-electron integrals, whereas the Coulomb integrals J_{ij} and exchange integrals K_{ij} are two-electron integrals. Also, one should note that constraint of $i \neq j$ in the summation of the second term in Eq. (28) is eliminated, because $i = j$ contribution is cancelled by $(J_{ij} - K_{ij})$.

The minimization of Eq. (28) under the constraints of $\int \psi_i(\mathbf{r}) \psi_j(\mathbf{r}) d\mathbf{r} = \delta_{ij}$ gives rise to a set of one-electron HF differential equations [2, 3]

$$\hat{F} \psi_i(\mathbf{r}) = \sum_{j=1}^{N_\mathrm{e}} \varepsilon_{ij}^{\mathrm{HF}} \psi_j(\mathbf{r}), \tag{32}$$

where the Fock operator $\hat{F}$ is given by

$$\hat{F} = -\frac{1}{2}\nabla^2 + V_{\mathrm{ext}}(\mathbf{r}) + \hat{j} - \hat{k}, \tag{33}$$

and the Coulomb operator $\hat{j}$ and the exchange operator $\hat{k}$ are defined by [2]

$$\begin{aligned} [\hat{j}f](\mathbf{r}) &= \sum_{i=1}^{N_\mathrm{e}} \int d\mathbf{r}'\, \psi_i^*(\mathbf{r}') \psi_i(\mathbf{r}') \frac{1}{|\mathbf{r} - \mathbf{r}'|} f(\mathbf{r}) \\ [\hat{k}f](\mathbf{r}) &= \sum_{i=1}^{N_\mathrm{e}} \int d\mathbf{r}'\, \psi_i^*(\mathbf{r}') f(\mathbf{r}') \frac{1}{|\mathbf{r} - \mathbf{r}'|} \psi_i(\mathbf{r}). \end{aligned} \tag{34}$$

It can be seen that the operator $\hat{j}$ is local, whereas the operator $\hat{k}$ is nonlocal, because its action on a particular coordinate $\mathbf{r}$ depends also on the integration over all other coordinates $\mathbf{r}'$.

Since there exist many possible solutions of the HF equations, it is always possible to find a unitary transformation matrix U that diagonalizes the HF matrix $\epsilon_{mn}^{\mathrm{HF}}$ such that

$$\sum_{mn} [U]_{im}^{\dagger} \epsilon_{mn}^{\mathrm{HF}} U_{nj} = \epsilon_i' \delta_{ij} \tag{35}$$

and

$$\psi_i'(\mathbf{r}) = \sum_j U_{ji}\psi_j(\mathbf{r}) \tag{36}$$

hold [5,6]. This leads to the canonical HF equations [5,6]

$$\hat{F}\psi_i'(\mathbf{r}) = \epsilon_i'\psi_i'(\mathbf{r}). \tag{37}$$

Similar to the Hartree equation, this equation should be solved self-consistently as well because the Fock operator is dependent of one-electron orbital $\psi_i'(\mathbf{r})$. Finally, the total energy of the many-electron system in the HF approximation can be calculated by [2]

$$E_{\mathrm{HF}} = \sum_i^{N_\mathrm{e}} \epsilon_i' - \frac{1}{2}\sum_{i=1}^{N_\mathrm{e}}\sum_{j=1}^{N_\mathrm{e}}(J_{ij} - K_{ij}), \tag{38}$$

where the Coulomb integrals J_{ij} and exchange integrals K_{ij} are calculated by using canonical HF orbitals $\psi_i'(\mathbf{r})$. Although the HF approximation explicitly treats the exchange effects by antisymmetric wave functions and also is self-interaction free due to the cancellation in K and J, the method does not incorporate electron-electron correlations between electrons with opposite spins. In other words, the HF ansatz is too restrictive, since general many-electron wave functions $\Psi(\mathbf{r}_1, \ldots, \mathbf{r}_n)$ cannot be represented by a single Slater determinant only. Instead, it should be more accurately described by adding the double, triple, $\cdots$, excited Slater determinants [5]. That is exactly what the configuration interaction (CI) [7] method does. The difference between the exact total energy E_{tot} of the many electron system and the HF energy E^{HF} is defined as the correlation energy [2,5]

$$E_\mathrm{c} = E_{\mathrm{tot}} - E_{\mathrm{HF}}. \tag{39}$$

1.5. Overview of DFT

1.5.1. Hohenberg-Kohn theorem

The Hartree-Fock approximation has already given some indications as to how to obtain the total energy from first-principles calculations. However, it only accounts for the exact exchange interactions between two electrons of same spins, whereas the correlation interactions of opposite spins are completely neglected. Therefore, the Hartree-Fock approximation yields too large band gaps for insulators, underestimates binding energies (by 50-70%) and predicts metals to be unstable (to name a few).

A satisfactory *ab initio* method is based on DFT, which owes to the fundamental theorems formulated by Hohenberg and Kohn in 1964 on the inhomogeneous electron gas [8]. They showed that for an interacting electron gas in an external potential $V_{\mathrm{ext}}(\mathbf{r})$, there exists an universal energy functional of the density $F[n(\mathbf{r})]$ which yields the correct ground state energy E_0 by minimizing the total energy $E_{\mathrm{HK}}[n(\mathbf{r})]$ with respect to the charge density $n(\mathbf{r})$ [8]

$$\begin{aligned} E_{\mathrm{HK}}[n(\mathbf{r})] =& \langle\Psi|T_{\mathrm{e}}|\Psi\rangle + \langle\Psi|V_{\mathrm{ee}}|\Psi\rangle + \langle\Psi|V_{\mathrm{ext}}|\Psi\rangle \\ =& \underbrace{T[n(\mathbf{r})] + E_{\mathrm{ee}}[n(\mathbf{r})]}_{F[n(\mathbf{r})]} + \int d\mathbf{r}\, V_{\mathrm{ext}}(\mathbf{r}) n(\mathbf{r}). \end{aligned} \tag{40}$$

and they proved that [8]

1. $F[n(\mathbf{r})]$ is a unique functional of the density $n(\mathbf{r})$, i.e., for an N_e electron system, there do not exist two ground state wave functions $\Psi_1 \neq \Psi_2$ resulting in the same density $n(\mathbf{r})$.

2. $E_{\mathrm{HK}}[n(\mathbf{r})] \geq E_{\mathrm{GS}}[n_0(\mathbf{r})]$

   The energy functional $E_{\mathrm{HK}}[n(\mathbf{r})]$ obeys a variational principle and always results in energies larger or equal to the ground state energy $E_{\mathrm{GS}}[n_0(\mathbf{r})]$.

3. $E_{\mathrm{HK}}[n_0(\mathbf{r})] = E_{\mathrm{GS}}[n_0(\mathbf{r})]$

   The energy functional $E_{\mathrm{HK}}[n(\mathbf{r})]$ reaches the ground state energy at the ground state density $n_0(\mathbf{r})$.

It should be noted that in DFT the electron density $n(\mathbf{r})$ is introduced as a natural variable, since it determines the number of electrons $N_{\mathrm{e}} = \int d\mathbf{r}\, n(\mathbf{r})$ and thus the external potential $V_{\mathrm{ext}}(\mathbf{r})$, which in turn determines all electronic properties of the system. Since $F[n(\mathbf{r})]$ describes all interactions beyond the external electron-nuclei electrostatic interaction, the functional should account for the kinetic energy of the electrons as well as all the electron-electron interactions including the electron-electron electrostatic interactions, exchange and correlation effects. Minimization of the energy functional $E_{\mathrm{HK}}[n(\mathbf{r})]$ gives rise to the exact ground state density $n_0(\mathbf{r})$. However, the exact functional $F[n(\mathbf{r})]$ is unknown and approximations are required [2].

1.5.2. Kohn-Sham DFT

In 1965, Kohn and Sham proposed an approximation for the functional $F[n(\mathbf{r})]$, which assumes that there exists an auxiliary non-interacting system that has exactly the same charge density as the interacting system [9]. The many-electron wave function of the auxiliary non-interacting system can thus be described by the Hartree wave function

$$\Psi(\mathbf{r}_1, \mathbf{r}_2, \ldots, \mathbf{r}_{N_e}) = \psi_1(\mathbf{r}_1)\psi_2(\mathbf{r}_2)\ldots\psi_{N_e}(\mathbf{r}_{N_e}). \tag{41}$$

The density of the auxiliary non-interacting system is given by

$$n(\mathbf{r}) = \sum_i^{\text{occ}} |\psi_i(\mathbf{r})|^2, \tag{42}$$

which is also the density of the real interacting system. $F[n]$ is defined as [9]

$$F[n] = T_0[n] + E_H[n] + E_{\text{xc}}[n], \tag{43}$$

where $T_0[n]$ is the kinetic energy of the auxiliary non-interacting system, which is straightforwardly obtained by

$$T_0[n(\mathbf{r})] = \sum_i^{\text{occ}} \langle\psi_i| - \frac{1}{2}\nabla_i^2|\psi_i\rangle. \tag{44}$$

$E_H[n]$ is the electron-electron electrostatic interaction energy, i.e., Hartree energy, which is given by

$$E_H[n(\mathbf{r})] = \frac{1}{2}\int d\mathbf{r}d\mathbf{r}'\frac{n(\mathbf{r})n(\mathbf{r}')}{|\mathbf{r}-\mathbf{r}'|}. \tag{45}$$

$E_{\text{xc}}[n]$ is the exchange correlation functional of the interacting system, which accounts for all the effects beyond the non-interacting ansatz. That is, it includes all energy contributions beyond the kinetic energy of free electrons and electrostatic Coulomb repulsions

$$E_{\text{xc}}[n] = T[n] - T_0[n] + E_{\text{ee}}[n] - V_H[n]. \tag{46}$$

Using these definitions for the functional $F[n]$ and the density $n(\mathbf{r})$, the so-called KS equations are obtained by applying the variational principle to the KS energy functional [9]

$$\begin{gathered}\left(-\frac{1}{2}\nabla^2 + V_{\text{eff}}(\mathbf{r})\right)\psi_n(\mathbf{r}) = \epsilon_n\,\psi_n(\mathbf{r})\\ V_{\text{eff}}(\mathbf{r}) = V_{\text{ext}}(\mathbf{r}) + V_{\text{H}}(\mathbf{r}) + V_{\text{xc}}(\mathbf{r}).\end{gathered} \tag{47}$$

Here, the energy values ϵ_n are called KS eigenvalues. The effective potential is the sum of the external potential V_{ext}, the Hartree potential V_{H} and the so-called exchange-correlation potential defined by

$$V_{\text{xc}}(\mathbf{r}) = \frac{\delta E_{\text{xc}}[n]}{\delta n(\mathbf{r})}. \tag{48}$$

Since $V_{\text{eff}}(\mathbf{r})$ depends on the density $n(\mathbf{r})$, which depends futher on $\psi_n(\mathbf{r})$ by definition, one has to solve this set of equations self-consistently, provided that E_{xc} is known. The iterative solution is shown in Fig. 1. First, the initial guess for the electron density is constructed from overlapping atomic densities. Then, the effective potential $V_{\text{eff}}(\mathbf{r}) = V_{\text{ext}}(\mathbf{r}) + V_{\text{H}}[n(\mathbf{r})] + V_{\text{xc}}[n(\mathbf{r})]$ and hereby the KS Hamiltonian $\text{H}^{\text{KS}} = -\frac{1}{2}\nabla^2 + V_{\text{eff}}(\mathbf{r})$ are constructed. Third, the eigenvalue problem is solved by diagonalizing the matrix H^{KS} in terms of the chosen basis sets such as plane waves. This results in a new set of KS orbitals from which one can construct a new density and thus a new Hamiltonian. These steps are repeated until the density is converged. Once the converged ground state density $n_0(\mathbf{r})$ is found, one could calculate the total energy, its first derivative with respect to nuclei coordinates (forces), band structure, density of states, and so on. The KS total energy can then be rewritten as [9]

$$E_{\text{KS}} = \sum_n \epsilon_n - E_{\text{H}}[n(\mathbf{r})] + E_{\text{xc}}[n(\mathbf{r})] - \int V_{\text{xc}}(\mathbf{r})n(\mathbf{r})d\mathbf{r}. \tag{49}$$

Although KS-DFT has already witnessed its success in solid states of physics and chemistry, such as the good agreement of KS-DFT band structure with experimental photoemission spectroscopies, the KS-DFT eigenvalues do not have any physical interpretation except for the maximum occupied KS orbital energy, which corresponds to the negative ionization potential (IP) [10–12] for insulators and the negative work function for metals. This is because the KS-DFT eigenvalue is just a Lagrange multiplier as a result of the variation principle. Therefore, KS-DFT fails to predicted excited state properties [13]. For example, KS-DFT with the local density approximation (LDA) [9] or generalized gradient approximation (GGA) always yields underestimated band gaps for semiconductors and insulators [14]. This is due to the so-called "self-interaction error" inherent within the LDA or GGA energy functionals, which lack a derivative discontinuity with respect to a change of the number of electrons. To solve the band gap problem, approximations beyond DFT should be made. The *GW* approximation has been proved to be the best choice so far to predict quasiparticle (QP) energies. We will discuss this point in more details in the Section (5). On the other hand, due to the "self-interaction error", local (LDA) and semilocal (GGA) functionals will prefer to spread out charge over the fragments instead of localizing charge at one of the fragments, since fractional occupancies are incorrectly preferred over integer occupancies [15]. Therefore, DFT also fails to describe strongly correlated systems, where the electrons are localized.

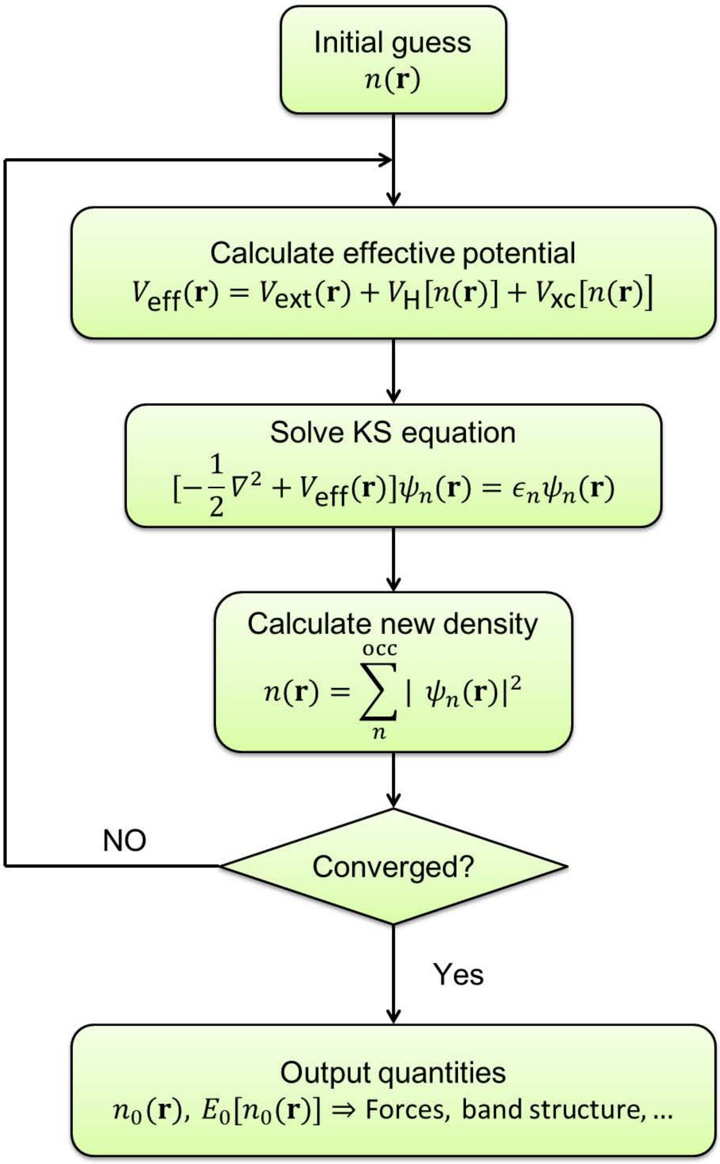

Figure 1: A flow chart of the iteration scheme in solving the KS equation. First, the initial guess for the electron density is constructed from overlapping atomic densities. Then, the effective potential $V_{\text{eff}}(\mathbf{r}) = V_{\text{ext}}(\mathbf{r}) + V_{\text{H}}[n(\mathbf{r})] + V_{\text{xc}}[n(\mathbf{r})]$ and hereby the KS Hamiltonian $\text{H}^{\text{KS}} = -\frac{1}{2}\nabla^2 + V_{\text{eff}}(\mathbf{r})$ are constructed. Third, the eigenvalue problem is solved by diagonalizing the matrix H^{KS} in terms of the chosen basis sets such as plane waves. This results in a new set of KS orbitals from which one can construct a new density and thus a new Hamiltonian. These steps are repeated until the density is converged. Once the converged ground state density $n_0(\mathbf{r})$ is found, one could calculate the total energy, its first derivative with respect to nuclei coordinates (forces), band structure, density of states, and so on.

1.5.3. The exchange correlation functionals: LDA and GGA

As mentioned above, in KS-DFT, the system of N_e interacting electrons is mapped to an auxiliary system of N_e non-interacting electrons with exactly the same density as the original system. The KS-DFT many-electron wave function is replaced by the Hartree many-electron wave function, which does not meet the antisymmetry of fermions. The kinetic energy is given in terms of the non-interacting auxiliary system. All the effects beyond the electrostatic interactions and the kinetic energy difference between real and auxiliary systems are all accounted for by an exchange and correlation energy functional $E_\mathrm{xc}[n(\mathbf{r})]$. KS-DFT is thus an exact theory provided that the exchange-correlation energy functional $E_\mathrm{xc}[n(\mathbf{r})]$ is exact and known.

Unfortunately, the exact form of the exchange correlation functional is unknown and approximations are required. Kohn and Sham [9] derived the exchange correlation energy functional of the homogenous electron gas. It is proved that this functional works very well even for the real systems, assuming the local density $n(\mathbf{r})$ to be locally approximately uniform. This is the so-called local density approximation (LDA) [9]

$$E_\mathrm{xc}^\mathrm{LDA}[n] = \int d\mathbf{r}\ \epsilon_\mathrm{xc}^\mathrm{HEG}[n(\mathbf{r})]\ n(\mathbf{r}). \tag{50}$$

The exchange correlation energy density functional $\epsilon_\mathrm{xc}^\mathrm{HEG}$ is derived from a homogenous electron gas with a density equal to the local density $n(\mathbf{r})$. Normally, $\epsilon_\mathrm{xc}^\mathrm{HEG}[n(\mathbf{r})]$ is separated into exchange and correlation parts [2,6]

$$\epsilon_\mathrm{xc}^\mathrm{HEG}[n(\mathbf{r})] = \epsilon_\mathrm{x}^\mathrm{HEG}[n(\mathbf{r})] + \epsilon_\mathrm{c}^\mathrm{HEG}[n(\mathbf{r})], \tag{51}$$

where $\epsilon_\mathrm{x}^\mathrm{HEG}$ is given by the Dirac exchange energy functional [16]

$$\epsilon_\mathrm{x}^\mathrm{HEG}[n(\mathbf{r})] = -\frac{3}{4}(\frac{3}{\pi})^{\frac{1}{3}}\Big(n(\mathbf{r})\Big)^{\frac{1}{3}}, \tag{52}$$

and $\epsilon_\mathrm{c}^\mathrm{HEG}$ is given by an analytic fit to quantum Monte Carlo simulations [17–19].

It is observed that the LDA works well for systems with nearly homogeneous local densities. However, it fails for systems with inhomogeneous local densities, for instance, defects, interfaces, and surfaces. Thus, more accurate approximations are required. To this end, Perdew *et.al* [20] proposed the generalized gradient approximation (GGA). As its name implies, the resulting functional depends not only on the electronic density but also its local gradient [20]

$$
\begin{aligned}
E_{\mathrm{xc}}^{\mathrm{PBE}}[n] &= E_{\mathrm{x}}^{\mathrm{PBE}}[n] + E_{\mathrm{c}}^{\mathrm{PBE}}[n] && (53)\\
E_{\mathrm{x}}^{\mathrm{PBE}}[n] &= \int d\mathbf{r}\, \epsilon_{\mathrm{x}}^{\mathrm{HEG}}[n(\mathbf{r})]\, F_{\mathrm{x}}[n(\mathbf{r}), \nabla n(\mathbf{r})]\, n(\mathbf{r}) && (54)\\
E_{\mathrm{c}}^{\mathrm{PBE}}[n] &= \int d\mathbf{r} \left(\epsilon_{\mathrm{c}}^{\mathrm{HEG}}[n(\mathbf{r})] + H[n(\mathbf{r}), \nabla n(\mathbf{r})] \right) n(\mathbf{r}). && (55)
\end{aligned}
$$

For the definition of the gradient contributions of the enhancement factor F_x and the factor H, we refer the readers to Refs. [20–22]

It should be noted that there are several flavors of the GGA functionals in literatures, among which two functionals are widely used. The first one is the so-called PBE functional [20], and the second one is called PBEsol functional [22], which is optimized for solids and surfaces. Although both are optimized for different conditions, they are based on the formulas in Eq. (54) and Eq. (55) and differ only in few parameters.

2. DFT in practice

2.1. Bloch theorem and plane wave expansion

In solid state systems, the systems of interest normally show a certain translational symmetry in the space. Thus, periodic boundary conditions (PBC) [23–25] can be used, allowing to greatly simplify the calculations of real system. Under PBC, the system is represented by a unit cell, that is periodically repeated in space and spanned by the cell vectors $\mathbf{a}_1$, $\mathbf{a}_2$, and $\mathbf{a}_3$ [26]. Any lattice point $\mathbf{R}$ can then be constructed by

$$\mathbf{R} = n_1\mathbf{a}_1 + n_2\mathbf{a}_2 + n_3\mathbf{a}_3, \tag{56}$$

using the three integer coefficients n_1, n_2, and n_3. Associated with the Bravais lattice, there is a reciprocal lattice

$$\mathbf{G} = m_1\mathbf{b}_1 + m_2\mathbf{b}_2 + m_3\mathbf{b}_3, \tag{57}$$

where any reciprocal lattice vector $\mathbf{G}$ is given by the superposition of the reciprocal basis vectors $\mathbf{b}_1$, $\mathbf{b}_2$, and $\mathbf{b}_3$. Here, m_1, m_2, and m_3 are again integer numbers. The reciprocal basis vectors are calculated from its real space counterparts

$$\mathbf{b}_1 = \tfrac{2\pi}{\Omega}(\mathbf{a}_2 \times \mathbf{a}_3) \tag{58}$$

$$\mathbf{b}_2 = \tfrac{2\pi}{\Omega}(\mathbf{a}_3 \times \mathbf{a}_1) \tag{59}$$

$$\mathbf{b}_3 = \tfrac{2\pi}{\Omega}(\mathbf{a}_1 \times \mathbf{a}_2), \tag{60}$$

where $\Omega = \mathbf{a}_1(\mathbf{a}_2 \times \mathbf{a}_3)$ is the volume of unit cell in the real space. Real and reciprocal basis vectors satisfy $\mathbf{b}_i \cdot \mathbf{a}_j = 2\pi\delta_{ij}$.

The Schrödinger equation of a single electron under PBC is given by [26]

$$\left(-\frac{1}{2}\nabla^2 + V(\mathbf{r})\right)\psi(\mathbf{r}) = E\psi(\mathbf{r}), \tag{61}$$

where $V(\mathbf{r})$ is a periodic potential $V(\mathbf{r} + \mathbf{R}) = V(\mathbf{r})$. For this periodic potential, the Bloch theorem states that all eigenstates $\psi(\mathbf{r})$ of the one-electron Hamiltonian can be expressed as a product of a plane wave phase factor $\mathbf{e}^{i\mathbf{kr}}$ and a periodic function $u_{n,\mathbf{k}}(\mathbf{r})$ that has exactly the same periodicity as the Bravais lattice [26]

$$\psi_{n,\mathbf{k}}(\mathbf{r}) = \mathbf{e}^{i\mathbf{kr}}u_{n,\mathbf{k}}(\mathbf{r}) \tag{62}$$

$$u_{n,\mathbf{k}}(\mathbf{r} + \mathbf{R}) = u_{n,\mathbf{k}}(\mathbf{r}). \tag{63}$$

Here, the quantum numbers n and $\mathbf{k}$ denote the band index and Bloch wave vector in the reciprocal space, respectively.

It is known that any periodic function can be expanded into a plane wave basis set [24]

$$u_{n,\mathbf{k}}(\mathbf{r}) = \sum_{\mathbf{G}} C_{n,\mathbf{k},\mathbf{G}}\ \mathbf{e}^{i\mathbf{G}\mathbf{r}}. \tag{64}$$

Hence, it follows that the one-electron wave function can be expanded by

$$\psi_{n,\mathbf{k}}(\mathbf{r}) = \sum_{\mathbf{G}} C_{n,\mathbf{k},\mathbf{G}}\ \mathbf{e}^{i(\mathbf{k}+\mathbf{G})\mathbf{r}}. \tag{65}$$

In practice, however, the plane waves have been truncated within a cut off $|\mathbf{G}_{max}|$, which corresponds to the energy cut off $E_{\text{cut}} = |\mathbf{k} + \mathbf{G}_{max}|^2/2$. Furthermore, the Bloch wave vectors $\mathbf{k}$ can be restricted to the Brillouin zone (BZ), which is the first Wigner Seitz cell in the reciprocal space. This is because all other Bloch states $\mathbf{k}$ can be calculated by a Bloch state of the BZ $\mathbf{k}_{\text{BZ}}$ and an additional reciprocal lattice vector $\mathbf{G}$ [26]

$$\mathbf{k} = \mathbf{k}_{\text{BZ}} + \mathbf{G}. \tag{66}$$

This implies that the Bloch states (eigenvalues and eigenfunctions) are periodic in the reciprocal space [26]. To further reduce the computational effort, symmetry is used. That is, only $\mathbf{k}$ points within the irreducible wedge of the BZ (IBZ) are considered with weights $\omega_{\mathbf{k}}$. In this case, the summation over $\mathbf{k}$ points for a periodic function $F(\mathbf{k})$ in the whole BZ reduces to

$$\frac{1}{\Omega_{\text{BZ}}} \int_{BZ} d\mathbf{k} F(\mathbf{k}) = \frac{\Omega}{(2\pi)^3} \int_{BZ} d\mathbf{k} F(\mathbf{k}) = \sum_{\mathbf{k}}^{BZ} F(\mathbf{k}) = \sum_{\mathbf{k}}^{\text{IBZ}} \omega_{\mathbf{k}} F(\mathbf{k}), \tag{67}$$

where $\mathbf{k}$ point grids and the weights $\omega_{\mathbf{k}}$ are usually generated by the Monkhorst and Pack scheme [27]. Ω_{BZ} is the volume of the BZ and Ω is the volume of the real-space unit cell.

The band structure of solids is given by $\epsilon_n(\mathbf{k})$, which is a function of $\mathbf{k}$ vector for a specific band n. The density of states (DOS) for each band n is given by integrating over the IBZ [26]

$$D_n(\epsilon) = \frac{\Omega}{(2\pi)^3} \int_{BZ} d\mathbf{k} \delta\big(\epsilon - \epsilon_n(\mathbf{k})\big) = \sum_{\mathbf{k}}^{\text{IBZ}} \omega_{\mathbf{k}} \delta\big(\epsilon - \epsilon_n(\mathbf{k})\big). \tag{68}$$

Thus, the total DOS, including the contributions of all bands, is obtained by $D(\epsilon) = \sum_n D_n(\epsilon)$.

2.2. The frozen core approximation and PS potential

As discussed in Section (2.1), to make possible the first-principles calculations of real systems, PBC has been employed. In addition, we have expanded the Bloch wave function with the

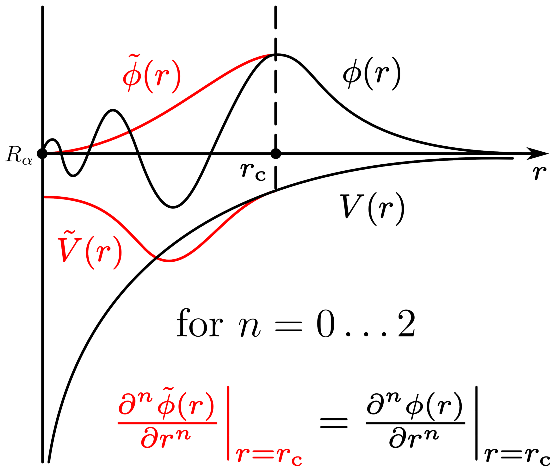

Figure 2: A schematic illustration of the pseudo potential inside and outside the core region of an atom at position R_α. The black and red lines represent the exact and pseudo potential (wave function), respectively. This figure is adapted from the thesis of Leif E. H. [28].

plane wave basis set that is truncated within a energy cut off E_{cut} [25] for practical calculations. Despite of these simplifications , it is still computationally demanding for a many-body system including core and valence electrons. Therefore, further approximations are needed.

One widely used approximation to reduce the number of electrons is the so-called frozen core approximation. The idea of this approximation is to freeze the core electrons within the inner shells. This approximation is justified because the core electrons almost do not contribute to the bonding. Instead, only the outmost valence electrons participate in the bonding. With the frozen core approximation, we can restricted ourselves to the calculations of wave functions of the valence electrons only.

Even though the number of electrons has been significantly reduced by the frozen core approximation, calculations of the wave functions are still demanding because of the strong oscillations of the wave functions around the core region due to the constraint of orthogonality between valence and core electron wave functions. As a consequence, a large basis set of plane waves is required to accurately describe the wave functions of the valence electrons in the core region, which definitely increases the computational cost.

In order to overcome this problem, pseudo (PS) potentials come into play. As shown in Fig. 2, the PS potential $\tilde{V}$, which is much smother, substitutes the exact potential V within the core region. The core region is defined by a sphere around the atomic position R_α with a cut off radius r_c. The PS potential is constructed such that the PS wave functions $\tilde{\phi}$ are nodeless within the core region and reproduce the scattering properties of the exact wave functions ϕ [25]. Moreover, the PS potential and the PS wave functions coincide with their exact counterparts outside the core region and at the boundary $r = r_c$, the PS wave functions are equal to the exact wave functions up to their second radial derivatives. Since the PS wave functions are much smoother than their exact wave functions, usage of PS potential can thus reduce the number of plane-wave basis sets significantly.

2.3. The PAW method

PS potential methods have been used extensively from roughly 1980 on [29]. The biggest merit of these methods is their formal simplicity, but unfortunately this simplicity has a price: first-row elements, transition metals, and rare-earth elements are computationally demanding to treat with standard norm-conserving PS potentials [30]. To solve this problem, ultrasoft PS potentials (US-PP) have been introduced by Vanderbilt [31]. Blöchl [32] further developed the US-PP concept by combining ideas from PS potential and linearized augmented-plane-wave (LAPW) method in a conceptually elegant framework, called the projector augmented-wave method (PAW). Afterwards, Kresse [30] established the relationship between US-PP and PAW methods: the only difference between Vanderbilt's US-PP and Blöchl's PAW approaches lies in the one-center terms.

Actually, the PAW method is a full potential method in the sense that it restores the correct features of the exact AE wave function. This is achieved by adding correction terms within the core regions of the atoms. Specifically, on the plane-wave grid, the Hamiltonian is represented in a PS-potential-like manner, but pseudo wave functions are not correctly normalized [33]. In order to correct for this error, local compensation charges are added around each atom such that the final charge density distribution has exactly the same multipoles and moments as the exact all-electron (AE) charge density. The electrostatic potential determined from this charge distribution is basically exact in the interstitial region, but the kinetic energy and the potentials are not accurately represented inside the PAW spheres [33]. To make up for the error, the PS wave functions and AE wave functions are reconstructed inside the PAW spheres, and the corresponding one-center energy terms are subtracted and added from the energy [33]. The

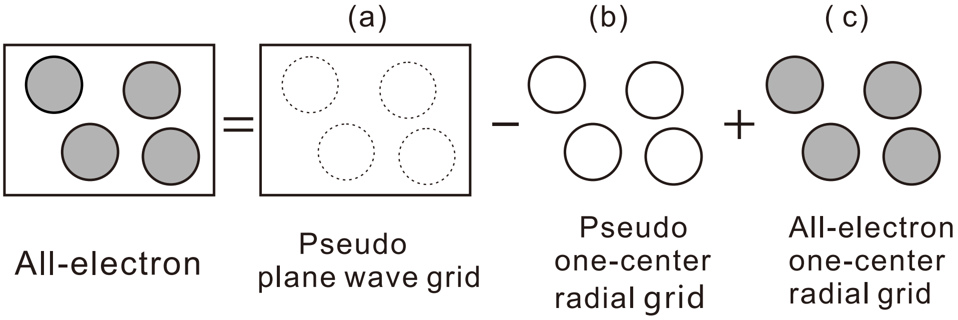

Figure 3: An illustration of additive augmentation in the PAW method. (a) Pseudized quantities are defined on a regular plane wave grid in the entire space. (b) Pseudo wave functions are reconstructed inside spheres and the corresponding one-center terms are subtracted. (c) The all-electron wave functions are reconstructed and the corresponding one-center energies are added. This figure is adapted from Ref. [33].

general idea of PAW method is schematically shown in Fig. 3.

Within the framework of the PAW method, the all-electron orbital $\psi_{n\mathbf{k}}$ is represented by the corresponding pseudo orbital $\tilde{\psi}_{n\mathbf{k}}$ via the linear transformation [30]

$$|\psi_{n\mathbf{k}}\rangle = |\tilde{\psi}_{n\mathbf{k}}\rangle + \sum_{\mu} \left(|\phi_\mu\rangle - |\tilde{\phi}_\mu\rangle\right) \langle \tilde{p}_\mu | \tilde{\psi}_{n\mathbf{k}}\rangle, \tag{69}$$

where ϕ_μ and $\tilde{\phi}_\mu$ are all-electron and pseudo partial waves, respectively. $\tilde{p}_\mu$ are the projectors, which are dual to the $\tilde{\phi}_\mu$ ($\langle \tilde{p}_i | \tilde{\phi}_j \rangle = \delta_{i,j}$) within the argumentation sphere. The index $\mu = (\mathbf{R}_\mu, n_\mu, l_\mu, m_\mu)$ is an abbreviation for the atomic site $\mathbf{R}_\mu$, the energy quantum number n_μ and angular momentum numbers (l_μ, m_μ) characterizing the solution of the Schrödinger equation for a reference atom.

The pseudo orbital $\tilde{\psi}_{n\mathbf{k}}$ can be expressed in terms of a plane wave expansion, while the radial wave functions are calculated by solving the radial Schrödinger equation of a single atom for each atom type within the core regions and stored on a radial grid [25, 30, 32]. Note that the correction of the PS wave functions only applies within the core regions of the atoms Ω_r, since the PS wave functions coincide with the AE wave functions outside of the core region.

With Eq. (69), the transformation operator that restores the AE wave function is given by [32]

$$\hat{T} = \hat{1} + \sum_{\mu} \left(|\phi_\mu\rangle - |\tilde{\phi}_\mu\rangle\right) \langle \tilde{p}_\mu |. \tag{70}$$

It allows to calculate expectation values of quasi-local operator A. By quasi-local operator we mean that $\langle \mathbf{r}|A|\mathbf{r}'\rangle = 0$ holds if $\mathbf{r} \neq \mathbf{r}'$. Specifically,

$$\begin{aligned}\langle A\rangle &= \sum_{n\mathbf{k}} f_{n\mathbf{k}}\langle\psi_{n\mathbf{k}}|A|\psi_{n\mathbf{k}}\rangle \\ &= \underbrace{\sum_{n\mathbf{k}} f_{n\mathbf{k}}\langle\tilde{\psi}_{n\mathbf{k}}|A|\tilde{\psi}_{n\mathbf{k}}\rangle}_{\tilde{A}} + \underbrace{\sum_{\mu,\nu}\rho_{\mu\nu}\langle\phi_\mu|A|\phi_\nu\rangle}_{A^1} - \underbrace{\sum_{\mu,\nu}\rho_{\mu\nu}\langle\tilde{\phi}_\mu|A|\tilde{\phi}_\nu\rangle}_{\tilde{A}^1},\end{aligned} \tag{71}$$

where the Hermitian one-center density matrix $\rho_{\mu\nu}$ is defined as

$$\rho_{\mu\nu} = \sum_{n\mathbf{k}} f_{n\mathbf{k}}\langle\tilde{\psi}_{n\mathbf{k}}|\tilde{p}_\mu\rangle\langle\tilde{p}_\nu|\tilde{\psi}_{n\mathbf{k}}\rangle, \tag{72}$$

with $f_{n\mathbf{k}}$ being the occupancy for the states $\psi_{n\mathbf{k}}$. The term $\tilde{A}$ arises from the contribution of PS wave functions. A^1 and $\tilde{A}^1$ are the contributions from AE and PS one centered partial waves, respectively. The essential point that makes the PAW method so efficient is that the terms with the PS wave functions $\tilde{\psi}_{n\mathbf{k}}(\mathbf{r})$ and the PS (AE) partial wave functions $\tilde{\phi}_\mu$ (ϕ_μ) are set apart so that mixed terms that involve $|\tilde{\psi}_{n\mathbf{k}}\rangle$ and $|\tilde{\phi}_\mu\rangle$ ($|\phi_\mu\rangle$) are vanishing in calculating the expectation value of quasi-local operator.

3. DFT+U method

3.1. Introduction to DFT+U method

In DFT all the effects beyond the electrostatic interactions have been described by an approximate exchange and correlation functional such as LDA and GGA. However, these approximate functionals do not exactly account for the exchange and correlation effects, leading to an incomplete cancellation of the electronic self-interaction contained in the density-density Coulomb integrals. Therefore, LDA or GGA tend to over-delocalize valence electrons and over-stabilize metallic ground states. In addition, exchange and correlation effects included in DFT are static and mean-field-like, and orbitals are not treated individually. Thus, for systems containing a partially filled d or f shell one obtains a partially-filled band with a metallic-type electronic structure. All these errors lead to DFT's dramatic failures in predicting the insulating character of the so-called Mott insulator, where the insulating character of the ground state arises from the strong Coulomb repulsions between electrons that prevail over the kinetic energy, forcing the electrons to localize on atomic-like orbitals [34]. For example, late transition metal oxides, which are insulators, are inaccurately predicted to be metals by the LDA due to the lack of exchange.

To rationalize the physics of correlated materials, the most simplest model is the Hubbard model [35]. In its simplest form, the one-band Hubbard Hamiltonian is given by

$$H = t \sum_{\langle i,j \rangle,\sigma} (c^{\dagger}_{i,\sigma} c_{j,\sigma} + h.c.) + U \sum_{i} n_{i,\uparrow} n_{j,\downarrow}, \tag{73}$$

where $\langle i, j \rangle$ represents nearest-neighbor atomic sites. $c^{\dagger}_{i,\sigma}$ and $c_{i,\sigma}$ are, respectively, the creation and annihilation operator for electrons of spin σ on atomic site i. $n_{i,\sigma} = c^{\dagger}_{i,\sigma} c_{i,\sigma}$ is the number operator.

Apparently, the Hubbard model includes two terms. The first term describes the electron hoping from one atomic site to its neighbors with a hoping amplitude t that is proportional to the bandwidth of the valence bands. The second term, however, accounts for the electronic Coulomb interactions of the opposite spins on the same atomic site. In normal materials, the hopping term dominates ($t \gg U$), leading to an itinerant band picture, which could be described well by DFT. In contrast, in the correlated materials the second term prevails so that electrons cannot hop easily because a sufficient energy is required to overcome the large Coulomb repulsion from other electrons on neighbor sites. In other words, the large Coulomb repulsion makes the electrons more localized, resulting in an insulating behavior. In the large U limit, the Hubbard model gives an atomic-picture-like solution.

Motivated by the Hubbard model, DFT+U method was proposed [36–39]. For a good review of the DFT+U method, we refer to Ref. [40]. Also, we refer the interested readers to the chapter 4 of the book [41], where one can find helpful discussions about the DFT+U method. As its name implies, DFT+U is a method that adds the orbital-dependent Coulomb U and exchange interactions J onto some localized states of the system, which are absent in DFT, so that the delocalized states, which are itinerant, are treated by DFT only, whereas the localized states are dealt with DFT+U. Due to the introduction of the on-site Coulomb U and exchange J corrections on some localized states, the DFT+U method gives a qualitative improvement compared to DFT, not only for excited-state properties such as energy gaps but also for ground-state properties such as magnetic moments and interatomic exchange parameters [40]. Also, the DFT+U method gives a correct orbital polarization and a corresponding Jahn-Teller distortion as well as polaron formation [40]. In addition, the incorporation of U and J does not significantly increase the computational effort compared to DFT, so that the DFT+U method become a popular method to study the Mott insulators such as transition metal and rare-earth metal oxides, long-ranged ordered magnetism and polaron physics [40]. In the following, a general introduction of the DFT+U method is given.

3.2. Formulations of the DFT+U method

The general idea of the DFT+U method is to add the orbital-dependent Coulomb and exchanges corrections onto the DFT, hence within the DFT+U framework the total energy of a system can be expressed as [41]

$$E_{DFT+U}[\rho(\mathbf{r})] = E_{DFT}[\rho(\mathbf{r})] + E_{Hub}[n^{I\sigma}_{mm'}] - E_{dc}[n^{I\sigma}], \tag{74}$$

where E_{Hub} is a term that contains electron-electron interactions as modeled in the Hubbard Hamiltonian. It is a function of electron occupation numbers $n^{I\sigma}_{mm'}$. $E_{dc}[n^{I\sigma}]$ is the so-called the double counting term. Because in $E_{DFT}[\rho(\mathbf{r})]$ partial exchange-correlations have already been taken into account, the interactions contained in DFT should be eliminated from the additive Hubbard-like correction term $E_{Hub}[n^{I\sigma}_{mm'}]$ to avoid double counting. The occupation numbers $n^{I\sigma}_{mm'}$ is usually defined as projections of occupied Kohn-Sham orbitals ($\psi^{\sigma}_{n\mathbf{k}}$) onto the states of a localized basis set (ϕ^I_m):

$$n^{I\sigma}_{mm'} = \sum_{n\mathbf{k}} f^\sigma_{n\mathbf{k}} \langle \phi^I_m | \psi^\sigma_{n\mathbf{k}} \rangle \langle \psi^\sigma_{n\mathbf{k}} | \phi^I_{m'} \rangle, \tag{75}$$

where $f^\sigma_{n\mathbf{k}}$ is the Fermi-Dirac occupations of the KS states with n and $\mathbf{k}$ being the band and k point indexes, respectively. Index m labels the localized states of the same atomic site I. It should be noted that the choice of the localized basis set is not unique. They can be chosen from either atomic orbitals or maximally localized Wannier functions [42, 43]. Compared to the Hubbard model in Eq. (73), it can be clearly seen that the DFT+U method corresponds to substituting the number operators appearing in Eq. (73) with their (mean-field) average on the occupied manifolds of the system.

Although the general energy functional of the DFT+U method has been given, there are many flavors and implementations regarding the form of the Hubbard-like energy functional and the double counting term. Anisimov *et al.* [37–39] first proposed an energy functional that uses the on-site Coulomb interaction U

$$E_{DFT+U}[\rho(\mathbf{r})] = E_{DFT}[\rho(\mathbf{r})] + \underbrace{\sum_I \frac{U^I}{2} \sum_{m,\sigma\neq m',\sigma'} n^{I\sigma}_m n^{I\sigma'}_{m'}}_{E_{Hub}[n^{I\sigma}_{mm'}]} - \underbrace{\sum_I \frac{U^I}{2} n^I (n^I - 1)}_{E_{dc}[n^{I\sigma}]}, \tag{76}$$

where $n^{I\sigma}_m$ are the diagonal elements of occupation number matrix, i.e., $n^{I\sigma}_m = n^{I\sigma}_{mm}$ and $n^I = \sum_{m,\sigma} n^{I\sigma}_m$. With this in hands, Eq. (76) can be simplified to

$$E_{DFT+U}[\rho(\mathbf{r})] = E_{DFT}[\rho(\mathbf{r})] + \sum_I \frac{U^I}{2} \left[\sum_{m,\sigma} n^{I\sigma}_{mm} - \sum_{m,\sigma} n^{I\sigma}_{mm} n^{I\sigma}_{mm} \right]. \tag{77}$$

Taking the variational derivative of the DFT+U energy functional $E_{DFT+U}[\rho(\mathbf{r})]$ with respect to $\langle \phi^I_m |$, one obtains

$$V_{DFT+U} | \psi^\sigma_{n\mathbf{k}} \rangle = V_{DFT} | \psi^\sigma_{n\mathbf{k}} \rangle + \sum_{I,m} U^I \left(\frac{1}{2} - n^{I\sigma}_m \right) | \phi^I_m \rangle \langle \phi^I_m | \psi^\sigma_{n\mathbf{k}} \rangle. \tag{78}$$

As evident from Eq. (78), the Hubbard-like potential [second term in Eq. (78)] is repulsive for less than half-filled orbitals ($n^{I\sigma}_m < 1/2$), whereas it is attractive for more than half-filled orbitals ($n^{I\sigma}_m > 1/2$). This means that the DFT+U method favors the localization of electrons, i.e., $n^{I\sigma}_m \to 1$ or $n^{I\sigma}_m \to 0$. For an occupied band, the energy is increased by $U^I/2$, while for an unoccupied band the energy is decreased by $U^I/2$. Therefore, an energy gap appears with the size of approximately U^I, consistent with the picture of the Hubbard model.

Although the DFT+U formulation presented in Eq. (78) captures the main essence of the DFT+U method, it is not invariant under rotation of the atomic orbital basis set used to define the occupation of d states $n^{I}_{m\sigma}$, which produces an undesirable dependence of the results on the specific choice of the localized basis set [41]. To solve these problems, A. Liechtenstein and coworkers [44] introduced a basis set independent formulation of DFT+U [41].

$$
\begin{aligned}
E_{DFT+U}[\rho(\mathbf{r})] = E_{DFT}[\rho(\mathbf{r})] + \frac{1}{2}\sum_{m_1m_2m_3m_4,\sigma,I}\left\{V_{m_1m_3m_2m_4}n^{I\sigma}_{m_1m_2}n^{I-\sigma}_{m_3m_4} + (V_{m_1m_3m_2m_4} - V_{m_1m_3m_4m_2})n^{I\sigma}_{m_1m_2}n^{I\sigma}_{m_3m_4}\right\} \\
+ \sum_{I}\left\{\frac{U^I}{2}n^I(n^I-1) - \frac{J^I}{2}[n^{I,\uparrow}(n^{I,\uparrow}-1) + n^{I,\downarrow}(n^{I,\downarrow}-1)]\right\}.
\end{aligned}
\tag{79}
$$

Here, the four-index super matrix $V_{m_1m_3m_2m_4}$ represents the bare (unscreened) electron-electron interaction, which is defined by [41]

$$
V_{m_1m_3m_2m_4} = \langle m_1m_3|\frac{1}{|\mathbf{r}-\mathbf{r}'|}|m_2m_4\rangle\delta_{\sigma_1,\sigma_2}\delta_{\sigma_3,\sigma_4}, \tag{80}
$$

with $|m\rangle$ being the spherical harmonics. $V_{m_1m_3m_2m_4}$ can be further expressed by Slater integrals [41]

$$
V_{m_1m_3m_2m_4} = \sum_k a_k(m_1,m_2,m_3,m_4)F^k, \tag{81}
$$

where $0 \le k \le 2l$ (l is the angular moment of the localized manifold; $-l \le m \le l$) and factors a_k can be obtained as products of Clebsch-Gordan coefficients [41]

$$
a_k(m_1,m_2,m_3,m_4) = \frac{4\pi}{2k+1}\sum_{q=-k}^{k}\langle lm_1|Y_{kq}|lm_2\rangle\langle lm_3|Y^*_{kq}|lm_4\rangle. \tag{82}
$$

For p electrons, only F^0 and F^2 are non-vanishing. For d electrons, apart from F^0 and F^2, F^4 is required, too. For f electrons, F^0,F^2, F^4 and F^6 are all required [41]. However, in practice these integrals are often treated as parameters, i.e., adjusted to reach agreement with experiments in terms of equilibrium volume, magnetic moment, or band gap. They are normally specified in terms of an effective on-site Coulomb and exchange parameters, U and J. Taking d electrons for instance

$$
U = \frac{1}{(2l+1)^2}\sum_{m_1.m_2}V_{m_1m_2m_1m_2} = F^0 \tag{83}
$$

$$
J = \frac{1}{2l(2l+1)}\sum_{m_1.m_2\neq m_1}V_{m_1m_2m_2m_1} = \frac{F^2+F^4}{14}, \tag{84}
$$

assuming F^4/F^2 has the same value as in an isolated atom (this value is 0.625 in VASP). Usually, U and J are extracted from constrained-LDA [45] or the constrained random phase approximation (cRPA) [46,47].

However, in most cases, a much simpler expression of the Hubbard correction (E_{Hub}), introduced by Dudarev *et al.* [48], is actually used and implemented

$$\begin{aligned} E_{DFT+U}[\rho(\mathbf{r})] =& E_{DFT}[\rho(\mathbf{r})] + E_{Hub}[n^{I\sigma}_{mm'}] - E_{dc}[n^{I\sigma}] \\ =& E_{DFT}[\rho(\mathbf{r})] + \sum_{I} \frac{U^I - J^I}{2} \left[(n^I)^2 - \sum_{\sigma} \mathrm{Tr}[(\mathbf{n}^{I\sigma})^2] \right] - \sum_{I} \frac{U^I - J^I}{2} n^I (n^I - 1) \\ =& E_{DFT}[\rho(\mathbf{r})] + \sum_{I,\sigma} \frac{U^I - J^I}{2} \mathrm{Tr}[\mathbf{n}^{I\sigma}(1 - \mathbf{n}^{I\sigma})]. \end{aligned} \tag{85}$$

Here, Tr represents the trace of the matrix. It was claimed [48] that Eq. (85) bridges the orbital-dependent formulation by Anisimov *et al.* [38] [Eq. (76)] with the rotationally invariant functional proposed by Liechtenstein *et al.* [Eq. (79)], retaining the simplicity of the former and the covariant character of the latter. It should be noted that in Dudarev's approach the parameters U and J do not enter separately, only the difference ($U - J$) is meaningful. The matrix of the one-electron potential is given by the derivative of Eq. (85) with respect to occupation number matrix $n^{I\sigma}_{ij}$

$$[V_{DFT+U}]^{I\sigma}_{ji} = \frac{\delta E_{DFT+U}}{\delta n^{I\sigma}_{ij}} = \frac{\delta E_{DFT}}{\delta n^{I\sigma}_{ij}} + (U^I - J^I)(\frac{1}{2}\delta_{ji} - n^{I\sigma}_{ji}). \tag{86}$$

3.3. Double counting

It should be noted that in the above formulations of the DFT+U total energy functional, the so-called "fully localized limit" (FLL) [40] double counting was employed. In this limit, Bloch states are assumed to be localized atomic states. Since DFT (LDA or GGA) treats the Hartree term exact for filled shells, there should be no corrections to the energy. Therefore, FLL uses the form of E_{Hub} for filled shells and also shells with other fillings as the double counting correction. The main effect of FLL is to decrease the energy of states that are more than half-filled, but increase the energy of states that are less than half-filled, yielding the energy difference of $U_{\mathrm{eff}} = U - J$ between occupied and unoccupied states. However, FLL will do nothing for the cases without spin symmetry breaking or orbital polarization. In addition, FLL has no correction to the total energy for completely closed/empty shells, but changes their density of states. For instance, even fully closed or empty states experience a shift, which is, however, purely a double counting artifact.

Another most often used double counting form is "around mean field" (AMF) [37], which assumes that DFT obtains a mean field solution of the Hubbard term E_{Hub}. Therefore, AMF uses the form of E_{Hub} with the average filling $n^{I\sigma} = \frac{1}{2l+1}\sum_m n_m^{I\sigma}$ as the double counting correction. The resulting DFT+U potential is given as:

$$V_{DFT+U}|\psi_{n\mathbf{k}}^{\sigma}\rangle = V_{DFT}|\psi_{n\mathbf{k}}^{\sigma}\rangle + \sum_{I,m} U^I \left(n^{I\sigma} - n_m^{I\sigma}\right) |\phi_m^I\rangle\langle\phi_m^I|\psi_{n\mathbf{k}}^{\sigma}\rangle. \tag{87}$$

In contrast to the DFT+U potential with the FLL double counting correction in Eq. (78), Eq. (87) uses the average filling $n^{I\sigma}$ instead of half filling $\frac{1}{2}$. The resulting effect of AMF is to push down the energy of states that are more than filled on average $n^{I\sigma}$, but push up the energy of states that are less than filled on average $n^{I\sigma}$. Thus, the "reference point" for energy shift in AMF is the average orbital occupation instead of half filling $\frac{1}{2}$ in FLL. Compared with FLL, the effect of such shifts is usually smaller since the "reference point" is the average filling. Since the form of the exchange-correlation functional in DFT is unknown, which kind of double counting correction is more correct and should be used in realistic calculations is not known a priori. One should carefully double-check the results, whether the double counting corrections are important.

3.4. Some remarks on the DFT+U method

Due to the on-site U correction to the localized states on which the electrons are localized, electrons with opposite spins would prefer to occupy different sites. In terms of the one-band Hubbard model, the lower and upper Hubbard bands form due to the introduction of U. The Mott gap formed between the lower and upper Hubbard bands increases as the U increases. Therefore, the DFT+U method can give a very good description of Mott physics. The electrons with U corrections are localized so that ordered magnetic states and polarons can be described as well. In addition, DFT+U is as fast as DFT, which promotes its great applications in large systems such as *ab initio* studies of surfaces and defects in transition metal oxides.

Although the DFT+U method describes well the Mott insulating states in the limit of strong localization and band gaps with a reasonable U parameter, it works well only if the states above and below the Fermi energy are all localized d or f states. However, often the valence bands are made up by O-2p states and then the DFT+U method fails. In addition, it is a intrinsically static and mean-field-like method, so that it cannot capture multideterminantal features such as the transfer of the spectral weights and correlated metals. Thus, for systems with partially filled 3d shells which are inherent metals, for instance, transition metals, the DFT+U method often produces nonphysical results since it splits the partially filled bands. Even though the U and J parameters could in principle be calculated by the constrained-LDA or cRPA, in practice, they are often adjusted to reach agreement with experiment in terms of equilibrium volume, magnetic moment, or band gap. Moreover, the existing implementations employ effective interaction parameters that correspond to atomically averaged quantities and are not individual orbital dependent. Furthermore, due to the lack of a precise diagrammatic representation of the DFT total energy, the so-called double counting term occurring in the DFT+U functional is not uniquely defined. For instance, using the FLL double counting would induce an unphysical shift for empty states even in $4d^0$ or $5f^0$ transition metal oxides. Despite the above-mentioned disadvantages of the DFT+U method, it is still widely used because of its efficiency, and it is often used to compare to other more expensive and accurate methods, such as hybrid functionals and dynamical mean field theory.

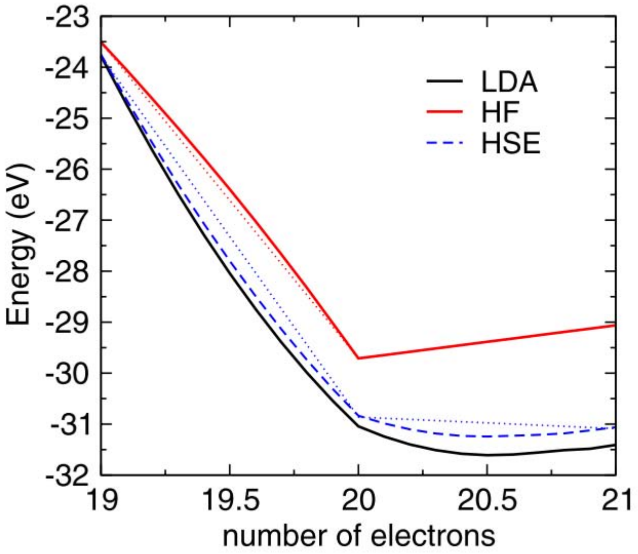

Figure 4: The total energy with respect to the number of electrons for the LDA, HF, and HSE for a Si_4H_4 cluster. The dotted straight lines denote the ideal exact solutions. This figure is adapted from Ref [15].

4. Hybrid functional approach

4.1. Introduction to hybrid functional approach

It has been shown [10, 49] from ensemble arguments that the total energy should be linear between integer numbers of electrons. Unfortunately, all the usual approximations fail for this property. Hartree-Fock calculation yields a concave behavior lying above the ideal straight line, whereas LDA underestimates the discontinuities at integer numbers, yielding a convex behavior below the ideal straight line, as shown in Fig. 4. This results in the localization error of HF and delocalization error of LDA or GGA. LDA or GGA lower the energy in spreading electrons out so that a fractional number of electrons is preferred. Instead, HF find it energetically favorable to localize electrons so that they integrate to an integer [50,51]. The localization error of HF stems from the fact that the HF approximation completely neglects the correlations of the electrons, thus overestimating the band gap. Due to the delocalization error of LDA or GGA, the electron density artificially spreads out because delocalization reduces the spurious self-repulsion of electrons. This gives rise to an inaccurate estimation of the ionization energy and the electron affinity, resulting in an underestimation of band gaps, see Fig. 5 for comparison between HF and DFT in the band gap predictions. Since the HF approximation overestimates the band gap, while KS-DFT underestimates it, it would be expected that the combination of two methods might improve the band gap. Indeed, inclusion of partial exact exchange not only yields better band

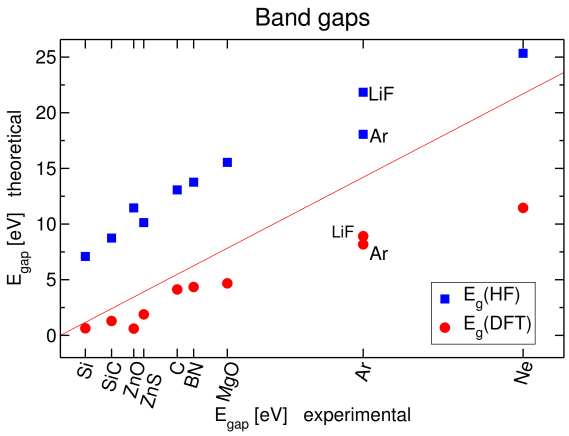

Figure 5: HF and DFT band gaps compared to the experimental values (red line). This figure is adapted from chapter 15 of Ref. [56].

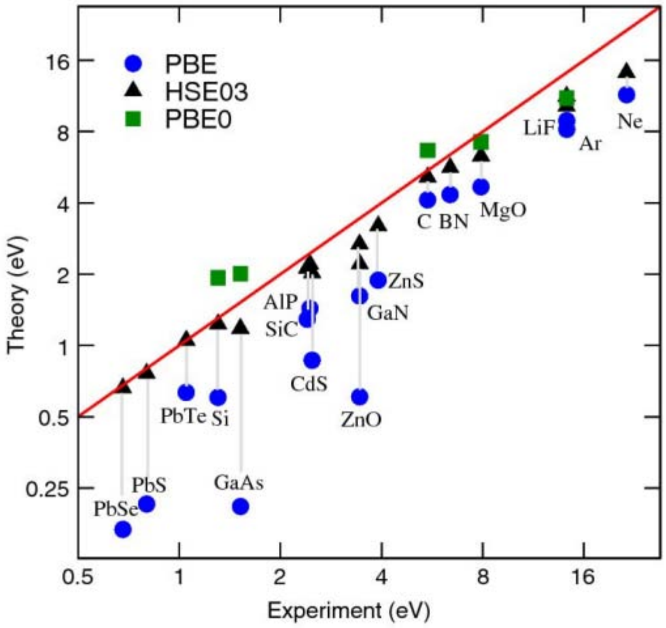

Figure 6: Comparison between computed (PBE, PBE0 and HSE) and experimental band gaps. This figure is taken from Ref. [57].

gaps (see Fig. 6), but also improves the description of the lattice constants, cohesive energies and electronic structures [52, 53]. In the following, a general introduction to the hybrid functionals approach will be given. For a more detailed discussion on hybrid functional approach, we refer to the reviews by Benjamin *et al.* [54] and Franchini [55] and chapter 15 of the book by Franchini [56].

4.2. Formulations of hybrid functional approach

In order to combine HF and DFT, starting from the adiabatic connection formula, Becke [58] first proposed a half-half hybrid functional

$$E_{XC}^{\text{Hybrid}} = \frac{1}{2}E_X^{HF} + \frac{1}{2}E_{XC}^{DFT}. \tag{88}$$

Afterwards, he introduced a practical parametric hybrid functional termed as B3LYP [59, 60], which includes exact exchange and LDA- and GGA-corrected exchange and correlation and becomes very popular in the quantum chemistry. The B3LYP incorporates only 20% of the exact HF exchange and has the form

$$E_{XC}^{\text{B3LYP}} = E_{XC}^{LDA} + \alpha_1(E_X^{HF} - E_X^{LDA}) + \alpha_2(E_X^{GGA} - E_X^{LDA}) + \alpha_3(E_C^{GGA} - E_C^{LDA}), \tag{89}$$

where the three mixing parameters $\alpha_1 = 0.20$, $\alpha_2 = 0.72$, and $\alpha_3 = 0.71$ are determined by fitting experimental atomization energies, electron and proton affinities, and ionization potentials of the molecules in Poples G1 data set [59, 60]. Although the B3LYP has been successfully used for atomic and molecular calculations, its applications to periodic systems is not that satisfactory. For instance, for the free-electron gas the B3LYP functional does not reproduce the correct exchange-correlation energy [56].

For solid-state applications, a more appropriate hybrid functional is PBE0, which was proposed by Perdew, Burke, and Ernzerhof [61]

$$E_{\text{xc}}^{\text{PBE0}} = \alpha E_{\text{x}}^{\text{HF}} + (1-\alpha)E_{\text{x}}^{\text{DFT}} + E_{\text{c}}^{\text{DFT}}, \tag{90}$$

where the parameter $\alpha = 1/4$ was suggested, which yields the best atomization energies of typical molecules [61]. PBE0 reproduces the homogeneous electron gas limit and significantly outperforms B3LYP in solids, in particular in systems with itinerant characters such as metals and small-gap semiconductors [62].

However, calculating the long-range (LR) exchange interactions in PBE0 can be computationally very demanding, and particularly difficult for metals where a dense k point sampling is required, resulting in very slow convergence [62, 63]. To address this issue, Heyd, Scuseria, and Ernzerhof [64] suggested a hybrid functional where the exchange interaction is split into a short-range (SR) and LR part

$$\frac{1}{|\mathbf{r}-\mathbf{r}'|} = \underbrace{\frac{\text{erfc}(\mu|\mathbf{r}-\mathbf{r}'|)}{|\mathbf{r}-\mathbf{r}'|}}_{\text{SR}} + \underbrace{\frac{\text{erf}(\mu|\mathbf{r}-\mathbf{r}'|)}{|\mathbf{r}-\mathbf{r}'|}}_{\text{LR}}, \tag{91}$$

where μ defines the characteristic length of the SR exchange interaction [65–67]. Now only the SR exchange part is evaluated by mixing the HF and PBE exchange energies $E_{\mathrm{x}}^{\mathrm{HF,SR}}$ and $E_{\mathrm{x}}^{\mathrm{PBE,SR}}$, whereas the correlation energy and the LR exchange part are calculated using the PBE functionals $E_{\mathrm{c}}^{\mathrm{PBE}}$ and $E_{\mathrm{x}}^{\mathrm{PBE,LR}}$

$$E_{\mathrm{xc}}^{\mathrm{HSE}} = \alpha E_{\mathrm{x}}^{\mathrm{HF,SR}}(\mu) + (1-\alpha) E_{\mathrm{x}}^{\mathrm{PBE,SR}}(\mu) + E_{\mathrm{c}}^{\mathrm{PBE}} + E_{\mathrm{x}}^{\mathrm{PBE,LR}}(\mu). \tag{92}$$

From Eq. (92) it can be seen that the HSE functional can be tuned by controlling two parameters: the proportion of the exact exchange α and the boundary between the SR and LR interaction region μ. For $\alpha = 1/4$ and $\mu \to \infty$, the HSE functional reduces to PBE, and for $\alpha = 1/4$ and $\mu = 0$, the HSE functional is equivalent to the PBE0 functional. To achieve a good compromise between computational effort and accuracy, $\alpha = 1/4$ and $\mu = 0.2$ Å^{-1} were suggested [63, 64]. Due to the split of the exchange interaction, HSE is much faster to compute compared to PBE0 without loss of accuracy.

4.3. Some remarks on HSE

Since the exact exchange energy shows a negative curvature with respect to the number of electrons, which could partially cancel the positive curvature appearing in LDA or GGA and thus reduce the self-interaction error, HSE has been successfully and intensively applied to many kinds of systems in terms of crystal structure, cohesive energy and bulk moduli [63], electronic structures [55, 68], and phone spectra [69]. Nevertheless, HSE is not entirely self-interaction-free, see Fig. 4. In addition, it is still limited to small systems due to its relatively heavy computational cost, which scales quadratically with the number of k points. Furthermore, there are two empirical adjustable parameters (the proportion of the exact exchange α, and the boundary between the SR and LR interaction regime μ) that could be tuned, and hence it is not *ab initio*, despite the fact that the commonly used α=1/4 and $\mu = 0.2$ yield satisfactory results for many systems. However, these two parameters are in principle system dependent. Since HSE in some sense is related to the GW approximation, it was suggested that the optimal parameter α is approximately equal to the inverse of infinite dielectric constant, i.e., $\alpha \approx 1/\epsilon_\infty$ [56]. Still, ϵ_∞ has to be calculated before the HSE calculations. In the next section, the GW approximation will be introduced.

5. GW approximation

5.1. Band gap problem

The infamous band gap problem typically arises from the derivative discontinuity of the exact exchange correlation functional, which occurs when the number of electrons is increased from $N_\mathrm{e} - \varepsilon$ to $N_\mathrm{e} + \varepsilon$ [11]

$$C = \lim_{\varepsilon \to 0^+} \left. \frac{\delta E_\mathrm{xc}[n]}{\delta n(\mathbf{r})} \right|_{N_\mathrm{e}+\varepsilon} - \lim_{\varepsilon \to 0^+} \left. \frac{\delta E_\mathrm{xc}[n]}{\delta n(\mathbf{r})} \right|_{N_\mathrm{e}-\varepsilon} . \tag{93}$$

Thus, the band gap should be calculated by means of

$$E_\mathrm{g} = \epsilon_\mathrm{CBM}(N_\mathrm{e}) - \epsilon_\mathrm{VBM}(N_\mathrm{e}) + C, \tag{94}$$

where CBM and VBM indicate the conduction band minimum and valence band maximum, respectively. However, existing approximate functionals such as LDA or GGA lack any such derivative discontinuity and thus fail to describe the electron addition and removal process. They also do not allow to determine C, leading to an underestimation of the band gaps compared to the exact ones [13]. On the other hand, the band gap refers to excited states, but DFT is just a ground state theory and there is no formal justification to interpret DFT eigenvalues as quasiparticle (QP) energies. Actually, the DFT eigenvalues are just Lagrange multipliers in obtaining the KS equation by the variational principle.

The DFT+U method is, however, designed for systems with localized states split by the Coulomb repulsion, forming the upper and lower Hubbard bands. Though in some cases, U is adjusted to match the experimental gap, it is still limited to a one-electron single-determinant picture and cannot be expected to correct for inherent shortcomings of LDA or GGA, i.e., the lack of a derivative discontinuity in the exchange correlation functional. In addition, applications to transition metals would lead to unreasonable results. Due to the introduction of the exact exchange, the HSE approach in general improves the agreement with experiments not only in ground state properties (lattice constants and cohesive energies), but also in excited state properties such as band gaps and photoemission spectra. However, it is not *ab initio* because there are two empirical parameters that can be tuned to yield good agreement with experiments. Furthermore, it is still a single-determinant (mean-field) method, that by construction lacks any fluctuations.

The GW approximation to the exchange correlation is derived systematically from many-body perturbation theory. The form of the self-energy in the GW approximation is similar as in the HF approximation but the Coulomb interaction is dynamically screened, remedying the most serious deficiency of the HF approximation. The GW approximation of Hedin [70, 71] has been widely and successfully applied to the calculations of QP energies for many kind of systems (for reviews see Refs. [13, 72, 73]), because it provides a good approximation for the electron's self-energy by including many-body effects in the electron-electron interaction. This is achieved by screening the bare exchange interaction with the inverse frequency-dependent dielectric function. The self-energy in the GW approximation is therefore non-local and energy dependent. It is found that the QP band structures obtained from the GW approximation agree well with the spectra measured from direct photoemission (PES) and inverse photoemission (IPES). In the following, starting from the introduction of photoemission spectroscopy, I will introduce the one particle Green's function, Dyson equation and Hedin equations, and then give an exhaustive formulation of the GW approximation followed by an overview of existing practical implementations.

5.2. Photoemission spectroscopy and quasiparticle

Fig. 7 shows the process of direct photoemission (PES) and inverse photoemission (IPES) spectroscopy. In PES, an incident beam of photons with an energy of $h\nu$ hits the surface of the material and kicks electrons out from occupied bands to the vacuum level with remaining kinetic energy E_{kin}, i.e., PES is a 'photon-in-electron-out' process. By measuring the kinetic energy E_{kin} of emitted electrons and using the energy conservation, one can obtain the energy levels for the occupied band

$$E_n^{\text{occ}} = E_{\text{kin}} - h\nu. \tag{95}$$

In the process of IPES, a beam of electrons with a kinetic energy E_{kin} hits the material and the impinging electrons relax into unoccupied states by emitting photons with energy $h\nu$, i.e., IPES is a 'electron-in-photon-out' process. Again, by measuring the energy of emitted photons $h\nu$ and using the energy conservation, one can obtain the energy levels for the unoccupied band

$$E_n^{\text{unocc}} = E_{\text{kin}} - h\nu. \tag{96}$$

In theory, the measured PES and IPES spectra can be explained by the total density of states $D(\omega)$, which can be calculated by integrating the spectral function $A_{n\mathbf{k}}(\omega)$

$$D(\omega) = \sum_n \frac{\Omega}{(2\pi)^3} \int_{BZ} d\mathbf{k} A_{n\mathbf{k}}(\omega). \tag{97}$$

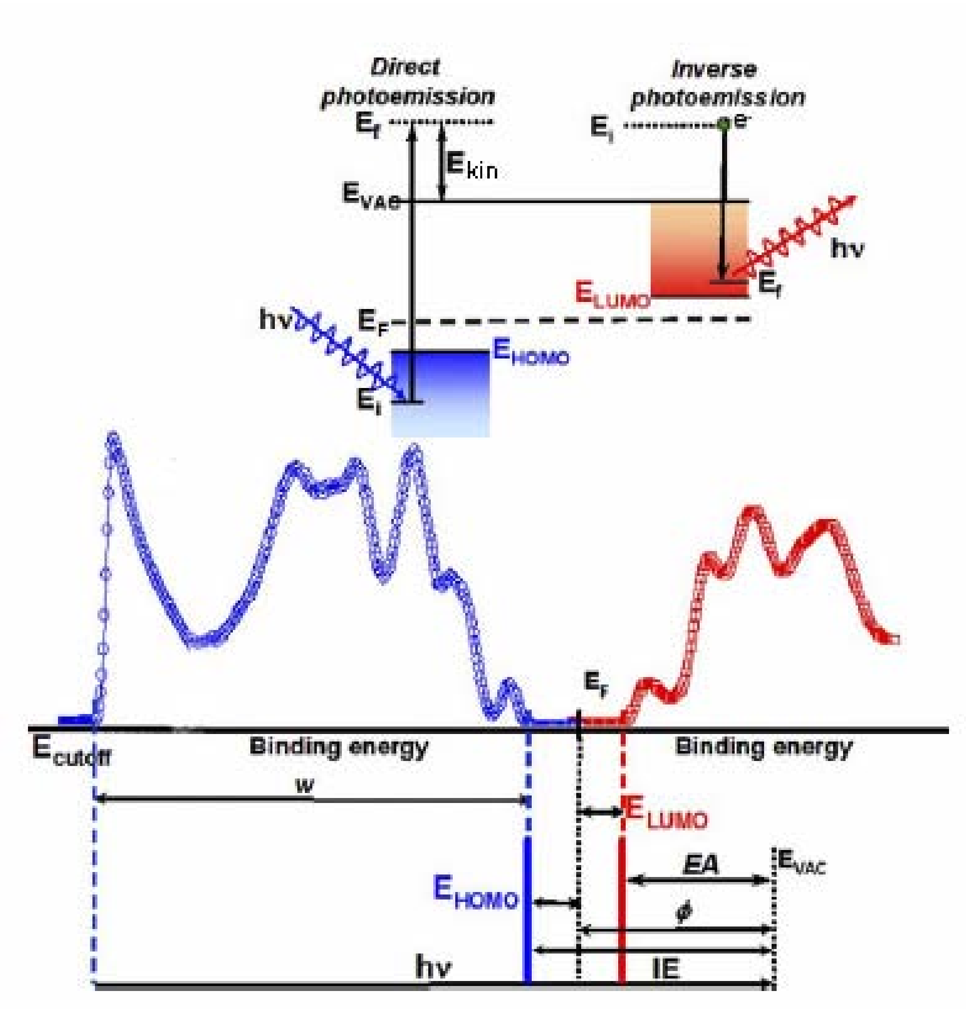

Figure 7: Schematic representation of direct photoemission (PES) and inverse photoemission (IPES) spectroscopy. IE and EA represent the ionization energy and electron affinity, respectively. HOMO and LUMO denote quasiparticle energies of the highest occupied orbital and lowest unoccupied orbital, respectively. E_{vac} is the vacuum level, E_F the Fermi energy and ϕ the work function of the material. Blue and red colors represent the occupied and unoccupied states, which can be measured by PES and IPES, respectively. This picture is adapted from Ref. [74].

For the non-interacting case, such as DFT, the spectral function is just a delta function and thus $D(\omega)$ reduces to

$$D(\omega) = \sum_n \frac{\Omega}{(2\pi)^3} \int_{BZ} d\mathbf{k}\delta\big(\epsilon - \epsilon_{n\mathbf{k}}\big), \tag{98}$$

where $\epsilon_{n\mathbf{k}}$ are the DFT eigenvalues. However, for the interacting case, as an electron propagates,

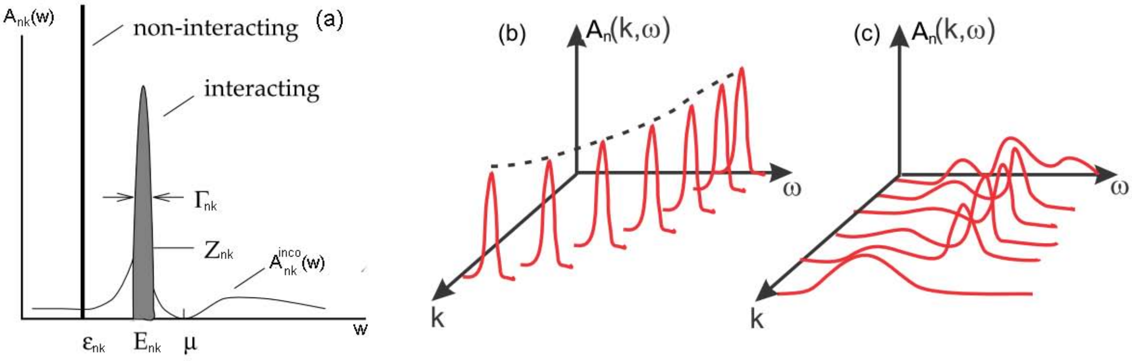

Figure 8: (a) Schematic representation of the spectral function $A_{n\mathbf{k}}(\omega)$ for a non-interacting and interacting many-body system. The QP energy is $\tilde{E}_{n\mathbf{k}} = E_{n\mathbf{k}} + \mathrm{i}\Gamma_{n\mathbf{k}}$ with $E_{n\mathbf{k}}$ and $\Gamma_{n\mathbf{k}}$ being the position and width of the QP peak, respectively. $Z_{n\mathbf{k}}$ is the renormalization factor (spectral weight), which can be related to the norm of the QP peak (shaded area) and is a measure of the degree of correlation. $A^{\mathrm{inco}}_{n\mathbf{k}}(\omega)$ is the incoherent part of the spectral function. Due to the existence of the incoherent part in the interacting system, $Z_{n\mathbf{k}}$ is thus always less than unity. For the non-interacting system, however, $Z_{n\mathbf{k}}$ is always unity. μ is the chemical potential. Schematic view of **k**-resolved spectral functions measured by angle-resolved photoemission spectroscopies (ARPES) for (b) normal (nearly non-interacting or weakly interacting) and (c) interacting (correlated electron) materials. Here, only one band is shown. This figure is adapted from Refs. [13] and [56].

the other electrons surrounding it would try to be far away due to the electron-electron Coulomb repulsions, leaving a positively charged polarization cloud (holes) around the electron. This electron and nearby holes form a quasiparticle which interacts weakly with other quasiparticles via a screened rather than bare Coulomb interaction. In contrast to the non-interacting bare particle, the quasiparticle has a finite lifetime. The energy difference between the quasiparticle and bare particle is described by the self-energy. According to the Fermi-liquid theory, the spectral function follows a Lorentzian energy distribution [13]

$$A_{n\mathbf{k}}(\omega) = \frac{Z_{n\mathbf{k}}}{\pi}\frac{\Gamma_{n\mathbf{k}}}{(\omega - E_{n\mathbf{k}})^2 + \Gamma^2_{n\mathbf{k}}} + A^{\mathrm{inco}}_{n\mathbf{k}}(\omega), \tag{99}$$

where $E_{n\mathbf{k}}$ and $\Gamma_{n\mathbf{k}}$ are the position and width of the QP peak, respectively. In other words, the pole of the self-energy is $\tilde{E}_{n\mathbf{k}} = E_{n\mathbf{k}} + \mathrm{i}\Gamma_{n\mathbf{k}}$. The lifetime of the quasiparticle is given by $1/\Gamma_{n\mathbf{k}}$. Thus, the smaller $\Gamma_{n\mathbf{k}}$ is, the longer the quasiparticle lives and the sharper the corresponding QP peak in spectral function $A_{n\mathbf{k}}(\omega)$. $Z_{n\mathbf{k}}$ is the renormalization factor, which can be related to the norm of the corresponding QP peak and is a measure of the degree of correlation. $A^{\mathrm{inco}}_{n\mathbf{k}}(\omega)$ is the incoherent part of the spectral function. It should be noted that spectral function is positive definite and normalized to unity. Due to the existence of the incoherent part in the interacting system, $Z_{n\mathbf{k}}$ is thus always less than unity. For a deeper understanding of the physical meaning of the spectral function, see Fig. 8(a). Actually, the **k**-resolved spectral function $A_{n\mathbf{k}}(\omega)$ can be measured by angle-resolved photoemission spectroscopy (ARPES), see Fig. 8(b) and (c) for the **k**-resolved spectral function of weakly and strongly interacting systems, respectively. For weakly interacting systems, the spectral function for each angular momentum **k** and band looks a bit like broadened a delta function, which clearly can be described by a single-particle theory, such as DFT, whereas for strongly interacting systems, such as correlated materials, apart from the sharp QP peak, the spectral function also shows some Hubbard-like band feature due to the electron-electron interactions and incoherent feature caused for instance by interacting with plasmons. For a better description of interacting systems, more accurate theories beyond single-particle theory, such as the *GW* approximation and dynamical mean field theory, are required.

5.3. One particle Green's function

5.3.1. Definition of the one particle Green's function

In order to describe the photoelectron spectra measured in PES and IPES experiments, a quantity that describes the propagation of a hole or an added electron is needed. A suitable quantity is the one-particle Green's function, which describes how one extra electron/hole propagates through the system. In an N-electron system at ground state ψ_0, the one particle time-ordered Green's function G is defined as [72, 75, 76]

$$\begin{aligned} G(\mathbf{r},t,\mathbf{r}',t') =& -i\langle\psi_0|\,\mathrm{T}\,\hat{\psi}(\mathbf{r},t)\hat{\psi}^{\dagger}(\mathbf{r}',t')\,|\psi_0\rangle \\ =& -i\,\Theta(t-t')\,\langle\psi_0|\,\hat{\psi}(\mathbf{r},t)\hat{\psi}^{\dagger}(\mathbf{r}',t')\,|\psi_0\rangle \\ & +i\,\Theta(t'-t)\,\langle\psi_0|\,\hat{\psi}^{\dagger}(\mathbf{r}',t')\hat{\psi}(\mathbf{r},t)\,|\psi_0\rangle. \end{aligned} \tag{100}$$

Here, T is the time-ordering operator, which has the effect of ordering the operator in such a way that the largest time is always on the left. The creation field operator $\hat{\psi}^{\dagger}(\mathbf{r},t) = e^{i\mathrm{H}t}\hat{\psi}^{\dagger}(\mathbf{r})e^{-i\mathrm{H}t}$ and the destruction field operator $\hat{\psi}(\mathbf{r},t) = e^{i\mathrm{H}t}\hat{\psi}(\mathbf{r})e^{-i\mathrm{H}t}$ are defined in the Heisenberg picture. Thus, for $t' < t$, $G(\mathbf{r},t,\mathbf{r}',t')$ is the probability amplitude of creating an electron at $(\mathbf{r}',t')$ and finding it later at $(\mathbf{r}, t)$, whereas for $t < t'$, it describes the probability amplitude of creating a hole at $(\mathbf{r}, t)$ and finding it later at $(\mathbf{r}', t')$. From the one-particle Green's function, it is possible to calculate [72,76]:

1. The expectation value of any single-particle operator in the ground state.

In the second-quantization framework, a single-particle operator $\hat{A}$ can be expressed as

$$\hat{A} = \int d\mathbf{r}d\mathbf{r}'dtdt'\delta(t'-t)\hat{\psi}^{\dagger}(\mathbf{r},t)J(\mathbf{r},t,\mathbf{r}',t')\hat{\psi}(\mathbf{r}',t'), \tag{101}$$

where $J(\mathbf{r}, t, \mathbf{r}', t')$ is the amplitude of operator $\hat{A}$. The ground-state expectation value is then given by

$$\begin{aligned}\bar{A} = \langle\psi_0^N|\hat{A}|\psi_0^N\rangle &= \int d\mathbf{r}d\mathbf{r}'dtdt'\delta(t'-t)J(\mathbf{r},t,\mathbf{r}',t')\langle\psi_0^N|\hat{\psi}^{\dagger}(\mathbf{r},t)\hat{\psi}(\mathbf{r}',t')|\psi_0^N\rangle \\ &= -\int d\mathbf{r}d\mathbf{r}'dtdt'\delta(t'-t^{+})J(\mathbf{r},t,\mathbf{r}',t')\langle\psi_0^N|\mathrm{T}\hat{\psi}(\mathbf{r}',t')\hat{\psi}^{\dagger}(\mathbf{r},t)|\psi_0^N\rangle,\end{aligned} \tag{102}$$

where $t^{+} = t + \eta$ with η being a positive infinitesimal, which is introduced because of the time-ordering operator T. $|\psi_0^N\rangle$ is the ground state of N electrons. Inserting Eq. (100) into Eq. (102), one obtains

$$\bar{A} = \langle\psi_0^N|\hat{A}|\psi_0^N\rangle = -\mathrm{i}\int d\mathbf{r}d\mathbf{r}'dtdt'\delta(t'-t^{+})J(\mathbf{r},t,\mathbf{r}',t')G(\mathbf{r}',t',\mathbf{r},t). \tag{103}$$

Now it is clear from Eq. (103) that the ground-state expectation value of any single-particle operator can be calculated by the one-particle Green's function. Take the density operator

$$\hat{\gamma} = \int d\mathbf{r}d\mathbf{r}'dtdt'\delta(t'-t)\hat{\psi}^{\dagger}(\mathbf{r},t)\delta(r'-r)\hat{\psi}(\mathbf{r}',t') \tag{104}$$

for instance, the total density reads

$$\begin{aligned}\rho &= -\mathrm{i}\int d\mathbf{r}d\mathbf{r}'dtdt'\delta(t'-t^{+})\delta(r'-r)G(\mathbf{r}',t',\mathbf{r},t) \\ &= -\mathrm{i}\int d\mathbf{r}dtG(\mathbf{r},t^{+},\mathbf{r},t).\end{aligned} \tag{105}$$

2. The ground state energy.

Galitskii-Migdal formula [77] states that the ground-state energy is a function of the one-particle Greens function only

$$E_0^{\mathrm{tot}} = -\frac{\mathrm{i}}{2}\sum_{\sigma,\sigma'}\delta_{\sigma,\sigma'}\int d\mathbf{r}\lim_{\mathbf{r}'\to\mathbf{r}}\lim_{t'\to t^{+}}\left(\mathrm{i}\frac{\partial}{\partial t} + h_0(\mathbf{r})\right)G(\mathbf{r},t,\mathbf{r}',t'), \tag{106}$$

where σ represents the spin and $h_0(\mathbf{r}) = -\nabla^2/2 + V_{\mathrm{ext}}(\mathbf{r})$ is the non-interacting one-particle Hamiltonian.

3. The single-particle excitation spectrum.

From the one-particle Green's function, it is also possible to calculate the single-particle excitation spectrum, i.e., QP band structure, by solving the QP equation, that we are going to introduce below.

It should be noted that here we just give the definition of the zero temperature time-ordering equilibrium Greens functions. It is also possible to define advanced and retarded Green's functions. For a finite temperature case, imaginary time Green's function (or Matsubara frequency Green's function) should be employed. For the definition of the finite temperature Green's functions, we refer the interested readers to the book written by Richard D. Mattuck [78]. In addition, we want to stress that despite its powerfulness of one-particle Green's function in explaining the photoemission spectroscopy, which itself is the one-particle (electron or hole) prorogation process, it cannot be used for explaining the absorption spectra, since one-particle Green's function is only a one-particle theory and hence does not describe the electron-hole interactions that need a two-particle description. To describe the propagation of electron and hole at the same time, two-particle Green's functions and solving the Bethe-Salpeter equation (BSE) are required [73].

5.3.2. Spectral representation of the Green's function

Using the fact that

$$\begin{aligned} \hat{\psi}^\dagger(\mathbf{r},t) &= e^{i\mathrm{H}t}\hat{\psi}^\dagger(\mathbf{r})e^{-i\mathrm{H}t} && (107)\\ \hat{\psi}(\mathbf{r},t) &= e^{i\mathrm{H}t}\hat{\psi}(\mathbf{r})e^{-i\mathrm{H}t}. && (108)\end{aligned}$$

and

$$\begin{aligned} \mathrm{H}|\psi_n^{N\pm1}\rangle &= E_n^{N\pm1}|\psi_n^{N\pm1}\rangle && (109)\\ \mathrm{H}|\psi_0^{N}\rangle &= E_0^{N}|\psi_0^{N}\rangle, && (110)\end{aligned}$$

we obtain

$$\langle\psi_0^N|\hat{\psi}(\mathbf{r},t)|\psi_n^{N\pm1}\rangle = \langle\psi_0^N|\hat{\psi}(\mathbf{r})|\psi_n^{N\pm1}\rangle\, e^{i(E_0^N-E_n^{N\pm1})t}. \tag{111}$$

Inserting a complete set of $N \pm 1$ particle eigenstates $\sum_n |\psi_n^{N\pm1}\rangle\langle\psi_n^{N\pm1}|$ into the one-particle Green's function Eq. (100), we obtain the spectral representation of the Green's function [79]

$$\begin{aligned} G(\mathbf{r},\mathbf{r}',t,t') = -i\Theta(t-t') &\sum_n \langle\psi_0^N|\,\hat{\psi}(\mathbf{r})|\psi_n^{N+1}\rangle\langle\psi_n^{N+1}|\hat{\psi}^\dagger(\mathbf{r}')\,|\psi_0^N\rangle e^{-i(E_n^{N+1}-E_0^N)(t-t')} \\ +i\Theta(t'-t) &\sum_n \langle\psi_0^N|\,\hat{\psi}^\dagger(\mathbf{r}')|\psi_n^{N-1}\rangle\langle\psi_n^{N-1}|\hat{\psi}(\mathbf{r})\,|\psi_0^N\rangle e^{-i(E_0^N-E_n^{N-1})(t'-t)}. \end{aligned} \tag{112}$$

Since the Green's function depends only on the time difference $\tau = t - t'$, we can Fourier transform $G(\mathbf{r},\mathbf{r}',\tau)$ to the frequency domain

$$\begin{aligned} G(\mathbf{r},\mathbf{r}',\omega) = &\sum_n \frac{\langle\psi_0^N|\,\hat{\psi}(\mathbf{r})|\psi_n^{N+1}\rangle\langle\psi_n^{N+1}|\hat{\psi}^\dagger(\mathbf{r}')\,|\psi_0^N\rangle}{\omega - (E_n^{N+1} - E_0^N) + i\eta} \\ &+ \sum_n \frac{\langle\psi_0^N|\,\hat{\psi}^\dagger(\mathbf{r}')|\psi_n^{N-1}\rangle\langle\psi_n^{N-1}|\hat{\psi}(\mathbf{r})\,|\psi_0^N\rangle}{\omega - (E_n^{N-1} - E_0^N) - i\eta}. \end{aligned} \tag{113}$$

Here, η is a positive infinitesimal number derived from a contour integration [79]. In the complex plane, it shifts the occupied states a little bit over the real axis and the unoccupied states a little bit under the real axis, see Fig. 9. In deriving Eq. (113), we have used the identity [79]

$$\int_{-\infty}^{+\infty} d\tau\, e^{i\omega\tau} e^{-i\epsilon_n\tau}\Theta(\pm\tau) = \pm\frac{i}{\omega - \epsilon_n \pm i\eta}. \tag{114}$$

Let us consider the energy terms appearing at the denominators. They can be rewritten as

$$E_n^{N+1} - E_0^N = \underbrace{(E_n^{N+1} - E_0^{N+1})}_{\epsilon_n^{N+1}} + \underbrace{(E_0^{N+1} - E_0^N)}_{\mu^{N+1}} \tag{115}$$

$$E_0^N - E_n^{N-1} = \underbrace{(E_0^N - E_0^{N-1})}_{\mu^N} - \underbrace{(E_n^{N-1} - E_0^{N-1})}_{\epsilon_n^{N-1}}. \tag{116}$$

Here, the chemical potential μ^{N+1} represents the minimum energy needed to add one electron to a system of N electrons, which is the electron affinity (EA), whereas the chemical potential μ^N represents the minimum energy needed to remove one electron (add a hole) to a system of N electrons, which is the ionization energy (IE). It can be shown that IE ≤ EA. If we define

$$E_g = \text{EA} - \text{IE}, \tag{117}$$

we obtain that E_g is always positive definite. In a solid, we define the chemical potential μ such that

$$\text{IE} \leq \mu \leq \text{EA} \tag{118}$$

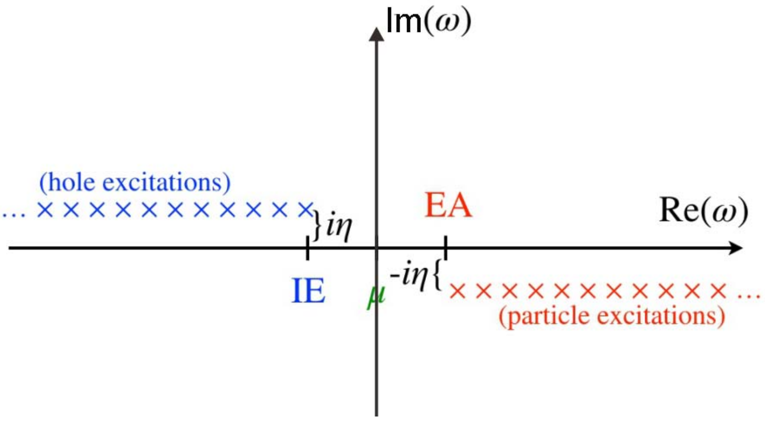

Figure 9: The poles of one-particle Green's function. This picture is adapted from Ref. [80].

holds. In the thermodynamic limit ($N, \Omega \to \infty$, with Ω/N=constant), we can distinguish metallic and insulating systems:

$$\text{metallic systems} \qquad \text{IE} \simeq \mu \simeq \text{EA}, E_g = 0 \tag{119}$$

$$\text{insulating systems} \qquad \text{IE} < \mu < \text{EA}, E_g > 0 \tag{120}$$

Now, we may define the excitation energies of the system

$$\epsilon_n = \begin{cases} E_n^{N+1} - E_0^N & \text{for} \quad \epsilon_n > \mu \\ E_0^N - E_n^{N-1} & \text{for} \quad \epsilon_n \leq \mu \end{cases}, \tag{121}$$

and Lehman amplitudes

$$\phi_n(\mathbf{r}) = \begin{cases} \langle\psi_0^N|\hat{\psi}(\mathbf{r})|\psi_n^{N+1}\rangle & \epsilon_n > \mu \\ \langle\psi_n^{N-1}|\hat{\psi}(\mathbf{r})\,|\psi_0^N\rangle & \epsilon_n \leq \mu \end{cases}, \tag{122}$$

With these, we finally obtain the Lehman representation of the one-particle Green's function

$$G(\mathbf{r}, \mathbf{r}', \omega) = \sum_n \frac{\phi_n(\mathbf{r})\phi_n^*(\mathbf{r}')}{\omega - \epsilon_n + i\eta\text{sgn}(\epsilon_n - \mu)}. \tag{123}$$

It can be seen from Eq. (123) that the poles of the Green's function are the exact excitation energies of the $N \pm 1$ electrons, see Fig. 9.

The one-particle Green's function can also be cast into the so-called spectral representation

$$G(\mathbf{r}, \mathbf{r}', \omega) = \int_{-\infty}^{\mu} d\omega' \frac{A(\mathbf{r}, \mathbf{r}', \omega')}{\omega - \omega' - i\eta} + \int_{\mu}^{\infty} d\omega' \frac{A(\mathbf{r}, \mathbf{r}', \omega')}{\omega - \omega' + i\eta}, \tag{124}$$

where

$$A(\mathbf{r}, \mathbf{r}', \omega) = \sum_n \phi_n(\mathbf{r})\phi_n^*(\mathbf{r}')\delta(\omega - \epsilon_n) \tag{125}$$

is the spectral function of the system. By applying the identity [79]

$$\frac{1}{\omega \pm i\eta} = P\frac{1}{\omega} \mp i\pi\delta(\omega) \tag{126}$$

to Eq. (123), we obtain the relationship between the spectral function and the Green's function

$$A(\mathbf{r}, \mathbf{r}', \omega) = -\frac{1}{\pi}\,\mathrm{Im}\,G(\mathbf{r}, \mathbf{r}', \omega)\,\mathrm{sgn}(\omega - \mu). \tag{127}$$

As discussed before, the spectral function is of significant importance, since it can be directly compared to the spectra measured by photoemission spectroscopy. It should be mentioned that the spectral function satisfy the so-called "sum rule"

$$\int_{-\infty}^{+\infty} d\omega A(\mathbf{r}, \mathbf{r}', \omega) = \delta(\mathbf{r} - \mathbf{r}'), \tag{128}$$

because of

$$\begin{aligned}
\int_{-\infty}^{+\infty} d\omega A(\mathbf{r}, \mathbf{r}', \omega) &= \int_{-\infty}^{+\infty} d\omega \sum_n \phi_n(\mathbf{r})\phi_n^*(\mathbf{r}')\delta(\omega - \epsilon_n) \\
&= \sum_n \phi_n(\mathbf{r})\phi_n^*(\mathbf{r}') \\
&= \sum_n \langle\psi_0^N|\hat{\psi}(\mathbf{r})|\psi_n^{N+1}\rangle\langle\psi_n^{N+1}|\hat{\psi}^\dagger(\mathbf{r}')|\psi_0^N\rangle + \sum_n \langle\psi_0^N|\hat{\psi}^\dagger(\mathbf{r}')|\psi_n^{N-1}\rangle\langle\psi_n^{N-1}|\hat{\psi}(\mathbf{r})|\psi_0^N\rangle \\
&= \langle\psi_0^N|[\hat{\psi}(\mathbf{r}), \hat{\psi}^\dagger(\mathbf{r}')]_+|\psi_0^N\rangle \\
&= \delta(\mathbf{r} - \mathbf{r}').
\end{aligned} \tag{129}$$

In deriving Eq. (129), we have used the definitions of Lehman amplitudes in Eq. (122), the completeness of sets $\{|\psi_n^{N+1}\rangle\}$ and $\{|\psi_n^{N-1}\rangle\}$, and anticommutation rule of field operators. Second, if we integrate the spectral function $A(\mathbf{r}, \mathbf{r}', \omega)$ with respect to ω up to Fermi level μ, one obtains the density matrix

$$\rho(\mathbf{r}, \mathbf{r}') = \int_{-\infty}^{\mu} A(\mathbf{r}, \mathbf{r}', \omega) = \langle\psi_0^N|\hat{\psi}^\dagger(\mathbf{r}')\hat{\psi}(\mathbf{r})|\psi_0^N\rangle. \tag{130}$$

For the non-interacting cases, the Lehman amplitudes are replaced by the one-particle wavefunctions ψ_n and excitation energies are replaced by one-particle eigenvalues ϵ_n satisfying

$$H_0\psi_n = \epsilon_n\psi_n. \tag{131}$$

The non-interacting Green's function is then given by

$$G_0(\mathbf{r}, \mathbf{r}', \omega) = \sum_n^{\mathrm{occ}} \frac{\psi_n(\mathbf{r})\psi_n^*(\mathbf{r}')}{\omega - \epsilon_n - i\eta} + \sum_n^{\mathrm{unocc}} \frac{\psi_n(\mathbf{r})\psi_n^*(\mathbf{r}')}{\omega - \epsilon_n + i\eta}, \tag{132}$$

where ϵ_n is measured with respect to the chemical potential μ. It should be noted that which kind of system is assumed as the non-interacting system depends on the problem under consideration. Most often the KS system is taken as the non-interacting reference.

5.4. Dyson equation and quasiparticle equation

For an interacting system, the one particle Green's function can be expressed in terms of so-called QP orbitals ψ_n and QP energies E_n, if the QP orbitals are complete [13]

$$G(\mathbf{r},\mathbf{r}',\omega) = \sum_n \frac{\psi_n(\mathbf{r})\psi_n^*(\mathbf{r}')}{\omega - E_n}. \tag{133}$$

In contrast to a non-interacting system, the QP energies of an interacting system are complex with real and imaginary parts that give the positions and widths of the QP peaks, respectively [see Fig. 7(a)]. The imaginary parts of the QP energies are further inverse proportional to the lifetime of the quasiparticles. For the non-interacting case, the spectral function is a delta function with an infinitesimal small width of QP peak and thus infinite lifetime. The time-dependent interacting Green's function G is given by the so-called Dyson equation [13]

$$G(\mathbf{r},\mathbf{r}',\omega) = G_0(\mathbf{r},\mathbf{r}',\omega) + \int d\mathbf{r}_1\, d\mathbf{r}_2\, G_0(\mathbf{r},\mathbf{r}_1,\omega)\Sigma(\mathbf{r}_1,\mathbf{r}_2,\omega)G(\mathbf{r}_2,\mathbf{r}',\omega), \tag{134}$$

where Σ is the irreducible self-energy, which defines the general differences between interacting and non-interacting systems. The self-energy comes from the interpretation that the bare particle interacts with the many-body system, creating the cloud, and the cloud in turn reacts back on the particle, disturbing its motion. Hence, the particle is, in a sense, interacting with itself via the many-body system and changing its own energy [78]. Diagrammatically, the Dyson equation reads

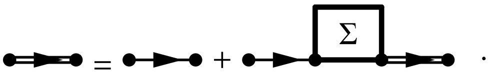

(135)

Here, we used double particle lines in Eq. (135) to indicate interacting Green's functions G. If $\hat{H}_0 = -\frac{1}{2}\nabla^2(\mathbf{r}) + V_{\text{ext}}(\mathbf{r})$ is assumed as the the non-interacting Hamiltonian, then the irreducible self-energy Σ reads [70]

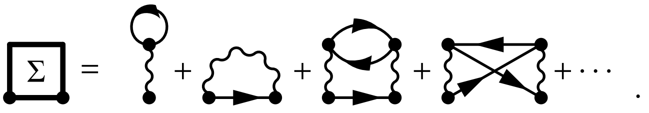

(136)

However, if the Hartree Hamiltonian $\hat{H}_0 = -\frac{1}{2}\nabla^2(\mathbf{r}) + V_{\text{ext}}(\mathbf{r}) + V_{\text{H}}(\mathbf{r})$ is assumed as the the non-interacting Hamiltonian, the irreducible self-energy become

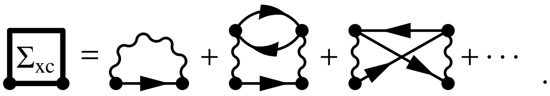

(137)

Here, Σ_{xc} is the non-local part of the self-energy. Similarly, if the Hartree-Fock Hamiltonian $\hat{H}_0 = -\frac{1}{2}\nabla^2(\mathbf{r}) + V_{\text{ext}}(\mathbf{r}) + V_{\text{H}}(\mathbf{r}) + V_{\text{x}}(\mathbf{r})$ is assumed as the the non-interacting Hamiltonian, then the irreducible self-energy become

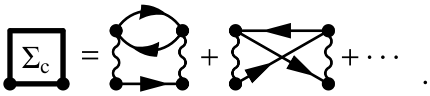

(138)

Furthermore, if the DFT Hamiltonian $\hat{H}_0 = -\frac{1}{2}\nabla^2(\mathbf{r}) + V_{\text{ext}}(\mathbf{r}) + V_{\text{H}}(\mathbf{r}) + V_{\text{x}c}(\mathbf{r})$ is assumed as the the non-interacting Hamiltonian, the irreducible self-energy Σ becomes

$$\Sigma = \Sigma_{\text{xc}} - V_{\text{xc}}. \tag{139}$$

Plugging the spectral representations of the Green's function Eq. (133) into the Dyson equation, the QP equation is obtained [13]

$$\Big[-\frac{1}{2}\nabla^2(\mathbf{r}) + V_{\text{ext}}(\mathbf{r}) + V_{\text{H}}(\mathbf{r})\Big]\psi_n(\mathbf{r}) + \int d\mathbf{r}'\, \Sigma_{\text{xc}}(\mathbf{r},\mathbf{r}',E_n)\,\psi_n(\mathbf{r}') = E_n\psi_n(\mathbf{r}). \tag{140}$$

The QP equation looks similar to the KS equation in Eq. (47). However, the exchange and correlation effects are now included through the self energy Σ_{xc} instead of V_{xc}. It turns out that the quasiparticle orbitals $\psi_n(\mathbf{r})$ and energies E_n can be obtained solving the QP equation [70, 81, 82]. Since the self-energy is non-local, non-Hermitian and frequency-dependent, direct solution of the QP equation without any further approximations is not possible. One of the good approximations is the *GW* approximation, where the electron-electron interactions are described by the screened Coulomb interaction W instead of the bare Coulomb interaction. It turns out that the *GW* approximation not only gives a better description of band gaps, but also describes the electronic structure of many weakly correlated materials reasonably well. In the following, I will first show the Hedin's equations and then the *GW* approximation followed by its practical implementations.

5.5. Hedin equations

In principle, the exact self-energy can be obtained from a closed set the so-called Hedin equations [70]:

$$\begin{aligned}
G(1,2) &= G_0(1,2) + \int \mathrm{d}3\mathrm{d}4 G_0(1,3)\Sigma_{\mathrm{xc}}(3,4)G(4,2) && (141)\\
\Sigma_{\mathrm{xc}}(1,2) &= i\int \mathrm{d}1'\mathrm{d}2'\; G(1',2)W(2',2^+)\Gamma(2',2';1,1') && (142)\\
W(1,2) &= v(1,2) + \int \mathrm{d}1'\mathrm{d}2'\; v(1,1')\chi(1',2')W(2',2) && (143)\\
\chi(1,2) &= -i\int \mathrm{d}1'\mathrm{d}2'\; \Gamma(1,1;1',2')G(2,1')G(2',2) && (144)\\
\Gamma(1,2;3,4) &= \Gamma^0(1,2;3,4) + \int \mathrm{d}(1')\cdots\mathrm{d}(6')\Gamma^0(1,2;3',4')I(3',4';5',6') && (145)\\
&\times\; G(1',5')G(6',2')\Gamma(1',2';3,4)\\
I(1,2;3,4) &= \frac{\delta\Sigma_{\mathrm{xc}}(1,2)}{\delta G(4,3)}, \quad \Gamma^0(1,2;3,4) = \delta(1,3)\delta(2,4). && (146)
\end{aligned}$$

Here, Σ_{xc} is the non-local part of the irreducible self-energy, G (G_0) the interacting (non-interacting) Green's function, W the screened Coulomb interaction, χ the irreducible polarizability, v bare Coulomb interaction, Γ the vertex correction, and I the scattering amplitude. Note that in deriving Eqs. (141-146) the following notations

$$\begin{aligned}
1 &= (\mathbf{r}_1, t_1), \quad 2 = (\mathbf{r}_2, t_2) && (147)\\
\delta(1,2) &= \delta(\mathbf{r}_1,\mathbf{r}_2)\delta(t_1,t_2) && (148)\\
v(1,2) &= v(\mathbf{r}_1,\mathbf{r}_2)\delta(t_1,t_2), \quad v(\mathbf{r}_1,\mathbf{r}_2) = \frac{1}{|\mathbf{r}_1-\mathbf{r}_2|} && (149)\\
\int d1 &= \int d\mathbf{r}_1 \int_{-\infty}^{+\infty} dt_1 && (150)\\
1^+ &= (\mathbf{r}_1, t_1+\eta), \quad \eta = 0^+ && (151)
\end{aligned}$$

are used. The corresponding Feynman diagrams read:

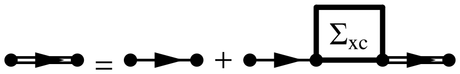

(152)

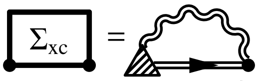

(153)

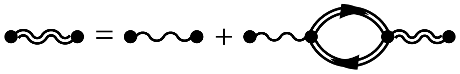

(154)

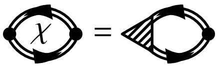

(155)

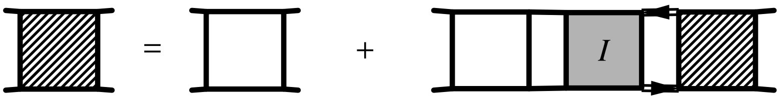

(156)

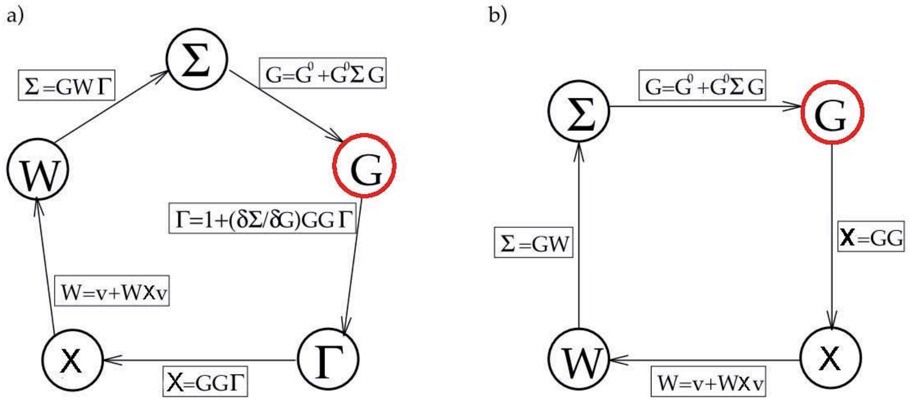

Figure 10: (a) Schematic representation of the iterative determination of the self-energy Σ using Hedin's equations Eqs. (141-146). (b) Schematic representation of the iterative determination of the self-energy Σ in the *GW* approximation. See the main text for the details. This figure is adapted from from Ref. [13].

$$\Gamma(1,2;3,4) = \tag{157}$$

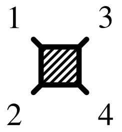

$$\Gamma(1,1;3,4) = \Gamma(1;3,4) = \quad . \tag{158}$$

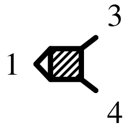

Here, double straight lines represent the interacting Green's function, while double wiggly lines denote the dressed (screened) Coulomb interaction. Although the compact structure of the Hedin's equations is appealing, a full solution remains a formidable challenge, since they are coupled to each other. Fig. 10(a) shows the Hedin's algorithm to solve the set of equations for Γ, χ, W, Σ and G self-consistently. Specifically, starting from the non-interacting Green's function G_0 (G^{Hartree}), the vertex correction Γ is calculated by Eqs. (145-146). Afterwards, the polarizability χ is calculated by Eq. (144). Screened Coulomb interaction W is then calculated by Eq. (143). After W is obtained, self-energy Σ is calculated by Eq. (142). With this self-energy, the interacting Green's function G is obtained by solving the Dyson equation Eq. (141). This procedure is repeated until the self-consistence is achieved.

5.6. *GW* approximation

Although in theory the exact self-energy can be obtained from a closed set of Hedin equations as introduced above, the calculations are extremely prohibitive without further approximations.

The GW approximation, which neglects vertex corrections in the irreducible self-energy and polarizability, provides a good approximation for the self-energy by including many-body effects in the electron-electron interaction. It can be regarded as a generalization of the Hartrre-Fock approximation. Apart from Hartrre and Fock terms, the GW approximation also accounts for the correlated self-energy, which is frequency dependent. Without the vertex corrections, the Dyson-equation shown in Eq. (134) and Hedin equations shown in Eqs. (141-146) reduce to

$$\begin{aligned} G(\mathbf{r},\mathbf{r}',t) &= G_0(\mathbf{r},\mathbf{r}',t) + \int d\mathbf{r}_1\, d\mathbf{r}_2\, G_0(\mathbf{r},\mathbf{r}_1,t)\Sigma^{GW}(\mathbf{r}_1,\mathbf{r}_2,t)G(\mathbf{r}_2,\mathbf{r}',t) && (159)\\ \chi^{GW}(\mathbf{r},\mathbf{r}',t) &= -iG(\mathbf{r},\mathbf{r}',t)G(\mathbf{r}',\mathbf{r},-t) && (160)\\ W(\mathbf{r},\mathbf{r}',t) &= v(\mathbf{r},\mathbf{r}') + \int d\mathbf{r}_1\, d\mathbf{r}_2\, v(\mathbf{r},\mathbf{r}_1)\chi^{GW}(\mathbf{r}_1,\mathbf{r}_2,t)W(\mathbf{r}_2,\mathbf{r}',t) && (161)\\ \Sigma^{GW}(\mathbf{r},\mathbf{r}',t) &= \mathrm{i}G(\mathbf{r},\mathbf{r}',t)W(\mathbf{r},\mathbf{r}',t). && (162) \end{aligned}$$

Here, $v(\mathbf{r},\mathbf{r}') = 1/|\mathbf{r}-\mathbf{r}'|$ is the bare Coulomb interaction kernel. The corresponding Feynman diagrams read

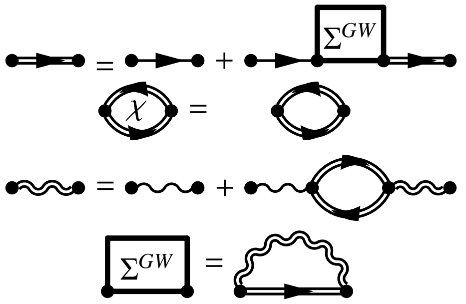

(163)

(164)

(165)

(166)

Fig. 10(b) shows the schematic representation of the iterative determination of the self-energy Σ in the GW approximation. Similar to Hedin's algorithm, in order to achieve the self-consistency, the following procedure should be performed. Starting from the non-interacting Green's function G_0 (G^{Hartree}), one then calculates the polarizability χ by Eq. (160). Screened Coulomb interaction W is calculated by Eq. (161). After W is obtained, self-energy Σ is calculated by Eq. (162). With this self-energy, the interacting Green's function G is obtained by solving the Dyson equation Eq. (159). This procedure is repeated until the self-consistence is achieved.

5.7. GW implementation in practice

Although the QP energies can be in principle elegantly calculated by a self-consistent solution of Eqs. (159-162), in practice, none of the publicly available computer codes allow for such a fully self-consistent solution for technical reasons: since the one-particle Green's function $G(\mathbf{r},\mathbf{r}',t-$

t') depends on the time difference $t-t'$, the accurate discretization in time is challenging [15]. In fact, all the available GW implementations restrict the Green's function to an "non-interacting" form

$$G(\mathbf{r}', \mathbf{r}, \omega) = \sum_n \frac{\psi_n(\mathbf{r}')\psi_n^*(\mathbf{r})}{\omega - \epsilon_n^{\mathrm{QP}} + i\eta \mathrm{sign}(\epsilon_n^{\mathrm{QP}} - \mu)}, \tag{167}$$

where ϵ_n^{QP} are the QP energies, η is a positive infinitesimal and μ is the Fermi energy. However, $\psi_n(\mathbf{r})$ are the normalized eigenfunctions of some Hermitian one-particle Hamiltonian (usually DFT Kohn-Sham Hamiltonian). It is clear from Eq. (167) that the QP energies can be easily identified as poles of the Green's function, so that the band gap is simply given as the energy difference between the energy of the lowest unoccupied and highest occupied quasiparticle [15]. This is a good approximation only if the DFT Kohn-Sham orbitals are close to the exact QP orbitals. This is so for most cases [83].

If the DFT Kohn-Sham Hamiltonian is taken as the one-particle Hamiltonian in Eq. (167) and we assume that the DFT Kohn-Sham orbitals are close to the exact QP orbitals, we will obtain an another simple approximate QP equation

$$\epsilon_n^{\mathrm{QP}} = \mathrm{Re}\left[\langle\psi_n|T + V_{\mathrm{ext}} + V_H + \Sigma_{\mathrm{xc}}(\epsilon_n^{\mathrm{QP}})|\psi_n\rangle\right], \tag{168}$$

where Σ_{xc} is the non-local part of GW self-energy. Eq. (168) is derived by comparing the interacting Green's function in Eq. (167) with the non-interacting Green's function

$$G_0(\mathbf{r}', \mathbf{r}, \omega) = \sum_n \frac{\psi_n(\mathbf{r}')\psi_n^*(\mathbf{r})}{\omega - \epsilon_n^{\mathrm{DFT}} + i\eta \mathrm{sign}(\epsilon_n^{\mathrm{DFT}} - \mu)}, \tag{169}$$

and using the Dyson equation

$$G^{-1} = G_0^{-1} - (\Sigma_{\mathrm{xc}} - V_{\mathrm{xc}}), \tag{170}$$

where V_{xc} is the DFT exchange-correlation energy functional. It should be mentioned that in deriving Eq. (168) it is implicitly assumed that the GW self-energy in the KS basis is diagonally dominant, which is found to be true for most cases [83].

Since the self-energy Σ_{xc} is energy dependent, Eq. (168) needs to be solved iteratively for ϵ^{QP}. One possible solution is to calculate the roots of this non-linear equation by, for instance, the Newton root-finding algorithm. This works for most cases, except for the cases where many poles exist around the predicted QP energies. This might not occur for solids, but it might happen for molecules, for instance, the closed shell molecules BN, O_3, BeO, MgO and CuCN, as reported in Ref. [84]. Given the observation that the QP energies are often not so far away from the DFT eigenvalues, the GW self-energy at the QP energies can be calculated to first order, by linearizing the self-energy around the DFT single particle eigenvalues $\epsilon_n^{\mathrm{DFT}}$

$$\Sigma_n(\epsilon_n^{\mathrm{QP}}) = \Sigma_n(\epsilon_n^{\mathrm{DFT}}) + \left.\frac{\partial \Sigma_n(\omega)}{\partial \omega}\right|_{\omega=\epsilon_n^{\mathrm{DFT}}} (\epsilon_n^{\mathrm{QP}} - \epsilon_n^{\mathrm{DFT}}). \tag{171}$$

Here, $\Sigma_n(\omega) = \langle \psi_n | \Sigma_{\mathrm{xc}}(\omega) | \psi_n \rangle$. Inserting Eq. (171) into Eq. (168), we obtain the linearized QP energies

$$\epsilon_n^{\mathrm{QP}} = \epsilon_n^{\mathrm{DFT}} + Z_n \mathrm{Re}[\langle \psi_n | T + V_{\mathrm{ext}} + V_H | \psi_n \rangle + \Sigma_n(\epsilon_n^{\mathrm{DFT}}) - \epsilon_n^{\mathrm{DFT}}], \tag{172}$$

where Z_n is the renormalization factor and related to the derivative of the self-energy at $\epsilon_n^{\mathrm{DFT}}$

$$Z_n = \left(1 - \left.\frac{\partial \mathrm{Re}[\Sigma_n(\omega)]}{\partial \omega}\right|_{\omega=\epsilon_n^{\mathrm{DFT}}} \right)^{-1}. \tag{173}$$

The correlation factor Z_n can be related to the norm of the corresponding QP peak and is a measure of the degree of correlation. Typically, Z_n is between 0.7-0.9, corresponding to a low to very low degree of correlation. It should be noted that apart from the neglect of vertex corrections, the GW approximation also neglects all but the first irreducible polarizability term describing the direct creation of a noninteracting (independent) electron-hole pair from the ground state. That means the independent-particle polarizability is used in almost all the existing practical implementations.

If one just does one-single shot iteration but does not update the Green's functions again in Fig. 10(b), one obtained the so-called G_0W_0 approximation. That is, one starts from the Kohn-Sham one-electron energies and orbitals to construct the non-interacting Green's functions G_0, then uses G_0 to calculate the independent particle polarizability χ_0 and furthermore the screened Colombo interaction W_0, afterwards, calculates the self-energy $\Sigma = -G_0W_0$ and finally obtains the QP energies by Eq. (172). It turns out that G_0W_0 obviously improves the band gaps towards the experimental values compared with the LDA or GGA [85, 86].

Even though G_0W_0 to some extent improves the band gaps of typical insulators and semiconductors, it underestimates the band gaps even for (weakly correlated) semiconductors. It fails even qualitatively in transition-metal and rare-earth-metal compounds such as CoO and ErAs [87]. This is because G_0W_0 depends strongly on the initial starting point and also implicitly assumes that the initial Kohn-Sham orbtials are close to the exact QP orbitals. Obviously,

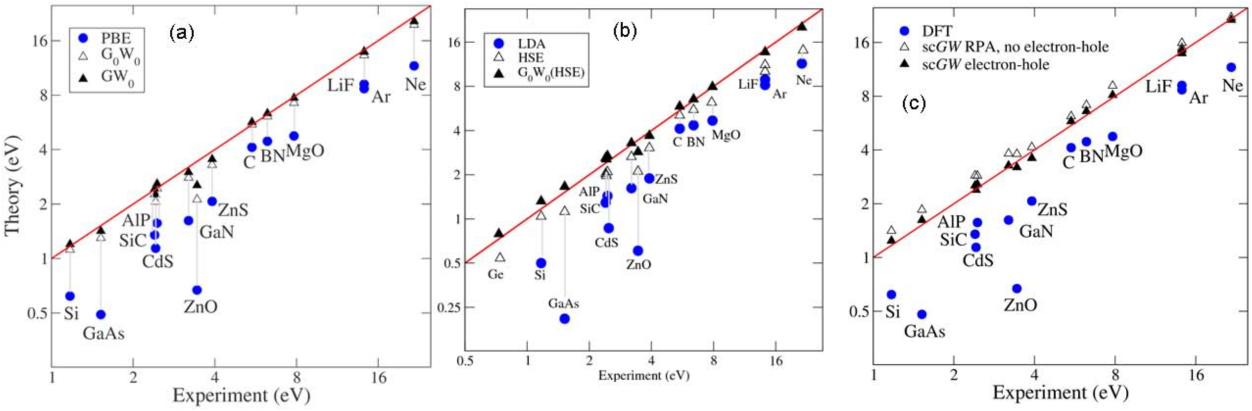

Figure 11: (a) Band gaps predicted by PBE, G_0W_0 and GW_0 (b) Band gaps predicted by LDA, HSE and G_0W_0@HSE. (c) Band gaps predicted by DFT, scGW without and with electron-hole vertex corrections. This figure is adapted from Refs. [86, 88, 89].

this is not always satisfied. One of the possible ways to improve the band gaps further is GW_0 [86], where the screened Coulomb interaction W is fixed at the DFT level, but the Green's function G is updated only in the one-electron energies. Indeed, with the update of the one-electron energies in GW_0, the predicted band gaps are much more closer to the experimental values than G_0W_0, as shown in Fig. 11(a). Another alternative method is G_0W_0@HSE [88], where the G_0W_0 is done on top of the HSE one-electron energies and orbitals instead of LDA or GGA. It can be seen from Fig. 11(b) that G_0W_0@HSE almost yields the same band gaps as GW_0. Which kind of methods one should choose, however, is not well understood or investigated. It seems to depend largely on personal prejudice.

It should be mentioned that analogous to G_0W_0, GW_0 is also starting point dependent, and of course G_0W_0@HSE depends on the HSE one-electron energies and orbitals and there is no guarantee that HSE orbitals are closer to the exact QP orbitals than PBE orbitals. To overcome the issue of the starting point dependence, one would expect that some self-consistency (not only update one-electron energies, but also one-electron orbitals) might help. However, full self-consistent GW (scGW) without inclusion of vertex corrections may lead to some problems. For instance, scGW always overestimates the band gaps [89], as shown in Fig. 11(c). The valence bandwidth of the homogeneous electron gas predicted by scGW is 15% wider than the noninteracting case, whereas the G_0W_0 width is 15% narrower, in agreement with experiment for Na [90]. In addition, scGW overestimates the valence bandwidth of Si and Ge, though the band gaps are reasonably described [91]. If one takes into account the vertex corrections in scGW, for instance, the electron-hole interactions in the pair-bubble irreducible polarizability Feynman diagram (vertex corrections in polarizability and thus in W), the overestimated band gaps are reduced and in better agreement with experimental values, see Fig. 11(c). Also, the importance of vertex corrections in the self-energy Σ has been highlighted for predicting the ionization potentials and d-electron binding energies of solids [92], with typical corrections for the d bands of 0.7 eV. However, the inclusion of vertex corrections becomes so expensive that GW_0 and G_0W_0@HSE are instead often used.

Instead of inclusion of vertex corrections in scGW, quasiparticle self-consistent GW (QPGW) tries to determine the optimum effective static exchange-correlation potential V_{xc} based on a self-consistent perturbation theory so that the time evolution determined by $H^0 = T + V_{\text{ext}} + V_H + V_{\text{xc}}$ is as close as possible to that determined by $H(\omega) = T + V_{\text{ext}} + V_H + \Sigma_{\text{xc}}(\omega)$ within the RPA [85]. One possible approximation for V_{xc} is [85]

$$V_{\text{xc}} = \frac{1}{2}\sum_{i,j} |\psi_i\rangle \left\{\text{Re}[\Sigma_{\text{xc}}(\epsilon_i)]_{ij} + \text{Re}[\Sigma_{\text{xc}}(\epsilon_j)]_{ij}\right\} \langle\psi_j|. \tag{174}$$

With V_{xc} in Eq. (174), the self-consistency is closed. Specifically, starting from DFT calculations with a Hamiltonian $H^0 = T + V_{\text{ext}} + V_H + V_{\text{xc}}$, in QPGW the full self-energy matrix is calculated and "quasiparticelized" $\Sigma_{ij}(\omega)$, which couples one-electron states i and j, is evaluated at the one-electron energies ϵ_i and ϵ_j, and then the average value is taken. This leads to a new static but non-local potential V_{xc} by means of Eq. (174). The new V_{xc} is then used to calculate a new $\Sigma_{ij}(\omega)$, and the process is iterated until the convergence of V_{xc} is achieved. QPGW theory is an elegant way to find the optimum noninteracting Hamiltonian H^0 for GW calculations. It removes the starting point dependence. It turns out that QPGW gives a better description in most respects. It not only describes very well the band gaps, but also yields a better bandwidth of Na, in good agreement with experiments [85].

For the existing GW implementations, there are two main schemes. One works in the reciprocal space and real frequency [33, 93–95], the other instead works in the real space and imaginary time [96–98]. The former is from now on called conventional GW and the latter is termed "space-time" method. In the following, the two schemes will be briefly introduced.

5.7.1. Conventional GW implementations

For the conventional GW implementations, calculations of the independent-particle polarizability is done in the reciprocal space and real frequency by using the Adler and Wiser formula [99, 100]

$$\chi^0_{\mathbf{q}}(\mathbf{G},\mathbf{G}',\omega) = \frac{1}{\Omega}\sum_{n,n',\mathbf{k}}^{\text{all}} 2w_k(f_{n'\mathbf{k}-\mathbf{q}} - f_{n\mathbf{k}})\frac{\langle\psi_{n'\mathbf{k}-\mathbf{q}}|e^{-i(\mathbf{q}+\mathbf{G})\mathbf{r}}|\psi_{n\mathbf{k}}\rangle\,\langle\psi_{n\mathbf{k}}|e^{i(\mathbf{q}+\mathbf{G}')\mathbf{r}'}|\psi_{n'\mathbf{k}-\mathbf{q}}\rangle}{\omega-(\epsilon_{n\mathbf{k}}-\epsilon_{n'\mathbf{k}-\mathbf{q}})+i\eta\,\mathrm{sgn}(\epsilon_{n\mathbf{k}}-\epsilon_{n'\mathbf{k}-\mathbf{q}})}, \tag{175}$$

where Ω is the volume of the system, w_k is the weight of the considered k point, and $f_{n\mathbf{k}}$ is the one electron occupancies of the states $(n,\mathbf{k})$. Again, η is a positive infinitesimal. The factor of 2 is due to the spin-degenerate systems considered here. It should be noted that in Eq. (175) band index n and n' run over all the bands considered due to the introduction of $(f_{n'\mathbf{k}-\mathbf{q}} - f_{n\mathbf{k}})$. One can see that this step is computationally rather demanding, since the calculation involves a summation over all pairs of occupied and unoccupied states at each frequency, with a rank-one update of the microscopic response function for each pair, which leads to an unfavorable scaling that is quadratic in the number of k points used to sample the Brillouin zone ($\mathbf{kq} \approx \mathbf{k}^2$), quartic in the number of plane waves ($\mathbf{GG}'nn' \approx \mathbf{G}^4$) and linear to the number of frequencies. Therefore, the conventional *GW* calculations are usually restricted to small systems and few k points.

To optimize the computational procedure one can instead first calculate the spectral representation of the polarizability [33, 101]

$$\chi^S_{\mathbf{q}}(\mathbf{G},\mathbf{G}',\omega') = \frac{1}{\Omega}\sum_{n,n',\mathbf{k}}^{\text{all}} 2w_k\,\mathrm{sgn}(\omega')\delta(\omega'+\epsilon_{n\mathbf{k}}-\epsilon_{n'\mathbf{k}-\mathbf{q}})(f_{n\mathbf{k}}-f_{n'\mathbf{k}-\mathbf{q}}) \tag{176}$$

$$\times\langle\psi_{n'\mathbf{k}-\mathbf{q}}|e^{-i(\mathbf{q}+\mathbf{G})\mathbf{r}}|\psi_{n\mathbf{k}}\rangle\,\langle\psi_{n\mathbf{k}}|e^{i(\mathbf{q}+\mathbf{G}')\mathbf{r}'}|\psi_{n'\mathbf{k}-\mathbf{q}}\rangle, \tag{177}$$

and then the polarizability can be calculated as

$$\chi^0_{\mathbf{q}}(\mathbf{G},\mathbf{G}',\omega) = \int_0^{+\infty} d\omega'\chi^S_{\mathbf{q}}(\mathbf{G},\mathbf{G}',\omega')\left\{\frac{1}{\omega-\omega'-i\eta}-\frac{1}{\omega+\omega'+i\eta}\right\}. \tag{178}$$

By using Eq. (176), for a given frequency ω' only states that satisfy $\omega'+\epsilon_{n\mathbf{k}}-\epsilon_{n'\mathbf{k}-\mathbf{q}}=0$ will be included into the summation, greatly enhancing the efficiency.

After $\chi^0_{\mathbf{q}}(\mathbf{G},\mathbf{G}',\omega)$ is known, the full screened Coulomb interaction $W_{\mathbf{q}}(\mathbf{G},\mathbf{G}',\mathrm{i}\omega)$ is evaluated by multiplying the bare Coulomb kernel with the inverse dielectric matrix

$$W_{\mathbf{q}}(\mathbf{G},\mathbf{G}',\omega) = v_{\mathbf{q}}(\mathbf{G},\mathbf{G}')\varepsilon^{-1}_{\mathbf{k}}(\mathbf{G},\mathbf{G}',\omega), \tag{179}$$

where the symmetric bare Coulomb kernel $v_{\mathbf{q}}(\mathbf{G},\mathbf{G}')$ is given by

$$v_{\mathbf{q}}(\mathbf{G},\mathbf{G}') = \frac{4\pi e^2}{|\mathbf{q}+\mathbf{G}||\mathbf{q}+\mathbf{G}'|}. \tag{180}$$

The symmetric dielectric matrix is calculated within the RPA as

$$\varepsilon_{\mathbf{q}}(\mathbf{G},\mathbf{G}',\omega) = \delta_{\mathbf{G},\mathbf{G}'} - v_{\mathbf{q}}(\mathbf{G},\mathbf{G}')\chi^0_{\mathbf{q}}(\mathbf{G},\mathbf{G}',\omega). \tag{181}$$

To make the integral over the imaginary frequency well-defined, the correlated screened Coulomb interaction is defined

$$\tilde{W}_{\mathbf{q}}(\mathbf{G},\mathbf{G}',\omega) = W_{\mathbf{q}}(\mathbf{G},\mathbf{G}',\omega) - v_{\mathbf{q}}(\mathbf{G},\mathbf{G}'). \tag{182}$$

With $\tilde{W}_{\mathbf{q}}(\mathbf{G},\mathbf{G}',\omega)$, the diagonal matrix elements of the correlated self-energy is then calculated by [33]

$$\begin{aligned}
\tilde{\Sigma}(\omega)_{n\mathbf{k},n\mathbf{k}} =& \frac{1}{\Omega}\sum_{\mathbf{q}}\sum_{\mathbf{G},\mathbf{G}'}\sum_{n'}^{\text{all}}\frac{i}{2\pi}\int_{-\infty}^{+\infty} d\omega' \tilde{W}_{\mathbf{q}}(\mathbf{G},\mathbf{G}',\omega')\frac{\langle\psi_{n'\mathbf{k}-\mathbf{q}}|e^{-i(\mathbf{q}+\mathbf{G})\mathbf{r}}|\psi_{n\mathbf{k}}\rangle\langle\psi_{n\mathbf{k}}|e^{i(\mathbf{q}+\mathbf{G}')\mathbf{r}'}|\psi_{n'\mathbf{k}-\mathbf{q}}\rangle}{\omega+\omega'-\epsilon_{n'\mathbf{k}-\mathbf{q}}+i\eta\,\mathrm{sgn}(\epsilon_{n'\mathbf{k}-\mathbf{q}}-\mu)} \\
=& \frac{1}{\Omega}\sum_{\mathbf{q}}\sum_{\mathbf{G},\mathbf{G}'}\sum_{n'}^{\text{all}}\frac{i}{2\pi}\int_{0}^{+\infty} d\omega' \tilde{W}_{\mathbf{q}}(\mathbf{G},\mathbf{G}',\omega')\langle\psi_{n'\mathbf{k}-\mathbf{q}}|e^{-i(\mathbf{q}+\mathbf{G})\mathbf{r}}|\psi_{n\mathbf{k}}\rangle\langle\psi_{n\mathbf{k}}|e^{i(\mathbf{q}+\mathbf{G}')\mathbf{r}'}|\psi_{n'\mathbf{k}-\mathbf{q}}\rangle \\
&\times\left\{\frac{1}{\omega+\omega'-\epsilon_{n'\mathbf{k}-\mathbf{q}}+i\eta\,\mathrm{sgn}(\epsilon_{n'\mathbf{k}-\mathbf{q}}-\mu)}+\frac{1}{\omega-\omega'-\epsilon_{n'\mathbf{k}-\mathbf{q}}+i\eta\,\mathrm{sgn}(\epsilon_{n'\mathbf{k}-\mathbf{q}}-\mu)}\right\}
\end{aligned} \tag{183}$$

In order to obtain the final self-energy, the exact Fock exchange term must be added back

$$\Sigma(\omega)_{n\mathbf{k},n\mathbf{k}} = \tilde{\Sigma}(\omega)_{n\mathbf{k},n\mathbf{k}} + \langle\psi_{n\mathbf{k}}|Gv_x|\psi_{n\mathbf{k}}\rangle. \tag{184}$$

For more implementation details about $\langle\psi_{n\mathbf{k}}|Gv_x|\psi_{n\mathbf{k}}\rangle$, see Ref. [52]. For the core-valence exchange-correlation interaction, the Hartree-Fock approximation is used. This is found to be more reliable than LDA since the GW self-energy approaches the bare Fock exchange operator in the short wavelength limit [33].

It should be noted that the evaluation of the self-energy by Eq. (184) is rather time consuming, at least two times more expensive than the evaluation of the polarizability. There are two methods that are used in the VASP implementation [33].

(1) If the full frequency-dependent self-energy is required, the following method is employed. The first step is to calculate the screened two electron integrals for each pair $(n\mathbf{k}, n'\mathbf{k}-\mathbf{q})$ [33]

$$\tilde{W}_{n\mathbf{k},n'\mathbf{k}-\mathbf{q}}(\omega) = \frac{1}{\Omega}\sum_{\mathbf{G},\mathbf{G}'}\tilde{W}_{\mathbf{q}}(\mathbf{G},\mathbf{G}',\omega)\langle\psi_{n'\mathbf{k}-\mathbf{q}}|e^{-i(\mathbf{q}+\mathbf{G})\mathbf{r}}|\psi_{n\mathbf{k}}\rangle\langle\psi_{n\mathbf{k}}|e^{i(\mathbf{q}+\mathbf{G}')\mathbf{r}'}|\psi_{n'\mathbf{k}-\mathbf{q}}\rangle. \tag{185}$$

In the second step, a Hilbert transform of $\tilde{W}_{n\mathbf{k},n'\mathbf{k}-\mathbf{q}}(\omega)$ is performed to obtain $\tilde{\Sigma}_{n\mathbf{k},n'\mathbf{k}-\mathbf{q}}(\omega)$ [33]

$$\begin{aligned}\tilde{\Sigma}_{n\mathbf{k},n'\mathbf{k}-\mathbf{q}}(\omega) = {} & \frac{\mathrm{i}}{2\pi}\int_0^{+\infty} d\omega' \tilde{W}_{n\mathbf{k},n'\mathbf{k}-\mathbf{q}}(\omega') \\ & \times \left\{ \frac{1}{\omega + \omega' - \epsilon_{n'\mathbf{k}-\mathbf{q}} + i\eta\,\mathrm{sgn}(\epsilon_{n'\mathbf{k}-\mathbf{q}} - \mu)} + \frac{1}{\omega - \omega' - \epsilon_{n'\mathbf{k}-\mathbf{q}} + i\eta\,\mathrm{sgn}(\epsilon_{n'\mathbf{k}-\mathbf{q}} - \mu)} \right\}.\end{aligned} \tag{186}$$

Finally, the full frequency-dependent diagonal elements of the self-energy are obtained by [33]

$$\tilde{\Sigma}_{n\mathbf{k},n\mathbf{k}}(\omega) = \sum_{\mathbf{q}} \sum_{n'} \tilde{\Sigma}_{n\mathbf{k},n'\mathbf{k}-\mathbf{q}}(\omega). \tag{187}$$

(2) If only QP energies are required, one does not need to calculate the full frequency-dependent screened two electron integrals and self-energy. Instead, only the screened two electron integrals at those two frequencies, say, $\bar{\omega}_i$ and $\bar{\omega}_{i+1}$, which are closest to $|\epsilon_{n\mathbf{k}} - \epsilon_{n'\mathbf{k}-\mathbf{q}}|$, satisfying $\bar{\omega}_i < |\epsilon_{n\mathbf{k}} - \epsilon_{n'\mathbf{k}-\mathbf{q}}| < \bar{\omega}_{i+1}$, are required. Specifically, first, two auxiliary quantities are calculated [33]

$$C^+_{\mathbf{q}}(\mathbf{G},\mathbf{G}',\bar{\omega}) = \frac{\mathrm{i}}{2\pi}\int_0^{\infty} d\omega' W_{\mathbf{q}}(\mathbf{G},\mathbf{G}',\omega') \left\{ \frac{1}{\bar{\omega} + \omega' + i\eta} + \frac{1}{\bar{\omega} - \omega' + i\eta} \right\} \tag{188}$$

$$C^-_{\mathbf{q}}(\mathbf{G},\mathbf{G}',\bar{\omega}) = \frac{\mathrm{i}}{2\pi}\int_0^{\infty} d\omega' W_{\mathbf{q}}(\mathbf{G},\mathbf{G}',\omega') \left\{ \frac{1}{\bar{\omega} + \omega' - i\eta} + \frac{1}{\bar{\omega} - \omega' - i\eta} \right\}, \tag{189}$$

which are evaluated only for positive and negative complex shift, respectively, with $\bar{\omega}$ lying on the same frequency grid as other quantities such as the polarizability.

Second, the screened two-electron integrals are calculated as [33]

$$S^+_{n\mathbf{k},n'\mathbf{k}-\mathbf{q}}(\bar{\omega}) = \frac{1}{\Omega}\sum_{\mathbf{G},\mathbf{G}'} C^+_{\mathbf{q}}(\mathbf{G},\mathbf{G}',\bar{\omega}) \langle \psi_{n'\mathbf{k}-\mathbf{q}} | e^{-i(\mathbf{q}+\mathbf{G})\mathbf{r}} | \psi_{n\mathbf{k}} \rangle \langle \psi_{n\mathbf{k}} | e^{i(\mathbf{q}+\mathbf{G}')\mathbf{r}'} | \psi_{n'\mathbf{k}-\mathbf{q}} \rangle \tag{190}$$

$$S^-_{n\mathbf{k},n'\mathbf{k}-\mathbf{q}}(\bar{\omega}) = \frac{1}{\Omega}\sum_{\mathbf{G},\mathbf{G}'} C^-_{\mathbf{q}}(\mathbf{G},\mathbf{G}',\bar{\omega}) \langle \psi_{n'\mathbf{k}-\mathbf{q}} | e^{-i(\mathbf{q}+\mathbf{G})\mathbf{r}} | \psi_{n\mathbf{k}} \rangle \langle \psi_{n\mathbf{k}} | e^{i(\mathbf{q}+\mathbf{G}')\mathbf{r}'} | \psi_{n'\mathbf{k}-\mathbf{q}} \rangle. \tag{191}$$

Finally, the self-energy at $\epsilon_{n\mathbf{k}}$ can be calculated as a sum of these screened two-electron integrals [33]

$$\tilde{\Sigma}_{n\mathbf{k},n\mathbf{k}}(\epsilon_{n\mathbf{k}}) = \sum_{n'} \sum_{\mathbf{q}} \mathrm{sgn}(\epsilon_{n\mathbf{k}} - \epsilon_{n'\mathbf{k}-\mathbf{q}}) S^{\mathrm{sgn}(\epsilon_{n'\mathbf{k}-\mathbf{q}} - \mu)\,\mathrm{sgn}(\epsilon_{n\mathbf{k}} - \epsilon_{n'\mathbf{k}-\mathbf{q}})}_{n\mathbf{k},n'\mathbf{k}-\mathbf{q}}(\epsilon_{n\mathbf{k}} - \epsilon_{n'\mathbf{k}-\mathbf{q}}). \tag{192}$$

It should be noted that the screened two electron integrals are originally calculated at a discrete set of frequencies $\bar{\omega}_i$, the values of S^+ or S^- at the points $\Delta_{nn'} = \epsilon_{n\mathbf{k}} - \epsilon_{n'\mathbf{k}-\mathbf{q}}$ need to be obtained by a linear interpolation from those two frequency points of the grid which are closest to the energy $\Delta_{nn'}$ [33]

$$
\begin{aligned}
S^{+}_{n\mathbf{k},n'\mathbf{k}-\mathbf{q}}(|\Delta_{nn'}|) =& \theta(|\Delta_{nn'}| - \bar{\omega}_i)\theta(\bar{\omega}_{i+1} - |\Delta_{nn'}|) \\
&\times\left(\frac{\bar{\omega}_{i+1} - |\Delta_{nn'}|}{\bar{\omega}_{i+1} - \bar{\omega}_i} S^{+}_{n\mathbf{k},n'\mathbf{k}-\mathbf{q}}(\bar{\omega}_i) + \frac{|\Delta_{nn'}| - \bar{\omega}_i}{\bar{\omega}_{i+1} - \bar{\omega}_i} S^{+}_{n\mathbf{k},n'\mathbf{k}-\mathbf{q}}(\bar{\omega}_{i+1})\right)
\end{aligned}
\tag{193}
$$

$$
\begin{aligned}
S^{-}_{n\mathbf{k},n'\mathbf{k}-\mathbf{q}}(|\Delta_{nn'}|) =& \theta(|\Delta_{nn'}| - \bar{\omega}_i)\theta(\bar{\omega}_{i+1} - |\Delta_{nn'}|) \\
&\times\left(\frac{\bar{\omega}_{i+1} - |\Delta_{nn'}|}{\bar{\omega}_{i+1} - \bar{\omega}_i} S^{-}_{n\mathbf{k},n'\mathbf{k}-\mathbf{q}}(\bar{\omega}_i) + \frac{|\Delta_{nn'}| - \bar{\omega}_i}{\bar{\omega}_{i+1} - \bar{\omega}_i} S^{-}_{n\mathbf{k},n'\mathbf{k}-\mathbf{q}}(\bar{\omega}_{i+1})\right).
\end{aligned}
\tag{194}
$$

For a negative $\Delta_{nn'}$, the following simple transformations are used [33]

$$
S^{+}_{n\mathbf{k},n'\mathbf{k}-\mathbf{q}}(-|\Delta_{nn'}|) = -S^{-}_{n\mathbf{k},n'\mathbf{k}-\mathbf{q}}(|\Delta_{nn'}|) \tag{195}
$$

$$
S^{-}_{n\mathbf{k},n'\mathbf{k}-\mathbf{q}}(-|\Delta_{nn'}|) = -S^{+}_{n\mathbf{k},n'\mathbf{k}-\mathbf{q}}(|\Delta_{nn'}|). \tag{196}
$$

Similarly, one could easily calculate the self-energy at $\epsilon_{n\mathbf{k}} - \delta$ and $\epsilon_{n\mathbf{k}} + \delta$ with small postive δ, say 0.1 eV, from

$$
S^{+}_{n\mathbf{k},n'\mathbf{k}-\mathbf{q}}(|\Delta_{nn'}| + \delta) = S^{+}_{n\mathbf{k},n'\mathbf{k}-\mathbf{q}}(|\Delta_{nn'}|) + \delta \left.\frac{dS^{+}_{n\mathbf{k},n'\mathbf{k}-\mathbf{q}}(\omega)}{d\omega}\right|_{\omega=|\Delta_{nn'}|} \tag{197}
$$

$$
S^{-}_{n\mathbf{k},n'\mathbf{k}-\mathbf{q}}(|\Delta_{nn'}| + \delta) = S^{+}_{n\mathbf{k},n'\mathbf{k}-\mathbf{q}}(|\Delta_{nn'}|) + \delta \left.\frac{dS^{-}_{n\mathbf{k},n'\mathbf{k}-\mathbf{q}}(\omega)}{d\omega}\right|_{\omega=|\Delta_{nn'}|}. \tag{198}
$$

After $\Sigma_{n\mathbf{k},n\mathbf{k}}(\epsilon_{n\mathbf{k}}-\delta)$, $\Sigma_{n\mathbf{k},n\mathbf{k}}(\epsilon_{n\mathbf{k}})$ and $\Sigma_{n\mathbf{k},n\mathbf{k}}(\epsilon_{n\mathbf{k}}+\delta)$ are obtained, $\left.\frac{\partial\Sigma_{n\mathbf{k},n\mathbf{k}}(\omega)}{\partial\omega}\right|_{\omega=\epsilon_{n\mathbf{k}}}$ can be trivially calculated by the finite difference method. Finally, the QP energy $\epsilon^{\mathrm{QP}}_{n\mathbf{k}}$ is evaluated by Eq. (172).

One could see that to obtain the QP energy $\epsilon^{\mathrm{QP}}_{n\mathbf{k}}$, the screened two electron integrals $S^{\pm}_{n\mathbf{k},n'\mathbf{k}-\mathbf{q}}(\bar{\omega})$ are required to be calculated at two frequencies $\bar{\omega}_i$ and $\bar{\omega}_{i+1}$ only, which are closest to $|\epsilon_{n\mathbf{k}} - \epsilon_{n'\mathbf{k}-\mathbf{q}}|$ satisfying $\bar{\omega}_i < |\epsilon_{n\mathbf{k}} - \epsilon_{n'\mathbf{k}-\mathbf{q}}| < \bar{\omega}_{i+1}$. Therefore, this method is independent of the frequency grid and significantly improves the efficiencies in the evaluation of QP energies. However, one should note that this method cannot be used to obtain the full frequency-dependent self-energy.

5.7.2. Space-time method

As discussed above, the direct evaluation of the polarizability in reciprocal space and real frequency results in an unfavorable scaling, that is quartic in the system size and quadratic in the number of k points used to sample the Brillouin zone (BZ). Even though the spectral representation of the polarizability greatly enhances the efficiency, one still needs to take care of the integration along the real frequency axis. To achieve a reasonably converged polarizability, many real frequency grid points (~50 or more) are required, increasing the computational cost and memory storage. However, the polarizability is simply multiplicative, when evaluated in the real space and imaginary time domain [96, 102]

$$\chi(\mathbf{r}, \mathbf{r}', \mathrm{i}\tau) = G(\mathbf{r}, \mathbf{r}', \mathrm{i}\tau) G^{*}(\mathbf{r}, \mathbf{r}', -\mathrm{i}\tau). \tag{199}$$

Also, the calculation of the self-energy becomes much simpler, when evaluated in real space and imaginary time [96]:

$$\Sigma(\mathbf{r}, \mathbf{r}', \mathrm{i}\tau) = -G(\mathbf{r}, \mathbf{r}', \mathrm{i}\tau) W(\mathbf{r}, \mathbf{r}', \mathrm{i}\tau). \tag{200}$$

By doing so, one actually avoids the expensive convolution of the Green's function and screened Coulomb interaction in the reciprocal space and real frequency domain, as used in the conventional GW implementations. Instead, only a few imaginary time points are required in the space-time method, due to the smooth behavior of the Green's functions and screened Coulomb interaction along the imaginary axis.

However, in the original implementation of the space-time method by Godby *et al.* [96, 102] the Green's functions, screened Coulomb interaction and self-energy are built and stored directly using the real space grid points, which are in the order of ten thousands, definitely increasing the memory requirement. In addition, it is implemented within the pseudo-potential framework and thus not full-potential. Another drawback of the space-time method is that to obtain the experimental observables of interest, such as QP energies and spectral functions, which are obviously measured all along the real frequency axis, analytic continuation from the imaginary axis to the real axis should be performed. In the work of Godby *et al.* [96], a multipole expansion was used by taking into account the pole structure of the self-energy

$$\Sigma(i\omega) = a_0 + \sum_{k=1}^{n} \frac{a_k}{i\omega - z_k}, \tag{201}$$

where a_0, a_k and z_k are complex numbers, and n is the number of poles. However, it turns out that the multipole expansion method is rather unstable when the number of poles exceeds three. The fitted parameters are rather sensitive to the initial starting parameters. We have put a separate discussion on the analytic continuation in Appendix (C). Another thing is that if the GW method is implemented in the Matsubara-time domain [97, 98], many Matsubara frequencies are required. For instance, for T= 300 K around 3078 Matsubara frequencies are needed within 0 and 500 eV. This definitely increases the memory storage.

In order to overcome the disadvantages of the conventional GW implementation and space-time method, we will present a promising low-scaling GW implementation in Section (6). It allows for fast quasiparticle calculations with a scaling that is cubic in the system size and linear in the number of k points used to sample the Brillouin zone. This makes possible the GW calculations on large systems.

Part II.

Methodological Developments

6. Low scaling GW method: implementation

As already mentioned in Section (5.7), conventional GW calculations are usually restricted to small systems and few k points, while the space-time method demands considerable storage for the Green's function and self-energy due to the huge number of real-space grid points and fairly dense imaginary time/frequency grids. To circumvent the large storage requirement of the space-time method, a promising scheme has been recently proposed by Kaltak *et al.* [103, 104]. It allows to calculate the random phase approximation (RPA) correlation energy with a cubic scaling in the system size and a linear scaling in the number of k points used to sample the BZ. As in Rojas *et al.*'s work [96], this is achieved by calculating the polarizability in real space and imaginary time via contraction over the Green's functions of occupied and unoccupied states. The transformation of the polarizability from the imaginary time to the frequency domain is performed by an efficient discrete Fourier transformation with only a few nonuniform grid points [103]. Spatial fast Fourier transformations (FFT) within a supercell are utilized to go from real space to reciprocal space and vice versa [104].

In this section, we extend Kaltak's scheme [103, 104] to QP calculations in the GW approximation, in which the screened Coulomb interaction W is calculated within the RPA and the self-energy is efficiently evaluated via contraction over the Green's function and W in real space and imaginary time. Similar spatial FFT as discussed in Ref. [104] are employed, whenever transformations between the real and reciprocal space are required. To transform the self-energy from the imaginary time to the frequency domain, nonuniform cosine and sine transformations are used for the even and odd part of the self-energy, respectively. For the sake of brevity, here, we focus only on the formulations for the low-scaling single-shot GW implementation within the framework of the PAW, where the one electron energies and wave functions required in G and W are fixed at the DFT level. To avoid confusion with the conventional G_0W_0, we denote our low-scaling single-shot GW as G_0W_0r. Its applications on extended systems and molecules will be shown in Sections (7.1) and (7.2), respectively. The self-consistent low-scaling GW will be discussed in Section (9). Given that DMFT is usually formulated on the imaginary frequency axis as well [105, 106], our method provides a natural interface for the combination of GW with DMFT, which will be discussed in Section (10).

This section was published in Ref. [107].

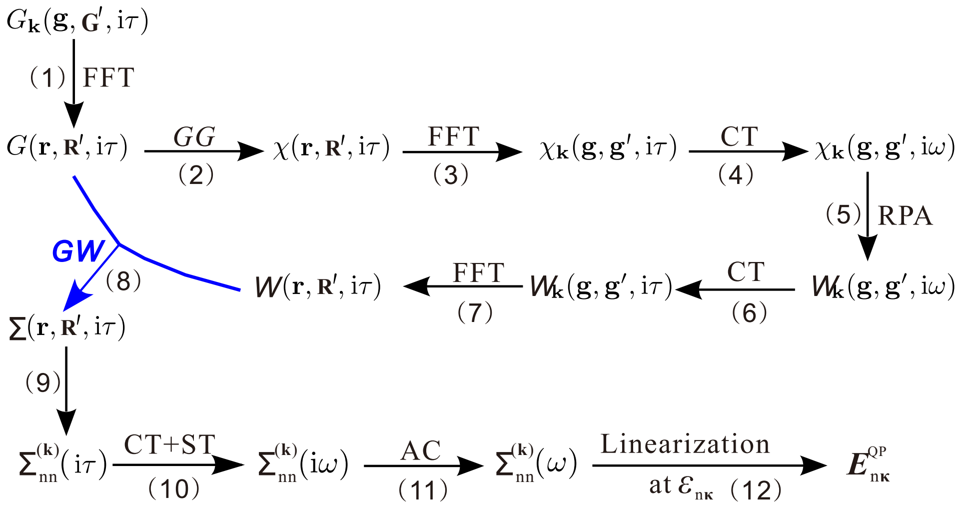

Figure 12: Schematic work flow for the low-scaling *GW* QP calculations showing the necessary steps [(1)–(12)] to obtain the QP energies from the Green's function G via the polarizability χ, screened Coulomb interaction W, and self-energy Σ. FFT denote fast Fourier transformations between real and reciprocal space. CT and ST are nonuniform cosine and sine transformations between imaginary time and frequency.

6.1. Computational Scheme of low scaling *GW* method

Figure 12 shows our scheme for the low-scaling *GW* QP calculations. The polarizability $\chi(\mathbf{r},\mathbf{R}',i\tau)$ is calculated via the contraction (GG) of the occupied and unoccupied Green's functions within the PAW framework [104]. The contraction is performed in real space and the necessary quantities are obtained by fast Fourier transformations (FFT) within a supercell [104]. Subsequently, the screened interaction $W_{\mathbf{k}}(\mathbf{g},\mathbf{g}',i\omega)$ is obtained within the RPA. To transform the polarizability χ and screened Coulomb interaction W from imaginary time to frequency domain and vice versa, efficient nonuniform cosine transformations (CT) [103] are used. The self-energy $\Sigma(\mathbf{r},\mathbf{R}',i\tau)$ is calculated by contracting the Green's function and W within the *GW* approximation. The matrix elements of the self-energy in the orbital basis are evaluated within the PAW. To transform the self-energy from the imaginary time to the frequency domain, CT and sine transformations (ST), respectively, are used for the even and odd part of the self-energy. The self-energy along the real frequency axis is obtained by an analytic continuation (AC). Finally, the QP energies $E^{QP}_{n\mathbf{k}}$ within single-shot G_0W_0r are calculated by linearizing the diagonal elements of the self-energy around the DFT one-electron eigenvalues $\epsilon_{n\mathbf{k}}$. The subsequent subsections describe these steps in detail.

6.2. Description of notations and definitions

In this part, we will give the description of the notations used throughout the thesis, the definition of the Green's functions, as well as the spatial and temporal Fourier transformations.

6.2.1. Definitions of Green's functions

We have defined two types of Green's functions: occupied and unoccupied Green's functions, which are evaluated for the negative and positive time, respectively.

$$\underline{G}(\mathbf{r},\mathbf{r}',\mathrm{i}\tau) = \sum_{i}^{\mathrm{occ}} \psi_i(\mathbf{r})\psi_i^*(\mathbf{r}')\mathbf{e}^{-\epsilon_i\tau} \quad (\tau < 0), \tag{202}$$

$$\overline{G}(\mathbf{r},\mathbf{r}',\mathrm{i}\tau) = -\sum_{a}^{\mathrm{unocc}} \psi_a(\mathbf{r})\psi_a^*(\mathbf{r}')\mathbf{e}^{-\epsilon_a\tau} \quad (\tau > 0). \tag{203}$$

Here the indices i and a label occupied and unoccupied orbitals, respectively. $\psi_i(\mathbf{r})$ ($\psi_a(\mathbf{r})$) is the one-electron orbital with the energy of ϵ_i (ϵ_a) and the Fermi energy is set to zero. This implies that all occupied (unoccupied) one-electron energies ϵ_i (ϵ_a) are negative (positive), yielding exponentially decaying Green's functions $\underline{G}$ and $\overline{G}$. With the definitions in Eqs. (202–203), the single particle Green's function can be expressed as

$$G(\mathbf{r},\mathbf{r}',\mathrm{i}\tau) = \Theta(\tau)\overline{G}(\mathbf{r},\mathbf{r}',\mathrm{i}\tau) + \Theta(-\tau)\underline{G}(\mathbf{r},\mathbf{r}',\mathrm{i}\tau), \tag{204}$$

where Θ is the Heaviside step function.

6.2.2. Nonuniform imaginary time and frequency grids

The imaginary time $\{\mathrm{i}\tau_j\}_{j=1}^{N}$ and frequency $\{\mathrm{i}\omega_k\}_{k=1}^{N}$ grids used in the present work have been determined by minimizing the discretization error of the direct Møller-Plesset energy in the imaginary time and frequency domain, respectively [103]

$$\hat{\eta}(\vec{\sigma},\vec{\tau},x) = \frac{1}{x} - \sum_{j=1}^{N} \sigma_j \mathbf{e}^{-2x|\tau_j|}, \tag{205}$$

$$\eta(\vec{\theta},\vec{\omega},x) = \frac{1}{x} - \frac{1}{2\pi}\sum_{k=1}^{N} \theta_k \left[\frac{2x}{x^2+\omega_k^2}\right]^2, \tag{206}$$

for all transition energies $x \in [\epsilon_{\min}, \epsilon_{\max}]$ with $\epsilon_{\min} = \min\{\epsilon_a - \epsilon_i\}$ and $\epsilon_{\max} = \max\{\epsilon_a - \epsilon_i\}$. $\{\sigma_j\}_{j=1}^N$ and $\{\theta_k\}_{k=1}^N$ are the corresponding weights. For more detailed information concerning how such optimized imaginary time/frequency grids are obtained, please refer to Appendix (B.1). It has been found that the two grids are dual to each other. That is, given $\{\mathrm{i}\tau_j\}_{j=1}^N$, the discretization error function is minimal at the grid points $\{\mathrm{i}\omega_k\}_{k=1}^N$, and vice versa [103]. It has also been observed that the RPA correlation energy can be evaluated accurately with a modest number of grid points [103]. For instance, to achieve μeV accuracy per atom, 16 time and frequency points are usually sufficient [103]. In the present work, we also found that with 20 grid points, we could obtain converged QP energies with 0.01 eV accuracy for all the materials considered. With a few imaginary grid points, the memory requirements are obviously much reduced.

6.2.3. Nonuniform cosine and sine transformations

To go from the imaginary time to imaginary frequency, and vice versa, nonuniform discrete cosine and sine transformations have been exploited for the even and odd functions, respectively. Specifically, for an even function F with respect to imaginary time/frequency, such as the polarizability χ and screened Coulomb interaction W, the forward Fourier transformation is given by

$$F(\mathrm{i}\omega) = 2\int_0^\infty \mathrm{d}\tau \cos(\omega\tau) F(\mathrm{i}\tau). \tag{207}$$

We approximate it by a discrete CT

$$F(\mathrm{i}\omega_k) = \sum_{j=1}^{N} \gamma_{kj} \cos(\omega_k \tau_j) F(\mathrm{i}\tau_j). \tag{208}$$

Here the imaginary time $\{\mathrm{i}\tau_j\}_{j=1}^N$ and frequency $\{\mathrm{i}\omega_k\}_{k=1}^N$ grids are precalculated. The coefficients γ_{kj} are determined in analogy to the imaginary time and frequency grids by minimizing the error function [103]

$$\eta^c(x, \gamma) = \underbrace{\frac{2x}{x^2 + \omega_k^2}}_{2\int_0^\infty \mathrm{d}\tau \cos(\omega_k\tau) \mathrm{e}^{-x\tau}} - \sum_{j=1}^{N} \gamma_{kj} \cos(\omega_k \tau_j) \mathrm{e}^{-x\tau_j}, \tag{209}$$

for all transition energies $x \in [\epsilon_{\min}, \epsilon_{\max}]$ and each known frequency point ω_k separately.

Analogously, the inverse CT is given by [103]

$$F(\mathrm{i}\tau_j) = \sum_{k=1}^{N} \xi_{jk} \cos(\tau_j \omega_k) F(\mathrm{i}\omega_k), \tag{210}$$

where the coefficients ξ_{jk} are determined by minimizing the error function [103]

$$\hat{\eta}^c(x,\boldsymbol{\xi}) = \underbrace{\mathrm{e}^{-x|\tau_j|}}_{2\int_0^\infty \frac{\mathrm{d}\omega}{2\pi}\cos(\tau_j\omega)\frac{2x}{x^2+\omega^2}} - \sum_{k=1}^{N} \xi_{jk}\cos(\tau_j\omega_k)\frac{2x}{x^2+\omega_k^2}. \tag{211}$$

It can be proved that the matrix $\boldsymbol{\xi}\,\mathbf{cos}\,(\boldsymbol{\tau\omega})$ is the inverse of the matrix $\boldsymbol{\gamma}\,\mathbf{cos}\,(\boldsymbol{\omega\tau})$ in Eq. (208).

In contrast, for an odd function F with respect to imaginary time/frequency, the forward Fourier transformation is described by

$$F(\mathrm{i}\omega) = 2\mathrm{i}\int_0^\infty \mathrm{d}\tau\sin(\omega\tau)F(\mathrm{i}\tau), \tag{212}$$

which is approximated by a discrete ST

$$F(\mathrm{i}\omega_k) = \mathrm{i}\sum_{j=1}^{N}\lambda_{kj}\sin(\omega_k\tau_j)F(\mathrm{i}\tau_j). \tag{213}$$

Again, $\{\mathrm{i}\tau_j\}_{j=1}^N$ and $\{\mathrm{i}\omega_k\}_{k=1}^N$ are precalculated and chosen to be identical to the cosine grid. However, the coefficients λ_{kj} are determined by minimizing the error function

$$\eta^s(x,\boldsymbol{\lambda}) = \underbrace{\frac{2\omega_k}{x^2+\omega_k^2}}_{2\int_0^\infty \mathrm{d}\tau\sin(\omega_k\tau)\mathrm{e}^{-x\tau}} - \sum_{j=1}^{N}\lambda_{kj}\sin(\omega_k\tau_j)\mathrm{e}^{-x\tau_j}. \tag{214}$$

To this end, similar strategies as discussed in Ref. [103] are used. The inverse ST is then obtained by

$$F(\mathrm{i}\tau_j) = -\mathrm{i}\sum_{k=1}^{N}\zeta_{jk}\sin(\tau_j\omega_k)F(\mathrm{i}\omega_k), \tag{215}$$

where the matrix $\boldsymbol{\zeta}\,\mathbf{sin}\,(\boldsymbol{\tau\omega})$ is the inverse of the matrix $\boldsymbol{\lambda}\,\mathbf{sin}\,(\boldsymbol{\omega\tau})$ in Eq. (213). It should be noted that the matrices $\boldsymbol{\gamma}$, $\boldsymbol{\xi}$, $\boldsymbol{\lambda}$, and $\boldsymbol{\zeta}$ are all precalculated and stored after the imaginary time $\{\mathrm{i}\tau_j\}_{j=1}^N$ and frequency $\{\mathrm{i}\omega_k\}_{k=1}^N$ grids are determined. For more derivation details on the nonuniform cosine and sine transformations, we refer the readers to Appendix (B.2).

6.2.4. Spatial fast Fourier transformation

To transform the Green's functions from reciprocal to real space, we employ fast discrete Fourier transformation within a supercell [104]. Considering the symmetry of the Green's functions, only the irreducible stripe $G(\mathbf{r},\mathbf{R}')$ needs to be calculated in two steps [104]:

$$G(\mathbf{r},\mathbf{G}') = \sum_{\mathbf{g}\in\mathcal{L}_c^*}\mathrm{e}^{\mathrm{i}(\mathbf{k}+\mathbf{g})\mathbf{r}}G_{\mathbf{k}}(\mathbf{g},\mathbf{g}'), \tag{216}$$

$$G(\mathbf{r},\mathbf{R}') = \sum_{\mathbf{G}'\in\mathcal{L}_s^*}G(\mathbf{r},\mathbf{G}')\mathrm{e}^{-\mathrm{i}\mathbf{G}'\mathbf{R}'}. \tag{217}$$

Here, position vector $\mathbf{r}$ is restricted to the unit cell (C), whereas $\mathbf{R}$ extends over the entire supercell (S). $\mathbf{g}$ and $\mathbf{G}$, respectively, represent the lattice vector of the reciprocal cell ($\mathcal{L}_c^*$) and reciprocal supercell ($\mathcal{L}_s^*$). Furthermore, $\mathbf{k}$ is a k point used to sample the Brillouin zone (BZ) and $\mathbf{G}' = \mathbf{k} + \mathbf{g}'$. The time complexity of the spatial FFT is of the order: $\ln(N_b^2 N_k) N_b^2 N_k$ with N_b and N_k being the total number of considered basis vectors $\mathbf{g}$ and k points in the BZ, respectively [104].

Similarly, the inverse spatial FFT is given by [104]

$$G(\mathbf{r}, \mathbf{G}') = \sum_{\mathbf{R}' \in S} G(\mathbf{r}, \mathbf{R}') \mathrm{e}^{\mathrm{i}\mathbf{G}'\mathbf{R}'}, \tag{218}$$

$$G_{\mathbf{k}}(\mathbf{g}, \mathbf{g}') = \sum_{\mathbf{r} \in C} \mathrm{e}^{-\mathrm{i}(\mathbf{k}+\mathbf{g})\mathbf{r}} G(\mathbf{r}, \mathbf{G}'), \tag{219}$$

which has the same time complexity as the spatial FFT.

Considering that the polarizability χ has the same spatial symmetry as the Green's functions, the above mentioned spatial and inverse spatial FFT applies to the polarizability χ as well.

6.3. Calculation of the polarizability $\chi(\mathbf{r}, \mathbf{R}', i\tau)$ within the PAW

In this section, we discuss the steps (1–2) in Fig. 12 and derive a suitable expression for the polarizability in real space $\chi(\mathbf{r}, \mathbf{R}', \mathrm{i}\tau)$ within the framework of the PAW method.

It is known that the evaluation of the polarizability in reciprocal space and real frequency results in an unfavorable scaling. However, the polarizability is simply multiplicative, when evaluated in the real space and imaginary time domain [96, 102]

$$\chi(\mathbf{r}, \mathbf{R}', \mathrm{i}\tau) = G(\mathbf{r}, \mathbf{R}', \mathrm{i}\tau) G^*(\mathbf{r}, \mathbf{R}', -\mathrm{i}\tau). \tag{220}$$

For simplicity, we restrict our considerations to positive imaginary times $\tau > 0$ in the following, since the expressions for $\tau < 0$ are obtained by exchanging $\overline{G} \leftrightarrow \underline{G}$.

Inserting expression (204) for the Green's function into (220) and using the explicit representations in Eqs. (202–203) yields for $\tau > 0$,

$$\chi(\mathbf{r}, \mathbf{R}', \mathrm{i}\tau) = -\sum_a^{\text{unocc}} \psi_a(\mathbf{r}) \psi_a^*(\mathbf{R}') \mathrm{e}^{-\epsilon_a \tau} \sum_i^{\text{occ}} \psi_i(\mathbf{R}') \psi_i^*(\mathbf{r}) \mathrm{e}^{\epsilon_i \tau}. \tag{221}$$

However, within the PAW method [30, 32], this expression is more involved, because the all-electron orbitals $\psi_{n\mathbf{k}}$ are related to the corresponding pseudo orbitals $\tilde{\psi}_{n\mathbf{k}}$ by a linear transformation

$$|\psi_{n\mathbf{k}}\rangle = |\tilde{\psi}_{n\mathbf{k}}\rangle + \sum_\mu \left(|\phi_\mu\rangle - |\tilde{\phi}_\mu\rangle \right) \langle \tilde{p}_\mu | \tilde{\psi}_{n\mathbf{k}} \rangle. \tag{222}$$

The pseudo orbitals $\tilde{\psi}_{n\mathbf{k}}$ are the variational quantity of the PAW method and are expanded in plane waves, whereas ϕ_μ and $\tilde{\phi}_\mu$ are all-electron and pseudo partial waves, respectively and $\tilde{p}_\mu$ are projectors, which are dual to the $\tilde{\phi}_\mu$ within the augmentation sphere. The index $\mu = (\mathbf{R}_\mu, n_\mu, l_\mu, m_\mu)$ is an abbreviation for the atomic site $\mathbf{R}_\mu$ and the energy quantum number n_μ and angular momentum numbers (l_μ, m_μ) that characterize the solution of the Schrödinger equation for a reference atom.

Inserting Eq. (222) into Eq. (221) yields four terms for $\tau > 0$,

$$\chi^{(1)}(\mathbf{r}, \mathbf{R}', \mathrm{i}\tau) = -\sum_a^{\mathrm{unocc}} \tilde{\psi}_a(\mathbf{r})\tilde{\psi}_a^*(\mathbf{R}')\mathrm{e}^{-\epsilon_a\tau} \sum_i^{\mathrm{occ}} \tilde{\psi}_i(\mathbf{R}')\tilde{\psi}_i^*(\mathbf{r})\mathrm{e}^{\epsilon_i\tau}, \tag{223}$$

$$\begin{aligned}\chi^{(2)}(\mathbf{r}, \mathbf{R}', \mathrm{i}\tau) = -\sum_{\mu\nu} Q_{\mu\nu}(\mathbf{r}) &\sum_a^{\mathrm{unocc}} \langle \tilde{p}_\nu | \tilde{\psi}_a \rangle \tilde{\psi}_a^*(\mathbf{R}')\mathrm{e}^{-\epsilon_a\tau} \\ &\times \sum_i^{\mathrm{occ}} \tilde{\psi}_i(\mathbf{R}')\langle \tilde{\psi}_i | \tilde{p}_\mu \rangle \mathrm{e}^{\epsilon_i\tau},\end{aligned} \tag{224}$$

$$\begin{aligned}\chi^{(3)}(\mathbf{r}, \mathbf{R}', \mathrm{i}\tau) = -\sum_{\alpha\beta} Q_{\alpha\beta}(\mathbf{R}') &\sum_a^{\mathrm{unocc}} \tilde{\psi}_a(\mathbf{r})\langle \tilde{\psi}_a | \tilde{p}_\alpha \rangle \mathrm{e}^{-\epsilon_a\tau} \\ &\times \sum_i^{\mathrm{occ}} \langle \tilde{p}_\beta | \tilde{\psi}_i \rangle \tilde{\psi}_i^*(\mathbf{r})\mathrm{e}^{\epsilon_i\tau},\end{aligned} \tag{225}$$

$$\begin{aligned}\chi^{(4)}(\mathbf{r}, \mathbf{R}', \mathrm{i}\tau) = -\sum_{\mu\nu\alpha\beta} &Q_{\mu\nu}(\mathbf{r})Q_{\alpha\beta}(\mathbf{R}') \sum_a^{\mathrm{unocc}} \langle \tilde{p}_\nu | \tilde{\psi}_a \rangle \langle \tilde{\psi}_a | \tilde{p}_\alpha \rangle \mathrm{e}^{-\epsilon_a\tau} \\ &\times \sum_i^{\mathrm{occ}} \langle \tilde{p}_\beta | \tilde{\psi}_i \rangle \langle \tilde{\psi}_i | \tilde{p}_\mu \rangle \mathrm{e}^{\epsilon_i\tau},\end{aligned} \tag{226}$$

where the auxiliary function $Q_{\alpha\beta}(\mathbf{r})$ is defined as

$$Q_{\alpha\beta}(\mathbf{r}) = \phi_\alpha^*(\mathbf{r})\phi_\beta(\mathbf{r}) - \tilde{\phi}_\alpha^*(\mathbf{r})\tilde{\phi}_\beta(\mathbf{r}), \tag{227}$$

and describes the difference between the charge density of all-electron and pseudo partial waves. In practice, one needs further approximations for $Q_{\alpha\beta}(\mathbf{r})$, since normally this function is oscillatory within the augmentation sphere. In the present implementation, the function is expanded in an orthogonal set of functions, and the rapid spatial oscillations are neglected beyond a certain plane-wave energy cutoff [30].

According to the definitions of the Green's functions in Eqs. (202–203) and four expressions in Eqs. (223–226), we define here four auxiliary functions for unoccupied Green's functions:

$$\begin{aligned}
\overline{G}^{(1)}(\mathbf{r},\mathbf{R}',i\tau) &= -\sum_{a}^{\text{unocc}} \tilde{\psi}_a(\mathbf{r})\tilde{\psi}_a^*(\mathbf{R}')\mathrm{e}^{-\epsilon_a\tau}, && (228)\\
\overline{G}^{(2)}(\nu,\mathbf{R}',i\tau) &= -\sum_{a}^{\text{unocc}} \langle\tilde{p}_\nu|\tilde{\psi}_a\rangle\tilde{\psi}_a^*(\mathbf{R}')\mathrm{e}^{-\epsilon_a\tau}, && (229)\\
\overline{G}^{(3)}(\mathbf{r},\alpha,i\tau) &= -\sum_{a}^{\text{unocc}} \tilde{\psi}_a(\mathbf{r})\langle\tilde{\psi}_a|\tilde{p}_\alpha\rangle\mathrm{e}^{-\epsilon_a\tau}, && (230)\\
\overline{G}^{(4)}(\nu,\alpha,i\tau) &= -\sum_{a}^{\text{unocc}} \langle\tilde{p}_\nu|\tilde{\psi}_a\rangle\langle\tilde{\psi}_a|\tilde{p}_\alpha\rangle\mathrm{e}^{-\epsilon_a\tau}, && (231)
\end{aligned}$$

and four auxiliary functions for occupied Green's functions:

$$\begin{aligned}
\underline{G}^{*(1)}(\mathbf{r},\mathbf{R}',-i\tau) &= \sum_{i}^{\text{occ}} \tilde{\psi}_i(\mathbf{R}')\tilde{\psi}_i^*(\mathbf{r})\mathrm{e}^{\epsilon_i\tau}, && (232)\\
\underline{G}^{*(2)}(\mu,\mathbf{R}',-i\tau) &= \sum_{i}^{\text{occ}} \tilde{\psi}_i(\mathbf{R}')\langle\tilde{\psi}_i|\tilde{p}_\mu\rangle\mathrm{e}^{\epsilon_i\tau}, && (233)\\
\underline{G}^{*(3)}(\mathbf{r},\beta,-i\tau) &= \sum_{i}^{\text{occ}} \langle\tilde{p}_\beta|\tilde{\psi}_i\rangle\tilde{\psi}_i^*(\mathbf{r})\mathrm{e}^{\epsilon_i\tau}, && (234)\\
\underline{G}^{*(4)}(\mu,\beta,-i\tau) &= \sum_{i}^{\text{occ}} \langle\tilde{p}_\beta|\tilde{\psi}_i\rangle\langle\tilde{\psi}_i|\tilde{p}_\mu\rangle\mathrm{e}^{\epsilon_i\tau}. && (235)
\end{aligned}$$

It is easy to prove that

$$\begin{aligned}
G^{(2)}(\nu,\mathbf{R}',i\tau) &= \sum_{\mathbf{r}\in C}\langle\tilde{p}_\nu|\mathbf{r}\rangle G^{(1)}(\mathbf{r},\mathbf{R}',i\tau), && (236)\\
G^{(3)}(\mathbf{r},\alpha,i\tau) &= \sum_{\mathbf{R}'\in S} G^{(1)}(\mathbf{r},\mathbf{R}',i\tau)\langle\mathbf{R}'|\tilde{p}_\alpha\rangle, && (237)\\
G^{(4)}(\nu,\alpha,i\tau) &= \sum_{\mathbf{r}\in C}\sum_{\mathbf{R}'\in S}\langle\tilde{p}_\nu|\mathbf{r}\rangle G^{(1)}(\mathbf{r},\mathbf{R}',i\tau)\langle\mathbf{R}'|\tilde{p}_\alpha\rangle, && (238)
\end{aligned}$$

holds for both auxiliary unoccupied and occupied Green's functions.

With the definitions in Eqs. (228–235), we obtain the central expression for the polarizability $\chi(\mathbf{r},\mathbf{R}',i\tau)$ at $\tau > 0$ within the PAW framework as follows:

$$\begin{aligned}
\chi(\mathbf{r},\mathbf{R}',\mathrm{i}\tau) =&\overline{G}^{(1)}(\mathbf{r},\mathbf{R}',i\tau)\underline{G}^{*(1)}(\mathbf{r},\mathbf{R}',-i\tau)\\
&+\sum_{\mu\nu} Q_{\mu\nu}(\mathbf{r})\overline{G}^{(2)}(\nu,\mathbf{R}',i\tau)\underline{G}^{*(2)}(\mu,\mathbf{R}',-i\tau)\\
&+\sum_{\alpha\beta} Q_{\alpha\beta}(\mathbf{R}')\overline{G}^{(3)}(\mathbf{r},\alpha,i\tau)\underline{G}^{*(3)}(\mathbf{r},\beta,-i\tau)\\
&+\sum_{\mu\nu\alpha\beta} Q_{\mu\nu}(\mathbf{r})Q_{\alpha\beta}(\mathbf{R}')\overline{G}^{(4)}(\nu,\alpha,i\tau)\underline{G}^{*(4)}(\mu,\beta,-i\tau).
\end{aligned} \qquad (239)$$

Here, the atomic positions $\mathbf{R}_\mu$, $\mathbf{R}_\nu$ are restricted to the unit cell C, whilst $\mathbf{R}_\alpha$, $\mathbf{R}_\beta$ take values within the supercell S. Note that the polarizability for $\tau < 0$ is recovered from Eq. (239) by exchanging $\overline{G} \leftrightarrow \underline{G}$.

In practice, we do not store the auxiliary Green's functions in Eqs. (228–230) and (232–234) directly using the real-space grids, since this would demand considerable storage due to the large number of real-space grid points. Instead, we evaluate them in the reciprocal space using a plane wave representation first, and successively Fourier transform the functions to real space whenever required. Since the number of plane-wave coefficients is at least twice but often up to sixteen times smaller than the number of real-space grid points, the storage demand is dramatically reduced. Fourier transforming Eqs. (228–230) to the reciprocal space yields another three auxiliary unoccupied Green's functions:

$$\overline{G}^{(1)}_{\mathbf{k}}(\mathbf{g}, \mathbf{G}', i\tau) = -\sum_{a}^{\text{unocc}} \langle \mathbf{g}|\tilde{\psi}_a\rangle\langle\tilde{\psi}_a|\mathbf{G}'\rangle \mathrm{e}^{-\epsilon_a\tau}, \tag{240}$$

$$\overline{G}^{(2)}_{\mathbf{k}}(\nu, \mathbf{G}', i\tau) = -\sum_{a}^{\text{unocc}} \langle \tilde{p}_\nu|\tilde{\psi}_a\rangle\langle\tilde{\psi}_a|\mathbf{G}'\rangle \mathrm{e}^{-\epsilon_a\tau}, \tag{241}$$

$$\overline{G}^{(3)}_{\mathbf{k}}(\mathbf{g}, \alpha, i\tau) = -\sum_{a}^{\text{unocc}} \langle \mathbf{g}|\tilde{\psi}_a\rangle\langle\tilde{\psi}_a|\tilde{p}_\alpha\rangle \mathrm{e}^{-\epsilon_a\tau}. \tag{242}$$

Analogously, Fourier transforming Eqs. (232–234) to the reciprocal space yields another three auxiliary occupied Green's functions [108]:

$$\underline{G}^{*(1)}_{\mathbf{k}}(\mathbf{g}, \mathbf{G}', -i\tau) = \sum_{i}^{\text{occ}} \langle \mathbf{G}'|\tilde{\psi}_i\rangle\langle\tilde{\psi}_i|\mathbf{g}\rangle \mathrm{e}^{\epsilon_i\tau}, \tag{243}$$

$$\underline{G}^{*(2)}_{\mathbf{k}}(\mu, \mathbf{G}', -i\tau) = \sum_{i}^{\text{occ}} \langle \mathbf{G}'|\tilde{\psi}_i\rangle\langle\tilde{\psi}_i|\tilde{p}_\mu\rangle \mathrm{e}^{\epsilon_i\tau}, \tag{244}$$

$$\underline{G}^{*(3)}_{\mathbf{k}}(\mathbf{g}, \beta, -i\tau) = \sum_{i}^{\text{occ}} \langle \tilde{p}_\beta|\tilde{\psi}_i\rangle\langle\tilde{\psi}_i|\mathbf{g}\rangle \mathrm{e}^{\epsilon_i\tau}, \tag{245}$$

where the notation

$$\langle \mathbf{g}|\tilde{\psi}\rangle = \sum_{\mathbf{r}\in C} \mathrm{e}^{-\mathrm{i}(\mathbf{k}+\mathbf{g})\mathbf{r}}\tilde{\psi}(\mathbf{r}), \tag{246}$$

$$\langle \tilde{\psi}|\mathbf{G}'\rangle = \sum_{\mathbf{R}'\in S} \tilde{\psi}^*(\mathbf{R}')\mathrm{e}^{\mathrm{i}\mathbf{G}'\mathbf{R}'}, \tag{247}$$

is used. The computational complexity for evaluating both $\underline{G}^{(j)}$ and $\overline{G}^{(j)}$ is of the order: $NN_kN_b^3$ showing a roughly cubic scaling in the system size ($\approx N_b$) and linear scaling in the number of k points N_k and imaginary grid points N.

We point out that the widely used conventional *GW* implementation [33], where the polarizability is directly evaluated in the reciprocal space and real frequency domain, shows an unfavorable scaling that is quartic in the system size and quadratic in the number of *k* points. This scaling is acceptable or even beneficial for small systems, but prohibitive as the system size becomes larger. In contrast, in our new *GW* implementation, the computational cost in calculating the polarizability reduces to a scaling that is nearly cubic in the system size and linear in the number of *k* points. This definitely increases the efficiency of *GW* calculations for large systems. This is also true for the original space-time implementation of Godby *et al.* [96, 102], but we emphasize that our implementation has the following advantages: (i) The Green's functions are stored in a plane wave representation at a few optimized imaginary time/frequency grid points, which dramatically reduces the memory requirement. (ii) It is implemented within the PAW method. (iii) Discrete CT and ST transformations and spatial FFT are used and the implementation is highly parallelized. (iv) Although similar strategies were used in Ref. [102], an auxiliary supercell Green's function was defined without the Bloch phase factors $\mathbf{e}^{\mathbf{ik(r-r')}}$. The present method is applicable to all electron Hamiltonians, whereas the augmentation terms cannot be straightforwardly implemented following Ref. [102].

6.4. Calculation of the correlated screened Coulomb interaction $\tilde{W}(\mathbf{r},\mathbf{R}',\mathrm{i}\omega)$

Now we describe the evaluation of the dynamical correlated screened Coulomb interaction $\tilde{W}(\mathbf{r},\mathbf{R}',\mathrm{i}\omega)$, which corresponds to the steps (3–7) in Fig. 12.

Once the polarizability $\chi(\mathbf{r},\mathbf{R}',\mathrm{i}\tau)$ has been calculated, one has to Fourier transform it to the reciprocal space and imaginary frequency domain where the screened Coulomb interaction is much more comfortable to be calculated. The calculation of $\tilde{W}(\mathbf{r},\mathbf{R}',\mathrm{i}\omega)$ involves five steps:

(i) $\chi_{\mathbf{k}}(\mathbf{g},\mathbf{g}',\mathrm{i}\tau)$ is determined by an inverse spatial FFT of $\chi(\mathbf{r},\mathbf{R}',\mathrm{i}\tau)$ in two steps:

$$\chi(\mathbf{r},\mathbf{G}',\mathrm{i}\tau) = \sum_{\mathbf{R}'\in S} \chi(\mathbf{r},\mathbf{R}',\mathrm{i}\tau)\mathrm{e}^{\mathrm{i}\mathbf{G}'\mathbf{R}'}, \tag{248}$$

$$\chi_{\mathbf{k}}(\mathbf{g},\mathbf{g}',\mathrm{i}\tau) = \sum_{\mathbf{r}\in C} \mathrm{e}^{-\mathrm{i}(\mathbf{k}+\mathbf{g})\mathbf{r}}\chi(\mathbf{r},\mathbf{G}',\mathrm{i}\tau). \tag{249}$$

Actually, in our implementation the polarizability $\chi(\mathbf{r},\mathbf{R}',\mathrm{i}\tau)$ is never stored. Instead, once $\chi(\mathbf{r},\mathbf{R}',\mathrm{i}\tau)$ is known for a specific $\mathbf{r}$ and all $\mathbf{R}'$, Eq. (248) is used to Fourier transform the second index to the reciprocal space where the reciprocal wave vectors are restricted to a cutoff sphere, and $\chi(\mathbf{r}, \mathbf{G}', \mathrm{i}\tau)$ is then stored. The second FFT in Eq. (249) cannot be performed until $\chi(\mathbf{r}, \mathbf{G}', \mathrm{i}\tau)$ for all $\mathbf{r}$ has been calculated.

(ii) $\chi_{\mathbf{k}}(\mathbf{g}, \mathbf{g}', \mathrm{i}\omega)$ is computed by a CT of $\chi_{\mathbf{k}}(\mathbf{g}, \mathbf{g}', \mathrm{i}\tau)$,

$$\chi_{\mathbf{k}}(\mathbf{g}, \mathbf{g}', \mathrm{i}\omega_k) = \sum_{j=1}^{N} \gamma_{kj} \cos(\omega_k \tau_j) \chi_{\mathbf{k}}(\mathbf{g}, \mathbf{g}', \mathrm{i}\tau_j). \tag{250}$$

(iii) The full screened Coulomb interaction $W_{\mathbf{k}}(\mathbf{g}, \mathbf{g}', \mathrm{i}\omega)$ is evaluated by multiplying the bare Coulomb kernel with the inverse dielectric matrix,

$$W_{\mathbf{k}}(\mathbf{g}, \mathbf{g}', \mathrm{i}\omega) = v_{\mathbf{k}}(\mathbf{g}, \mathbf{g}') \varepsilon_{\mathbf{k}}^{-1}(\mathbf{g}, \mathbf{g}', \mathrm{i}\omega), \tag{251}$$

where the symmetric bare Coulomb kernel $v_{\mathbf{k}}(\mathbf{g}, \mathbf{g}')$ is

$$v_{\mathbf{k}}(\mathbf{g}, \mathbf{g}') = \frac{4\pi e^2}{|\mathbf{k} + \mathbf{g}||\mathbf{k} + \mathbf{g}'|}. \tag{252}$$

The symmetric dielectric matrix is calculated within the RPA as

$$\varepsilon_{\mathbf{k}}(\mathbf{g}, \mathbf{g}', \mathrm{i}\omega) = \delta_{\mathbf{g},\mathbf{g}'} - v_{\mathbf{k}}(\mathbf{g}, \mathbf{g}') \chi_{\mathbf{k}}(\mathbf{g}, \mathbf{g}', \mathrm{i}\omega). \tag{253}$$

Note that matrix multiplication and inversion are implicitly used in Eq. (251) and Eq. (253).

To make the integral over the imaginary frequency well-defined, we further define the correlated screened Coulomb interaction

$$\tilde{W}_{\mathbf{k}}(\mathbf{g}, \mathbf{g}', \mathrm{i}\omega) = W_{\mathbf{k}}(\mathbf{g}, \mathbf{g}', \mathrm{i}\omega) - v_{\mathbf{k}}(\mathbf{g}, \mathbf{g}'). \tag{254}$$

(iv) $\tilde{W}_{\mathbf{k}}(\mathbf{g}, \mathbf{g}', \mathrm{i}\tau)$ is determined by an inverse CT of $\tilde{W}_{\mathbf{k}}(\mathbf{g}, \mathbf{g}', \mathrm{i}\omega)$,

$$\tilde{W}_{\mathbf{k}}(\mathbf{g}, \mathbf{g}', \mathrm{i}\tau_j) = \sum_{k=1}^{N} \xi_{jk} \cos(\tau_j \omega_k) \tilde{W}_{\mathbf{k}}(\mathbf{g}, \mathbf{g}', \mathrm{i}\omega_k). \tag{255}$$

(iv) Finally, $\tilde{W}(\mathbf{r}, \mathbf{R}', \mathrm{i}\tau)$ is calculated by a spatial FFT in two steps:

$$\tilde{W}(\mathbf{r}, \mathbf{G}', \mathrm{i}\tau) = \sum_{\mathbf{g} \in \mathcal{L}_c^*} \mathrm{e}^{\mathrm{i}(\mathbf{k}+\mathbf{g})\mathbf{r}} \tilde{W}_{\mathbf{k}}(\mathbf{g}, \mathbf{g}', \mathrm{i}\tau), \tag{256}$$

$$\tilde{W}(\mathbf{r}, \mathbf{R}', \mathrm{i}\tau) = \sum_{\mathbf{G}' \in \mathcal{L}_s^*} \tilde{W}(\mathbf{r}, \mathbf{G}', \mathrm{i}\tau) \mathrm{e}^{-\mathrm{i}\mathbf{G}'\mathbf{R}'}. \tag{257}$$

6.5. Calculation of the self-energy

In this section, we give a detailed description how the matrix elements of the self-energy in the orbital basis along the imaginary frequency axis are evaluated. This corresponds to the steps (8–10) in Fig. 12.

6.5.1. Evaluation of the self-energy $\Sigma(\mathbf{r}, \mathbf{R}', \mathrm{i}\tau)$ within the GWA

Within the GW approximation, the self-energy in the reciprocal space and real frequency domain is evaluated by a convolution of the Green's function and screened Coulomb interaction and is used in the conventional GW implementation [33]. However, to obtain converged self-energies, a reasonable number of the real frequency points ($\sim$50 or more) is required to evaluate the convolution integral, thus increasing the computational cost. In contrast, when the self-energy is evaluated in real space and time, it is simply multiplicative [96] [see Appendix (A.4) for discussions on the convolution theorem],

$$\Sigma(\mathbf{r}, \mathbf{R}', \mathrm{i}\tau) = -G(\mathbf{r}, \mathbf{R}', \mathrm{i}\tau) W(\mathbf{r}, \mathbf{R}', \mathrm{i}\tau). \tag{258}$$

In addition, only a few imaginary time points are required due to the smooth behavior of the Green's functions and screened Coulomb interaction along the imaginary axis.

6.5.2. Evaluation of $\tilde{\Sigma}^{(\mathbf{k})}_{nn}(\mathrm{i}\tau)$ within the PAW

In the following, we evaluate the matrix elements of the self-energy in the orbital basis within the PAW framework. We focus only on the frequency/time-dependent correlation contribution $-\langle\psi_{n\mathbf{k}}|G\tilde{W}|\psi_{n\mathbf{k}}\rangle$, since the bare exchange part $-\langle\psi_{n\mathbf{k}}|Gv_x|\psi_{n\mathbf{k}}\rangle$ within the PAW has already been discussed elsewhere [52]. Furthermore, we define "occupied" $\underline{\tilde{\Sigma}}$ and "unoccupied" $\overline{\tilde{\Sigma}}$ correlated self-energies, i.e., the self-energies evaluated at negative and positive time, respectively, analogous to the Green's functions.

Here we concentrate on the occupied self-energy $\underline{\tilde{\Sigma}}$ only. The evaluation of the matrix elements of the unoccupied self-energy $\overline{\tilde{\Sigma}}$ is done by replacing $\underline{G}$ with $\overline{G}$. Within the PAW, the diagonal matrix elements of the occupied self-energy ($\tau < 0$) can be calculated as

$$\begin{aligned}\underline{\tilde{\Sigma}}^{(\mathbf{k})}_{\mathrm{nn}}(\mathrm{i}\tau) &= \langle\psi_{n\mathbf{k}}|\underline{\tilde{\Sigma}}(\mathrm{i}\tau)|\psi_{n\mathbf{k}}\rangle = -\langle\psi_{n\mathbf{k}}|\underline{G}(\mathrm{i}\tau)\tilde{W}(\mathrm{i}\tau)|\psi_{n\mathbf{k}}\rangle \\ &= -\sum_{\mathbf{r}\in C}\sum_{\mathbf{R}'\in S}\langle\tilde{\psi}_{n\mathbf{k}}|\left\{|\mathbf{r}\rangle\langle\mathbf{r}| + \sum_{\mu\nu} Q_{\mu\nu}(\mathbf{r})|\tilde{p}_\mu\rangle\langle\tilde{p}_\nu|\right\}\underline{G}(\mathrm{i}\tau) \\ &\times \tilde{W}(\mathrm{i}\tau)\left\{|\mathbf{R}'\rangle\langle\mathbf{R}'| + \sum_{\alpha\beta} Q_{\alpha\beta}(\mathbf{R}')|\tilde{p}_\alpha\rangle\langle\tilde{p}_\beta|\right\}|\tilde{\psi}_{n\mathbf{k}}\rangle.\end{aligned} \tag{259}$$

Here $|\mathbf{r}\rangle\langle\mathbf{r}| + \sum_{\mu\nu} Q_{\mu\nu}(\mathbf{r})|\tilde{p}_\mu\rangle\langle\tilde{p}_\nu|$ is the density operator within the PAW at the position $\mathbf{r}$ [30,32]. The one-center term $\sum_{\mu\nu} Q_{\mu\nu}(\mathbf{r})|\tilde{p}_\mu\rangle\langle\tilde{p}_\nu|$ arises from the additive augmentation of the PAW.

The calculation is performed in two steps, starting with the contraction $\tilde{\Sigma} = -G\tilde{W}$ in real space and imaginary time. In analogy to the four auxiliary components of the Green's function, we obtain four quantities that store the self-energy,

$$\begin{aligned}
\underline{\tilde{\Sigma}}^{(1)}(\mathbf{r},\mathbf{R}',\mathrm{i}\tau) &= -\underline{G}^{(1)}(\mathbf{r},\mathbf{R}',\mathrm{i}\tau)\tilde{W}(\mathbf{r},\mathbf{R}',\mathrm{i}\tau), && (260)\\
\underline{\tilde{\Sigma}}^{(2)}(\mu,\mathbf{R}',\mathrm{i}\tau) &= -\sum_{\nu} D^{(2)}(\mu\nu,\mathbf{R}',\mathrm{i}\tau)\underline{G}^{(2)}(\nu,\mathbf{R}',\mathrm{i}\tau), && (261)\\
\underline{\tilde{\Sigma}}^{(3)}(\mathbf{r},\beta,\mathrm{i}\tau) &= -\sum_{\alpha} \underline{G}^{(3)}(\mathbf{r},\alpha,\mathrm{i}\tau)D^{(3)}(\mathbf{r},\alpha\beta,\mathrm{i}\tau), && (262)\\
\underline{\tilde{\Sigma}}^{(4)}(\mu,\beta,\mathrm{i}\tau) &= -\sum_{\nu\alpha} \underline{G}^{(4)}(\nu,\alpha,\mathrm{i}\tau)D^{(4)}(\mu\nu,\alpha\beta,\mathrm{i}\tau), && (263)
\end{aligned}$$

where the auxiliary quantities $D^{(2)}$, $D^{(3)}$ and $D^{(4)}$ are defined as

$$\begin{aligned}
D^{(2)}(\mu\nu,\mathbf{R}',\mathrm{i}\tau) &= \sum_{\mathbf{r}\in C} Q_{\mu\nu}(\mathbf{r})\tilde{W}(\mathbf{r},\mathbf{R}',\mathrm{i}\tau), && (264)\\
D^{(3)}(\mathbf{r},\alpha\beta,\mathrm{i}\tau) &= \sum_{\mathbf{R}'\in S} \tilde{W}(\mathbf{r},\mathbf{R}',\mathrm{i}\tau)Q_{\alpha\beta}(\mathbf{R}'), && (265)\\
D^{(4)}(\mu\nu,\alpha\beta,\mathrm{i}\tau) &= \sum_{\mathbf{r}\in C}\sum_{\mathbf{R}'\in S} Q_{\mu\nu}(\mathbf{r})\tilde{W}(\mathbf{r},\mathbf{R}',\mathrm{i}\tau)Q_{\alpha\beta}(\mathbf{R}'). && (266)
\end{aligned}$$

Again, the Green's functions and the screened interaction are stored in reciprocal space and Fourier transformed to the real space on the fly, whenever they are required. In the second step, the matrix elements of the self-energy are then obtained as

$$\begin{aligned}
\underline{\tilde{\Sigma}}^{(\mathbf{k})}_{\mathrm{nn}}(\mathrm{i}\tau) = &\sum_{\mathbf{r}\in C}\sum_{\mathbf{R}'\in S}\tilde{\psi}^{*}_{n\mathbf{k}}(\mathbf{r})\underline{\tilde{\Sigma}}^{(1)}(\mathbf{r},\mathbf{R}',\mathrm{i}\tau)\tilde{\psi}_{n\mathbf{k}}(\mathbf{R}')\\
&+\sum_{\mu}\sum_{\mathbf{R}'\in S}\langle\tilde{\psi}_{n\mathbf{k}}|\tilde{p}_{\mu}\rangle\underline{\tilde{\Sigma}}^{(2)}(\mu,\mathbf{R}',\mathrm{i}\tau)\tilde{\psi}_{n\mathbf{k}}(\mathbf{R}')\\
&+\sum_{\mathbf{r}\in C}\sum_{\beta}\tilde{\psi}^{*}_{n\mathbf{k}}(\mathbf{r})\underline{\tilde{\Sigma}}^{(3)}(\mathbf{r},\beta,\mathrm{i}\tau)\langle\tilde{p}_{\beta}|\tilde{\psi}_{n\mathbf{k}}\rangle\\
&+\sum_{\mu}\sum_{\beta}\langle\tilde{\psi}_{n\mathbf{k}}|\tilde{p}_{\mu}\rangle\underline{\tilde{\Sigma}}^{(4)}(\mu,\beta,\mathrm{i}\tau)\langle\tilde{p}_{\beta}|\tilde{\psi}_{n\mathbf{k}}\rangle.
\end{aligned} \qquad (267)$$

For more derivation details on how the self-energy is derived within the PAW method, we refer the readers to Appendix (E). To reduce the memory requirements, the self-energy is also stored in the reciprocal space,

$$\begin{aligned}\underline{\tilde{\Sigma}}^{(\mathbf{k})}_{\mathrm{nn}}(\mathrm{i}\tau) = &\sum_{\mathbf{g}\in\mathcal{L}_c^*}\sum_{\mathbf{G}'\in\mathcal{L}_s^*}\langle\tilde{\psi}_{n\mathbf{k}}|\mathbf{g}\rangle\underline{\tilde{\Sigma}}^{(1)}(\mathbf{g},\mathbf{G}',\mathrm{i}\tau)\langle\mathbf{G}'|\tilde{\psi}_{n\mathbf{k}}\rangle\\ &+\sum_{\mu}\sum_{\mathbf{G}'\in\mathcal{L}_s^*}\langle\tilde{\psi}_{n\mathbf{k}}|\tilde{p}_{\mu}\rangle\underline{\tilde{\Sigma}}^{(2)}(\mu,\mathbf{G}',\mathrm{i}\tau)\langle\mathbf{G}'|\tilde{\psi}_{n\mathbf{k}}\rangle\\ &+\sum_{\mathbf{g}\in\mathcal{L}_c^*}\sum_{\beta}\langle\tilde{\psi}_{n\mathbf{k}}|\mathbf{g}\rangle\underline{\tilde{\Sigma}}^{(3)}(\mathbf{g},\beta,\mathrm{i}\tau)\langle\tilde{p}_{\beta}|\tilde{\psi}_{n\mathbf{k}}\rangle\\ &+\sum_{\mu}\sum_{\beta}\langle\tilde{\psi}_{n\mathbf{k}}|\tilde{p}_{\mu}\rangle\underline{\tilde{\Sigma}}^{(4)}(\mu,\beta,\mathrm{i}\tau)\langle\tilde{p}_{\beta}|\tilde{\psi}_{n\mathbf{k}}\rangle.\end{aligned} \tag{268}$$

Here, $\underline{\tilde{\Sigma}}^{(1)}(\mathbf{g},\mathbf{G}',\mathrm{i}\tau)$, $\underline{\tilde{\Sigma}}^{(2)}(\mu,\mathbf{G}',\mathrm{i}\tau)$ and $\underline{\tilde{\Sigma}}^{(3)}(\mathbf{g},\beta,\mathrm{i}\tau)$ are the Fourier transformation of $\underline{\tilde{\Sigma}}^{(1)}(\mathbf{r},\mathbf{R}',\mathrm{i}\tau)$, $\underline{\tilde{\Sigma}}^{(2)}(\mu,\mathbf{R}',\mathrm{i}\tau)$ and $\underline{\tilde{\Sigma}}^{(3)}(\mathbf{r},\beta,\mathrm{i}\tau)$, respectively.

One point that should be mentioned here is that in the present implementation, the core-valence exchange-correlation interaction is treated in the same way as in the conventional *GW* implementation, that is, the Hartree-Fock approximation is used. This is found to be more reliable than LDA since the *GW* self-energy approaches the bare Fock exchange operator in the short wavelength limit [33].

6.5.3. Evaluation of $\tilde{\Sigma}^{(\mathbf{k})}_{nn}(\mathrm{i}\omega)$ by CT+ST

After the matrix elements of the self-energy along the imaginary time have been obtained, one needs to Fourier transform them to the imaginary frequency domain to calculate the QP energies. However, the self-energy (like the Green's function) is neither an even nor an odd function in imaginary time/frequency. Hence, we split the Green's functions into even and odd parts,

$$G(\mathrm{i}\tau) = \frac{1}{2}[G(\mathrm{i}\tau)+G(-\mathrm{i}\tau)] + \frac{1}{2}[G(\mathrm{i}\tau)-G(-\mathrm{i}\tau)]\,. \tag{269}$$

Then, the self-energy along the imaginary frequency is given by the temporal Fourier transformation

$$\begin{aligned}\tilde{\Sigma}(\mathrm{i}\omega) = &-\int_{-\infty}^{\infty} \mathrm{d}\tau G(\mathrm{i}\tau)\tilde{W}(\mathrm{i}\tau)\mathrm{e}^{\mathrm{i}\omega\tau}\\ =&2\int_{0}^{\infty}\mathrm{d}\tau\tilde{\Sigma}^{c}(\mathrm{i}\tau)\cos(\omega\tau) + 2\mathrm{i}\int_{0}^{\infty}\mathrm{d}\tau\tilde{\Sigma}^{s}(\mathrm{i}\tau)\sin(\omega\tau),\end{aligned} \tag{270}$$

where the cosine $\tilde{\Sigma}^c$ and sine $\tilde{\Sigma}^s$ part read

$$\tilde{\Sigma}^c(\mathrm{i}\tau) = -\frac{1}{2}\left[\overline{G}(\mathrm{i}\tau) + \underline{G}(-\mathrm{i}\tau)\right]\tilde{W}(\mathrm{i}\tau), \tag{271}$$

$$\tilde{\Sigma}^s(\mathrm{i}\tau) = -\frac{1}{2}\left[\overline{G}(\mathrm{i}\tau) - \underline{G}(-\mathrm{i}\tau)\right]\tilde{W}(\mathrm{i}\tau). \tag{272}$$

Therefore, the corresponding diagonal matrix elements are given by

$$\tilde{\Sigma}^{c(\mathbf{k})}_{\mathrm{nn}}(\mathrm{i}\tau) = \frac{1}{2}\left[\overline{\tilde{\Sigma}}^{(\mathbf{k})}_{\mathrm{nn}}(\mathrm{i}\tau) + \underline{\tilde{\Sigma}}^{(\mathbf{k})}_{\mathrm{nn}}(-\mathrm{i}\tau)\right], \tag{273}$$

$$\tilde{\Sigma}^{s(\mathbf{k})}_{\mathrm{nn}}(\mathrm{i}\tau) = \frac{1}{2}\left[\overline{\tilde{\Sigma}}^{(\mathbf{k})}_{\mathrm{nn}}(\mathrm{i}\tau) - \underline{\tilde{\Sigma}}^{(\mathbf{k})}_{\mathrm{nn}}(-\mathrm{i}\tau)\right]. \tag{274}$$

Finally, the diagonal matrix elements of the correlated self-energy along the imaginary frequency axis are evaluated as

$$\tilde{\Sigma}^{(\mathbf{k})}_{\mathrm{nn}}(\mathrm{i}\omega) = \tilde{\Sigma}^{c(\mathbf{k})}_{\mathrm{nn}}(\mathrm{i}\omega) + \tilde{\Sigma}^{s(\mathbf{k})}_{\mathrm{nn}}(\mathrm{i}\omega), \tag{275}$$

where $\tilde{\Sigma}^{c(\mathbf{k})}_{\mathrm{nn}}(\mathrm{i}\omega)$ and $\tilde{\Sigma}^{s(\mathbf{k})}_{\mathrm{nn}}(\mathrm{i}\omega)$, respectively, are determined by discrete CT and ST:

$$\tilde{\Sigma}^{c(\mathbf{k})}_{\mathrm{nn}}(\mathrm{i}\omega_k) = \sum_{j=1}^{N} \gamma_{kj}\cos(\omega_k\tau_j)\tilde{\Sigma}^{c(\mathbf{k})}_{\mathrm{nn}}(\mathrm{i}\tau_j), \tag{276}$$

$$\tilde{\Sigma}^{s(\mathbf{k})}_{\mathrm{nn}}(\mathrm{i}\omega_k) = \mathrm{i}\sum_{j=1}^{N} \lambda_{kj}\sin(\omega_k\tau_j)\tilde{\Sigma}^{s(\mathbf{k})}_{\mathrm{nn}}(\mathrm{i}\tau_j). \tag{277}$$

6.6. Calculation of QP energies and spectral functions

In this section, we describe the calculation of QP energies and spectral functions, which corresponds to the last two steps in Fig. 12.

6.6.1. Analytic continuation

In our present implementation, the self-energy and Green's function are calculated in the imaginary frequency domain. However, the experimental observables of interest, such as QP energies and spectral functions, are obviously measured all along the real frequency axis. This implies that an analytic continuation from the imaginary to the real frequency domain has to be performed. Given that our self-energy is exact in the sense that there are no stochastic noises (unlike the Green's functions $G(\mathrm{i}\tau)$ obtained from quantum Monte-Carlo (QMC) simulations), here we utilize the N-point Padé approximant and combine the Thiele's reciprocal difference method [109] and least-squares method [110]. For more details regarding the analytic continuation, please refer to Appendix (C).

6.6.2. Evaluation of $E^{QP}_{n\mathbf{k}}$ and $A_{n\mathbf{k}}(\omega)$

After the diagonal elements of the self-energy along the real frequency axis $\Sigma^{(\mathbf{k})}_{\mathrm{nn}}(\omega)$ including contributions from the core-valence exchange-correlation, bare exchange and dynamical interactions (hereafter we denote it as $\Sigma_{n\mathbf{k}}(\omega)$) have been obtained by the analytic continuation, the QP energies are evaluated as in conventional GW implementations, as shown in Eqs. (171-173) (we rewrite them here for readers' convenience).

$$E^{QP}_{n\mathbf{k}} = \epsilon_{n\mathbf{k}} + Z_{n\mathbf{k}}\mathrm{Re}[\langle\psi_{n\mathbf{k}}|T + V_{\mathrm{ext}} + V_H|\psi_{n\mathbf{k}}\rangle + \Sigma_{n\mathbf{k}}(\epsilon_{n\mathbf{k}}) - \epsilon_{n\mathbf{k}}], \tag{278}$$

where

$$Z_{n\mathbf{k}} = \left(1 - \left.\frac{\partial\mathrm{Re}[\Sigma_{n\mathbf{k}}(\omega)]}{\partial\omega}\right|_{\omega=\epsilon_{n\mathbf{k}}}\right)^{-1}. \tag{279}$$

In principle, one could calculate the QP energies by searching the root of equation $E^{\mathrm{QP}}_{n\mathbf{k}} = \mathrm{Re}[\langle\psi_{n\mathbf{k}}|T + V_{\mathrm{ext}} + V_H|\psi_{n\mathbf{k}}\rangle + \Sigma_{n\mathbf{k}}(E^{\mathrm{QP}}_{n\mathbf{k}})]$ numerically. For solids, this does not make a sizeable difference in the QP energies compared to the linearization. In the present work we therefore only show the calculated QP energies from the linearized version to compare with the conventional implementation where the linearization was used as well.

The spectral functions are calculated as the imaginary part of the interacting Green's function, which is calculated from the Dyson-equation [111]

$$\begin{aligned} A_{n\mathbf{k}}(\omega) &= \frac{1}{\pi}|\mathrm{Im}[G_{n\mathbf{k}}(\omega)]| \\ &= \frac{1}{\pi}\cdot\frac{|\mathrm{Im}[\Delta\Sigma_{n\mathbf{k}}(\omega)]|}{(\omega - \epsilon_{n\mathbf{k}} - \mathrm{Re}[\Delta\Sigma_{n\mathbf{k}}(\omega)])^2 + \mathrm{Im}[\Delta\Sigma_{n\mathbf{k}}(\omega)]^2}, \end{aligned} \tag{280}$$

where $\Delta\Sigma_{n\mathbf{k}}(\omega) = \langle\psi_{n\mathbf{k}}|\hat{T} + \hat{V}_{n-e} + \hat{V}_H|\psi_{n\mathbf{k}}\rangle + \Sigma_{n\mathbf{k}}(\omega) - \epsilon_{n\mathbf{k}}$.

6.7. Implementation details of low scaling GW method

Here, we will show how the self-energy are actually calculated within VASP. As already discussed, to reduce the memory storage, the quantities such as Green's functions G, screened interaction W and self-energy Σ are all stored in reciprocal space. However, it requires spatial fast Fourier transformations (FFT) whenever the real space contractions are needed. Three kinds of arrays are required: $A(\mathbf{G},\mathbf{G}',i\tau)$, $A(\mathbf{G},\alpha',i\tau)$, and $A(\alpha,\alpha',i\tau)$. $A(\mathbf{G},\mathbf{G}',i\tau)$ is used to store quantities such as $G^{(1)}(\mathbf{G},\mathbf{G}',i\tau)$ and $G^{(1)}(\mathbf{r},\mathbf{r}',i\tau)$. $A(\mathbf{G},\alpha',i\tau)$ is used to store quantities such as $G^{(3)}(\mathbf{G},\alpha',i\tau)$ and $G^{(3)}(\mathbf{r},\alpha',i\tau)$. Since $G^{(2)}(\alpha,\mathbf{G}',i\tau)$ $[G^{(2)}(\alpha,\mathbf{r}',i\tau)]$ is a complex conjugation of $G^{(3)}(\mathbf{G},\alpha',i\tau)$ $[G^{(3)}(\mathbf{r},\alpha',i\tau)]$, $A(\mathbf{G},\alpha',i\tau)$ is used to store $G^{(2)}(\alpha,\mathbf{G}',i\tau)$ and $G^{(2)}(\alpha,\mathbf{r}',i\tau)$ as well. Finally, $A(\alpha,\alpha',i\tau)$ is used to store quantities like $G^{(4)}(\alpha,\alpha',i\tau)$. It should be noted that the self-energy is stored in a similar way as Green's functions, the data are distributed, and the code is highly parallelized in terms of time/frequency. For the sake of brevity, in the following we will omit the time index.

The arrays are distributed on different nodes over the second index, which allows to perform FFT over the first index on a single core and perform multiplications over contiguous parts of memory. However, the data need to be transposed during the calculation.

(1) We start by calculating $\tilde{\Sigma}^{(1)}(\mathbf{G},\mathbf{G}')$. $G^{(1)}(\mathbf{G},\mathbf{G}')$ and $\tilde{W}(\mathbf{G},\mathbf{G}')$ are first partially Fourier transformed to $G^{(1)}(\mathbf{r},\mathbf{G}')$ and $\tilde{W}(\mathbf{r},\mathbf{G}')$ along the first index. Then, the arrays are transposed to $G^{(1)}(\mathbf{G}',\mathbf{r})$ and $\tilde{W}(\mathbf{G}',\mathbf{r})$. Third, they are needed to be Fourier transformed to $G^{(1)}(\mathbf{r}',\mathbf{r})$ and $\tilde{W}(\mathbf{r}',\mathbf{r})$, such that the self-energy

$$\tilde{\Sigma}^{(1)}(\mathbf{r}',\mathbf{r}) = -G^{(1)}(\mathbf{r}',\mathbf{r})\tilde{W}(\mathbf{r}',\mathbf{r}) \tag{281}$$

is calculated on the fly and immediately Fourier transformed to $\tilde{\Sigma}^{(1)}(\mathbf{G}',\mathbf{r})$ along the first index and then transposed to $\tilde{\Sigma}^{(1)}(\mathbf{r},\mathbf{G}')$, which is stored. $\tilde{\Sigma}^{(1)}(\mathbf{G},\mathbf{G}')$ cannot be performed until $\tilde{\Sigma}^{(1)}(\mathbf{r},\mathbf{G}')$ for all $\mathbf{r}$ has been calculated.

(2) Next, we will show how $\tilde{\Sigma}^{(2)}(\beta,\mathbf{G}')$ is calculated. $\tilde{W}(\mathbf{r},\mathbf{G}')$ obtained already in the first step is used to calculate

$$D(\alpha\beta,\mathbf{G}') = \sum_{\mathbf{r}} \tilde{W}(\mathbf{r},\mathbf{G}')Q_{\alpha\beta}(\mathbf{r}). \tag{282}$$

$D(\alpha\beta,\mathbf{G}')$ and $G^{(2)}(\alpha,\mathbf{G}')$ are then transposed to $D(\mathbf{G}',\alpha\beta)$ and $G^{(2)}(\mathbf{G}',\alpha)$. Afterwards, the arrays are Fourier transformed to $D(\mathbf{r}',\alpha\beta)$ and $G^{(2)}(\mathbf{r}',\alpha)$ along the first index on a single core. Then,

$$\tilde{\Sigma}^{(2)}(\mathbf{r}',\beta) = -\sum_{\alpha} D(\mathbf{r}',\alpha\beta)G^{(2)}(\mathbf{r}',\alpha) \tag{283}$$

is calculated and stored. $\tilde{\Sigma}^{(2)}(\mathbf{G}',\beta)$ cannot be performed until $\tilde{\Sigma}^{(2)}(\mathbf{r}',\beta)$ for all $\mathbf{r}'$ has been calculated. Finally, $\tilde{\Sigma}^{(2)}(\beta,\mathbf{G}')$ is obtained by transposing $\tilde{\Sigma}^{(2)}(\mathbf{G}',\beta)$.

(3) The third component of the self-energy $\tilde{\Sigma}^{(3)}(\mathbf{G},\beta')$ can be calculated in a similar way as $\tilde{\Sigma}^{(2)}(\beta,\mathbf{G}')$. Specifically, $G^{(3)}(\mathbf{G},\alpha')$ is first partially Fourier transformed to $G^{(3)}(\mathbf{r},\alpha')$. Then, $D(\mathbf{r},\alpha'\beta')$ calculated already in the second step and $G^{(3)}(\mathbf{r},\alpha')$ are transposed to $D(\alpha'\beta',\mathbf{r})$ and $G^{(3)}(\alpha',\mathbf{r})$. The self-energy $\tilde{\Sigma}^{(3)}(\beta',\mathbf{r})$ is calculated by

$$\tilde{\Sigma}^{(3)}(\beta',\mathbf{r}) = -\sum_{\alpha'} D(\alpha'\beta',\mathbf{r})G^{(3)}(\alpha',\mathbf{r}). \tag{284}$$

Afterwards, $\tilde{\Sigma}^{(3)}(\beta',\mathbf{r})$ is transposed to $\tilde{\Sigma}^{(3)}(\mathbf{r},\beta')$. $\tilde{\Sigma}^{(3)}(\mathbf{G},\beta')$ cannot be performed until $\tilde{\Sigma}^{(3)}(\mathbf{r},\beta')$ for all $\mathbf{r}$ has been calculated.

(4) The calculation of the last component of the self-energy $\tilde{\Sigma}^{(4)}(\beta,\beta')$ is straightforward. $D(\mathbf{r},\alpha'\beta')$ obtained in the second step is used to calculate $D(\alpha\beta,\alpha'\beta')$ by

$$D(\alpha\beta,\alpha'\beta') = \sum_{\mathbf{r}} Q_{\alpha\beta}(\mathbf{r})D(\mathbf{r},\alpha'\beta'). \tag{285}$$

Finally, $\tilde{\Sigma}^{(4)}(\beta,\beta')$ is obtained by

$$\tilde{\Sigma}^{(4)}(\beta,\beta') = \sum_{\alpha}\sum_{\alpha'} D(\alpha\beta,\alpha'\beta')G^{(4)}(\alpha,\alpha'). \tag{286}$$

After all four components of the self-energy are obtained in reciprocal space, the matrix elements of the self-energy in the orbital basis can be finally calculated by Eq. (268).

7. Low scaling GW method: applications

7.1. Applications for extended systems

In this section, we apply our new implementation to predict the QP energies and spectral functions for typical semiconductors (Si, GaAs, SiC, and ZnO), insulators (C, BN, MgO, and LiF), and metals (Cu and $SrVO_3$), and compare our results with the conventional GW implementation. It is found that the QP energies and spectral functions predicted by G_0W_0r are in good agreement with G_0W_0 but with a reduced scaling in the system size and number of k points, highlighting the power of the present method. This section was published in Ref. [107].

7.1.1. Technical details

Our low-scaling GW scheme has been implemented in the Vienna *Ab initio* Simulation Package (VASP) [112, 113]. For all the calculations presented here, the ultrasoft (US) PAW potentials with an appendix (`_GW`) released with VASP.5.2 were used unless otherwise explicitly specified. These potentials are constructed by using additional projectors above the vacuum level and thus describe well the high-energy scattering properties of the atoms. The plane-wave cutoff for the orbitals was chosen to be the maximum of all elements in the considered material. The energy cutoff for the response function was chosen to be half of the plane-wave cutoff. To sample the Brillouin zone, 8×8×8 k-point grids centered at the Γ point were used except for Cu where the grids were increased to 10×10×10. For the tested materials, the experimental lattice constants at low temperature (if available, otherwise at room temperature) were used. The total number of bands was chosen to be 480, which is sufficient to obtain the converged QP energies for most of the materials considered, except for GaAs and ZnO where the convergence is very slow. It was suggested that thousands of orbitals are required for accurate predictions for ZnO [114], but this finite-basis-set correction is beyond the scope of this work. In fact, for the present setup the errors in some QP energies are large, with errors of, e.g., 0.5 eV for ZnO. For more accurate results we refer to the previous publication by some of the present authors [115].

Clearly, the purpose of the present section is not to basis set converge the calculations (this is of course possible with the present implementation, as it was possible in the standard framework). Instead, we restrict ourselves to validating the low-scaling GW implementation by comparing the results with the already widely used conventional GW implementation. Hence, same

Table 1: Positions of conduction band (CB) minimum at Γ (Γ_c) and X (X_c), valence band (VB) maximum at X (X_v) with respect to the VB maximum at Γ, as well as the band gap. Spin-orbit coupling (SOC) and finite basis-set corrections are not included. The crystal structures, lattice constants, and experimental band gaps are identical to Ref. [86] and references therein.

	Γ_c		X_c		X_v		band gap			Crystal structure	Lattice constant (Å)
	G_0W_0r	G_0W_0	G_0W_0r	G_0W_0	G_0W_0r	G_0W_0	G_0W_0r	G_0W_0	Expt.		
Si	3.22	3.23	1.24	1.25	-2.89	-2.89	1.15	1.16	1.17	diamond	5.430
GaAs	1.33	1.34	1.86	1.88	-2.79	-2.77	1.33	1.34	1.52	zincblende	5.648
SiC	7.40	7.41	2.30	2.31	-3.36	-3.35	2.30	2.31	2.40	zincblende	4.350
ZnO	2.10	2.06	6.73	6.66	-2.31	-2.28	2.10	2.06	3.44	zincblende	4.580
C	7.39	7.39	6.07	6.08	-6.66	-6.66	5.49	5.50	5.48	diamond	3.567
BN	11.14	11.14	6.16	6.17	-5.28	-5.27	6.16	6.17	6.1-6.4	zincblende	3.615
MgO	7.27	7.27	11.47	11.48	-1.55	-1.54	7.27	7.27	7.83	rocksalt	4.213
LiF	13.68	13.68	20.20	20.20	-1.21	-1.19	13.68	13.68	14.20	rocksalt	4.010

setups (crystal structure, potential, k points and so on) were used for both G_0W_0r and G_0W_0 calculations. In addition, finite basis-set corrections for QP energies discussed in Ref. [115] are not taken into account for neither G_0W_0r nor G_0W_0 calculations.

The actual GW calculations involve three steps: (i) A self-consistent KS-DFT calculation was performed using the Perdew-Burke-Ernzerhof (PBE) functional [21]. (ii) The one-electron wave functions and eigenenergies of all unoccupied (virtual) orbitals spanned by the plane wave basis set were evaluated by an exact diagonalization of the previously determined self-consistent KS Hamiltonian. (iii) The GW calculations were carried out. For all the materials considered, the number of imaginary time/frequency points in G_0W_0r calculations was set to 20, whereas the number of real frequency points was chosen to be 200 for G_0W_0 calculations. Increasing the number of grid points further changes the QP energies by less than 0.01 eV.

7.1.2. Results for semiconductors and insulators

Table 1 shows the QP energies and band gaps for the tested semiconductors and insulators predicted by G_0W_0r and G_0W_0. First, we emphasize that our G_0W_0@PBE results are consistent with previous calculations [86]. As expected, the band gaps calculated by G_0W_0@PBE are

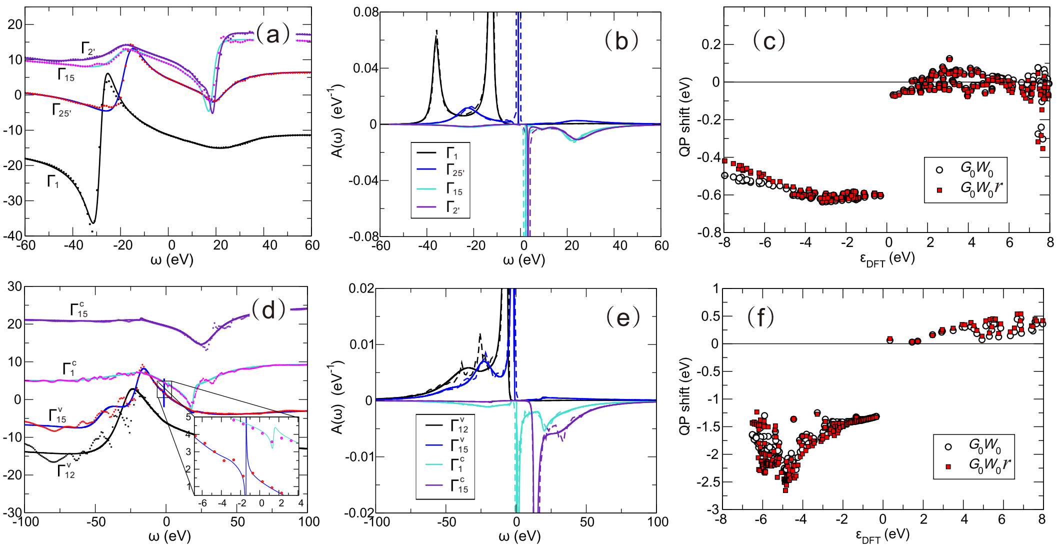

Figure 13: (color online) The real part of the diagonal elements of the self-energy Re[$\Sigma_{n\mathbf{k}}(w)$] [(a) and (d)], and the spectral functions $A_{n\mathbf{k}}(w)$ of the Green's functions at the Γ point [(b) and (e)], as well as the QP shift versus the DFT eigenvalues [(c) and (f)] for Si (first row) and ZnO (second row). The solid lines and dotted (broken) lines in [(a), (d), (b) and (e)], respectively, specify the results from G_0W_0r and G_0W_0. Note that the sign of the spectral functions for the unoccupied states in (b) and (e) is intentionally reversed for clarity. The inset in (d) shows the zoom-in plot for the local satellites.

slightly underestimated compared to the experimental values. Improvements further towards experimental gaps have been achieved either by GW_0@PBE (iterating the one-electron energies only in G) [86], or by G_0W_0@HSE (using the hybrid functionals as a starting point) [88]. The best agreement with experimental values thus far has been achieved by $GW^{\text{TC-TC}}$ (self-consistent GW with the vertex correction only in W) [89]. We note again that finite basis-set corrections [115] have not been used here, which would increase the gap for ZnO by 0.3-0.4 eV, for instance. Second, one can see that the agreement between the results from G_0W_0r and G_0W_0 is remarkably good, validating our low-scaling GW implementation. Specifically, for the *sp* semiconductors and insulators (Si, SiC, C, BN, MgO and LiF), the difference in QP energies and band gaps between G_0W_0r and G_0W_0 is not larger than 0.02 eV. This is even true for GaAs with localized *d*-orbitals. Except for ZnO the G_0W_0r seems to have the tendency to yield a slightly smaller downwards shift (below 0.02 eV) for valence and conduction bands compared to G_0W_0. However, for ZnO the difference of the calculated gaps between G_0W_0r and G_0W_0 is larger (0.04 eV) since the self-energy exhibits many poles from *d*-*p* excitations at energies around −40 eV [see Fig. 13(e) below].

To further assess our low-scaling *GW* implementation, we plot the diagonal elements of the self-energies and spectral functions at the Γ point for some chosen bands around the Fermi level, as well as the QP shift versus the DFT eigenvalues for Si and ZnO in Fig. 13. The results obtained from the conventional G_0W_0 are also presented for comparison. Overall, the agreement between the results from G_0W_0r and G_0W_0 is very good, in particular for the region close to the Fermi level. Specifically, for Si, the self-energies and spectral functions (including the spectral background and contributions from plasmons) calculated by G_0W_0r agree nicely with the ones from G_0W_0 [see Fig. 13(a) and 13(b)]. This is achieved by employing Thiele's reciprocal difference method. Solving for the Padé coefficients directly, however, yields less satisfactory results (not shown here). For ZnO, the agreement in the self-energies and spectral functions is still good. Even the small satellites in bands Γ_{15}^{v} and Γ_{1}^{c} are reproduced [see the inset in Fig. 13(d)]. However, satellites far from the Fermi level have been smoothed by the analytic continuation.

In contrast, there exist larger deviations in the region far away from the Fermi level. As shown in Fig. 13(c) and 13(f), the difference in the QP shift between G_0W_0r and G_0W_0 increases as the binding energies increase above 4 eV. The reason can be easily understood. Considering band Γ_1 of Si for instance, the QP peak is not sharp. Instead, it is broadened with a width of around 5 eV, as shown in Fig. 13(b). Therefore, it is difficult to obtain the exact position of the quasiparticle. This is true for both G_0W_0r and G_0W_0. In addition, the QP peaks measured from the angle-resolved photoelectron spectroscopy (ARPES) would be as broad as in the *GW* approximation so that the errors are in fact negligible compared to the width of the peak.

7.1.3. Results for metals

Now we turn to the QP calculations for metals where some extra considerations are required. For metallic systems there exists a non-vanishing probability that an electron is excited within one and the same band. These transitions are called intraband transitions and lead to the so called Drude term for the long-wavelength limit ($\mathbf{q} \to 0$). Following similar strategies as in Refs. [116, 117] we derived the head of the intraband dielectric function in the imaginary fre-

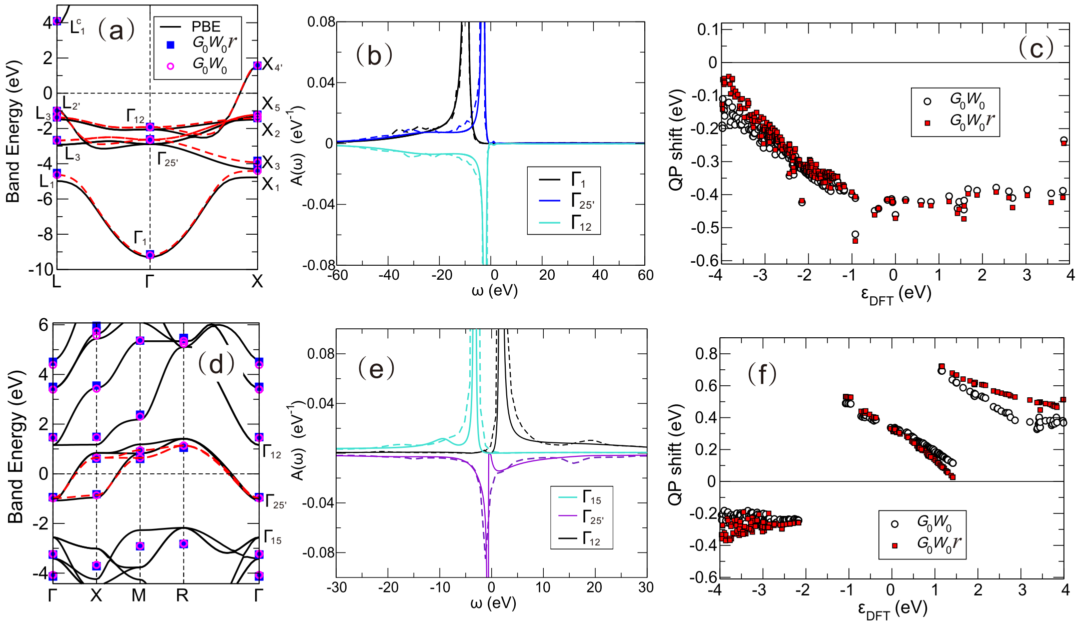

Figure 14: (color online) Band structures [(a) and (d)], spectral functions $A_{n\mathbf{k}}(w)$ of the Green's functions at the Γ point [(b) and (e)], and QP shift versus the DFT eigenvalues [(c) and (f)] for Cu (first row) and $SrVO_3$ (second row). Note that in (a) and (d) the red broken lines specify the Wannier interpolated band structure from G_0W_0. PBE and GW Fermi energies are aligned at zero.

quency domain,

$$\epsilon^{intra}_{\alpha\beta}(\mathrm{i}\omega) = \frac{\bar{\omega}^2_{\alpha\beta}}{\omega^2}. \tag{287}$$

Here the tensor $\bar{\omega}_{\alpha\beta}$ is the plasma frequency and its square is defined as,

$$\bar{\omega}^2_{\alpha\beta} = -\frac{4\pi e^2}{\Omega_C}\sum_{n\mathbf{k}} 2\frac{\partial f(\epsilon_{n\mathbf{k}})}{\partial \epsilon_{n\mathbf{k}}}\left(\mathbf{e}_\alpha\cdot\frac{\partial\epsilon_{n\mathbf{k}}}{\partial\mathbf{k}}\right)\left(\mathbf{e}_\beta\cdot\frac{\partial\epsilon_{n\mathbf{k}}}{\partial\mathbf{k}}\right), \tag{288}$$

where the factor of 2 is due to the spin-degenerate systems considered here, Ω_C is the volume of the unit cell and $\mathbf{e}_\alpha$ is the unit vector along the cartesian coordinate α. It should be noted that the intraband transitions are only non-vanishing for the head of the dielectric functions. For the wings and body they are both zero. For the explicit derivation of the head of intra-band dielectric functions, please refer to Appendix (D).

As a test, we calculated the QP energies for the metals Cu and $SrVO_3$ and compare the results with the ones from the conventional G_0W_0 in Fig. 14(a) and 14(d). To guide the eye, the

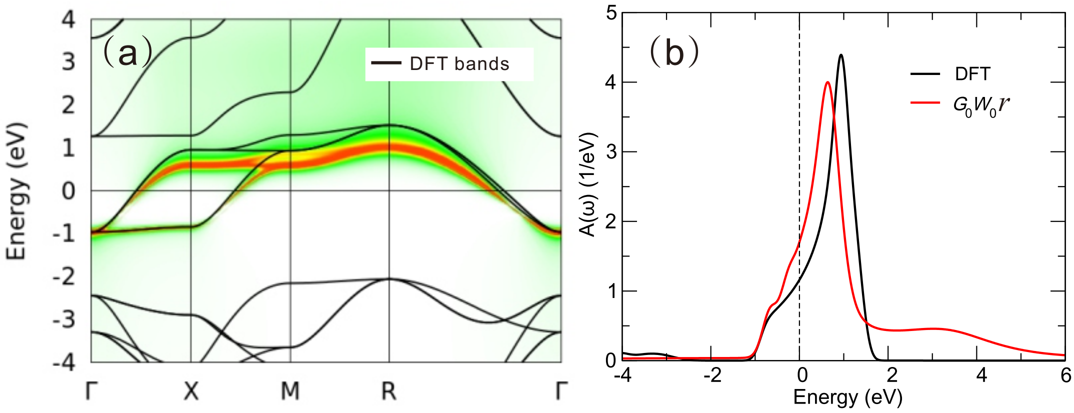

Figure 15: (color online) (a) Momentum resolved spectral function in the G_0W_0 approximation (color/gray) and DFT (black line). (b) Comparison of the DFT and local G_0W_0 spectral function $A(\omega)$. The results are obtained from our low-scaling G_0W_0r implementation.

PBE band structures and interpolated G_0W_0 QP band structures obtained with the wannier90 code [42,43] are also displayed. One can see that good agreement between G_0W_0r and G_0W_0 is achieved for both Cu and SrVO$_3$, indicating that our low-scaling GW implementation is robust and applies to metals as well. However, if we take a closer look at the spectral functions, as shown in Fig. 14(b) and 14(e), we observed that although the main QP peaks are well reproduced, the plasma and some satellites are again smoothed by the analytic continuation.

Fig. 14(c) and 14(f) further show the QP shift versus DFT eigenvalues for Cu and SrVO$_3$, respectively. For the noble metal Cu, in the energy region of the plot, overall, the QP shift difference between G_0W_0r and G_0W_0 is not exceeding 0.1 eV. Analogous behavior as for Si is observed for Cu. The further one moves away from the Fermi level, the larger is the QP shift difference. This is due to the large broadening of the QP peak for the corresponding bands. This is also true for the metal SrVO$_3$. The negative slope of the QP shift between -1.5 and 1.5 eV implies a shrinking of the t_{2g} bands as compared to the DFT results, which was observed in other GW studies as well [111,118]. In the region far away from the Fermi level QP differences are visible, but the maximum difference is smaller than 0.2 eV.

Figure 15(a) shows the momentum resolved spectral function from single-shot G_0W_0r. Compared to DFT, the t_{2g} bandwidth is reduced by 20 % in G_0W_0r. In the G_0W_0 approximation, spectral weight is transferred to satellites. This is much more clearly seen in the local,

Table 2: QP energies (eV) of Cu predicted by G_0W_0r and G_0W_0 using the norm-conserving (NC) GW PAW potential (Cu_sv_GW_nc). Basis-set corrected G_0W_0 QP energies are also given for comparison. The labeling of the high-symmetry points are shown in Fig. 14(a). The results are compared to the pseudopotential plane wave (PPW) values obtained by Marini *et al.* [122] and the full potential linear muffin-tin orbital (LMTO) calculations by Zhukov *et al.* [123]. Experimental data are taken from Ref. [124].

		PBE	G_0W_0r	G_0W_0	corrected G_0W_0	PPW [122]	LMTO [123]	Expt. [124]
Positions of d bands	Γ_{12}	−2.05	−1.92	−1.92	−2.11	−2.81	−2.36	−2.78
	X_5	−1.33	−1.22	−1.23	−1.45	−2.04	−1.63	−2.01
	L_3	−1.47	−1.36	−1.37	−1.58	−2.24	−1.78	−2.25
Widths of d bands	$\Gamma_{12} - \Gamma_{25'}$	0.84	0.70	0.72	0.69	0.60	0.81	0.81
	$X_5 - X_3$	2.97	2.61	2.68	2.60	2.49	2.92	2.79
	$X_5 - X_1$	3.44	3.05	3.18	3.10	2.90	3.37	3.17
	$L_3 - L_3$	1.44	1.30	1.31	1.26	1.26	1.43	1.37
	$L_3 - L_1$	3.51	3.16	3.26	3.16	2.83	3.42	2.91
Positions of s/p bands	Γ_1	−9.29	−9.14	−9.20	−9.18	−9.24	−9.35	−8.60
	$L_{2'}$	−0.92	−1.00	−0.98	−1.02	−0.57	−0.92	−0.85
L gap	$L_1^c - L_{2'}$	4.80	5.09	5.08	4.98	4.76	4.78	4.95

momentum-integrated, spectral function as shown in Fig 15(b). The plasmon satellite of the t_{2g} quasi-particle band at ∼3 eV arising from the t_{2g} contribution to the fully screened interaction at the plasmon frequency [119, 120] is well reproduced. Further, a plasmon peak deriving from transitions outside the t_{2g} subspace is seen at ∼15 eV [47, 119]. We note, however, that in our calculations repeated plasmon peaks at higher frequencies are absent. This is a well known issue of the G_0W_0 approximation [121].

In Table 2 we show in detail the QP energies of Cu predicted by G_0W_0r and G_0W_0 and compare our results with other theoretical calculations and experiment. The most significant error in the PBE one-electron energies is the wrong description of the absolute positions and the bandwidth of the d bands. For instance, the highest d band at X_5 is located at -1.33 eV in PBE, 0.68 eV above the experimental value of -2.01 eV [124]. The bandwidth of the d bands is widened compared to the experiment (see $X_5 - X_1$). Unfortunately though, our G_0W_0 does not improve the results significantly. It shrinks the bandwidth of the d bands towards the experimental values, but predicts worse positions for the d bands than PBE. However, as already mentioned basis set errors might be substantial for the 480 bands employed in the present case. To improve the results, finite basis-set corrections were used as discussed in Ref. [115]. Indeed, with these corrections the absolute positions of the d bands are lowered by about 0.2 eV. Agreement with the full potential LMTO method [123] is then reasonable. However, our QP d-band energies are still way above those of Marini *et al.* [122]. We are pretty confident that the good agreement of these calculations with experiment is largely fortuitous: the applied pseudopotentials somehow canceled the errors introduced by the G_0W_0 approximation. Compared to the LMTO data, we note that all our QP energies are shifted upwards by 0.2 eV (except for $L_{2'}$). Of course, our QP energies are reported with respect to the G_0W_0 Fermi energy, whereas, Ref. [123] does not mention how and whether the Fermi energy was determined at the G_0W_0 level. Using the DFT Fermi energy would improve agreement with Ref. [123]. For the widths of the d bands the present results are in very good agreement with experiment, though, slightly improving upon the LMTO data, which were generally above the experimental data.

We feel that the residual errors compared to experiment are to be expected and arise from (i) the neglect of self-consistency (the DFT d orbitals of Cu are most likely too strongly hybridized with the sp states), and (ii) spurious self-interactions in the GW approximation. The latter error can be only eliminated via the inclusion of vertex corrections in the self-energy. Indeed, the importance of vertex corrections has been highlighted for predicting the ionization potentials and d-electron binding energies of solids [92], with typical corrections for the d bands of 0.7 eV.

7.1.4. Time complexity for large systems

In order to investigate the scaling with respect to the system size in our new implementation, we performed G_0W_0r calculations on different bulk Si diamond supercells with 16, 24, 36, and 54 atoms using the Γ point only. For comparison, similar calculations have been done for the conventional G_0W_0 code. Our G_0W_0r implementation displays clearly a better than cubic scaling in the system size, as shown in Table 3. The reason for this good scaling is that the contraction steps such as GG and GW scale only quadratically in system size, and for the number of atoms considered here, construction of the Green's function and manipulations of the self-energy matrix, which scale profoundly cubically, are not yet dominating the total compute time. Furthermore, it needs to be mentioned that the G_0W_0r compute time includes the calculation of the full non-diagonal self-energy at all frequency points (including *all* off-

Table 3: Timings in minutes for G_0W_0r and G_0W_0 calculations for different bulk Si diamond supercells. The calculations were done for 64 QP energies using the Γ point only and using the real valued Γ only VASP version.

Atoms	Cores	Time		Time×cores/atoms^3 × 10^3	
		G_0W_0	G_0W_0r	G_0W_0	G_0W_0r
16	16	9.18	2.50	35.86	9.78
24	20	18.94	4.14	27.40	5.99
36	48	41.68	5.65	42.88	5.82
54	64	104.53	12.07	42.49	4.91

diagonal elements), whereas the G_0W_0 code calculates only few diagonal elements of the self-energy for the occupied and some unoccupied states. Despite this the G_0W_0r code substantially outperforms the older G_0W_0 code. Concerning scaling, the old G_0W_0 code shows a slightly less beneficial scaling, nevertheless it is also closer to cubic than quartic in system size. This relates to the fact that the quartic part (construction of polarizability and self-energy in orbital basis) is done using high efficiency BLAS level 3 calls, and hence this part becomes only dominant for very large systems, typically beyond 100 atoms.

To test the scaling with respect to the number of k points, we performed calculations on a bulk Si diamond supercell with 16 atoms using 64 cores. We note that the new code does not yet perform optimally if the number of cores exceeds the number of atoms. This and the need to use a complex code version explain why the timings for a single k point in Fig. 16 are hardly better than for 16 cores shown in Table 3. As shown in Fig. 16, the computational demand increases almost perfectly linear in the number of k points for G_0W_0r. The slight deviation for the $4\times4\times4$ case arises from the need to pick a less efficient parallelization strategy for this k-point set to be able to perform the calculation using the memory available on 64 cores. In contrast, G_0W_0 shows a roughly quadratic scaling in the number of k points. The bad scaling of the old code is, however, somewhat masked by its efficient handling of symmetry. The old implementation uses small point group operations compatible with the considered momentum transfer q, whereas the new code uses yet no symmetry when contracting GG or GW. Concomitantly, if symmetry is switched off, the new code becomes only slower by a factor 2 for the $3\times3\times3$ k points, whereas the time for the old code increases to 162 minutes (off the scale, see the blue and pink broken

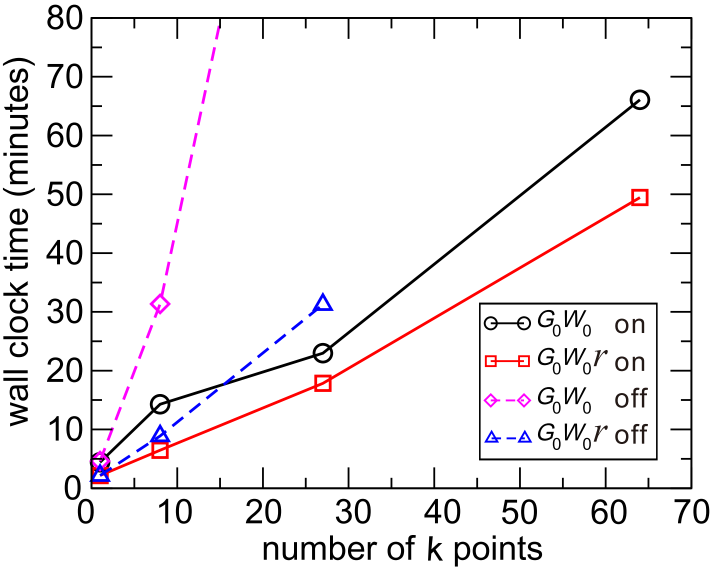

Figure 16: (color online) Computational time for G_0W_0r and G_0W_0 calculations with symmetry switched on or off on a bulk Si diamond supercell with 16 atoms as a function of the number of k points (in the full Brillouin zone). Note that the computational time of G_0W_0 for the $3 \times 3 \times 3$ case without symmetry is about 162 minutes, which is not shown in the figure. The calculations are done for 64 QP energies using 64 cores.

lines in Fig. 16). Therefore, one would expect that the G_0W_0r code outperforms the old G_0W_0 code, in particular, if large low-symmetry unit cells are used and/or if many k points are used. It is however also clear that the old code can be competitive or superior for small high-symmetry unit cells, even if many k points are used to sample the Brillouin zone. For instance, for a cubic diamond unit cell or for fcc Cu, the old code is usually much faster than the new GW code.

7.2. Applications for 100 closed shell molecules

In a recent work, van Setten and coworkers have presented a carefully converged G_0W_0 study of 100 closed shell molecules [84]. For two different codes they found excellent agreement to within few 10 meV if identical Gaussian basis sets were used. We inspect the same set of molecules using the projector augmented wave method and the Vienna ab initio simulation package (VASP). For the ionization potential, the basis set extrapolated plane wave results agree very well with the Gaussian basis sets, often reaching better than 50 meV agreement. In order to achieve this agreement, we correct for finite basis set errors as well as errors introduced by periodically repeated images. For positive electron affinities differences between Gaussian basis sets and VASP are slightly larger. We attribute this to larger basis set extrapolation errors for the Gaussian basis sets. For quasi particle (QP) resonances above the vacuum level, differences between VASP and Gaussian basis sets are, however, found to be substantial. This is tentatively explained by insufficient basis set convergence of the Gaussian type orbital calculations as exemplified for selected test cases.

This section was published in Ref. [125].

7.2.1. Introduction

The GW approximation suggested by Lars Hedin [70] has a long history in solid state physics. First practical applications were already published in the 1980s by Hanke and coworkers soon followed by the often quoted study of Hybertsen and Louie [83,126–128]. For solids, it is generally found that even the simplest approximation G_0W_0 yields reasonably accurate quasiparticle (QP) energies and band gaps in good agreement with experiment [85, 86, 88]. The results often improve if the Green's function is iterated to self-consistency, either updating the QP-energies only or even the one-electron orbitals [85, 86, 129–135]. Applications of the GW approximation to molecules, however, have been comparatively rare, since codes based on local orbitals, which are by construction particularly well suited to treat molecules, did not incorporate the GW approximation until recently. This has changed, with many local basis set codes, such as FHI-aims, MOLGW, Turbomole, and CP2K now supporting GW calculations [136–142]. Also, efficient plane wave codes using a Sternheimer approach, such as ABINIT and West [143, 144], are becoming available. As for solids, carefully converged QP calculations are, however, still comparatively scarce [115].

To fill this gap, Bruneval recently performed systematic studies for about 30 molecules [145]. van Setten and coworkers went one step further and evaluated basis set extrapolated GW QP energies for 100 closed shell molecules using several codes [84]. They found that the GW QP energies of the highest occupied orbital (HOMO) and lowest unoccupied orbital (LUMO) of two local basis set codes, FHI-aims and Turbomole, virtually agree, *if identical basis sets are used.* In many respects this is not astonishing, since two codes ought to yield the same results, if the computational parameters are identical. The two codes are, however, technically quite different. For instance, they introduce auxiliary basis sets to avoid storing the two-electron four orbital integrals. Furthermore, FHI-aims uses a numerical representation of the Gaussians and calculates the self-energy along the imaginary axis (Wick rotation) requiring an analytic continuation to the real axis. All these factors can introduce small uncertainties. Clearly, the study impressively demonstrates that all these intricacies are well under control, and technically well converged results can be obtained using both codes.

The paper by van Setten *et al.* [84] also reports results using the GW Berkeley plane wave code [146]. Although agreement of that code with experiment is very good if the plasmon-pole model is used, comparison of the fully frequency dependent G_0W_0 HOMO and LUMO with Gaussian basis set results is less satisfactory. For the considered molecules, the mean absolute difference between Gaussian type orbitals (GTO) and plane waves (PWs) is about 200 meV for the HOMO. We note on passing that the agreement between GTO and other plane wave studies is seemingly superior [143, 144], although, this could be related to the fact that these studies only considered a subset of the $GW100$ set. The disagreement between the Berkeley GW PW code and GTO codes is certainly slightly disconcerting, since it puts decades of studies using PW based GW calculations into question. Remarkably, on the level of DFT, the reported one-electron energies of the HOMO agree to within few 10 meV. So how can one understand the much larger discrepancies for GW QP energies?

A partial answer is given by the observation that QP energies converge very slowly with respect to the basis set size, as well established for Gaussian type orbitals [84, 140, 145]. van Setten *et al.* obtained basis set converged QP energies by extrapolating against the basis set size or against $1/C_n^3$, where C_n is the basis set cardinal number [84]. Extrapolation was based on def2-SVP, def2-TZVP and def2-QZVP, but even though def2-QZVP constitutes a fairly complete set, the extrapolated values can differ by more than 300 meV from the values at the largest considered basis set. Astonishingly, the reported PW results were not extrapolated to the basis set limit, although a recent work of Klimes *et al.* shows that the GW QP energies converge like one over the number of plane waves [115] and this behaviour is also confirmed by purely analytical arguments [147]. Early evidence of this slow convergence using PWs exist aplenty [114, 148, 149]. In view of this slow convergence, a brute force approach to predict QP energies seems elusive considering that most codes scale cubically with respect to the number of basis functions. The present work tries to rectify this issue by reporting QP energies using the plane wave code VASP, carefully correcting for basis set incompleteness errors, as detailed in Section 7.2.2

Another point that we briefly mention in the present work is that the calculation of the poles of the G_0W_0 Green's function can be unphysical, if the initial Green's function yields too small excitation energies. In this case, first linearizing the G_0W_0 self-energy and then determining the poles of the Green's function yields more robust QP energies. We, finally, finish with discussions and our conclusions.

7.2.2. Technical details

As in the $GW100$ paper of van Setten *et al.* [84], we use the PBE functional for the DFT starting point. However, all calculations include scalar relativistic effects, in contrast to the calculations of van Setten *et al.* that are based on non-relativistic potentials. The potentials used in the present work are the GW potentials distributed with the latest release of VASP (vasp.5.4), and we followed the recommendations in the VASP manual on which version to use. Generally this means that lower lying semi-core states were not correlated in the calculations, except for the alkali and alkali-earth metals, as well as Ti and Ga. For He, we found issues with the originally distributed potential. The `He_GW` potential failed to converge in DFT calculations when the plane wave cutoff was increased, because a ghost state was introduced as the basis set size increased. The potential was slightly modified to remove this problem and will be distributed with the next release. Furthermore, for boron to fluorine the potentials `B_GW_new`, ..., `F_GW_new` were used (also already distributed with vasp.5.4). These potentials include *d* partial waves, whereas the standard GW potentials choose the *d* potential as local potential.

The potentials used in this work are not the most accurate GW potentials yet available for VASP. Specifically, we have recently shown that norm-conserving (NC) GW potentials are necessary to predict very accurate QP energies for 3*d*, 4*d* and 5*d* elements [115] with the NC potentials generally increasing the QP binding energies. In our experience, such highly accurate potentials are, however, not required in the present case for the following reasons. For *s* and *p* elements the standard potentials conserve the norm very well to within about 70 %, often even 90 %. Furthermore, errors introduced by violating the norm-conservation can only occur at very high scattering energies, since the standard GW-PAW potentials predict the scattering properties correctly up to about 400 eV. Beyond that energy, the PAW projectors become incomplete. For the elements considered here, we expect that the combination of these two effects means that the results for the HOMO and LUMO will be accurate even though we do not use NC potentials.

The only exceptions are copper, neon, fluorine, oxygen and possibly nitrogen. These elements possess strongly localized $3d$ and $2p$ orbitals. We will return to this point later.

In the calculations presented here we calculate the Green's function, the screened interaction W as well as the self-energy in imaginary time and frequency. This has several advantages compared to the full real frequency implementation also available in VASP. The fully frequency dependent version along the real axis requires at least 100, but for molecules with their sharp resonances often even several hundred frequency points to converge. Since the boxes considered in this work are quite large, we also need several thousands of plane waves to describe the frequency dependent screened interaction and Green's function accurately. This becomes very quickly prohibitive. In the imaginary frequency, on the other hand, only relatively few frequency points are required. In the calculations presented here, 16 frequency points and the time and frequency grids discussed by Kaltak *et al.* are used [103, 104]. These 16 points were found to be sufficient to converge the QP energies of the HOMO and LUMO to about 10 meV [107]. The downside of working in the imaginary frequency domain is that the results along the imaginary frequency axis need to be continued to the real axis. This was done using a (16 point) Padé fit following Thiele's reciprocal difference method based on continued fractions [109]. We note that the reported FHI-aims results in Ref. 84 were— with few problematic exceptions —also obtained using 16 parameter Padé fits. These exceptions are BN, O_3, BeO, MgO and CuCN where many more points were required. For the other molecules, the 16 parameter Padé fits yielded excellent agreement with Turbomole, which calculates the exact GW self-energy along the real axis. Details of our implementation are reported elsewhere [107].

The other crucial issues are basis set extrapolation and convergence with respect to the box size. To obtain basis set converged results, we used a relatively small box, but one that still faithfully reproduces the character of the HOMO and LUMO. For this box, we performed calculations for the default cutoff as specified by the VASP potentials, and calculations for three additional plane wave cutoffs, with the largest calculation corresponding to twice the number of plane waves used in the default setup. These four data points are fitted assuming that the QP energies as a function of the number of plane waves N_{pw} converge like

$$E^{\text{QP}}(N_{\text{pw}}) = E^{\text{QP}}(\infty) + \frac{C}{N_{\text{pw}}}, \tag{289}$$

where N_{pw} is the number of plane waves in the basis set [115, 150–152]. A four point fit and a two point fit with the largest and smallest PW basis set yielded a maximum difference of

10 meV in the QP energies. To illustrate that the basis set dependence is indeed following a $1/N_{\mathrm{pw}}$ behavior to great accuracy, we will show data for selected molecules in Sec. 7.2.4. The only subtlety impeding an accurate and automatic extrapolation is the use of the Padé fit. The slope of the self-energy can vary somewhat between different calculations causing some variations in the predicted QP energies. Extrapolation from these "noisy" data is difficult and error prone. To circumvent this issue, we perform the extrapolation for the self-energy evaluated at the DFT one-electron energies, specifically on $\Delta E = \mathrm{Re}\left[\langle\phi|T + V^{\mathrm{H}} + \Sigma(\epsilon^{\mathrm{DFT}})|\phi\rangle\right] - \epsilon^{\mathrm{DFT}}$ instead of $\Delta E = E^{\mathrm{QP}} - \epsilon^{\mathrm{DFT}}$, and scale the correction by the Z-factor at the smallest, *i.e.* default, PW cutoff. In this way, we neglect variations of the Z-factor between different basis sets, but these variations are small and dominated by noise.

A few final comments are in place here. In the calculations presented herein, we calculate *all* orbitals spanned by the PW basis set. This implies that the number of orbitals also increases as the number of plane waves increases. Second, the kinetic energy cutoff for the response function (`ENCUTGW` in VASP) is set to 2/3 of the cutoff used for the plane wave basis of the orbitals (`ENCUT` in VASP). Whenever the PW cutoff for the orbitals is increased, the PW cutoff for the basis set of the response function is increased accordingly. This means that a single parameter, the PW cutoff for the orbitals (`ENCUT`), entirely controls the accuracy of the calculations (at least with respect to the basis sets). Since all the intermediate control parameters are set automatically by VASP, and since the QP energy corrections converge like one over the number of plane waves and orbitals [115], extrapolation to the infinite basis set limit is straightforward and robust.

Let us now comment on the second point, convergence with respect to the cell size. In plane wave codes, it is common practice to truncate the Coulomb kernel at a certain distance r_c, say half the box size, so that the periodically repeated orbitals can not screen the central atom. The downside of this approach is that it modifies the Coulomb kernel to become [153]

$$V_{\mathbf{g}} = \frac{4\pi e^2}{|\mathbf{g}|^2}(1 - \cos(|\mathbf{g}|r_c)), \tag{290}$$

where $\mathbf{g}$ is a plane wave vector. Obviously, this modifies the Coulomb kernel at large reciprocal lattice vectors $\mathbf{g}$. In test calculations we found that this spoils the previously mentioned basis set extrapolation (289): as one increases the plane wave cutoff, one moves through maxima and minima of the truncated Coulomb kernel, causing superimposed oscillations in the QP energies. Basis set extrapolation becomes then uncontrolled. To deal with the repeated images, we instead resort to the standard trick used in periodic codes: $k \cdot p$ perturbation theory [154]. We calculate the first order change of the orbitals with respect to k [116], and accordingly the head and wings of the polarizability and a correction to the $\mathbf{g} \to 0$ component of the self-energy. This term corrects the leading monopole-monopole interaction between repeated images, but leaves the monopole-dipole and dipole-dipole interactions uncorrected. These two terms fall off like $1/V$ and $1/V^2$, where V is the cell size volume [155]. To deal with this, we perform four calculations at different volumes, with the box size progressively increased by 1 Å and fit the data to

$$a_0 + a_1/V + a_2/V^2. \tag{291}$$

For most molecules the corrections are small and only of the order of 10-20 meV, whereas for the alkali dimers and some polar molecules the corrections can be as large as 100-200 meV. In these cases the correction is very well described by the theoretical equation. We hope to find a better solution in future work, for instance, an explicit subtraction of monopole and dipole interactions between periodic images. In terms of compute time, however, the additional calculations for smaller boxes only require a modest amount of time: since the total compute time scales quadratic to cubic with respect to the number of plane waves, the calculations scale also quadratic to cubic in the volume. Typically we need 12 Å large boxes to obtain results converged to 20 meV with respect to the box size. The additional smaller volumes used for the extrapolation require only half of the compute time of the largest final box.

The final QP energies reported in the next section were obtained by calculating the PBE one-electron HOMO and LUMO for a 25 Å box at an energy cutoff that is 30 % increased compared to the VASP default values. The vacuum level, evaluated as the Hartree plus ionic potential, was evaluated at the position furthest from the center of the molecule and subtracted from the PBE one-electron energies. We checked that the DFT one-electron energies are converged to a few meV with this setup. To the DFT one-electron energies, the shift of the QP energies $E^{\mathrm{QP}} - \epsilon^{\mathrm{DFT}}$ for the largest considered box, box size corrections, and basis set corrections as described above are added. It goes without saying that this procedure is rather involved and since errors are expected to accumulate, we estimate that the present predictions are only accurate to about ±50 meV, where convergence with cell size is the main source of errors and difficult to estimate precisely.

To give a feeling for the required compute time and computational effort, we need to stress that our plane wave code is mainly designed for solids. Nevertheless, a calculation for C_6H_6 in a 10 Å box at the default cutoff takes about 4 hours on a single node with 16 Xeon v2 cores.

The compute time stays roughly constant if the box size is increased by 1 Å and the number of cores is simultaneously doubled. Furthermore, the compute time is mostly independent of the number of atoms in the box, but increases cubically with the box size as the total number of plane waves increases linearly with the box size.

7.2.3. HOMO for GW100

Let us first note on the agreement at the level of DFT (not shown). In general, our values agree exceedingly well with the PBE values reported in the supplementary material of Ref. 84. In most cases, our PBE HOMO is located between the basis set extrapolated values and the values obtained with the best basis sets used in the GTO calculations (def2-QZVP). On average, our PW HOMOs agree better with the non basis set extrapolated values with a mean deviation (MD) of 7 meV and a mean absolute deviation (MAD) of 19 meV. Compared to the GTO basis set extrapolated values, the MD and MAD are -25 meV and 30 meV (in both cases, CH_2CHBr was excluded, see below).

van Setten *et al.* [84] extrapolated the DFT eigenvalues using a cubic polynomial in the inverse of the cardinal number of the basis set (C_n^{-3}); we believe that this is not appropriate and will overestimate the basis set corrections. It is commonly agreed that DFT calculations converge exponentially with the cardinal number, whereas any correlated wave function calculation converges with the inverse of the basis set size (corresponding roughly to C_n^{-3}) [84, 115, 145]. This is a result of Kato's cusp condition [231] causing a kink in the many-body wave function as two coordinates approach each other. We have shown that this problem carries over to GW calculations [115]. As a one-electron theory, density functional theory does not suffer from this slow convergence. We hence believe that van Setten overestimated the basis set corrections for DFT. This is supported by the observation that our PBE results tend to be closer to the non-extrapolated Gaussian results at the level of def2-QZVP.

We now turn to the QP energies predicted at the level of G_0W_0 shown in Table 4. The agreement between the VASP PW and the GTO results is generally very good. We note that the G_0W_0 approximation used here is identical to the one applied by van Setten *et al.* [84]. Specifically, van Setten determined the nodes of Eq. (168), and we do exactly the same in the present work. Linearization of the QP equation (171) yields generally somewhat larger QP energies and often improves agreement with experiment slightly (column lin-G_0W_0). This

Table 4: Ionization potential (IP, negative of HOMO QP energies) for 100 molecules using G_0W_0 and linearized lin-G_0W_0 method. For comparison the basis set extrapolated values [84] and the experimental IPs are given (vertical IPs are in italics). If basis set extrapolated values are not specified in Ref. [84], the AIMS-P16 values are shown in the column GTO (marked by *). Last column shows the differences between GTO and PW results. The * indicates differences to non basis set extrapolated values.

		G_0W_0 GTO [84]	G_0W_0 PW	lin-G_0W_0 PW	EXP	Δ PW-GTO
1	He	23.49(0.03)	23.38	23.62	*24.59* [156]	-0.11
2	Ne	20.33(0.01)	20.17	20.36	*21.56* [156]	-0.16
3	Ar	15.28(0.03)	15.32	15.42	*15.76* [157]	0.04
4	Kr	13.89(0.16)	13.93	14.03	14.00 [158]	0.04
5	Xe	12.02*	12.14	12.22	12.13 [159]	0.12*
6	H_2	15.85(0.09)	15.85	16.06	15.43 [160]	0.00
7	Li_2	5.05(0.02)	5.09	5.32	4.73 [161]	0.04
8	Na_2	4.88(0.03)	4.93	5.06	4.89 [162]	0.05
9	Na_4	4.14(0.03)	4.17	4.23	4.27 [163]	0.03
10	Na_6	4.34(0.06)	4.34	4.40	4.12 [163]	0.00
11	K_2	4.08(0.04)	4.12	4.24	4.06 [162]	0.04
12	Rb_2	3.79*	4.02	4.14	3.90 [162]	0.23*
13	N_2	15.05(0.04)	14.93	15.06	15.58 [164]	-0.12
14	P_2	10.38(0.04)	10.35	10.40	10.62 [165]	-0.03
15	As_2	9.67(0.10)	9.59	9.62	10.0 [166]	-0.08
16	F_2	15.10(0.04)	14.93	15.08	15.70 [167]	-0.17
17	Cl_2	11.31(0.05)	11.32	11.40	*11.49* [168]	0.01
18	Br_2	10.56(0.18)	10.57	10.65	*10.51* [168]	0.01
19	I_2	9.23*	9.52	9.59	*9.36* [169]	0.29*
20	CH_4	14.00(0.06)	14.02	14.14	*13.6* [170]	0.02
21	C_2H_6	12.46(0.06)	12.50	12.58	*11.99* [169]	0.04
22	C_3H_8	11.89(0.06)	11.90	11.98	*11.51* [169]	0.01
23	C_4H_{10}	11.59(0.05)	11.61	11.69	*11.09* [169]	0.02
24	C_2H_4	10.40(0.03)	10.42	10.50	*10.68* [170]	0.02
25	C_2H_2	11.09(0.01)	11.07	11.24	*11.49* [170]	-0.02
26	C_4	10.91(0.03)	10.89	10.97	12.54 [171]	-0.02
27	C_3H_6	10.65(0.04)	10.72	10.78	*10.54* [172]	0.07
28	C_6H_6	9.10(0.01)	9.11	9.16	*9.23* [173]	0.01

(continued)

		G_0W_0	G_0W_0	lin-G_0W_0	EXP	Δ
		GTO	PW	PW		PW-GTO
29	C_8H_8	8.18(0.02)	8.19	8.24	*8.43* [174]	0.01
30	C_5H_6	8.45(0.02)	8.47	8.51	*8.53* [175]	0.02
31	CH_2CHF	10.32(0.02)	10.28	10.36	*10.63* [176]	-0.04
32	CH_2CHCl	9.89(0.02)	9.92	10.00	*10.20* [177]	0.03
33	CH_2CHBr	9.14(0.01)	9.75	9.83	*9.90* [177]	0.61
34	CH_2CHI	9.01*	9.27	9.36	*9.35* [178]	0.26*
35	CF_4	15.60(0.06)	15.41	15.53	*16.20* [179]	-0.19
36	CCl_4	11.21(0.06)	11.20	11.31	*11.69* [169]	-0.01
37	CBr_4	10.22(0.16)	10.25	10.38	*10.54* [180]	0.03
38	CI_4	8.71*	9.11	9.23	*9.10* [181]	0.40*
39	SiH_4	12.40(0.06)	12.40	12.53	*12.3* [182]	0.00
40	GeH_4	12.11(0.04)	12.13	12.24	*11.34* [183]	0.02
41	H_6Si_2	10.41(0.06)	10.44	10.52	*10.53* [184]	0.03
42	$H_{12}Si_5$	9.05(0.05)	9.13	9.19	*9.36* [184]	0.08
43	LiH	6.58(0.04)	6.46	7.20	7.90 [185]	-0.12
44	KH	4.99(0.01)	4.97	5.37	8.00 [186]	-0.02
45	BH_3	12.96(0.06)	12.95	13.09	12.03 [187]	-0.01
46	B_2H_6	11.93(0.06)	11.94	12.04	*11.90* [188]	0.01
47	NH_3	10.39(0.05)	10.32	10.44	*10.82* [189]	-0.07
48	HN_3	10.55(0.02)	10.50	10.56	*10.72* [190]	-0.05
49	PH_3	10.35(0.05)	10.35	10.45	*10.59* [191]	0.00
50	AsH_3	10.21(0.02)	10.26	10.36	*10.58* [192]	0.05
51	H_2S	10.13(0.04)	10.11	10.30	*10.50* [193]	-0.02
52	HF	15.37(0.01)	15.37	15.38	*16.12* [194]	0.00
53	HCl	12.36(0.01)	12.45	12.51	12.79 [195]	0.09
54	LiF	10.27(0.03)	10.07	10.45	11.30 [196]	-0.20
55	MgF_2	12.50(0.06)	12.41	12.77	13.30 [197]	-0.09
56	TiF_4	14.07(0.05)	14.01	14.22	*15.30* [198]	-0.06
57	AlF_3	14.48(0.06)	14.33	14.53	15.45 [199]	-0.15
58	BF	10.73(0.05)	10.46	10.67	11.00 [200]	-0.27
59	SF_4	12.38(0.07)	12.20	12.29	11.69 [201]	-0.18
60	KBr	7.57(0.13)	7.80	8.04	*8.82* [202]	0.23
61	$GaCl$	9.74(0.07)	9.89	9.99	*10.07* [203]	0.15
62	$NaCl$	8.43(0.14)	8.47	8.76	*9.80* [202]	0.04
63	$MgCl_2$	11.20(0.07)	11.19	11.41	*11.80* [204]	-0.01
64	AlI_3	9.30*	9.58	9.69	*9.66* [205]	0.28*

(continued)

		G_0W_0	G_0W_0	lin-G_0W_0	EXP	Δ
		GTO	PW	PW		PW-GTO
65	BN	11.15(0.03)	-	10.61	11.50	-
66	HCN	13.32(0.01)	13.29	13.43	*13.61* [206]	-0.03
67	PN	11.29(0.04)	11.24	11.41	11.88 [207]	-0.05
68	N_2H_4	9.37(0.04)	9.33	9.45	*8.98* [208]	-0.04
69	H_2CO	10.46(0.02)	10.42	10.57	10.88 [209]	-0.04
70	CH_3OH	10.67(0.05)	10.61	10.72	*10.96* [210]	-0.06
71	CH_3CH_2OH	10.27(0.05)	10.21	10.33	*10.64* [211]	-0.06
72	CH_3CHO	9.66(0.03)	9.63	9.80	*10.24* [212]	-0.03
73	$CH_3CH_2OCH_2CH_3$	9.42(0.05)	9.43	9.52	*9.61* [211]	0.01
74	HCOOH	10.87(0.01)	10.81	10.98	*11.50* [213]	-0.06
75	H_2O_2	11.10(0.01)	10.96	11.12	*11.70* [214]	-0.14
76	H_2O	12.05(0.03)	11.84	12.05	*12.62* [169]	-0.21
77	CO_2	13.46(0.06)	13.36	13.44	*13.77* [215]	-0.10
78	CS_2	9.95(0.05)	9.96	10.01	*10.09* [216]	0.01
79	CSO	11.11(0.05)	11.06	11.13	*11.19* [217]	-0.05
80	COSe	10.43(0.09)	10.42	10.50	10.37 [218]	-0.01
81	CO	13.71(0.04)	13.62	13.76	*14.01* [217]	-0.09
82	O_3	11.49(0.03)	-	12.07	*12.73* [219]	-
83	SO_2	12.06(0.06)	11.91	12.04	*12.50* [169]	-0.15
84	BeO	8.60(0.01)	-	9.50	10.10 [220]	-
85	MgO	6.75(0.03)	-	7.10	8.76 [221]	-
86	$C_6H_5CH_3$	8.73(0.02)	8.75	8.79	*8.82* [173]	0.02
87	C_8H_{10}	8.66(0.02)	8.69	8.73	*8.77* [173]	0.03
88	C_6F_6	9.74(0.07)	9.63	9.69	*10.20* [179]	-0.11
89	C_6H_5OH	8.51(0.01)	8.38	8.43	8.75 [222]	-0.13
90	$C_6H_5NH_2$	7.78(0.01)	7.78	7.84	*8.05* [223]	0.00
91	C_5H_5N	9.17(0.01)	9.16	9.31	*9.66* [224]	-0.01
92	Guanine	7.87(0.01)	7.85	7.90	*8.24* [225]	-0.02
93	Adenine	8.16(0.01)	8.12	8.18	*8.48* [226]	-0.04
94	Cytosine	8.44(0.01)	8.40	8.50	*8.94* [225]	-0.04
95	Thymine	8.87(0.01)	8.83	8.89	*9.20* [227]	-0.04
96	Uracil	9.38(0.01)	9.36	9.55	*9.68* [228]	-0.02
97	NH_2CONH_2	9.46(0.02)	9.35	9.59	*9.80* [193]	-0.11
98	Ag_2	7.08^*	7.83	7.95	7.66 [229]	0.75^*
99	Cu_2	7.78(0.06)	7.19	7.40	7.46 [230]	-0.59
100	CuCN	9.56(0.04)	-	9.99	-	-

Table 5: IP (negative HOMO G_0W_0 QP energies) and G_0W_0 LUMO for selected molecules. The GTO values have been calculated using frozen core potentials, scalar relativistic corrections, and are extrapolated to the infinite basis set limit.

		IP GTO	IP PW	LUMO GTO	LUMO PW
5	Xe	12.22	12.14	-0.07	0.28
12	Rb_2	4.07	4.02	-0.85	-0.74
19	I_2	9.48	9.52	-2.28	-2.21
34	CH_2CHI	9.13	9.27	0.56	0.37
38	CI_4	8.97	9.11	-2.47	-2.42
64	AlI_3	9.50	9.58	-1.18	-1.02
98	Ag_2	7.96	7.83	-1.40	-1.35

trend has also been observed in a recent benchmark for an unrelated set of molecules [232]. In agreement with van Setten [84], we have found poles in the self-energy close to the predicted QP energies for BN, O_3, BeO, MgO and CuCN. Since analytic continuation has difficulties to resolve the precise pole structure of the Green's function, we only report the values obtained from the linearized self-energy.

Our discussion starts with the molecules that show large discrepancies between VASP and GTO's. A large out-liner is seemingly CH_2CHBr. However, for this molecule, as well as C_6H_5OH, we found large forces in the preparatory PBE calculations. Double checking the original literature [233] suggests that the $GW100$ paper used incorrect geometries. Since the ultimate purpose is certainly to compare with experiment, we decided to update the geometries to the correct literature values.

Among the remaining molecules, errors are large for compounds containing iodine, rubidium, and silver with a maximum deviation of 400 meV for CI_4 and Rb_2, and 750 meV for Ag_2. However, in Ref. 84 no basis set extrapolation was performed for these molecules. From CCl_4 to CBr_4, the basis set corrections increase from 300 meV to 350 meV, suggesting a basis set error of 400 meV for CI_4 using GTOs. Similarly, for Rb_2 the GTO results were not basis set corrected, and estimating the basis set error from Na_2 and K_2 again suggests that the VASP results are accurate. For Ag_2, the difference between VASP and GTO seem on first sight to be

Table 6: IP (negative HOMO G_0W_0 QP energies) for selected molecules calculated for a 9 Å box for the standard GW potentials and normconserving GW potentials. Results differ from the previous table, since calculations in Table 4 have been performed for larger boxes and include a correction for the box size error. The column Δ reports the difference between the standard PAW and NC PAW potential.

		GW PAW	NC GW PAW	Δ
13	N_2	14.98	15.02	-0.04
16	F_2	14.97	15.13	-0.15
35	CF_4	15.42	15.58	-0.16
52	HF	15.39	15.32	0.06
58	BF	10.42	10.46	-0.04
59	SF_4	12.19	12.26	-0.07
76	H_2O	11.86	11.94	-0.09
99	Cu_2	7.03	7.53	-0.50

too large to be ascribed to basis set errors alone. To resolve the issue, one of us (MvS) repeated the Xe, Rb_2, I_2, CH_2CHI, CI_4, AlI_3, and Ag_2 calculations using scalar relativistic corrections and frozen core SVP, TZVP and QZVP basis sets. This yielded basis set extrapolated values summarized in Table 5 certainly now in good to very good agreement with the VASP values, as also evidenced in Fig. 17.

For the remaining molecules, the mean absolute deviation between the two codes and thus two completely different basis sets is only 60 meV, if we also exclude Cu_2. For Cu_2, the fluorine containing compounds, H_2O, as well as Ne the ionization potentials (IPs) are smaller in VASP, which we will now show to be related to slight deficiencies in the PAW potentials. Copper, neon, and fluorine and, to a lesser extent, oxygen are particularly difficult to describe using a plane wave based approach, since the $3d$ and $2p$ electrons are strongly localized. To cope with this, the Cu, F and Ne potentials are already the three smallest core and hardest potentials used in the present work. But still, the partial waves do not conserve the norm exactly, which results in errors, if an electron is scattered into a plane wave with very high kinetic energy [115]. To determine this error, we performed calculations with norm-conserving (or almost norm-conserving) GW potentials for the molecules Cu_2, N_2, F_2, CF_4, HF, BF, SF_4 and H_2O reported

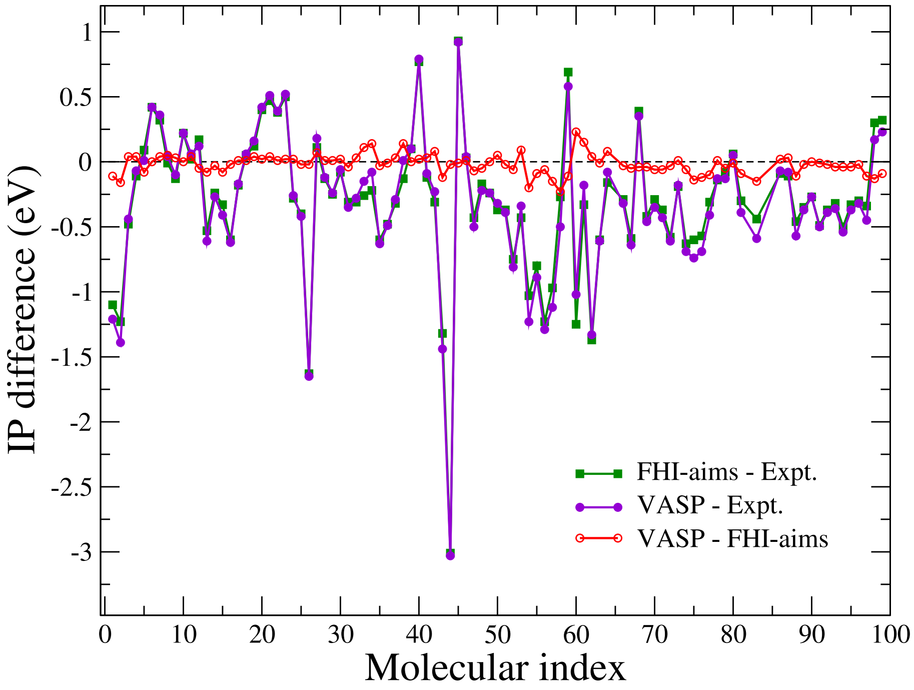

Figure 17: (color online) IP differences between PW and GTO results (VASP−FHI-aims in red color), between GTO and experimental results (FHI-aims−Expt. in green color), and between PW and experimental results (VASP−Expt. in purple color) as a function of molecular indices. Note that all the data are taken from the Table 4 except for those molecules shown in Table 5, for which the IPs are updated with new calculated values. In addition, corrections due to the inaccuracies of GW PAW potentials for some molecules shown in Table 6 are included. For BN, O_3, MgO, BeO and CuCN, where the roots of QP equations are difficult to obtain, they are not shown in the plot. Furthermore, after we informed van Setten that crystal structures of CH_2CHBr and C_6H_5OH were wrong in the *GW*100 paper [84], he redid these two calculations with correct structures, so that in this plot we have used the corrected IPs of CH_2CHBr and C_6H_5OH provided by van Setten. Now for the molecules considered in the plot, excellent agreement between PW and GTO results is achieved. Lines are shown for guiding the eyes.

in Tab. 6 using the potentials `Cu_sv_GW_nc`, `N_h_GW`,...,`F_h_GW`. Except for HF, the QP energies are clearly shifted towards higher binding energies in these calculations, and the discrepancies to the GTO calculations are reduced to an acceptable level of 100 meV. We also note that the PAW error increases from nitrogen, over oxygen to fluorine. HF and BF are exceptions, since the HOMOs possess predominantly hydrogen and boron character and, therefore, do not depend strongly on the F potential (we note that the HF results were already accurate using the standard potentials). Finally, the standard carbon and boron potentials used here are already almost norm conserving, and hence negligible changes are found for carbon based compounds with harder potentials (not shown).

The final case worthwhile mentioning is KBr. Here the $GW100$ paper [84] reports relatively large extrapolation errors of 130 meV, indicating that in this case the GTO based extrapolation might be inaccurate.

For the remaining systems, we find the agreement to be excellent (see Fig. 17). Specifically, for all considered organic molecules the absolute differences are typically below 50 meV, with very few out-liners. This clearly demonstrates that plane wave codes can be competitive in terms of precision with GTOs. Certainly the agreement between GTOs and PWs is better than originally reported in the $GW100$ paper, a point discussed in more detail in the next section.

7.2.4. Basis set convergence and comparison to other PW calculations

In Fig. 18, we show the convergence of the HOMO with respect to the plane wave cutoff for the orbitals. This cutoff also determines the total number of orbitals as well as the cutoff for the response function. The number of plane waves and total orbitals is proportional to one over the cutoff to the power of 3/2. It is clearly visible that the curves follow almost exactly a straight line. In few cases, out-liners are visible. For instance for H_2O, we have included results for two box sizes 8 and 9 Å. The 9 Å box results have a slight jump, which is not present for the 8 Å box. However, this out-liner is small (about 10 meV), and changes extrapolated results only by less than 10 meV. Usually the out-liners could be dealt with by just changing the box size slightly. We believe that they are related to ”shell”-effects, *i.e.* a sudden increase in the number of plane waves when the cutoff is changed through certain values. Furthermore, the analytic continuation is not always entirely well behaved and can cause changes of the order of 20 meV. Overall, the plot demonstrates that extrapolation with respect to the energy-cutoff is very well under control and can be done with great accuracy.

As noted before, the differences between the GTO and the Berkeley GW calculations reported in Ref. 84 are more sizable. If we exclude the difficult multipole cases, BN, O_3, MgO and BeO, the mean absolute deviation between Berkeley GW and basis set extrapolated GTOs was 0.2 eV

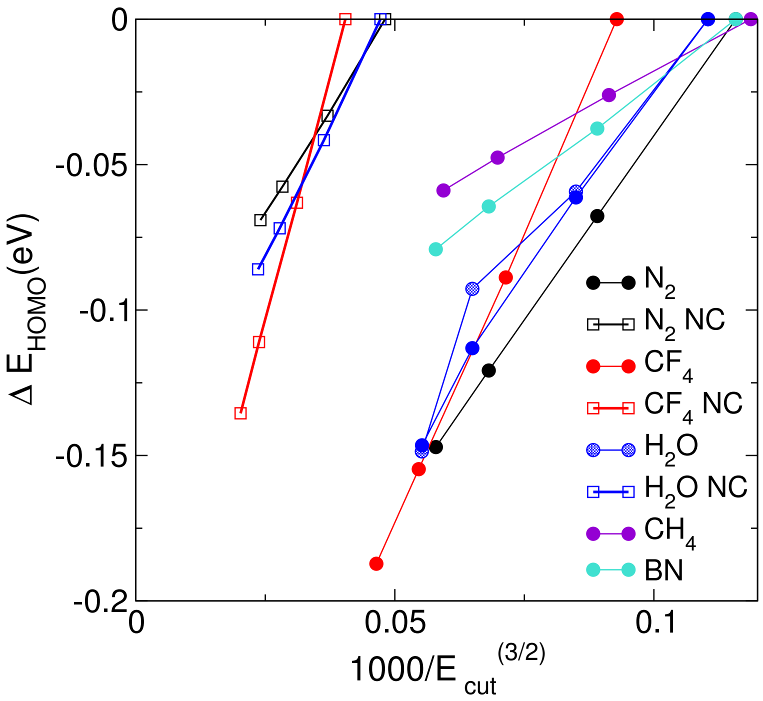

Figure 18: (color online) Convergence of QP HOMO with respect to the employed cutoff for various materials. For N_2, CF_4 and H_2O, results are shown for two potentials, the standard *GW* potentials, as well as NC potentials. The slopes are steeper for the NC potentials, which is particularly obvious for CF_4. For H_2O results for two box sizes (8 and 9 Å) are shown (see text).

in Ref. 84, whereas it is reduced to 0.05 eV for VASP PAW potentials (for the same subset). We speculate that this is mostly related to neglecting basis set extrapolation errors or— less likely —to an inaccurate treatment of the core-valence interaction. Typically our basis set corrections are of the order of 300-400 meV at the default cutoff and therefore very sizable. Even doubling the number of basis functions and therefore increasing the compute time by a factor of about 8 (cubic scaling), reduces the error only by a factor 2, to about 150-200 meV. Hence, calculations without basis set corrections are hardly affordable or practicable, and it is certainly advisable to perform an extrapolation whenever possible.

For the core-valence interaction, we emphasize that VASP always evaluates the interaction at the level of Hartree-Fock if correlated calculations are performed. More precisely, VASP calculates the PBE core orbitals on the fly and then recalculates the action of the PBE core states on the valence states using the Hartree-Fock approximation. Not doing so can have a sizable effect on the QP energies for heavier atoms [33]. We are not aware of other pseudopotential codes following a similar route. This might be responsible for a small part of the errors in the reported Berkeley *GW* calculations of Ref. 84, if heavier atoms are involved.

Calculations for another fairly large set of molecules have been reported by Govoni and Galli using the West code [144]. 29 molecules are identical to the GW100 set considered here. The mean absolute difference between the basis set extrapolated GTO results and the VASP results for this subset is 60 meV, whereas the difference between the West results and the basis set extrapolated GTO results is about twice as large 120 meV (mean absolute difference between VASP and West is 90 meV). In many cases, the West IPs are too small indicating again basis set incompleteness errors. Anyhow, the West results are closer to the basis set converged values than the *GW* Berkeley results.

7.2.5. Comparison to experiment

When comparing the present results against the experimental ionisation energies, a mean absolute error of 0.5 eV is observed. This large discrepancy is not unexpected given that in this computational approach self-consistency, vertex corrections and finite temperature effects are omitted. However we can comment on the biggest outliers in the set. A first example is C_4: it is well known that the smaller C_2 molecule is particularly challenging to describe, owing to strong electron correlation [234]. For the larger cluster we expect similar effects, hence the inclusion of the vertex should improve the agreement with the experiment. We have a similar expectation for the case of F_2. Our conjecture is substantiated by previous electron propagator calculations [235], where the poles of the Green's function in the Lehmann representation were located to give the IP, and where a comparable mismatch to experiment was ascribed to the poor description of dynamic correlation. For AlF_3, LiF and KH we have to bear in mind that the experimental value for a vertical transition was not available, therefore geometry relaxations may explain the mismatch. This is only partially true for KH, where the inclusion of adiabatic effects in the perturbative calculations still leaves a sizable disagreement (~2 eV) [236]; in this case it is not completely unreasonable to call for a further assessment of the experimental value.

7.2.6. Linearized QP-HOMO for GW100

We now turn to results obtained by first linearizing the self-energy and then determining the QP energy from this linearized equation. This procedure is in our experience more ”robust” and better behaved than seeking the poles in the non-linearized equation. The main issue of the latter approach is that, in the G_0W_0 approximation, the first pole in the self-energy is approximately located at the energy of the DFT HOMO minus the first excitation energy in the DFT (LUMO−HOMO):

$$\epsilon_{\text{HOMO}} - (\epsilon_{\text{LUMO}} - \epsilon_{\text{HOMO}}).$$

This is a simple Auger like excitation, where the hole has sufficient energy, *i.e.* is sufficiently below the HOMO to be able to excite an electron-hole pair. As discussed by van Setten, such poles lead to multiple solutions for the QP energy [84] and make the determination of the QP energies difficult for molecules with small excitation energies. These poles are, however, an artifact of the G_0W_0 approximation. If the GW procedure were done self-consistently, the first pole in the self-energy would move to approximately

$$E^{\text{QP}}_{\text{HOMO}} - (E^{\text{QP}}_{\text{LUMO}} - E^{\text{QP}}_{\text{HOMO}}).$$

In other words, at the valence band edge (HOMO) and conduction band edge (LUMO) the self-energy never possesses poles. However, in a single shot procedure and when starting from much too small band gaps, the quasiparticle energy E^{QP} might move into regions where the self-energy evaluated from DFT orbitals has a pole. Linearization at the DFT eigenenergies resolves this issue, as the G_0W_0 self-energy has no poles in the direct vicinity of the DFT HOMO. The problem is also less severe, if the calculations are done selfconsistently or when starting from a prescription that yields larger HOMO-LUMO Kohn-Sham gaps, as shown in a recent evaluation of the difference between the quasi-particle orbital energies and their linearized counterparts by Govoni *et al.* [144]. Therein it is shown that, for a wide range of molecules, this difference is substantially more pronounced for GW calculations on a PBE reference state than if a hybrid functional with non-local exchange is used.

In summary, we feel that for code benchmarking as well as for a comparison with experiment determining the poles of the linearized equation is preferable, at least, if a PBE reference state is employed. However, it also needs to be emphasized that for comparison with the already published GW100 data, it is of paramount importance to exactly follow the procedures laid out in the the initial GW100 paper.

7.2.7. LUMO for $GW100$

The calculated LUMOs are shown in Table 7. A few important comments are in place here. First, the table reports the QP energy of the lowest unoccupied orbital in the preceeding DFT calculations to maintain compatibility with the previous publication. In some cases (Xe, H_2O, CH_2CHCl, CH_3CHO, and HCOOH) PW calculations predict at the DFT level a very weakly bound LUMO+1 state (just below the vacuum level) whose G_0W_0 QP energy is below the QP state corresponding to the DFT LUMO level. These energy levels are not shown in Tab. 7.

If we consider the G_0W_0 values corresponding to the DFT LUMOs, the agreement between the $GW100$ reference GTO data and plane waves is reasonable, although not quite as good as for the HOMO. Specifically troublesome is the observation that the GTO calculations sometimes predict too positive LUMOs. Admittedly, box size convergence can be troublesome for QP energies above the vacuum level, and we therefore only show few selected positive LUMOs—those where we are confident that convergence to 50 meV was attained for the cell sizes considered in our calculations. All positive (unbound) G_0W_0 LUMOs are marked by a superscript " + " sign in the last column. The differences are particularly striking for Ne, Xe, H_2, H_2O and CH_4 reaching 11 eV for Ne.

To investigate this issue, we compared the DFT-LUMOs of the PW and GTO calculations (the latter are available upon request to MvS), and found that the deviations between PWs and GTOs are much larger than for the DFT HOMOs on average, and especially large for some of the problematic cases, e.g. Ne, Xe, H_2, or H_2O which are the largest outliners in the subsequent QP calculations. Specifically, for Ne and H_2 the PW DFT calculations predict very shallow bound LUMOs, a few 10 meV below the vacuum level. These can not be reproduced with any of the available GTO basis sets.

For the other cases with larger discrepencies, we now show that the GTO basis sets are often not sufficiently flexible to describe unoccupied orbitals. This is supported by several observations. (i) Basis set corrections using GTOs are much larger for the LUMO than for the HOMO, as for instance exemplified for As_2, F_2 or Cl_2. To make this very clear, we have included in Table 7 both, the basis set extrapolated values (with estimated error bars), as well as the values at the largest considered GTO basis set. (ii) Non basis set extrapolated GTO values deviate markedly from PW results. As before, these are marked by a star superscript in the last column. GTO basis set extrapolated values are tabulated in Tab. 5 and clearly improve the

Table 7: LUMO QP energies for selected molecules using G_0W_0 and the linearized lin-G_0W_0. For comparison, the non basis set extrapolated values (AIMS-P16), the basis set extrapolated values [84], and the negative of the experimental electron affinities are shown (vertical attachment energies are in italics). Differences between PW and GTO are shown in last column. The $^{+}$ indicates energies above the vacuum level, and * indicates differences to non basis set extrapolated values.

		G_0W_0	G_0W_0	G_0W_0	lin-G_0W_0	EXP	Δ
		AIMS-P16	GTO-EXTRA	PW	PW		PW-GTO
2	Ne	11.64	-	0.40	0.40	-	-11.24^{+}
5	Xe	4.28	-	0.70	0.70	-	-3.58^{+}
6	H_2	3.50	3.30(0.52)	0.07	0.07	-	-3.23^{+}
7	Li_2	-0.63	-0.75(0.04)	-0.61	-0.54	-	0.14
8	Na_2	-0.55	-0.66(0.70)	-0.60	-0.56	-0.54	0.06
9	Na_4	-1.01	-1.15(0.90)	-1.07	-1.03	-0.91 [237]	0.08
10	Na_6	-0.97	-1.13(0.10)	-1.07	-1.03	-	0.06
11	K_2	-0.65	-0.75(0.05)	-0.74	-0.70	-0.50	0.01
12	Rb_2	-0.62	-	-0.74	-0.70	-0.50 [237]	-0.12^{*}
14	P_2	-0.72	-1.08(0.08)	-0.99	-0.97	-0.68 [238]	0.09
15	As_2	-0.85	-1.52(0.35)	-1.07	-1.06	-0.74 [239]	0.45
16	F_2	-0.70	-1.23(0.14)	-0.96	-0.84	*-1.24* [240]	0.27
17	Cl_2	-0.89	-1.40(0.12)	-1.25	-1.22	*-1.02* [240]	0.15
18	Br_2	-1.40	-1.96(0.29)	-1.99	-1.97	*-1.60* [240]	-0.03
19	I_2	-1.68	-	-2.21	-2.20	*-1.70* [240]	-0.53^{*}
20	CH_4	2.45	2.03(0.35)	0.63	0.63	-	-1.40^{+}
26	C_4	-2.94	-3.15(0.06)	-3.09	-3.08	-3.88 [241]	0.06
29	C_8H_8	0.06	-0.12(0.02)	-0.05	-0.02	-0.57 [242]	0.07
32	CH_2CHCl	1.42	1.17(0.03)	1.19	1.25	-	0.02^{+}
36	CCl_4	-0.01	-0.54(0.13)	-0.32	-0.28	-	0.22
37	CBr_4	-1.08	-1.56(0.29)	-1.47	-1.44	-	0.09
38	CI_4	-2.14	-	-2.42	-2.40	-	-0.28^{*}
42	$H_{12}Si_5$	0.16	0.00(0.07)	0.03	0.05	-	0.03
43	LiH	-0.07	-0.16(0.09)	-0.07	-0.04	-0.34 [243]	0.09
44	KH	-0.18	-0.32(0.01)	-0.25	-0.22	-	0.07
45	BH_3	0.12	0.03(0.05)	0.03	0.08	-0.04 [244]	0.00

(continued)

		G_0W_0 AIMS-P16	G_0W_0 GTO-EXTRA	G_0W_0 PW	lin-G_0W_0 PW	EXP	Δ PW-GTO
54	LiF	0.09	-0.01(0.01)	0.17	0.17	-	0.18
55	MgF_2	-0.14	-0.31(0.06)	-0.29	-0.28	-	0.02
56	TiF_4	-0.60	-1.06(0.13)	-0.79	-0.66	-2.50 [245]	0.27
57	AlF_3	0.16	-0.23(0.10)	0.08	0.09	-	0.31
59	SF_4	0.38	-0.10(0.13)	0.07	0.12	-1.50 [246]	0.17
60	KBr	-0.31	-0.42(0.06)	-0.32	-0.31	-0.64 [247]	0.10
61	GaCl	-0.02	-0.39(0.15)	-0.19	-0.15	-	0.20
62	NaCl	-0.39	-0.42(0.01)	-0.46	-0.43	-0.73 [247]	-0.04
63	$MgCl_2$	-0.43	-0.68(0.08)	-0.61	-0.59	-	0.07
64	AlI_3	-0.80	-	-1.02	-0.99	-	-0.22*
72	CH_3CHO	1.05	0.83(0.05)	0.87	0.87	-	0.04$^+$
74	HCOOH	1.91	1.59(0.00)	1.64	1.72	-	0.05$^+$
76	H_2O	2.37	2.01(0.16)	1.04	1.04	-	-0.97$^+$
78	CS_2	-0.20	-0.55(0.09)	-0.42	-0.40	-0.55 [248]	0.13
82	O_3	-2.30	-2.69(0.11)	-2.50	-2.52	-2.10 [249]	0.19
83	SO_2	-1.00	-1.49(0.12)	-1.25	-1.19	-1.11 [250]	0.24
84	BeO	-2.56	-2.72(0.04)	-2.73	-2.37	-	-0.01
85	MgO	-1.89	-2.13(0.09)	-2.05	-2.12	-	0.08
88	C_6F_6	0.66	0.36(0.08)	0.24	0.27	-0.70 [251]	-0.12$^+$
94	Cytosine	0.26	0.01(0.01)	0.12	0.15	-0.23 [252]	0.11
95	Thymine	0.06	-0.18(0.01)	-0.06	-0.04	*0.29* [253]	0.12
96	Uracil	0.01	-0.25(0.01)	-0.11	-0.09	*0.22* [253]	0.14
98	Ag_2	-1.05	-	-1.35	-1.31	*-1.10* [254]	-0.30*
99	Cu_2	-0.92	-1.23(0.08)	-1.24	-1.21	-0.84 [255]	-0.01
100	CuCN	-1.65	-1.85(0.05)	-1.91	-1.81	*-1.47* [256]	-0.06

agreement with the PW results. For Xe, where the discrepancy was previously 3.6 eV, the error is reduced to about 0.3 eV. Furthermore, we recalculated the QP energies of H_2O and CH_4 using Dunning correlation consistent basis sets and found basis set extrapolated G_0W_0 QP energies of 1.00 eV and 0.89 eV, now in excellent and reasonable agreement with the PW results. All in all, we therefore conclude that the Gaussian basis set results for unoccupied states need to be considered with some caution, and Dunning correlation consistent basis sets are seemingly better suited to predict accurate values.

If we restrict the comparison between PWs and GTOs to states below the vacuum level, we find the agreement to be generally, as for the HOMO, rather satisfactory. Differences are about a factor two larger than for the HUMO, but considering the previous discussion on the possible issues with the Gaussian basis sets for unoccupied orbitals, this is certainly not astonishing.

Finally, concerning the agreement with the experiment, we find a similar absolute deviation as for the first ionization energies (compare with Tab. 4). To make the comparison between the LUMO energies and the experiment more immediate, the second last column reports the negative of the experimental electron affinities, which is overall in quite satisfactory agreement with experiment.

7.2.8. Discussions and Conclusions

The main purpose of the present work is a careful comparison of *GW* QP energies obtained using Gaussian type orbitals and plane waves. One important motivation was that the values reported for the Berkeley *GW* code were typically 200 meV smaller than the basis set extrapolated GTO results. However, the Gaussian basis set extrapolation also often increased the predicted QP energies by some 100 meV. Since basis set extrapolation using GTOs is not necessarily accurate, and since the Berkeley *GW* calculations are often closer to the uncorrected values than the basis set extrapolated values, we felt that it is important to bring in a third independent set of calculations, hopefully confirming one or the other of the previous values.

The main outcome of our work is that our VASP predicted HOMOs are in excellent agreement with the basis set extrapolated GTO results. We believe this establishes beyond doubt that the values reported in Ref. 84 are very reliable and can be used as a rigorous benchmark for future implementations. In the few cases (iodine compounds, Br_2 and Ag_2), where the GTO calculations were not extrapolated to the basis set limit, we find— not unexpectedly —that the non basis set extrapolated GTO values underestimate the IP by about 300-400 meV. The present work also reports basis set extrapolated GTO values for these molecules finding good agreement with VASP PW results.

Although the mean absolute deviation between our PAW PW results and the GTO results is only 60 meV, we found larger discrepancies for molecules containing copper, fluorine and nitrogen. We traced these differences back to the use of non-normconserving PAW potentials: using normconserving PAW potentials the agreement between PW calculations and GTOs improves further.

For the LUMO, results are slightly less satisfactory. Agreement between GTOs and PWs is good for QP energies below the vacuum level, although even for those there are more out-liners and the average deviation is larger. For instance, differences are sizable for some seemingly simple dimers. We attribute this to very large basis set corrections for GTOs for some molecules (e.g. 700 meV for As_2).

If the predicted QP LUMOs are above the vacuum level, the differences between the PW and GTO results can be very large and can reach 11 eV (Ne). Our explanation for this behavior is that the GTO basis sets employed in Ref. 84 are not always sufficiently flexible to model unoccupied states. This is particularly true for atoms and small dimers, where the LUMO has a character that is very different from a linear combination of atomic like orbitals. In most cases, these basis set issues lead to small but noticeable errors on the level of DFT, but they are dramatically amplified at the level of G_0W_0. For Xe, H_2O and CH_4, GTO calculations with improved basis sets have been reported finding very good to good agreement with the PW results.

If we disregard the slightly disconcerting propagation of errors in going from DFT to G_0W_0 for LUMOs, we are satisfied by the agreement between plane waves and Gaussian type orbitals. As already stated, for the HOMO the mean absolute deviation is only 60 meV, which is excellent if one considers that the computational details are so different. Furthermore, our results have been obtained using the GW PAW potentials distributed with vasp.5.4, so that similar calculations e.g. for molecules adsorbed on surfaces can be readily performed using the projector augmented wave method.

8. $G_0W_0(\mathrm{i}\omega)$: GW in imaginary frequency

Considering the advantages of the low-scaling scheme discussed in Sections (6) and (7), one would wonder if it is possible to extend this scheme to the conventional GW implementation. Such extension will be rather promising for the following two reasons: (i) Due to the reduced imaginary time/frequency points as will be used in the modified version (hereafter we denote it as $G_0W_0(\mathrm{i}\omega)$), the computational effort and memory requirement would be significantly reduced. This allows us to perform GW calculations on moderately large systems and thus overcomes the drawback of the conventional GW implementation, which is currently restricted to small systems. (ii) Since the spin-orbit coupling (SOC) has not yet been implemented in the low-scaling GW implementation, the modified version might be a good method applicable for systems where SOC is nonnegligible.

Therefore, in this section, we will show how this extension could be achieved and how it performs. We will first give detailed practical formulations and then show our test results on ZnO and CdTe. For ZnO, comparisons with conventional G_0W_0 and low-scaling G_0W_0r are given. For CdTe, we include SOC and comparison is only done between $G_0W_0(\mathrm{i}\omega)$ and conventional G_0W_0. It turns out that the agreement with conventional G_0W_0 or low-scaling G_0W_0r is pretty good, highlighting the potential of the modified $G_0W_0(\mathrm{i}\omega)$ method.

8.1. Computational scheme of $G_0W_0(\mathrm{i}\omega)$

Actually, there are three possible alternatives to perform the computations in imaginary frequency. However, the three methods bear a resemblance in the first step. That is, the evaluation of the screened two electron integrals for each pair $(n\mathbf{k}, n'\mathbf{k}-\mathbf{q})$ is always done along the imaginary frequency axis using the optimized frequency grids $\{\mathrm{i}\omega_k\}_{k=1}^{N}$ (for more information on the optimized grids, please refer to Appendix (B) and Ref. [103]):

$$W_{n\mathbf{k},n'\mathbf{k}-\mathbf{q}}(\mathrm{i}\omega) = \frac{1}{\Omega}\sum_{\mathbf{G},\mathbf{G}'} W_{\mathbf{q}}(\mathbf{G},\mathbf{G}',\mathrm{i}\omega)\langle\psi_{n'\mathbf{k}-\mathbf{q}}|e^{-i(\mathbf{q}+\mathbf{G})\mathbf{r}}|\psi_{n\mathbf{k}}\rangle\langle\psi_{n\mathbf{k}}|e^{i(\mathbf{q}+\mathbf{G}')\mathbf{r}'}|\psi_{n'\mathbf{k}-\mathbf{q}}\rangle. \qquad (292)$$

This is the fundamental distinction with the conventional GW implementation, where the screened two electron integrals are calculated along the real frequency axis [see Eq. (185)]. In the following, we will show the three possible schemes one by one all starting from $W_{n\mathbf{k},n'\mathbf{k}-\mathbf{q}}(\mathrm{i}\omega)$.

8.1.1. Direct method

Direct calculation of the self-energy $\Sigma_{n\mathbf{k},n'\mathbf{k}-\mathbf{q}}(\mathrm{i}\omega)$ in imaginary frequency from $W_{n\mathbf{k},n'\mathbf{k}-\mathbf{q}}(\mathrm{i}\omega)$ using the optimized frequencies $\{\mathrm{i}\omega_k\}_{k=1}^{N}$ is not doable, since only few optimized frequencies are used in evaluating the integral. Since screened two electron integrals are rather smooth along the imaginary frequency axis, one could perform a Padé interpolation of $W_{n\mathbf{k},n'\mathbf{k}-\mathbf{q}}(\mathrm{i}\omega)$ from the few optimized frequencies $\{\mathrm{i}\omega_k\}_{k=1}^{N}$ to a denser imaginary frequency grid $\{\mathrm{i}\omega'\}$. This step is relatively cheap.

To obtain $\Sigma_{n\mathbf{k},n'\mathbf{k}-\mathbf{q}}(\mathrm{i}\omega)$ at the optimized frequencies $\{\mathrm{i}\omega_k\}_{k=1}^{N}$, a Hilbert transformation of $W_{n\mathbf{k},n'\mathbf{k}-\mathbf{q}}(\mathrm{i}\omega')$ is then performed

$$\begin{aligned}\Sigma_{n\mathbf{k},n'\mathbf{k}-\mathbf{q}}(\mathrm{i}\omega) &= \frac{\mathrm{i}}{2\pi}\int_{-\infty}^{+\infty} d(\mathrm{i}\omega')\frac{W_{n\mathbf{k},n'\mathbf{k}-\mathbf{q}}(\mathrm{i}\omega')}{\mathrm{i}\omega + \mathrm{i}\omega' - \epsilon_{n'\mathbf{k}-\mathbf{q}}} \\ &= \frac{\mathrm{i}}{2\pi}\int_{0}^{+\infty} d\omega' W_{n\mathbf{k},n'\mathbf{k}-\mathbf{q}}(\mathrm{i}\omega')\left\{\frac{1}{\omega + \omega' + \mathrm{i}\epsilon_{n'\mathbf{k}-\mathbf{q}}} + \frac{1}{\omega - \omega' + \mathrm{i}\epsilon_{n'\mathbf{k}-\mathbf{q}}}\right\}.\end{aligned} \tag{293}$$

In deriving Eq. (293) we have used the fact that $W_{n\mathbf{k},n'\mathbf{k}-\mathbf{q}}(\mathrm{i}\omega')$ is an even function with respect to $\mathrm{i}\omega'$.

Then, the matrix elements of the self-energy $\Sigma_{n\mathbf{k},n\mathbf{k}}(\mathrm{i}\omega)$ are calculated by summation over $\mathbf{q}$ and n'

$$\Sigma_{n\mathbf{k},n\mathbf{k}}(\mathrm{i}\omega) = \sum_{\mathbf{q}}\sum_{n'}\Sigma_{n\mathbf{k},n'\mathbf{k}-\mathbf{q}}(\mathrm{i}\omega). \tag{294}$$

When $\Sigma_{n\mathbf{k},n\mathbf{k}}(\mathrm{i}\omega)$ is known, we perform an analytic continuation of $\Sigma_{n\mathbf{k},n\mathbf{k}}(\mathrm{i}\omega)$ to the real frequency grids by Thiele's reciprocal difference approach or least-squares method, as discussed in Appendix (C).

It should be noted that if one wants to obtain the QP energies only but not the spectral functions, the analytic continuation can be done only for three frequency points: $\epsilon_{n\mathbf{k}} - \delta$, $\epsilon_{n\mathbf{k}}$ and $\epsilon_{n\mathbf{k}} + \delta$ with $\epsilon_{n\mathbf{k}}$ being the DFT one-electron energies and δ a positive small energy, say 0.1 eV. Finally, the QP energy $\epsilon_{n\mathbf{k}}^{\mathrm{QP}}$ is evaluated by Eq. (172). Although this scheme works equally well with conventional G_0W_0 (not shown), the efficiency is still not much improved. The computationally most demanding step lies in the evaluation of the integral in Eq. (293) at dense grids.

8.1.2. Spectral method

Another alternative is to use the spectral representations of the self-energy and the relationship between the screened two electron integrals and the self-energy

$$\mathrm{Im}[\Sigma_{n\mathbf{k},n'\mathbf{k-q}}(E)] = \begin{cases} -\mathrm{Im}[W_{n\mathbf{k},n'\mathbf{k-q}}(\epsilon_{n'\mathbf{k-q}} - E)\theta(\epsilon_{n'\mathbf{k-q}} - E)\theta(\mu - \epsilon_{n'\mathbf{k-q}})] \\ \quad \text{if } E < \epsilon_{n'\mathbf{k-q}} < \mu,\ \epsilon_{n'\mathbf{k-q}} \in \text{occ} \\ \\ +\mathrm{Im}[W_{n\mathbf{k},n'\mathbf{k-q}}(E - \epsilon_{n'\mathbf{k-q}})\theta(E - \epsilon_{n'\mathbf{k-q}})\theta(\epsilon_{n'\mathbf{k-q}} - \mu)] \\ \quad \text{if } E > \epsilon_{n'\mathbf{k-q}} > \mu,\ \epsilon_{n'\mathbf{k-q}} \in \text{unocc} \end{cases} \tag{295}$$

which is derived in Appendix (F). Here, μ is the Fermi energy and θ is the Heaviside step function.

Specifically, after the screened two electron integrals $W_{n\mathbf{k},n'\mathbf{k-q}}(\mathrm{i}\omega)$ have been calculated by Eq. (292), we perform the analytic continuation of $W_{n\mathbf{k},n'\mathbf{k-q}}(\mathrm{i}\omega)$ to a dense real frequency grid, yielding $W_{n\mathbf{k},n'\mathbf{k-q}}(\omega')$. Afterwards, the self-energy along the real frequency axis $\Sigma_{n\mathbf{k},n'\mathbf{k-q}}(\omega)$ is calculated by the spectral transformation

$$\Sigma_{n\mathbf{k},n'\mathbf{k-q}}(\omega) = -\frac{1}{\pi}\int_0^{+\infty} d\omega'\ \mathrm{Im}[W_{n\mathbf{k},n'\mathbf{k-q}}(\omega')]\left\{\frac{\theta(\mu - \epsilon_{n'\mathbf{k-q}})}{\omega + \omega' - \epsilon_{n'\mathbf{k-q}} - \mathrm{i}\eta} + \frac{\theta(\epsilon_{n'\mathbf{k-q}} - \mu]}{\omega - \omega' - \epsilon_{n'\mathbf{k-q}} + \mathrm{i}\eta}\right\}. \tag{296}$$

Here, the relationship in Eq. (295) was used. Finally, the matrix elements of the self-energy $\Sigma_{n\mathbf{k},n\mathbf{k}}(\omega)$ are calculated by summation over $\mathbf{q}$ and n'

$$\Sigma_{n\mathbf{k},n\mathbf{k}}(\omega) = \sum_{\mathbf{q}}\sum_{n'}\Sigma_{n\mathbf{k},n'\mathbf{k-q}}(\omega). \tag{297}$$

Again, if one wants to obtain the QP energies only but not the spectral functions, the evaluation of $\Sigma_{n\mathbf{k},n'\mathbf{k-q}}(\omega)$ can be performed only for three frequency points: $\epsilon_{n\mathbf{k}} - \delta$, $\epsilon_{n\mathbf{k}}$ and $\epsilon_{n\mathbf{k}} + \delta$ and the QP energy $\epsilon_{n\mathbf{k}}^{\mathrm{QP}}$ is evaluated by Eq. (172). This scheme also works equally well with conventional G_0W_0 (not shown), but performing the integral in Eq. (296) at denser real frequency grid points is as expensive as the first scheme.

8.1.3. Using discrete Fourier transformations

As mentioned before, the first step is always the same: calculation of the screened two electron integrals $W_{n\mathbf{k},n'\mathbf{k-q}}(\mathrm{i}\omega)$ at the optimized frequencies $\{\mathrm{i}\omega_k\}_{k=1}^{N}$. Then, we Fourier transform

$W_{n\mathbf{k},n'\mathbf{k-q}}(\mathrm{i}\omega)$ to the imaginary time domain by an inverse cosine transformation

$$W_{n\mathbf{k},n'\mathbf{k-q}}(\mathrm{i}\tau_j) = \sum_{k=1}^{N} \xi_{jk} \cos(\tau_j \omega_k) W_{n\mathbf{k},n'\mathbf{k-q}}(\mathrm{i}\omega_k), \tag{298}$$

where $\{\mathrm{i}\tau_j\}_{j=1}^{N}$ are optimized imaginary time grids and ξ_{jk} are the transformation matrix [see Eq. (210) and Appendix (B)], which are both precalculated and stored.

After $W_{n\mathbf{k},n'\mathbf{k-q}}(\mathrm{i}\tau)$ is known, the occupied (unoccupied) self-energy $\underline{\Sigma}$ ($\overline{\Sigma}$) are calculated in the imaginary time domain

$$\begin{aligned} \underline{\Sigma}_{n\mathbf{k},n'\mathbf{k-q}}(-\mathrm{i}\tau) &= -\underline{G}_{n\mathbf{k},n'\mathbf{k-q}}(-\mathrm{i}\tau) W_{n\mathbf{k},n'\mathbf{k-q}}(\mathrm{i}\tau) & (299)\\ \overline{\Sigma}_{n\mathbf{k},n'\mathbf{k-q}}(\mathrm{i}\tau) &= -\overline{G}_{n\mathbf{k},n'\mathbf{k-q}}(\mathrm{i}\tau) W_{n\mathbf{k},n'\mathbf{k-q}}(\mathrm{i}\tau), & (300) \end{aligned}$$

where the occupied and unoccupied Green's functions, respectively, are given by

$$\begin{aligned} \underline{G}_{n\mathbf{k},n'\mathbf{k-q}}(\mathrm{i}\tau) &= \mathbf{e}^{-(\epsilon_{n'\mathbf{k-q}}-\mu)\tau} \quad (\epsilon_{n'\mathbf{k-q}} \in \mathrm{occ},\ \tau < 0) & (301)\\ \overline{G}_{n\mathbf{k},n'\mathbf{k-q}}(\mathrm{i}\tau) &= -\mathbf{e}^{-(\epsilon_{n'\mathbf{k-q}}-\mu)\tau} \quad (\epsilon_{n'\mathbf{k-q}} \in \mathrm{unocc},\ \tau > 0). & (302) \end{aligned}$$

Here, μ is the Fermi energy.

Afterwards, we Fourier transform the self-energy back to the imaginary frequency domain by cosine and sine transformations

$$\begin{aligned} \Sigma_{n\mathbf{k},n'\mathbf{k-q}}(\mathrm{i}\omega_k) = &\sum_{j=1}^{N} \gamma_{kj} \cos(\omega_k \tau_j) \frac{[\overline{\Sigma}_{n\mathbf{k},n'\mathbf{k-q}}(\mathrm{i}\tau) + \underline{\Sigma}_{n\mathbf{k},n'\mathbf{k-q}}(-\mathrm{i}\tau)]}{2} \\ &+\mathrm{i} \sum_{j=1}^{N} \lambda_{kj} \sin(\omega_k \tau_j) \frac{[\overline{\Sigma}_{n\mathbf{k},n'\mathbf{k-q}}(\mathrm{i}\tau) - \underline{\Sigma}_{n\mathbf{k},n'\mathbf{k-q}}(-\mathrm{i}\tau)]}{2}. \end{aligned} \tag{303}$$

After $\Sigma_{n\mathbf{k},n'\mathbf{k-q}}(\mathrm{i}\omega)$ has been obtained, we follow a similar procedure as in the first scheme: the matrix elements of the self-energy $\Sigma_{n\mathbf{k},n\mathbf{k}}(\mathrm{i}\omega)$ are first calculated by summation over $\mathbf{q}$ and n' by Eq. (294), and then the analytic continuation of $\Sigma_{n\mathbf{k},n\mathbf{k}}(\mathrm{i}\omega)$ to the real frequency grids is performed. As soon as the self-energy along the real frequency axis $\Sigma_{n\mathbf{k},n\mathbf{k}}(\omega)$ has been obtained, the QP energy $\epsilon_{n\mathbf{k}}^{\mathrm{QP}}$ is evaluated by Eq. (172).

It turns out that this scheme performs very well, with rather high efficiencies. This is achieved by employing the efficient discrete Fourier transformations, so that the computationally expensive evaluation of the integral at denser grids is avoided. Therefore, we finally adopt this scheme and in the following we will show how well this scheme performs by comparing to low-scaling G_0W_0r implementation and conventional G_0W_0 implementation.

Table 8: Calculated QP shifts for the valence band maximum (VBM) (first upper panel) and conduction band minimum (CBM) (middle panel) of ZnO with zinc-blend structure as a function of the number of bands using different implementations. G_0W_0 denotes the conventional implementation, while $G_0W_0(\mathrm{i}\omega)$ indicates G_0W_0 operating in imaginary frequency with optimized imaginary grids. G_0W_0r represents the low-scaling implementation. Also, the basis-set-corrected values and band gap are given. For both $G_0W_0(\mathrm{i}\omega)$ and G_0W_0r, 16 imaginary frequency grid points are used, while for G_0W_0 120 real frequencies are used. The predicted PBE band gap is about 0.68 eV. Note that SOC is not included.

	1000/bands	G_0W_0	$G_0W_0(\mathrm{i}\omega)$	G_0W_0r
VBM	0.807	-1.27	-1.27	-1.26
	0.581	-1.34	-1.33	-1.32
	0.403	-1.39	-1.38	-1.37
	corrected	-1.51	-1.48	-1.48
CBM	0.807	-0.06	-0.06	-0.06
	0.581	-0.08	-0.07	-0.07
	0.403	-0.10	-0.08	-0.07
	corrected	-0.12	-0.09	-0.09
band gap		2.37	2.38	2.38

8.2. Applications of $G_0W_0(\mathrm{i}\omega)$

Table 8 shows the calculated QP shifts and band gap of ZnO from $G_0W_0(\mathrm{i}\omega)$. For comparison, the results obtained from G_0W_0 and G_0W_0r with almost similar setups except for the frequency grids are also given. For this compound with localize d orbitals, it was suggested that thousands of orbitals are required for accurate QP energies predictions for ZnO [114]. Therefore, we correct for finite basis set errors following the procedure discussed in Ref. [115]. Specifically, the plane-wave cutoff $E_{\mathrm{cut}}^{\mathrm{pw}}$ was chosen to be the maximum of all elements in the considered material. To determine basis-set converged GW values, the plane-wave cutoff was systematically increased by a factor of 1.25 and 1.587, corresponding to an increase of the number of plane waves by a factor 1.4 and 2, respectively. The plane-wave cutoff for the response function was

Table 9: Calculated QP shifts for the valence band maximum (VBM) (first upper panel) and conduction band minimum (CBM) (middle panel) of CdTe with zinc-blend structure (lattice constant 6.481 Å [257]) as a function of the number of bands using different implementations with or without SOC. Also, the basis-set-corrected values and band gap are given. The notations and technical setups used here are the same as in Table 8. Note that for the cases with SOC, more bands are employed. The predicted PBE band gap without (with) SOC is about 0.544 (0.268) eV.

	without SOC				with SOC		
	1000/bands	G_0W_0	$G_0W_0(\mathrm{i}\omega)$	G_0W_0r	1000/bands	G_0W_0	$G_0W_0(\mathrm{i}\omega)$
VBM	1.667	-0.543	-0.553	-0.547	0.807	-0.533	-0.534
	1.136	-0.557	-0.565	-0.561	0.568	-0.541	-0.543
	0.781	-0.576	-0.586	-0.580	0.391	-0.563	-0.564
	corrected	-0.603	-0.610	-0.605	corrected	-0.587	-0.588
CBM	1.667	0.181	0.210	0.214	0.807	0.162	0.186
	1.136	0.183	0.203	0.208	0.568	0.165	0.182
	0.781	0.152	0.186	0.191	0.391	0.134	0.164
	corrected	0.136	0.169	0.174	corrected	0.116	0.147
band gap		1.374	1.410	1.411		1.011	1.043

always chosen to be $2/3E_{\mathrm{cut}}^{\mathrm{pw}}$, such that it increases simultaneously as $E_{\mathrm{cut}}^{\mathrm{pw}}$ increases. The results were then extrapolated to the infinite-basis-set limit, assuming that the QP energies converge like $(E_{\mathrm{cut}}^{\mathrm{pw}})^{3/2} = 1/N_{\mathrm{pw}}$ [115]. Since the convergence behavior of the QP energies with respect to the basis-set size depends weakly on the k-point set used [115], to reduce the overall computational cost, we used $4\times4\times4$ k-points to obtain a basis-set size correction as the difference of the basis-set converged values and data obtained with a smaller basis-set size. We then added this correction to the results calculated with a smaller basis-set size using $8\times8\times8$ k-points by [115]

$$E_\infty(8\times8\times8) = E_{\mathrm{red}}(8\times8\times8) + [E_\infty(4\times4\times4) - E_{\mathrm{red}}(4\times4\times4)]. \tag{304}$$

Here, E_∞ is the QP energy extrapolated to the infinite basis set, and E_{red} is the QP energy calculated with a reduced basis set (in this case we have used 560 bands). It can be seen from Table 8 that excellent agreement is achieved for each case with different number of bands among the three implementations, validating the implementation of $G_0W_0(\mathrm{i}\omega)$ in imaginary frequency. Compared with the PBE one-electron energies, the VBM and the CBM shift down by 1.48 eV and 0.09 eV, respectively. The basis-set-corrected band gap for ZnO is estimated to be 2.38 eV, which is 0.26 eV larger than non-corrected value predicted by M. Shishkin and G. Kresse [86] on the same single-shot G_0W_0 level.

Following the same procedures as discussed for ZnO, we have done similar calculations on CdTe, where the SOC is non-negligible due to the heavy atomic mass. Since the SOC is not implemented yet in the low-scaling G_0W_0r implementation, here, we show the comparison between $G_0W_0(\mathrm{i}\omega)$ and G_0W_0 only, as shown in Table 9. In contrast to ZnO, the basis-set corrections for CdTe are much smaller. Again, the agreement among the three implementations is very good not only for the cases without SOC, but also for the cases with SOC. The deviation between $G_0W_0(\mathrm{i}\omega)$ and G_0W_0 is about 0.036 eV, which is still acceptable within the GW approximation (<0.05 eV). As expected, inclusion of SOC reduces the band gap by 0.367 eV, in good agreement with the estimation obtained from Ref. [92].

To summarize, we have successfully extended the imaginary frequency scheme in G_0W_0r to the conventional G_0W_0 implementation and applied it to the semiconductors ZnO with localized d orbitals and CdTe where SOC is important. It turns out that this modified version $G_0W_0(\mathrm{i}\omega)$ works pretty well for both cases with and without SOC. Of course, $G_0W_0(\mathrm{i}\omega)$ also has the potential for applications to moderately large systems with SOC. However, since there are not data available for direct comparison (G_0W_0 is restricted to small systems, while G_0W_0r does not support SOC yet), we have not performed such test calculations.

9. Partially self-consistent GW: GW_0r

Up to now, we have only discussed the single-shot G_0W_0, but not touched any self-consistency on neither G nor W. However, the single-shot G_0W_0 violates the conservation laws such as particle number conservation, since the GW approximation is only conserving when the Dyson equation for the Green's function is solved fully self-consistently. Another unsatisfactory aspect of non-self-consistent schemes, such as G_0W_0, is that the values of the observables depend on the starting point (PBE or HSE) and the way they are calculated [258]. Therefore, it is essential to take into account the self-consistency. Although different self-consistencies have been implemented, for instance, eVGW_0 [iterating the eigenvalues (QP energies) only in G] [86], QPGW (quasiparticle self-consistent GW) [85], eV$GW^{\text{TC-TC}}$ (quasiparticle self-consistent GW with vertex corrections only in W) [89], eV$GW\Gamma$ (quasiparticle self-consistent GW with vertex corrections in self-energy) [92], and full self-consistent GW (scGW) [90, 130, 135], there are few self-consistent GW implementations available for solids. Therefore, in this section, we will concentrate on how the self-consistency could be achieved using our low-scaling G_0W_0 implementation by determining the full interacting Green's functions G from the Dyson equation shown in Eq. (134). It should be noted that here we consider iterating G only, while W is still fixed on the level of DFT, since full self-consistent GW (scGW) without inclusion of vertex corrections leads to some problems such as overestimation of band gaps and band width as discussed in Section (5.7). Since the term of GW_0 has been used in literatures, where only eigenvalues (QP energies) are updated, to avoid any confusion we denote our partially self-consistent GW as GW_0r. It has been shown that GW_0r conserves the particle number, which has been tested on the electron gas [259]. In addition, since GW_0r avoids the self-consistent calculation of the screened interaction W, the computational cost is considerably reduced compared to the scGW. However, it should also be noted that for time-dependent and inhomogeneous systems W_0 is not invariant under spatial and time translations and thus GW_0r will not be momentum or energy conserving [258].

9.1. Computational scheme of GW_0r

Figure 19 shows the computational scheme for the low-scaling self-consistent GW_0r implementation. For the sake of brevity, in the following we suppress the spin index and k-point index.

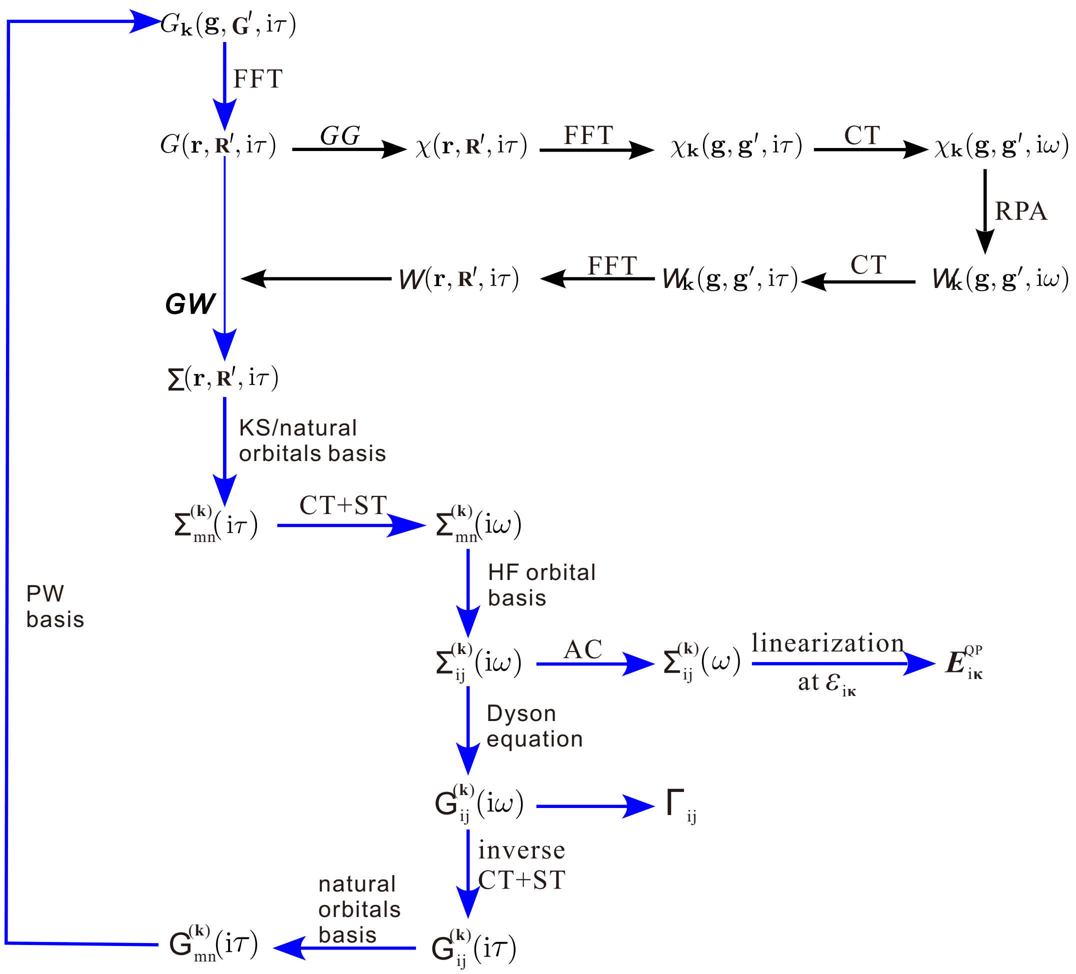

Figure 19: Schematic work flow for the low-scaling self-consistent GW_0r implementation showing the necessary steps to iterate the Green's function G and obtain the QP energies. The notations used here are the same as in Fig. 12. Note that screened interaction W is not updated and fixed on the DFT level (black arrows) and only G is updated (shown in blue arrows). To avoid confusion, indices (m, n) are always used to represent the KS orbital basis in the first iteration and the natural orbitals basis beyond the first iteration, whereas indices (i, j) are always used to denote HF orbitals basis, unless otherwise explicitly stated. Γ is the density matrix, see the main text.

We start with the full G_0W_0r action matrix in the KS orbital basis

$$H_{mn}(\mathrm{i}\omega) = H^{\mathrm{HF}}_{mn} + \tilde{\Sigma}_{mn}(\mathrm{i}\omega), \tag{305}$$

where H^{HF}_{mn} is the Hartree-Fock Hamiltonian matrix, which are frequency-independent and $\tilde{\Sigma}_{mn}(\mathrm{i}\omega)$ is the correlated GW self-energy. Then, we transform $H_{mn}(\mathrm{i}\omega)$ from the KS orbital basis to the HF orbital basis, because it is more convenient to apply the Dyson-equation [Eq. (134)] in the HF orbital basis. To this aim, we first diagonalize the HF Hamiltonian matrix

$$\sum_{mn}[U]^{\dagger}_{im}H^{\mathrm{HF}}_{mn}U_{nj} = \epsilon^{\mathrm{HF}}_{i}\delta_{ij}. \tag{306}$$

Here, U is a unitary transformation matrix and $\epsilon^{\mathrm{HF}}_{i}$ are the HF eigenvalues. Obviously, HF Hamiltonian matrix is diagonal in its own basis. Then, we rotate the correlated self-energy from the KS orbital basis to the HF orbital basis using

$$\tilde{\Sigma}_{ij}(\mathrm{i}\omega) = \sum_{mn}[U]^{\dagger}_{im}\tilde{\Sigma}_{mn}(\mathrm{i}\omega)U_{nj}. \tag{307}$$

In addition, the KS orbitals are rotated to HF orbitals as well by means of

$$|\psi^{\mathrm{HF}}_{j\mathbf{k}}\rangle = \sum_{m} U_{mj}|\psi^{\mathrm{KS}}_{m\mathbf{k}}\rangle. \tag{308}$$

It should be noted that in order to avoid any confusion, indices (m, n) are always used to represent the KS orbital basis in the first iteration and the natural orbital basis beyond the first iteration, whereas indices (i, j) are always used to denote HF orbital basis, unless otherwise explicitly stated. After the GW Hamiltonian in the HF orbital basis has been obtained, the QP energies can be calculated in a similar way as we have used in the G_0W_0r implementation, where the KS orbital basis are used instead.

The interacting Green's functions $G(\mathrm{i}\omega)$ can be calculated in the HF orbital basis by solving the Dyson-equation [Eq. (134)]

$$[G^{-1}(\mathrm{i}\omega)]_{ij} = \mathrm{i}\omega\delta_{ij} - (H^{\mathrm{HF}}_{ij} + \tilde{\Sigma}_{ij}(\mathrm{i}\omega) - \mu\delta_{ij}), \tag{309}$$

where μ is the Fermi energy. The density matrix is then calculated by

$$\Gamma_{ij} = G_{ij}(\mathrm{i}\tau = 0^{-}) = \frac{1}{2\pi}\int_{-\infty}^{+\infty} d\omega G_{ij}(\mathrm{i}\omega). \tag{310}$$

However, this integral involving $G(\mathrm{i}\omega)$ diverges and cannot be evaluate with the chosen optimized frequency grids. To address this issue, the interacting Green's function $G(\mathrm{i}\omega)$ is split into two parts:

$$G_{ij}(\mathrm{i}\omega) = G^{\mathrm{HF}}_{ij}(\mathrm{i}\omega) + G^{c}_{ij}(\mathrm{i}\omega). \tag{311}$$

Here, $G^{\mathrm{HF}}(\mathrm{i}\omega)$ is the non-interacting HF Green's function

$$[G^{\mathrm{HF}}]^{-1}_{ij} = \mathrm{i}\omega\delta_{ij} - (H^{\mathrm{HF}}_{ij} - \mu\delta_{ij}), \tag{312}$$

which is known to be diagonal in its own basis

$$[G^{\mathrm{HF}}]^{-1}_{ij} = [\mathrm{i}\omega - (\epsilon^{\mathrm{HF}}_i - \mu)]\delta_{ij}. \tag{313}$$

The correlated part of the Green's function $G^c(\mathrm{i}\omega)$ can thus be expressed as

$$G^c_{ij}(\mathrm{i}\omega) = G_{ij}(\mathrm{i}\omega) - G^{\mathrm{HF}}_{ij}(\mathrm{i}\omega), \tag{314}$$

which decays like $1/\omega^2$ and can be accurately dealt with using the implemented numerical frequency grids and quadrature rules. Due to the split of the interacting Green's function in Eq. (311), the density matrix thus includes two contributions:

$$\Gamma_{ij} = \Gamma^{\mathrm{HF}}_{ij} + \Gamma^c_{ij}, \tag{315}$$

where the calculation of the HF density matrix Γ^{HF} is straightforward

$$\Gamma^{\mathrm{HF}}_{ij} = \Theta(\mu - \epsilon^{\mathrm{HF}}_i)\delta_{ij}. \tag{316}$$

Here, Θ is the Heaviside step function. The correlated contribution Γ^c can be calculated using the quadrature rules

$$\begin{aligned}\Gamma^c_{ij} =& \frac{1}{2\pi}\int_{-\infty}^{+\infty} d\omega G^c_{ij}(\mathrm{i}\omega) = \frac{1}{2\pi}\int_0^{+\infty} d\omega \left\{G^c_{ij}(\mathrm{i}\omega) + G^c_{ij}(-\mathrm{i}\omega)\right\} \\ =& \frac{1}{\pi}\int_0^{+\infty} d\omega \mathrm{Re}[G^c_{ij}(\mathrm{i}\omega)] = \frac{1}{2\pi}\sum_k^N \gamma_k \mathrm{Re}[G^c_{ij}(\mathrm{i}\omega_k)].\end{aligned} \tag{317}$$

where $\{\mathrm{i}\omega_k\}_{k=1}^N$ are optimized imaginary frequency grids and $\{\gamma_k\}_{k=1}^N$ are the corresponding weights [see Appendix (B.1)]. In deriving Eq. (317), $G^c(-\mathrm{i}\omega) = [G^c(\mathrm{i}\omega)]^*$ has been used.

After the total density matrix Γ has been obtained, the particle number is then calculated by

$$N_{\mathrm{particle}} = \mathbf{Tr}[\Gamma]. \tag{318}$$

It should be noted that the trace involves the summation over a band index n, a spin index and a k-point index, though we drop the spin index and k-point index at the beginning. The particle number will be an indicator how well the particle number is converged and conserved after a few iterations. In addition, we diagonalize the density matrix Γ such that

$$\sum_{ij}[B]^{\dagger}_{mi}\Gamma_{ij}B_{jn} = f_m\delta_{mn}, \tag{319}$$

where f are one-electron occupancies and B is a unitary transformation matrix that will be used to transform the HF orbital basis to the natural orbital basis.

To close the self-consistency loop shown in Fig. 19, a Fourier transformation (FT) of G from the imaginary frequency domain to the imaginary time domain is needed. Again, direct FT of the interacting Green's function G is ill-defined. Therefore, we follow a similar strategy as used in addressing the problem of the density matrix. The interacting Green's function in imaginary time $G(\mathrm{i}\tau)$ involves two parts: the HF contribution $G^{\mathrm{HF}}(\mathrm{i}\tau)$ and the correlated contribution $G^{c}(\mathrm{i}\tau)$. In addition, analogous to the definitions in Eqs. (202) and (203), for each Green's function, here we also define occupied ($\underline{G}$) and unoccupied ($\overline{G}$) Green's functions, which are evaluated for negative and positive imaginary time, respectively.

$$\underline{G}(\mathrm{i}\tau) = \underline{G}^{\mathrm{HF}}(\mathrm{i}\tau) + \underline{G}^{c}(\mathrm{i}\tau) \quad (\tau < 0), \tag{320}$$

$$\overline{G}(\mathrm{i}\tau) = \overline{G}^{\mathrm{HF}}(\mathrm{i}\tau) + \overline{G}^{c}(\mathrm{i}\tau) \quad (\tau > 0). \tag{321}$$

The evaluation of $G^{\mathrm{HF}}(\mathrm{i}\tau)$ is straightforward, since it is diagonal

$$\underline{G}^{\mathrm{HF}}_{ij}(\mathrm{i}\tau) = \quad \delta_{ij}\mathbf{e}^{-(\epsilon_i^{\mathrm{HF}}-\mu)\tau} \quad (i \in \text{occ}, \quad \tau < 0), \tag{322}$$

$$\overline{G}^{\mathrm{HF}}_{ab}(\mathrm{i}\tau) = \; -\delta_{ab}\mathbf{e}^{-(\epsilon_a^{\mathrm{HF}}-\mu)\tau} \quad (a \in \text{unocc}, \quad \tau > 0). \tag{323}$$

The correlated contribution $G^{c}(\mathrm{i}\tau)$ can be efficiently calculated by an inverse discrete cosine and sine transformations, as shown in Appendix (B.2)

$$\begin{aligned}\underline{G}_{ij}(\mathrm{i}\tau) = &\sum_{n=1}^{N} \xi_{mn} \cos(\tau_m\omega_n) \frac{[G_{ij}(\mathrm{i}\omega_n) + G^{*}_{ij}(\mathrm{i}\omega_n)]}{2} \\ &+\mathrm{i}\sum_{n=1}^{N} \zeta_{mn}\sin(\tau_m\omega_n) \frac{[G_{ij}(\mathrm{i}\omega_n) - G^{*}_{ij}(\mathrm{i}\omega_n)]}{2}, \quad (\tau < 0)\end{aligned} \tag{324}$$

$$\begin{aligned}\overline{G}_{ij}(\mathrm{i}\tau) = &\sum_{n=1}^{N} \xi_{mn} \cos(\tau_m\omega_n) \frac{[G_{ij}(\mathrm{i}\omega_n) + G^{*}_{ij}(\mathrm{i}\omega_n)]}{2} \\ &-\mathrm{i}\sum_{n=1}^{N} \zeta_{mn}\sin(\tau_m\omega_n) \frac{[G_{ij}(\mathrm{i}\omega_n) - G^{*}_{ij}(\mathrm{i}\omega_n)]}{2}, \quad (\tau > 0)\end{aligned} \tag{325}$$

where G^{*} means the complex conjugation of G.

After the matrixes $\underline{G}_{ij}(\mathrm{i}\tau)$ and $\overline{G}_{ij}(\mathrm{i}\tau)$ in the HF orbital basis have been obtained, they are then rotated to the natural orbitals with the unitary matrix B obtained in Eq. (319).

$$\underline{G}_{mn}(\mathrm{i}\tau) \;=\; \sum_{ij}[B]^{\dagger}_{mi}\underline{G}_{ij}(\mathrm{i}\tau)B_{jn}, \tag{326}$$

$$\overline{G}_{mn}(\mathrm{i}\tau) \;=\; \sum_{ij}[B]^{\dagger}_{mi}\overline{G}_{ij}(\mathrm{i}\tau)B_{jn}. \tag{327}$$

Moreover, the orbitals are rotated into the natural orbitals as well

$$|\psi^{\mathrm{NA}}_{m\mathbf{k}}\rangle = \sum_{j} B_{jm}|\psi^{\mathrm{HF}}_{j\mathbf{k}}\rangle, \tag{328}$$

since it is more convenient to evaluate the Hartree-Fock contribution in the next step in the natural orbital basis. Afterwards, $\underline{G}_{mn}(\mathrm{i}\tau)$ and $\overline{G}_{mn}(\mathrm{i}\tau)$ are transformed from the natural orbital basis to the plane wave (PW) basis by means of

$$\begin{aligned}
\overline{G}^{(1)}_{\mathbf{k}}(\mathbf{g},\mathbf{G}',\mathrm{i}\tau) &= \sum_m\sum_n \langle\mathbf{g}|\tilde{\psi}^{\mathrm{NA}}_{m\mathbf{k}}\rangle\overline{G}_{mn}(\mathrm{i}\tau)\langle\tilde{\psi}^{\mathrm{NA}}_{n\mathbf{k}}|G'\rangle && (329)\\
\overline{G}^{(2)}_{\mathbf{k}}(\nu,\mathbf{G}',\mathrm{i}\tau) &= \sum_m\sum_n \langle\tilde{p}_\nu|\tilde{\psi}^{\mathrm{NA}}_{m\mathbf{k}}\rangle\overline{G}_{mn}(\mathrm{i}\tau)\langle\tilde{\psi}^{\mathrm{NA}}_{n\mathbf{k}}|G'\rangle && (330)\\
\overline{G}^{(3)}_{\mathbf{k}}(\mathbf{g},\alpha',\mathrm{i}\tau) &= \sum_m\sum_n \langle\mathbf{g}|\tilde{\psi}^{\mathrm{NA}}_{m\mathbf{k}}\rangle\overline{G}_{mn}(\mathrm{i}\tau)\langle\tilde{\psi}^{\mathrm{NA}}_{n\mathbf{k}}|\tilde{p}'_\alpha\rangle && (331)\\
\overline{G}^{(4)}_{\mathbf{k}}(\nu,\alpha',\mathrm{i}\tau) &= \sum_m\sum_n \langle\tilde{p}_\nu|\tilde{\psi}^{\mathrm{NA}}_{m\mathbf{k}}\rangle\overline{G}_{mn}(\mathrm{i}\tau)\langle\tilde{\psi}^{\mathrm{NA}}_{n\mathbf{k}}|\tilde{p}'_\alpha\rangle, \quad (\tau > 0) && (332)
\end{aligned}$$

and

$$\begin{aligned}
\underline{G}^{(1)}_{\mathbf{k}}(\mathbf{g},\mathbf{G}',\mathrm{i}\tau) &= \sum_m\sum_n \langle\mathbf{g}|\tilde{\psi}^{\mathrm{NA}}_{m\mathbf{k}}\rangle\underline{G}_{mn}(\mathrm{i}\tau)\langle\tilde{\psi}^{\mathrm{NA}}_{n\mathbf{k}}|G'\rangle && (333)\\
\underline{G}^{(2)}_{\mathbf{k}}(\nu,\mathbf{G}',\mathrm{i}\tau) &= \sum_m\sum_n \langle\tilde{p}_\nu|\tilde{\psi}^{\mathrm{NA}}_{m\mathbf{k}}\rangle\underline{G}_{mn}(\mathrm{i}\tau)\langle\tilde{\psi}^{\mathrm{NA}}_{n\mathbf{k}}|G'\rangle && (334)\\
\underline{G}^{(3)}_{\mathbf{k}}(\mathbf{g},\alpha',\mathrm{i}\tau) &= \sum_m\sum_n \langle\mathbf{g}|\tilde{\psi}^{\mathrm{NA}}_{m\mathbf{k}}\rangle\underline{G}_{mn}(\mathrm{i}\tau)\langle\tilde{\psi}^{\mathrm{NA}}_{n\mathbf{k}}|\tilde{p}'_\alpha\rangle && (335)\\
\underline{G}^{(4)}_{\mathbf{k}}(\nu,\alpha',\mathrm{i}\tau) &= \sum_m\sum_n \langle\tilde{p}_\nu|\tilde{\psi}^{\mathrm{NA}}_{m\mathbf{k}}\rangle\underline{G}_{mn}(\mathrm{i}\tau)\langle\tilde{\psi}^{\mathrm{NA}}_{n\mathbf{k}}|\tilde{p}'_\alpha\rangle, \quad (\tau < 0). && (336)
\end{aligned}$$

They will be used in the second iteration to calculate $\chi = \underline{G}\overline{G}$. Note that here $|\tilde{\psi}^{\mathrm{NA}}_{n\mathbf{k}}\rangle$ are pseudo natural orbitals in the PAW method. With Eqs. (329)–(336), the self-consistency loop (shown in blue arrows) in Fig. 19 has been closed. It should be noted that in the second iteration and beyond, the GW Hamiltonian in Eq. (305) is always first evaluated in the natural orbital basis and then transformed to the HF orbital basis, where the analytic continuation and linearization around DFT eigenvalues are performed to obtain the QP energies (see Fig. 19). In the next section, we will show results of the self-consistent GW_0r implementation and test how well it works.

9.2. Test of GW_0r on Si

We apply the partially self-consistent GW_0r method on the test material Si, for which a large amount of theoretical data from different flavors of the GW approximation and also experimental values are available. The obtained results are shown in Table 10. One can see that upon

Table 10: QP shifts (eV), corresponding renormalization factor Z, and band gap for selected bands at Γ and K points, as well as the particle number N_{particle} of Si predicted by GW_0r as a function of self-consistent iterations. Note that $8 \times 8 \times 8$ k points are used to sample the BZ and SOC is not included.

number of	$\Gamma_{25'}$		Γ_{15}		K_2		K_3		band gap	N_{particle}
iteration	QP	Z	QP	Z	QP	Z	QP	Z		
1	-0.460	0.759	0.186	0.755	-0.489	0.733	0.114	0.776	1.093	8.00874318
2	-0.502	0.804	0.635	0.800	-0.696	0.789	0.459	0.812	1.480	7.99174461
3	-0.486	0.801	0.699	0.804	-0.667	0.787	0.514	0.814	1.519	7.99871247
4	-0.492	0.801	0.712	0.804	-0.668	0.786	0.524	0.815	1.535	7.99981693
5	-0.495	0.801	0.715	0.804	-0.669	0.786	0.525	0.815	1.539	7.99999937
6	-0.496	0.801	0.715	0.804	-0.670	0.786	0.526	0.815	1.541	8.00000255

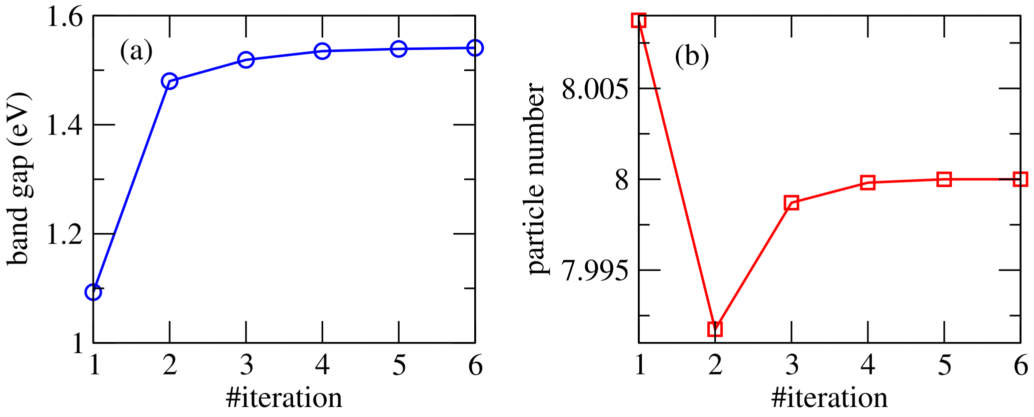

Figure 20: (a) band gap and (b) particle number as a function of iterations in GW_0r.

iterating of G the valence bands (see $\Gamma_{25'}$ and K_2) shift down, whereas the conduction bands shift up (see Γ_{15} and K_3), increasing the band gap. The convergence is achieved at the fifth iteration, as also evidenced by the band gap and particle number as a function of iterations in Fig. 20. The converged particle number is 8, confirming that the GW_0r method is a particle-conserving approximation.

In Table 11, we compile and compare the theoretical band gaps with the experimental value. As expected, PBE underestimates the band gap, while both single-shot G_0W_0r and one-electron energies updated GW_0 improve the band gap towards the experimental value. In contrast, partially self-consistent GW_0r gives rise to a much larger band gap of 1.54 eV. This is not unex-

Table 11: Band gap (eV) predicted by PBE and GW on different levels. The experimental value is also given for comparison. See the main text for the notations.

PBE	G_0W_0r@PBE	eVGW_0@PBE [86]	GW_0r	scGW [260]	eV$GW^{\text{TC-TC}}$ [89]	eV$GW\Gamma$ [92]	QPGW [89]	Exp. [261]
0.52	1.15	1.20	1.54	1.91	1.24	1.37	1.41	1.17

pected because the vertex corrections are not included. This is also true but even worse for the full self-consistent scGW [260](see Table 11). Indeed, the inclusion of vertex corrections either on W only $GW^{\text{TC-TC}}$ [89] or on the self-energy $GW\Gamma$ [92] remedies the problems in GW_0r and scGW. QPGW yields a slightly smaller band gap of 1.41 eV [89] compared to GW_0r, but still overestimates the band gap with respect to the experimental value. More tests of GW_0r on other materials are in progress.

10. Merging GW with DMFT

The interplay between localized electrons in open d- or f-shells and itinerant band states in strongly-correlated materials gives rise to rich physics, such as metal-to-insulator transition, high temperature superconductivity and spintronics. Thus, the first-principles description of strongly-correlated materials is currently one of the greatest challenges in condensed matter physics. One of the most successful approaches in this field is the dynamical mean field theory (DMFT) combined with density functional theory (DFT) in the local density approximation (LDA), i.e., LDA+DMFT [105,106], which treats local correlations in a small subset of orbitals exactly, while the reminder of the problem is treated using a static mean field manner.

For truly parameter-free *ab initio* calculations, however, two severe shortcomings persist: (i) a static Hubbard-like interaction U is used and usually considered to be an adjustable parameter in LDA+DMFT. Furthermore, the dynamical screening effects are often ignored. (ii) the so-called double counting problem, e.g., it is difficult to determine the electronic correlations already accounted for on the LDA level. In addition, the non-local effects are only partially considered in the exchange-correlation functional in the LDA, which results in an underestimation of the band gap for a variety of semiconductors and insulators. To overcome those drawbacks of LDA+DMFT, Biermann *et. al.* suggested to replace the LDA with the GW approximation [262]. Since the GW approximation takes into account the many-body effects in the electron-electron interaction by screening the bare exchange interaction with the inverse dynamical dielectric function, the inclusion of non-local GW self-energy results in a better description of the band gap compared to experiments than typical density functionals. Moreover, the GW self-energy is diagrammatically formulated in the same many-body framework as DMFT. Hence, the GW approximation not only enables an elegant combination with DMFT, i.e., GW+DMFT [263], but also overcomes the fundamental double counting problems occurring in LDA+DMFT. For GW+DMFT, one actually knows which Feynman diagrams (local ones) are counted twice [264], and hence one can trivially remove those diagrams. Furthermore, the dynamical partially screened Coulomb interaction can be calculated by the constrained random phase approximation (cRPA) in a similar framework as GW [264]. Therefore, merging GW with DMFT could make possible the predictions of strongly-correlated materials entirely *ab initio*.

In this section, we will first start by a layout of a feasible scheme to accomplish the combination of GW with DMFT. Then, we will put particular emphasis on how dynamical partially screened interactions are calculated within the cRPA based on the low-scaling scheme that is used in the G_0W_0r implementation. Finally, we will deal with the double counting problem. Note that this GW+DMFT work is still ongoing and for the DMFT part, we are collaborating with Karsten Held's group at the Technical University of Vienna.

10.1. Computational scheme of GW+DMFT

The essence of a self-consistent GW+DMFT algorithm is to calculate the fermionic and bosonic propagators G and W self-consistently. Specifically, it can be formulated as follows [265–267]:

(i) Calculate the lattice fermionic and bosonic propagators G^{GW} and W^{GW} in the GW approximation

$$[G^{GW}]^{-1} = [G_0]^{-1} - \Sigma^{GW} \tag{337}$$

$$[W^{GW}]^{-1} = [V]^{-1} - \chi^{GW} \tag{338}$$

using $\Sigma^{GW} = -G_0W_0$ and $\chi^{GW} = G_0G_0$ in the first iteration, where G_0 and W_0 are the Hartree non-interacting Green's function calculated from KS orbitals and the screened interaction, respectively.

(ii) Calculate the non-interacting impurity fermionic and bosonic propagators $\mathcal{G}$ and U by undressing respective local contributions of the self-energies Σ^{GW}_{loc} and χ^{GW}_{loc}

$$[\mathcal{G}]^{-1} = [G^{GW}]^{-1} + \Sigma^{GW}_{\text{loc}} \tag{339}$$

$$[U]^{-1} = [W^{GW}]^{-1} + \chi^{GW}_{\text{loc}}. \tag{340}$$

(iii) Compute the interacting impurity propagators G^{imp} and χ^{imp} with the extended DMFT (eDMFT) action [268]

$$\begin{aligned} S_{\text{eff}}[c^*, c] = &-\int_0^\beta d\tau \int_0^\beta d\tau' \sum_{ij} c_i^*(\tau)\mathcal{G}_{ij}^{-1}(\tau - \tau')c_j(\tau') \\ &+ \frac{1}{2}\int_0^\beta d\tau \int_0^\beta d\tau' \sum_{ijkl} c_i^*(\tau)c_j(\tau)U_{kl}^{ij}(\tau - \tau')c_k^*(\tau')c_l(\tau'), \end{aligned} \tag{341}$$

where c^* and c are Grassmann variables and $\beta = \frac{1}{k_BT}$ with k_B and T being the Boltzmann constant and temperature, respectively.

(iv) Compute the fermionic and bosonic impurity self-energies

$$\Sigma^{\text{imp}} = [\mathcal{G}]^{-1} - [G^{\text{imp}}]^{-1} \tag{342}$$

$$\chi^{\text{imp}} = [U]^{-1} - [W^{\text{imp}}]^{-1}. \tag{343}$$

(v) Calculate the GW+DMFT self-energies

$$\Sigma^{GW\text{+DMFT}} = \Sigma^{GW} - \Sigma^{GW}_{\text{loc}} + \Sigma^{\text{imp}} \tag{344}$$

$$\chi^{GW\text{+DMFT}} = \chi^{GW} - \chi^{GW}_{\text{loc}} + \chi^{\text{imp}}. \tag{345}$$

(vi) The calculation stops when the convergence

$$|\Sigma^{GW\text{+DMFT}} - \Sigma^{GW}| < \text{eps} \tag{346}$$

$$|\chi^{GW\text{+DMFT}} - \chi^{GW}| < \text{eps} \tag{347}$$

is achieved. Here, eps is the derived computational precision. Otherwise, one should go back to step (i), solve Eqs. (337) and (338) with new updated self-energies in Eqs. (344) and (345), and repeat steps (i)–(v) until self-consistency in step (vi) is fulfilled.

Although the above GW+eDMFT algorithm is elegant, it is technically challenging and only applies to a single-band Hubbard model [265,266]. Furthermore, the challenges originate from the difficulties to take into account a frequency-dependent $U(\text{i}\omega)$ in an impurity solver. It is also hampered by the challenges of solving the bosonic self-consistency loop for multiorbital systems. Very recently, L. Boehnke and co-anthers [120] seem to overcome those challenges and apply their implementation to the realistic material SrVO_3. However, self-consistent determination of bosonic propagators and self-energies are rather expensive. Thus far, we restrict ourselves to the single-shot GW+DMFT only, but using the frequency-dependent $U(\text{i}\omega)$ and double counting entirely from *ab initio* calculations.

Figure 21 shows our illustrative scheme of the single-shot GW+DMFT. The GW self-energy $\Sigma^{GW}(\mathbf{k}, \text{i}\omega)$ are taken from our low-scaling G_0W_0r calculations. The dynamical partially screened interaction $U(\text{i}\omega)$ are calculated by the cRPA, as will be discussed in Section (10.2). The lattice interacting Green's function is obtained by

$$G^{GW}(\mathbf{k}, \text{i}\omega) = \left[\text{i}\omega - (T + V_{ext} + V_H + \Sigma^{GW}(\mathbf{k}, \text{i}\omega) - \mu)\right]^{-1}, \tag{348}$$

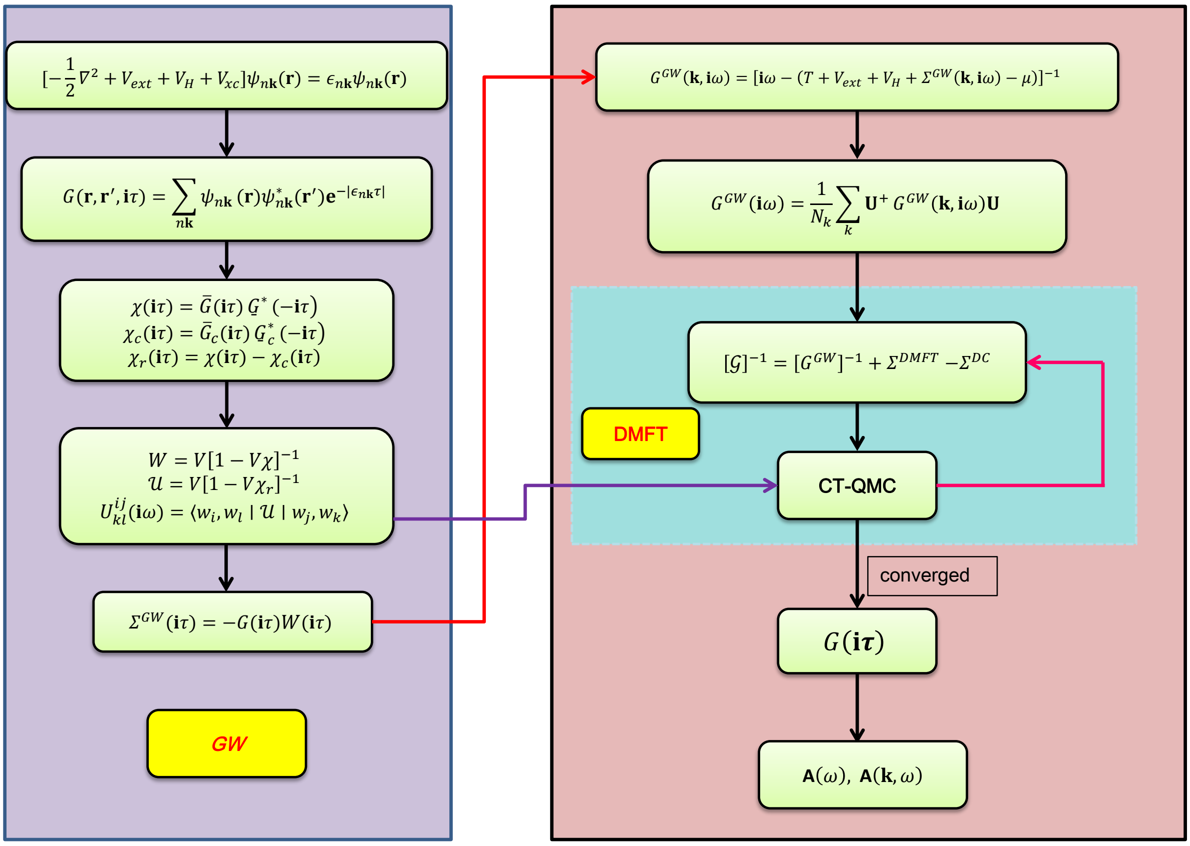

Figure 21: Schematic illustration on the scheme of the single-shot GW+DMFT. The left panel shows how to calculate the lattice self-energy $\Sigma^{GW}(\mathbf{k}, \mathrm{i}\omega)$ within the GW approximation and dynamical partially screened interaction $U^{IJ}_{KL}(\mathrm{i}\omega)$ by cRPA. $\Sigma^{GW}(\mathbf{k}, \mathrm{i}\omega)$ is then used to construct the lattice interacting Green's function $G^{GW}(\mathbf{k}, \mathrm{i}\omega)$ by the Dyson equation, which is further used to calculate the local lattice interacting Green's function $G^{GW}(\mathrm{i}\omega)$. The obtained $U^{IJ}_{KL}(\mathrm{i}\omega)$ and impurity non-interacting (bath) Green's function $[\mathcal{G}]^{-1}$ constructed by taking account of the GW self-energy, DMFT self-energy Σ^{DMFT}, and double counting Σ^{DC} are then taken as inputs for the Anderson impurity problem, which is solved by continuous-time quantum Monte Carlo (CT-QMC). After self-consistency is achieved within the DMFT loop, the converged new impurity interacting Green's function $G(\mathrm{i}\tau)$ is obtained. By an analytic continuation of $G(\mathrm{i}\tau)$ to the real frequency axis, the integrated spectral function $A(\omega)$ and momentum-resolved spectral function $A(\mathbf{k}, \omega)$ are finally calculated. See the main text for more information.

where μ is the Fermi energy. Then, the local lattice interacting Green's function is calculated in the Wannier basis

$$G^{GW}_{\mathrm{mn}}(\mathrm{i}\omega) = \frac{1}{N_{\mathbf{k}}}\sum_{\mathbf{k}}\sum_{\mathrm{ij}}[\mathbf{U}^{(\mathbf{k})}]^{\dagger}_{\mathrm{mi}}G^{GW}_{\mathrm{ij}}(\mathbf{k},\mathrm{i}\omega)[\mathbf{U}^{(\mathbf{k})}]_{\mathrm{jn}}, \tag{349}$$

where $[\mathbf{U}^{(\mathbf{k})}]$ are transformation matrices from the Bloch space to the Wannier space obtained from the wannier90 code [42, 43]. The impurity non-interacting (bath) Green's function are constructed by taking into account the GW self-energy, DMFT self-energy Σ^{DMFT}, and double counting correction Σ^{DC}

$$[\mathcal{G}]^{-1}(\mathrm{i}\omega) = [G^{GW}]^{-1}(\mathrm{i}\omega) + \Sigma^{\mathrm{DMFT}}(\mathrm{i}\omega) - \Sigma^{\mathrm{DC}}(\mathrm{i}\omega). \tag{350}$$

Calculation of the double counting correction Σ^{DC} will be discussed in Section (10.3). With $[\mathcal{G}]^{-1}(\mathrm{i}\omega)$ and $U(\mathrm{i}\omega)$ in hands, the impurity problem is solved by the continuous-time quantum Monte Carlo (CT-QMC) [269]. After convergence is achieved within the DMFT loop, the converged new impurity interacting Green's function $G(\mathrm{i}\tau)$ is obtained. In order to obtain the integrated spectral function $A(\omega) = \frac{-1}{\pi}\mathrm{Im}[G(\omega)]$ along the real frequency axis, a maximum entropy method (MEM) as shown in Appendix (C.1) is used to perform the analytic continuation to the real axis. To calculate the momentum-resolved spectral function $A(\mathbf{k},\omega)$ from the integrated spectral function $A(\omega)$ obtained from MEM, three steps are involved [270]: (i) First, the real part of the local interacting Green's function $G(\omega)$ is calculated by the Kramers-Kronig relation

$$\mathrm{Re}[G(\omega)] = \int_{-\infty}^{\infty}\frac{A(\omega')}{\omega-\omega'+\mathrm{i}\eta}d\omega', \tag{351}$$

where η is a positive infinitesimal. (ii) Then, the complex local self-energy $\Sigma(\omega)$ is fitted such that it reproduces the local Green's function

$$G(\omega) = \sum_{\mathbf{k}}[\omega - (T + V_{ext} + V_H + \Sigma(\omega) - \mu)]^{-1}. \tag{352}$$

(iii) Finally, $A(\mathbf{k},\omega)$ is obtained by

$$A(\mathbf{k},\omega) = -\frac{1}{\pi}\mathrm{Im}\left\{[\omega - (T + V_{ext} + V_H + \Sigma(\omega) - \mu)]^{-1}\right\}. \tag{353}$$

One point that should be mentioned here is that the GW self-energy obtained from our low-scaling G_0W_0r implementations are evaluated at a discrete optimized imaginary frequency grid, whereas DMFT works on the Matsubara frequencies. Fortunately, the GW self-energy is so

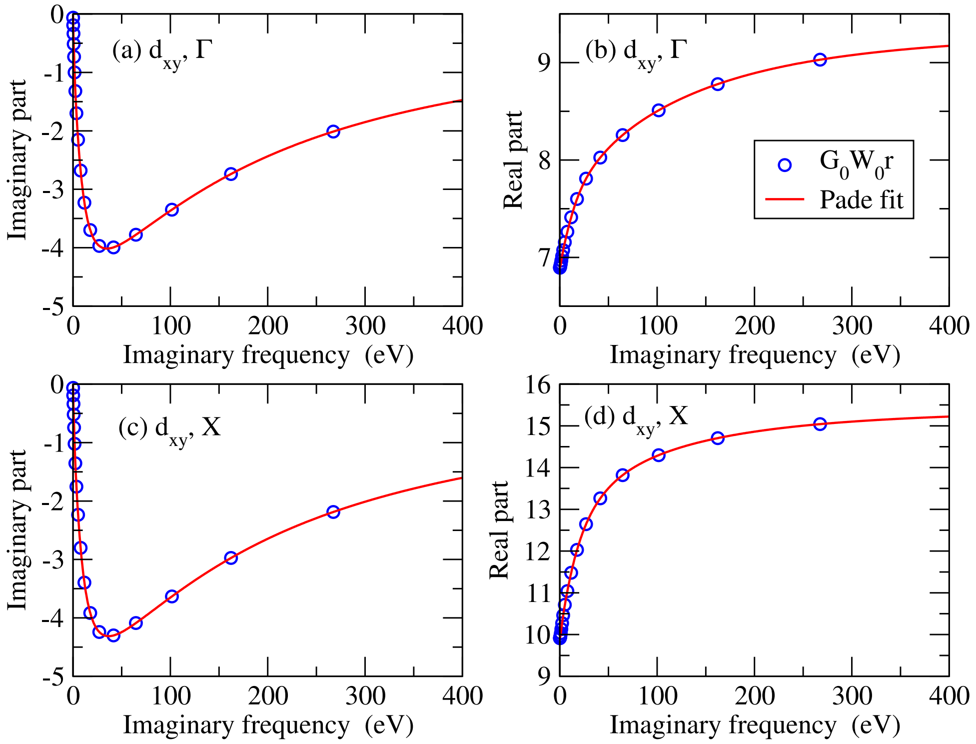

Figure 22: Calculated imaginary and real parts of the GW Hamiltonian $\langle m|T + V_{\text{ext}} + V_H + \Sigma(\mathbf{k}, i\omega)|m\rangle$ of SrVO$_3$ in the t_{2g} Wannier basis (blue circles) along with the Padé fit (red solid lines) as a function of imaginary frequencies at Γ [(a) and (b)] and X [(c) and (d)] points. Here, only elements corresponding to d_{xy} orbital are shown. 20 optimized imaginary frequency grid points and 8 × 8 × 8 k points are used in the calculations. The data for frequencies beyond 400 eV are truncated and not shown in the plot.

smooth along the imaginary frequency axis that it is possible to do the Padé interpolation from the discrete optimized frequency grid to the Matsubara frequencies. As an example, in Fig. 22 we show the GW Hamiltonian of SrVO$_3$ in the t_{2g} Wannier basis as a function of imaginary frequencies together with the Padé fit. Apparently, the fitting is perfect, which makes it possible to pass down the GW self-energy to the DMFT.

Another technical issue to merge GW with DMFT is that a very denser k points grid such as 20 × 20 × 20 points are required to obtain spectral functions with a good quality in DMFT, whereas such dense k-point grids are not doable in the GW calculations. To address this issue, a Wannier interpolation [43] is performed. Taking the GW action matrix for instance, the GW

action matrix is first transformed to the Wannier basis

$$\bar{H}_{\mathrm{mn}}(\mathbf{k},\mathrm{i}\omega)=\sum_{\mathrm{ij}}[\mathbf{U}^{(\mathbf{k})}]^{\dagger}_{\mathrm{mi}}H_{\mathrm{ij}}(\mathbf{k},\mathrm{i}\omega)[\mathbf{U}^{(\mathbf{k})}]_{\mathrm{jn}}. \tag{354}$$

Next, we Fourier transform $H_{\mathrm{mn}}(\mathbf{k},\mathrm{i}\omega)$ into a set of $N_{\mathbf{k}}$ Bravais lattice vectors $\mathbf{R}$ within a Wigner-Seitz supercell centered around $\mathbf{R}=0$

$$\bar{H}_{\mathrm{mn}}(\mathbf{R},\mathrm{i}\omega)=\frac{1}{N_{\mathbf{k}}}\sum_{\mathbf{k}}\mathbf{e}^{-\mathrm{i}\mathbf{k}\mathbf{R}}\bar{H}_{\mathrm{mn}}(\mathbf{k},\mathrm{i}\omega). \tag{355}$$

Finally, we Fourier transform back to an arbitrary $\mathbf{k}'$ point

$$\bar{H}_{\mathrm{mn}}(\mathbf{k}',\mathrm{i}\omega)=\sum_{\mathbf{R}}\mathbf{e}^{\mathrm{i}\mathbf{k}'\mathbf{R}}\bar{H}_{\mathrm{mn}}(\mathbf{R},\mathrm{i}\omega). \tag{356}$$

10.2. Dynamical partially screened interaction $U(\mathrm{i}\omega)$ by cRPA

In this section, we will first formulate how to calculate the dynamical partially screened interaction $U(\mathrm{i}\omega)$ by cRPA based on our low-scaling GW scheme, and then show how it works on the prototypical material SrVO$_3$. To distinguish with the conventional cRPA implementation, which directly works on the real frequency axis, we denote our present implementation as cRPAr.

10.2.1. Formulations of $U(\mathrm{i}\omega)$

We start by the total polarizability in the real space and imaginary time domain, which has been derived in Appendix (G).

$$\chi(\mathbf{r},\mathbf{R}',\mathrm{i}\tau)=-\sum_{\mathbf{k},\mathbf{q}}^{\mathrm{BZ}}\sum_{a}^{\mathrm{unocc}}\psi_{a\mathbf{k}+\mathbf{q}}(\mathbf{r})\psi^{*}_{a\mathbf{k}+\mathbf{q}}(\mathbf{R}')\mathbf{e}^{-\epsilon_{a\mathbf{k}+\mathbf{q}}\tau}\sum_{i}^{\mathrm{occ}}\psi_{i\mathbf{k}}(\mathbf{R}')\psi^{*}_{i\mathbf{k}}(\mathbf{r})\mathbf{e}^{\epsilon_{i\mathbf{k}}\tau}, \tag{357}$$

where $\psi_{n\mathbf{k}}(\mathbf{r})$ is a Bloch state. Similarly, the correlated polarizability is expressed by

$$\chi^{c}(\mathbf{r},\mathbf{R}',\mathrm{i}\tau)=-\sum_{\mathbf{k},\mathbf{q}}^{\mathrm{BZ}}\sum_{a\in C}^{\mathrm{unocc}}\bar{\psi}_{a\mathbf{k}+\mathbf{q}}(\mathbf{r})\bar{\psi}^{*}_{a\mathbf{k}+\mathbf{q}}(\mathbf{R}')\mathbf{e}^{-\epsilon_{a\mathbf{k}+\mathbf{q}}\tau}\sum_{i\in C}^{\mathrm{occ}}\bar{\psi}_{i\mathbf{k}}(\mathbf{R}')\bar{\psi}^{*}_{i\mathbf{k}}(\mathbf{r})\mathbf{e}^{\epsilon_{i\mathbf{k}}\tau}, \tag{358}$$

where $\bar{\psi}_{n\mathbf{k}}(\mathbf{r})$ is the correlated Bloch state, which is restricted within the correlated subspace C and defined by Eq. (607). For the sake of brevity, from now on we suppress the indices of the Bloch wave vector. Using the definitions of occupied and unoccupied Green's functions in Eqs. (202) and (203), the total polarizability in Eq. (357) can be simply expressed as

$$\chi(\mathbf{r},\mathbf{R}',\mathrm{i}\tau)=\overline{G}(\mathbf{r},\mathbf{R}',\mathrm{i}\tau)\underline{G}^{*}(\mathbf{r},\mathbf{R}',-\mathrm{i}\tau). \tag{359}$$

If we define correlated occupied and unoccupied Green's functions

$$\begin{aligned}
\underline{G^c}(\mathbf{r},\mathbf{R}',\mathrm{i}\tau) &= \quad \sum_{i\in C}^{\mathrm{occ}} \bar{\psi}_i(\mathbf{r})\bar{\psi}_i^*(\mathbf{R}')\mathbf{e}^{-\epsilon_i\tau} \quad (\tau<0), &(360)\\
\overline{G^c}(\mathbf{r},\mathbf{R}',\mathrm{i}\tau) &= \; -\sum_{a\in C}^{\mathrm{unocc}} \bar{\psi}_a(\mathbf{r})\bar{\psi}_a^*(\mathbf{R}')\mathbf{e}^{-\epsilon_a\tau} \quad (\tau>0), &(361)
\end{aligned}$$

the correlated polarizability in Eq. (358) can be simplified as well

$$\chi^c(\mathbf{r},\mathbf{R}',\mathrm{i}\tau) = \overline{G^c}(\mathbf{r},\mathbf{R}',\mathrm{i}\tau)\underline{G^{c*}}(\mathbf{r},\mathbf{R}',-\mathrm{i}\tau). \tag{362}$$

Within the PAW framework, the total polarizability $\chi(\mathbf{r},\mathbf{R}',i\tau)$ has been derived and given by Eq. (239). Similarly, the correlated polarizability $\chi^c(\mathbf{r},\mathbf{R}',i\tau)$ can be calculated as

$$\begin{aligned}
\chi^c(\mathbf{r},\mathbf{R}',\mathrm{i}\tau) =&\overline{G^c}^{(1)}(\mathbf{r},\mathbf{R}',i\tau)\underline{G^{c*}}^{(1)}(\mathbf{r},\mathbf{R}',-i\tau)\\
&+\sum_{\mu\nu} Q_{\mu\nu}(\mathbf{r})\overline{G^c}^{(2)}(\nu,\mathbf{R}',i\tau)\underline{G^{c*}}^{(2)}(\mu,\mathbf{R}',-i\tau)\\
&+\sum_{\alpha\beta} Q_{\alpha\beta}(\mathbf{R}')\overline{G^c}^{(3)}(\mathbf{r},\alpha,i\tau)\underline{G^{c*}}^{(3)}(\mathbf{r},\beta,-i\tau)\\
&+\sum_{\mu\nu\alpha\beta} Q_{\mu\nu}(\mathbf{r})Q_{\alpha\beta}(\mathbf{R}')\overline{G^c}^{(4)}(\nu,\alpha,i\tau)\underline{G^{c*}}^{(4)}(\mu,\beta,-i\tau).
\end{aligned} \tag{363}$$

Here, the auxiliary correlated unoccupied and occupied Green's functions are defined analogously to Eqs. (228–235), but keeping the summation restricted within the correlated space, i.e., $a \in C$ and $i \in C$, and using the counterparts of one-electron correlated Bloch state within the PAW method.

After the total $\chi(\mathbf{r},\mathbf{R}',\mathrm{i}\tau)$ and correlated $\chi^c(\mathbf{r},\mathbf{R}',\mathrm{i}\tau)$ polarizabilities have been obtained in the real space and imaginary time domain, they are immediately Fourier transformed to the reciprocal space and imaginary frequency domain $\chi_{\mathbf{q}}(\mathbf{g},\mathbf{g}',\mathrm{i}\omega)$ and $\chi^c_{\mathbf{q}}(\mathbf{g},\mathbf{g}',\mathrm{i}\omega)$ by Eqs. (248)–(250). The polarizability excluding the screening channels within the correlated space C is simply calculated as

$$\chi^r_{\mathbf{q}}(\mathbf{g},\mathbf{g}',\mathrm{i}\omega) = \chi_{\mathbf{q}}(\mathbf{g},\mathbf{g}',\mathrm{i}\omega) - \chi^c_{\mathbf{q}}(\mathbf{g},\mathbf{g}',\mathrm{i}\omega). \tag{364}$$

The partially screened Coulomb interaction kernel $\mathcal{U}$ is then calculated by the RPA

$$\mathcal{U}_{\mathbf{q}}(\mathbf{g},\mathbf{g}',\mathrm{i}\omega) = v_{\mathbf{q}}(\mathbf{g},\mathbf{g}')[\delta_{\mathbf{g},\mathbf{g}'} - v_{\mathbf{q}}(\mathbf{g},\mathbf{g}')\chi^r_{\mathbf{q}}(\mathbf{g},\mathbf{g}',\mathrm{i}\omega)]^{-1}, \tag{365}$$

where the bare Coulomb interaction is given by $v_{\mathbf{q}}(\mathbf{g},\mathbf{g}') = \frac{4\pi e^2}{|\mathbf{q}+\mathbf{g}||\mathbf{q}+\mathbf{g}'|}$. Note that matrix multiplication and inversion are implicitly used in Eq. (365). Finally, the on-site dynamical partially screened Coulomb interaction in terms of Wannier functions is obtained by

$$\begin{aligned}
U^{\mathrm{IJ}}_{\mathrm{KL}}(\mathrm{i}\omega) =& \langle \mathrm{IL}|\mathcal{U}(\mathbf{r},\mathbf{r}',\mathrm{i}\omega)|\mathrm{JK}\rangle \\
=& \int d\mathbf{r} \int d\mathbf{r}' w^*_{I\mathbf{R}}(\mathbf{r}) w^*_{L\mathbf{R}}(\mathbf{r}') \mathcal{U}(\mathbf{r},\mathbf{r}',\mathrm{i}\omega) w_{J\mathbf{R}}(\mathbf{r}) w_{K\mathbf{R}}(\mathbf{r}') \\
=& \frac{1}{N_{\mathbf{q}}N_{\mathbf{k}}} \sum_{\mathbf{q},\mathbf{k}} \sum_{\mathbf{g}\mathbf{g}'} \mathcal{U}_{\mathbf{q}}(\mathbf{g},\mathbf{g}',\mathrm{i}\omega) \langle \Psi_{I\mathbf{k}}|\mathbf{e}^{-\mathrm{i}(\mathbf{q}+\mathbf{g})\mathbf{r}}|\Psi_{J\mathbf{k}+\mathbf{q}}\rangle \langle \Psi_{K\mathbf{k}+\mathbf{q}}|\mathbf{e}^{\mathrm{i}(\mathbf{q}+\mathbf{g}')\mathbf{r}'}|\Psi_{L\mathbf{k}}\rangle,
\end{aligned} \tag{366}$$

where the mixed state $|\Psi_{\alpha\mathbf{k}}\rangle$ is defined as

$$|\Psi_{I\mathbf{k}}\rangle = \sum_{n} \mathbf{U}^{(\mathbf{k})}_{nI} |\psi_{n\mathbf{k}}\rangle, \tag{367}$$

with $\mathbf{U}$ being a transformation matrix from the Bloch space to the Wannier space. Note that in deriving Eq. (366), we have used

1. Wannier function centered at the site of $\mathbf{R}$ is given by

$$\begin{aligned}
|w_{I\mathbf{R}}\rangle =& \frac{1}{N_{\mathbf{k}}} \sum_{n\mathbf{k}} \mathbf{e}^{-\mathrm{i}\mathbf{k}\mathbf{R}} U^{(\mathbf{k})}_{nI} |\psi_{n\mathbf{k}}\rangle \\
=& \frac{1}{N_{\mathbf{k}}} \sum_{\mathbf{k}} \mathbf{e}^{-\mathrm{i}\mathbf{k}\mathbf{R}} |\Psi_{I\mathbf{k}}\rangle.
\end{aligned} \tag{368}$$

2. Spatial Fourier transformation is given by

$$\mathcal{U}(\mathbf{r},\mathbf{r}',\mathrm{i}\omega) = \frac{1}{N_{\mathbf{q}}} \sum_{\mathbf{q}} \sum_{\mathbf{g}\mathbf{g}'} \mathbf{e}^{+\mathrm{i}(\mathbf{q}+\mathbf{g})\mathbf{r}} \mathcal{U}_{\mathbf{q}}(\mathbf{g},\mathbf{g}',\mathrm{i}\omega) \mathbf{e}^{-\mathrm{i}(\mathbf{q}+\mathbf{g}')\mathbf{r}'}. \tag{369}$$

3. Translation-invariant symmetry.

The so-called Hubbard-Kanamori parameters (the intra-orbital U, inter-orbital U', and Hund's coupling J) are finally calculated by

$$U(\mathrm{i}\omega) = \frac{1}{N} \sum_{\alpha}^{N} U^{\alpha\alpha}_{\alpha\alpha}(\mathrm{i}\omega) \tag{370}$$

$$U'(\mathrm{i}\omega) = \frac{1}{N(N-1)} \sum_{\alpha}^{N} \sum_{\beta\neq\alpha}^{N} U^{\alpha\alpha}_{\beta\beta}(\mathrm{i}\omega) \tag{371}$$

$$J(\mathrm{i}\omega) = \frac{1}{N(N-1)} \sum_{\alpha}^{N} \sum_{\beta\neq\alpha}^{N} U^{\alpha\beta}_{\alpha\beta}(\mathrm{i}\omega). \tag{372}$$

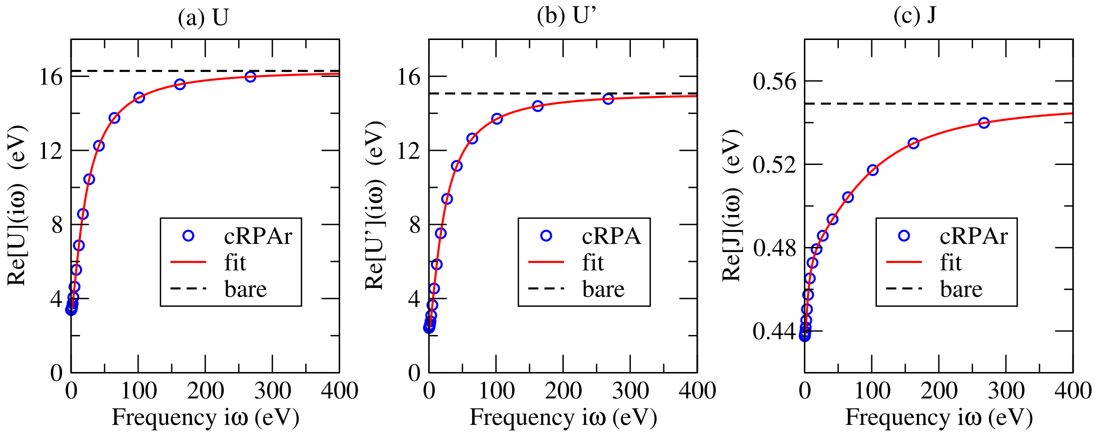

Figure 23: On-site dynamical partially screened (a) intra-orbital interactions $U(\mathrm{i}\omega)$, (b) inter-orbital $U'(\mathrm{i}\omega)$, and (c) Hund's coupling $J(\mathrm{i}\omega)$ of $SrVO_3$ using V-t_{2g}-like maximally localized Wannier functions as local orbitals as a function of the imaginary frequency (shown in blue circle). The corresponding bare (unscreened) counterparts are also shown in black dashed lines. The red solid lines are obtained from a Padé fit. 20 optimized imaginary frequency grid points and $8 \times 8 \times 8$ k points are used in the calculations. The data for frequencies beyond 400 eV are truncated and not shown in the plot. It should ne noted that U, U', and J are all real-valued quantities along the imaginary frequency axis.

10.2.2. Application on $SrVO_3$

Figure 23 shows our calculated on-site dynamical partially screened intra-orbital interactions $U(\mathrm{i}\omega)$, inter-orbital $U'(\mathrm{i}\omega)$, and Hund's coupling $J(\mathrm{i}\omega)$ of $SrVO_3$ using V-t_{2g}-like maximally localized Wannier functions as local basis sets. First of all, we want to point out that U, U', and J are all real-valued quantities along the imaginary frequency axis, because the polarizability in the reciprocal space and imaginary time domain is real-valued [see Eq. (611)] and the maximally localized Wannier functions can be chosen to be real-valued as well [42, 43]. Second, it is found that U, U' and J are rather smooth with respect to the imaginary frequency, so that it is possible to expand them from our optimized frequencies to Matsubara frequencies by the Padé interpolations (see the red solid lines in Fig. 23). This makes it possible to transfer them to a dynamical impurity solver, which has been recently implemented in the w2dynamics code by the group of Karsten Held at the Technical University of Vienna. Third, at the static limit ($\omega = 0$), U, U', and J are, respectively, calculated to be 3.38, 2.42, and 0.44 eV, agreeing

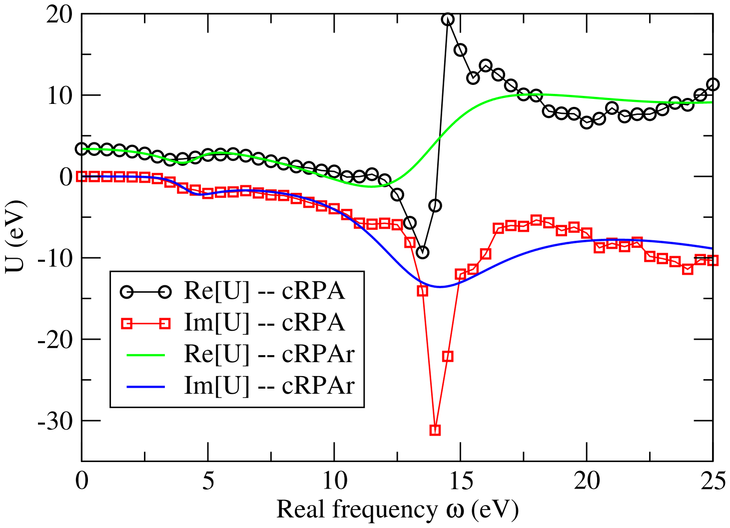

Figure 24: Real (Re) and imaginary (Im) parts of on-site dynamical partially screened intra-orbital interactions $U(\omega)$ of $SrVO_3$ using V-t_{2g}-like maximally localized Wannier functions as local orbitals as a function of the real frequency. The results from two different implementations are shown. cRPA represents the conventional cRPA implementation, which directly works on the real frequency axis, whereas cRPAr denotes our present implementation, which works instead on the optimized imaginary frequency grid points. Note that the Padé fit is used to analytically continue $U(\mathrm{i}\omega)$ obtained from cRPAr to the real frequency axis.

perfectly with the ones (3.38, 2.42 and 0.44 eV) directly obtained from the conventional implementation working on the real frequency axis. Moreover, they are in nice agreement with the published values [47, 271]. At the high-frequency limit ($\omega \to \infty$), it is expected that U, U', and J would approach their unscreened (bare) counterparts (16.29, 15.07, and 0.55 eV), since the electron density cannot follow such fast external perturbations, and the polarizability would be vanishing at the high-frequency limit. Indeed, this is observed in our calculations (see the asymptotic behaviors of U, U', and J compared to the black dashed lines in Fig. 23).

In order to further validate our implementation, we analytically continue the intra-orbital interaction $U(\mathrm{i}\omega)$ from the imaginary frequency axis to the real frequency axis. For comparison, we also calculate $U(\omega)$ directly from the conventional cRPA implementation. The calculated results are shown in Fig. 24. First, we want to mention that the calculated frequency-dependent $U(\omega)$ from the conventional implementation is in very good agreement with the work of F.

Aryasetiawa *et. al.* [47]. In the energy region 12–15 eV, the imaginary part of U is dominated by a single plasmon excitation induced mainly by free-electron-like O-2p states [47]. Second, it can be seen that, overall, good agreement is achieved between the conventional and present implementations, in particular in the low-frequency region. However, the strong plasmon excitation observed in the conventional implementation is smeared out by the analytic continuation in cRPAr. Finally, we would like to emphasize that considering that the dynamical impurity solver of DMFT is implemented on the imaginary Matsubara frequencies, our cRPAr thus provides an natural way to calculate the required imaginary-frequency-dependent $U(\mathrm{i}\omega)$, $U'(\mathrm{i}\omega)$, and $J(\mathrm{i}\omega)$ quantities, This is in contrast to the conventional implementation, where Hilbert transformations have to be performed to obtain those quantities along the imaginary frequency axis. Hence, we believe that our cRPAr implementation facilitates the merging of GW with DMFT..

It should be noted that apart from $SrVO_3$, we have also tested our cRPAr implementation on different kinds of systems such as $SrTiO_3$ and La_2CuO_4 with different models [t_{2g}/t_{2g}, d/d, and d/dp models (the notations here are taken from Ref. [271])]. It is found that our cRPAr implementation works pretty well for all the cases and the calculated results are in good agreement with the ones obtained from the conventional cRPA calculations (not shown).

10.3. Doubling counting in GW+DMFT

After the issue of $U(\mathrm{i}\omega)$ has been discussed, we are faced with the remaining challenge of the double counting (DC) correction. Since GW is formulated in the same many-body framework as DMFT, the DC correction for merging GW with DMFT is thus quite well-defined. Specifically, DMFT is a purely local theory and precisely includes all the local diagrams. In this sense, one should subtract all the local diagrams in the GW, i.e., the local Hartree and local GW diagrams, to avoid double counting [272, 273]. In the following, it will be shown that how one can deal with the DC correction and test how well it works in practice on a Be molecule and $SrVO_3$. For the sake of simplicity, so far the formulations of DC correction on the level of G_0W_0r+DMFT only are shown.

10.3.1. Formulations of the DC correction

Actually, the DC correction can be formulated in a similar way as is used in the low-scaling G_0W_0r implementation in Section (6). The main difference is that the DC correction here is

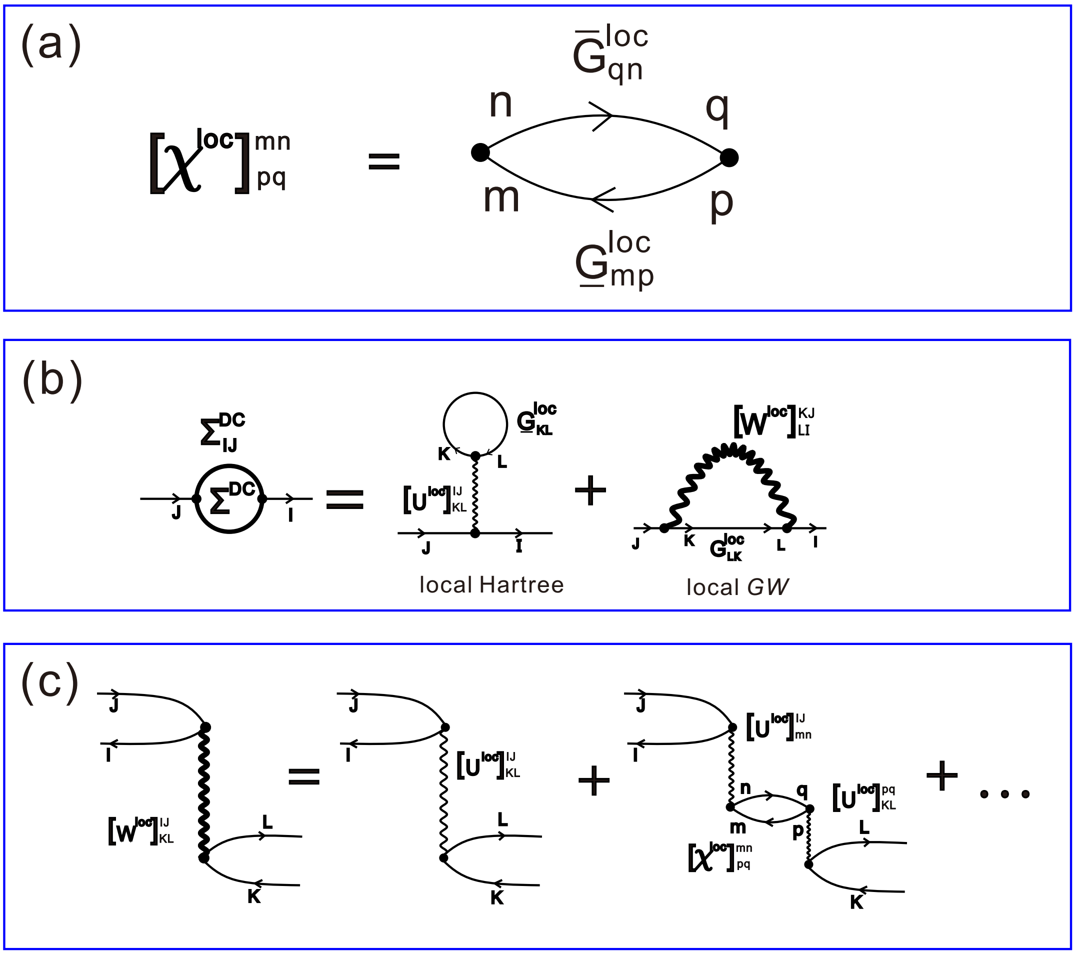

Figure 25: Feynman diagram representation of (a) the local independent-particle polarizability $\chi^{\rm loc}$, (b) the DC correction $\Sigma^{\rm DC}$ in GW+DMFT, which includes the local Hartree and local GW diagrams, and (c) the local screened interaction $\tilde{W}^{\rm loc}$, which is calculated by the RPA with $\chi^{\rm loc}$ and local partially screened interaction $U^{\rm loc}(\mathrm{i}\omega)$ calculated from the cRPA.

evaluated in the local orbital basis. To derive the DC correction , four steps are involved.

(1) The first step is to define and calculate the local Green's functions in the local orbital basis. Here, we employ the Wannier functions as the local orbitals. Analogous to the definitions of Green's functions in Eqs. (202) and (203), occupied and unoccupied local Green's functions are defined in the Wannier basis as

$$\underline{G}^{\rm loc}_{\rm mn}(-\mathrm{i}\tau) = \frac{1}{N_{\mathbf{k}}}\sum_{\mathbf{k}}\sum_{\rm ij}[\mathbf{U}^{(\mathbf{k})}]^{\dagger}_{\rm mi}\underline{G}_{\rm ij}(\mathbf{k},-\mathrm{i}\tau)[\mathbf{U}^{(\mathbf{k})}]_{\rm jn}, \qquad (373)$$

$$\overline{G}^{\mathrm{loc}}_{\mathrm{mn}}(\mathrm{i}\tau) = \frac{1}{N_{\mathbf{k}}}\sum_{\mathbf{k}}\sum_{\mathrm{ij}}[\mathbf{U}^{(\mathbf{k})}]^{\dagger}_{\mathrm{mi}}\overline{G}_{\mathrm{ij}}(\mathbf{k},\mathrm{i}\tau)[\mathbf{U}^{(\mathbf{k})}]_{\mathrm{jn}}, \tag{374}$$

which are defined in the negative and positive imaginary time, respectively. Here, $N_{\mathbf{k}}$ is the number of k points. Again, $[\mathbf{U}^{(\mathbf{k})}]$ are transformation matrices from the Bloch function basis to the Wannier basis obtained from the wannier90 code [42, 43]. The occupied and unoccupied Green's functions in the Bloch space are given by

$$\underline{G}_{\mathrm{ij}}(\mathbf{k},-\mathrm{i}\tau) = \langle\psi_{\mathrm{ik}}|\underline{G}(-\mathrm{i}\tau)|\psi_{\mathrm{jk}}\rangle = \delta_{\mathrm{i,j}}\mathbf{e}^{-|(\epsilon_{\mathrm{ik}}-\mu)\tau|}, \quad \mathrm{i} \in \mathrm{occ} \tag{375}$$

$$\overline{G}_{\mathrm{ab}}(\mathbf{k},\mathrm{i}\tau) = -\langle\psi_{\mathrm{ak}}|\overline{G}(\mathrm{i}\tau)|\psi_{\mathrm{bk}}\rangle = -\delta_{\mathrm{a,b}}\mathbf{e}^{-|(\epsilon_{\mathrm{ak}}-\mu)\tau|}, \quad \mathrm{a} \in \mathrm{unocc.} \tag{376}$$

Here, μ is the Fermi energy and $|\psi_{\mathrm{ik}}\rangle$ and $|\psi_{\mathrm{ak}}\rangle$ denote the occupied and unoccupied Bloch functions, respectively.

(2) Next, the local polarizability χ^{loc} is calculated via contraction over occupied and unoccupied local Green's functions in imaginary time, as shown in Fig. 25.

$$\begin{aligned}[\chi^{\mathrm{loc}}]^{\mathrm{mn}}_{\mathrm{pq}}(\mathrm{i}\tau) =& \langle w_{\mathrm{m}}w_{\mathrm{q}}|2\underline{G}^{\mathrm{loc}}(-\mathrm{i}\tau)\overline{G}^{\mathrm{loc}}(\mathrm{i}\tau)|w_{\mathrm{n}}w_{\mathrm{p}}\rangle \\ =& 2\underline{G}^{\mathrm{loc}}_{\mathrm{mp}}(-\mathrm{i}\tau)\overline{G}^{\mathrm{loc}}_{\mathrm{qn}}(\mathrm{i}\tau).\end{aligned} \tag{377}$$

Here, $|w_{\mathrm{n}}\rangle$ represents the Wannier function Note that a factor of "2" is due to the existence of fermionic loop in the pair-bubble diagram of the polarizability and applies for spin-degenerate system. Furthermore, a polarizability is treated as a four-index quantity here, instead of using a real-space representation. Then, a cosine transformation is used to transform the local polarizability from the imaginary time to the frequency domain

$$[\chi^{\mathrm{loc}}]^{\mathrm{mn}}_{\mathrm{pq}}(\mathrm{i}\omega_k) = \sum_{j=1}^{N}\gamma_{kj}\cos(\omega_k\tau_j)[\chi^{\mathrm{loc}}]^{\mathrm{mn}}_{\mathrm{pq}}(\mathrm{i}\tau_j), \tag{378}$$

where $\gamma_{kj}\cos(\omega_k\tau_j)$ matrix is precalculated [see Appendix (B.2)].

(3) Third, the local screened Coulomb interaction W^{loc} is calculated by the RPA (see Fig. 25)

$$\begin{aligned}[W^{\mathrm{loc}}]^{\mathrm{ij}}_{\mathrm{kl}}(\mathrm{i}\omega) =& [U^{\mathrm{loc}}]^{\mathrm{ij}}_{\mathrm{kl}}(\mathrm{i}\omega) + \sum_{\mathrm{mn}}\sum_{\mathrm{pq}}[U^{\mathrm{loc}}]^{\mathrm{ij}}_{\mathrm{mn}}(\mathrm{i}\omega)[\chi^{\mathrm{loc}}]^{\mathrm{mn}}_{\mathrm{pq}}(\mathrm{i}\omega)[W^{\mathrm{loc}}]^{\mathrm{pq}}_{\mathrm{kl}}(\mathrm{i}\omega) \\ =& \sum_{\mathrm{pq}}\left[1-\sum_{\mathrm{mn}}[U^{\mathrm{loc}}]^{\mathrm{ij}}_{\mathrm{mn}}(\mathrm{i}\omega)[\chi^{\mathrm{loc}}]^{\mathrm{mn}}_{\mathrm{pq}}(\mathrm{i}\omega)\right]^{-1}[U^{\mathrm{loc}}]^{\mathrm{pq}}_{\mathrm{kl}}(\mathrm{i}\omega).\end{aligned} \tag{379}$$

Here, $[U^{\mathrm{loc}}](\mathrm{i}\omega)$ is the local partially screened Coulomb interaction, which is calculated by the cRPA [see Section (10.2)]. After $[W^{\mathrm{loc}}](\mathrm{i}\omega)$ has obtained, we need to Fourier transform it to the imaginary time so that the local self-energy can be conveniently calculated. However, a direct

FT of $[W^{\mathrm{loc}}](\mathrm{i}\omega)$ is diverging. Thus, before the FT we split W^{loc} into correlated part $\tilde{W}^{\mathrm{loc}}$ and bare part V [corresponding to $W^{\mathrm{loc}}(\omega \to \infty)$],

$$[W^{\mathrm{loc}}]^{\mathrm{ij}}_{\mathrm{kl}}(\mathrm{i}\omega) = [\tilde{W}^{\mathrm{loc}}]^{\mathrm{ij}}_{\mathrm{kl}}(\mathrm{i}\omega) + V^{\mathrm{ij}}_{\mathrm{kl}}. \tag{380}$$

The correlated part $\tilde{W}^{\mathrm{loc}}(\mathrm{i}\tau)$ in imaginary time can be calculated by an inverse cosine transformation

$$[\tilde{W}^{\mathrm{loc}}]^{\mathrm{ij}}_{\mathrm{kl}}(\mathrm{i}\tau_n) = \sum_{m=1}^{N} \xi_{nm} \cos(\tau_n \omega_m)[\tilde{W}^{\mathrm{loc}}]^{\mathrm{ij}}_{\mathrm{kl}}(\mathrm{i}\omega_m). \tag{381}$$

Again, $\xi_{nm} \cos(\tau_n \omega_m)$ matrix is precalculated [see Appendix (B.2)].

(4) Finally, the DC correction Σ^{DC} including the local Hartree, local Fock and local correlated GW self-energies (see Fig. 25) are calculated as

$$\Sigma^{\mathrm{DC}}_{\mathrm{ij}}(\mathrm{i}\omega) = \Sigma^{\mathrm{loc,Hartree}}_{\mathrm{ij}} + \Sigma^{\mathrm{loc,Fock}}_{\mathrm{ij}} + \tilde{\Sigma}^{\mathrm{loc,GW}}_{\mathrm{ij}}(\mathrm{i}\omega), \tag{382}$$

where the local Hartree part is obtained by

$$\Sigma^{\mathrm{loc,Hartree}}_{\mathrm{ij}} = 2 \sum_{\mathrm{k,l}} \underline{G}^{loc}_{\mathrm{kl}}(-\mathrm{i}\tau)\big|_{\tau=0^+} [U^{\mathrm{loc}}(\mathrm{i}\omega = 0)]^{\mathrm{ij}}_{\mathrm{kl}}. \tag{383}$$

Note that the“-1” sign in the local Hartree self-energy is absorbed by the fact that there is a fermionic loop in the local Hartree diagram, which also introduces a factor of “2”. “0^+” means a positive infinitesimal.

The local Fock part can be calculated by

$$\Sigma^{\mathrm{loc,Fock}}_{\mathrm{ij}} = -\sum_{\mathrm{k,l}} \underline{G}^{\mathrm{loc}}_{\mathrm{lk}}(-\mathrm{i}\tau)\big|_{\tau=0^+} V^{\mathrm{kj}}_{\mathrm{li}}. \tag{384}$$

The frequency-dependent local correlated GW self-energy is determined by

$$\begin{aligned} \tilde{\Sigma}^{\mathrm{loc,GW}}_{\mathrm{ij}}(\mathrm{i}\omega_m) = & \sum_{n=1}^{N} \gamma_{mn} \cos(\omega_m \tau_n) \frac{\tilde{\overline{\Sigma}}^{\mathrm{loc,GW}}_{\mathrm{ij}}(\mathrm{i}\tau_n) + \underline{\tilde{\Sigma}}^{\mathrm{loc,GW}}_{\mathrm{ij}}(-\mathrm{i}\tau_n)}{2} \\ & + \mathrm{i} \sum_{n=1}^{N} \lambda_{mn} \sin(\omega_m \tau_n) \frac{\tilde{\overline{\Sigma}}^{\mathrm{loc,GW}}_{\mathrm{ij}}(\mathrm{i}\tau_n) - \underline{\tilde{\Sigma}}^{\mathrm{loc,GW}}_{\mathrm{ij}}(-\mathrm{i}\tau_n)}{2}, \end{aligned} \tag{385}$$

where $\gamma_{mn}\cos(\omega_m \tau_n)$ and $\lambda_{mn}\sin(\omega_m \tau_n)$ are cosine and sine transformation matrices [see Appendix (B.2)] and the auxiliary occupied and unoccupied local correlated GW self-energies are, respectively, given by

$$\underline{\tilde{\Sigma}}^{\mathrm{loc,GW}}_{\mathrm{ij}}(-\mathrm{i}\tau) = -\sum_{\mathrm{k,l}} \underline{G}^{\mathrm{loc}}_{\mathrm{lk}}(-\mathrm{i}\tau)[\tilde{W}^{\mathrm{loc}}]^{\mathrm{kj}}_{\mathrm{li}}(\mathrm{i}\tau), \tag{386}$$

and

$$\tilde{\overline{\Sigma}}^{\mathrm{loc,GW}}_{\mathrm{ij}}(\mathrm{i}\tau) = -\sum_{\mathrm{k,l}} \overline{G}^{\mathrm{loc}}_{\mathrm{lk}}(\mathrm{i}\tau)[\tilde{W}^{\mathrm{loc}}]^{\mathrm{kj}}_{\mathrm{li}}(\mathrm{i}\tau). \tag{387}$$

10.3.2. Tests on Be molecule

Since the above formulations of the DC correction follow quite closely the low-scaling G_0W_0r implementation, one would expect that in principle the two implementations should yield exactly the same self-energy if and only if the following four criteria are simultaneously satisfied:

1. Both implementations should work in the same basis.
2. The local partially screened Coulomb interaction $[U^{\mathrm{loc}}](\mathrm{i}\omega)$ in Eq. (379) are replaced by the bare Coulomb interaction V.
3. The Bloch space has the same dimension as the Wannier space and the transformation matrix $[\mathbf{U}^{(\mathbf{k})}]$ is unitary.
4. Only one k point is used to sample the Brillouin zone (BZ).

The first two criteria can be straightforwardly achieved. However, searching for a system that meets the last two criteria might not be trivial. Motivated by this idea, we select a Be molecule as our test material, because: (i) the Be atom has a simple $2s^2p^0$ electron configuration with only one s-like state fully occupied, whereas the other three p-like states are empty. It can be simply and accurately described by the $sppp$ model in the Wannier space, so that 4 Bloch states are mapped to 1 s-like Wannier function and 3 p-like Wannier functions. Hence, the transformation matrix $[\mathbf{U}^{(\mathbf{k})}]$ is unitary and criterion 3 is satisfied. (ii) To perform realistic calculations of a molecule, a reasonably large box is required to avoid virtual interactions induced by periodically repeated images. Usually, only one Γ point is sufficient to sample the BZ, and thus the last criterion is satisfied on the Be molecule as well . Therefore, the Be molecule is indeed a good test material for validating our DC correction formulations and implementation.

Technically, a supercell with the box size of $8\times7.2\times8.8$ Å is used to model the Be atom. For the test purpose, only 8 imaginary time/frequency grid points are used. 4 Bloch states are used and mapped onto 1 s-like and 3 p-like Wannier functions, which are treated as the correlated target orbitals. Therefore, the local U^{loc} calculated by the cRPA routine are exactly equal to the bare Coulomb interaction V, and thus the criterion 2 is automatically satisfied. Recall that in the cRPA, the correlated polarizability χ^c of the target space is subtracted from the total polarizability χ; hence if the target space is equivalent to the full space, $\chi^r = \chi - \chi^c$ is zero and $U^{\mathrm{loc}} = V$. To validate our DC routine, we have performed G_0W_0r calculations with the same

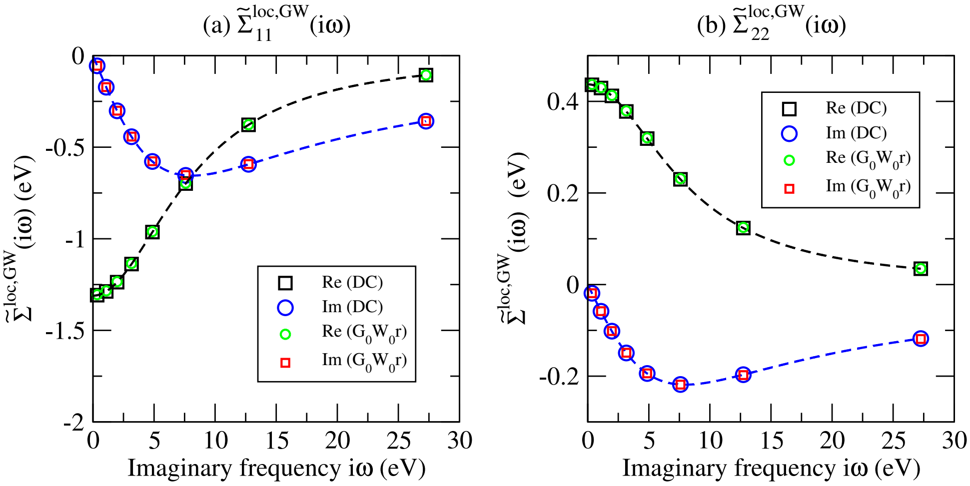

Figure 26: Comparison of the (a) first and (b) second diagonal elements of the correlated self-energy $\tilde{\Sigma}^{\text{loc,GW}}$ in the Wannier basis for the Be molecule calculated from the double counting (DC) routine and the G_0W_0r implementation. Re and Im represent the real and imaginary part, respectively. The dashed lines are obtained from Padé fit.

setups that are used in the DC calculations and then transformed the G_0W_0r Hamiltonian to the Wannier basis using exactly the same unitary matrix. It should be noted that the corrections for screened Coulomb interaction W in the long-wavelength limit (wave vector $\mathbf{q} \to 0$) was not included in the G_0W_0r calculations, which makes it possible to directly compare the results from the DC routine and G_0W_0r.

In Fig. 26, we compare the correlated GW self-energies in the Wannier basis obtained from the DC routine and G_0W_0r. Obviously, excellent agreement is achieved between the two independent calculations. This is also true as the box size or the number of imaginary time/frequency grid points increase (not shown). For the Fock part, we also obtain exactly the same matrix elements in the Wannier basis

$$\Sigma^{\text{loc,Fock}} = \begin{pmatrix} -9.708 & 0.000 & 0.000 & 0.000 \\ 0.000 & -1.725 & 0.000 & 0.000 \\ 0.000 & 0.000 & -1.732 & 0.000 \\ 0.000 & 0.000 & 0.000 & -1.748 \end{pmatrix},$$

because open boundary conditions are used in the calculation of the exchange energy within G_0W_0r [52]. This is also the way we treat the Fock part in the DC routine. The exchange energy of the Be molecule is -9.708 eV, which is equal to $\Sigma^{\text{loc,Hartree}}_{11}$ since in the *sppp* model only the *s*

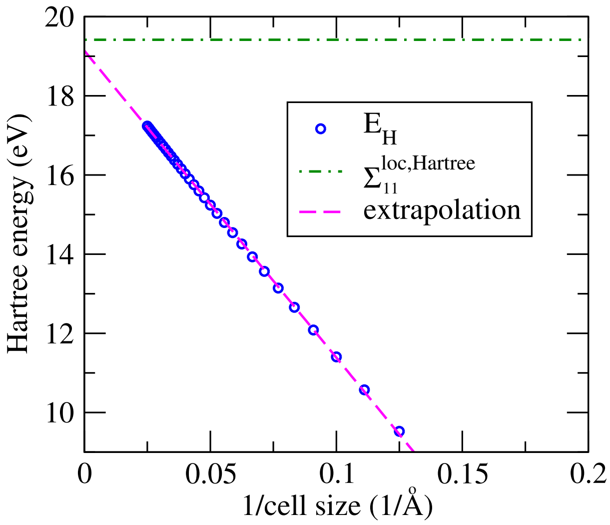

Figure 27: Hartree energies (blue circles) calculated from the Hartree-Fock calculations as a function of the inverse of the supercell size. The extrapolation to an infinite box size (pink dashed line) and $\Sigma_{11}^{\text{loc,Hartree}}$ (green dashed line) are shown for comparison.

state is occupied and the one-electron energy of the s state yields the exchange energy.

However, direct comparison of the Hartree part is not straightforward, since instead of open boundary conditions, periodic boundary conditions are used in G_0W_0r code to determine the Hartree energy [52]. To obtain the converged Hartree energy, one should converge it with respect to the box size, as shown in Fig. 27. As expected, the convergence is slow and Hartree energy alone converges like (box size)$^{-1}$. The converged Hartree energy is about 19.232 eV. For the Hartree part in the DC routine, the resulting matrix elements in the Wannier basis are

$$\Sigma^{\text{loc,Hartree}} = \begin{pmatrix} 19.416 & 0.000 & 0.000 & 0.000 \\ 0.000 & 17.830 & 0.000 & 0.000 \\ 0.000 & 0.000 & 18.105 & 0.000 \\ 0.000 & 0.000 & 0.000 & 18.476 \end{pmatrix}.$$

One would see that the Hartree energy is 19.416 eV, which is exactly twice the exchange energy. In addition, it is also consistent with the converged Hartree energy from G_0W_0r (see Fig. 27).

It should be emphasized that such good agreement between the results (correlated self-energy, Fock, and Hartree energy) obtained from the DC routine and G_0W_0r is also found in the sp^3 model, where 4 Bloch states are mapped to 4 sp^3 hybrid Wannier functions, indicating that our DC formulations and implementations are robust and valid. With this, in the following I will

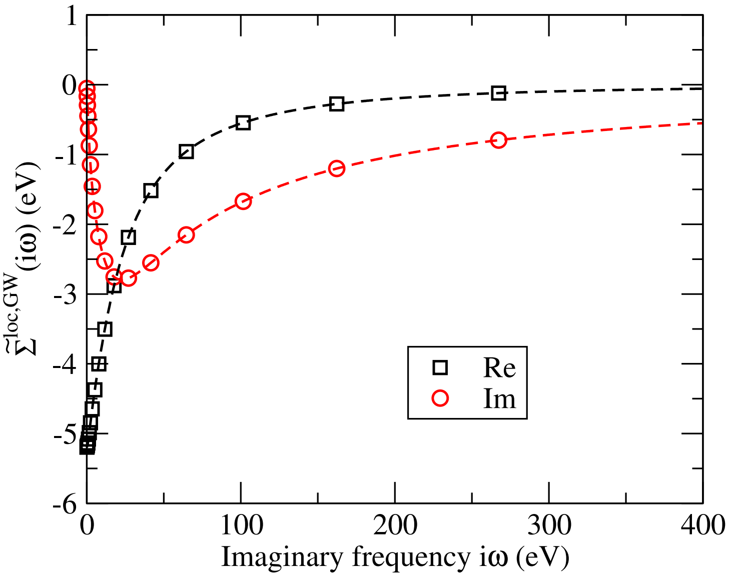

Figure 28: Local correlated GW self-energy $\tilde{\Sigma}^{\rm loc,GW}_{11}(\mathrm{i}\omega)$ versus imaginary frequency $\mathrm{i}\omega$. Re and Im represent the real and imaginary part, respectively. The dashed lines are obtained from Padé fit. 20 optimized imaginary frequency grid points and $8 \times 8 \times 8$ k points are used in the calculations. The data for frequencies beyond 400 eV are truncated and not shown in the plot.

apply this method to calculate the DC correction for $SrVO_3$.

10.3.3. Double counting corrections of $SrVO_3$

Here, we show the matrix elements of the local Hartree, local Fock and local correlated GW self-energy of $SrVO_3$ in the V-t_{2g}-like maximally localized Wannier basis in the order of d_{xy}, d_{xz} and d_{yz}. The imaginary-frequency-dependent partially screened Coulomb interaction $[U^{\rm loc}]^{\rm IJ}_{\rm KL}(\mathrm{i}\omega)$ are taken from cRPA calculations in Section (10.2).

The calculated matrix elements of the local Hartree are

$$\Sigma^{\rm loc,Hartree} = \begin{pmatrix} 2.442 & 0.000 & 0.000 \\ 0.000 & 2.442 & 0.000 \\ 0.000 & 0.000 & 2.442 \end{pmatrix}.$$

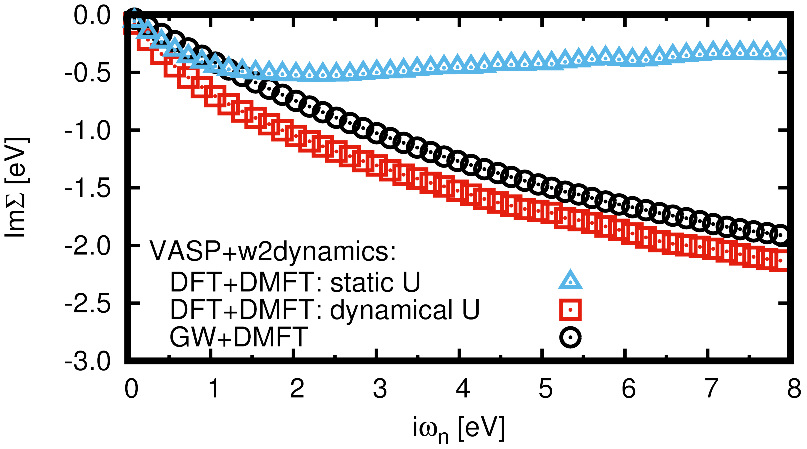

Figure 29: Local Matsubara self energies ($T = 300$K) for the t_{2g} orbitals of SrVO$_3$ using (i) DFT+DMFT with static $U = U(\omega = 0)$, (ii) DFT+DMFT with the dynamical interaction $U(\mathrm{i}\omega)$ from cRPA, and (iii) GW+DMFT. Data obtained using the new GW implementation of VASP in combination with w2dynamics.

The matrix elements of the local Fock are

$$\Sigma^{\text{loc,Fock}} = \begin{pmatrix} -2.581 & 0.000 & 0.000 \\ 0.000 & -2.581 & 0.000 \\ 0.000 & 0.000 & -2.581 \end{pmatrix}.$$

For the local correlated self-energy of SrVO$_3$, the off-diagonal elements are quite minute and thus negligible. In addition, three t_{2g}-like Wannier functions are degenerate in the energy, i.e., $\Sigma_{11}^{\text{loc,GW}} = \Sigma_{22}^{\text{loc,GW}} = \Sigma_{33}^{\text{loc,GW}}$ at each frequency, and hence we show the plot for $\Sigma_{11}^{\text{loc,GW}}(\mathrm{i}\omega)$ only in Fig. 28.

10.4. Preliminary results of GW+DMFT on SrVO$_3$

In Fig. 29 we compare Matsubara self energies for the t_{2g} orbitals of SrVO$_3$ obtained with our new implementation that combines the VASP GW code [107] with the w2dynamics DMFT code [274, 275]. We employ the same approximations (1)-(3) as in Ref. [119]. (1) Omitting global self-consistency, i.e., performing only one-shot G_0W_0 calculations starting with $G = G^{DFT}$. (2) Fixing the double-counting polarization χ_{loc}^{GW} to the dynamical cRPA result and approximating $\chi^{\text{imp}} \approx \chi_{\text{loc}}^{GW}$ (see Eq. (345)). (3) Approximating the double-counting self energy by the local projection of the GW self energy: $\Sigma^{GW}_{\text{loc}}(\mathrm{i}\omega) \approx \sum_{\mathbf{k}} \Sigma^{GW}(\mathbf{k}, \mathrm{i}\omega)$. [1]. However, instead of the approximative Bose-factor Ansatz [276], we use a numerical exact continuous-time quantum Monte Carlo algorithm [277], as implemented in w2dynamics by D. Springer. Our reference is a standard DFT+DMFT calculation that uses a static Hubbard $U(\omega = 0)$ and Hund's $J(\omega = 0)$ as provided by the cRPA. From the low-energy slope of $\mathrm{Im}\Sigma(\mathrm{i}\omega_n)$ we extract a quasi-particle weight $Z = 0.6$. Turning on the retardation in the interaction, i.e. solving DFT+DMFT with dynamical $U(\mathrm{i}\omega)$ adds band-renormalizations of plasmonic origin; Z decreases to 0.5. Also, since the dynamical interaction recovers at high frequencies the unscreened Coulomb interaction, $\mathrm{Re}U(\mathrm{i}\omega \to \infty) \approx 16\mathrm{eV}$, also the self energy Σ lives on a much larger energy scale [276] than in the standard static DFT+DMFT case. Adding the non-local GW self energy decreases effective masses, i.e. the ratio of U over bandwidth diminishes and so does the strength of correlations: In our GW+DMFT the local quasi-particle weight is $Z = 0.7$, in qualitative agreement with previous results from Ref. [118]. It should be noted that these are just our preliminary results and the merger of GW and DMFT is still developing.

---

[1] Note that inclusion of the double-counting correction shown in Section (10.3.3) is still ongoing and thus here we do not use it

11. Conclusions

To summarize, we have presented a promising low-scaling *GW* implementation within the framework of the full potential projector-augmented wave methodology. It allows for quasiparticle calculations with a scaling that is cubic in the system size and linear in the number of *k* points used to sample the Brillouin zone. This is achieved by calculating the polarizability and self-energy in real space and imaginary time. The transformation from the imaginary time to the frequency domain is done by an efficient discrete Fourier transformation with only a few nonuniform grid points. Fast Fourier transformations are used to go from real space to reciprocal space and vice versa. The analytic continuation from the imaginary to the real frequency axis is performed by exploiting Thiele's reciprocal difference scheme and least-squares method. Finally, the method is applied successfully to predict the quasiparticle energies and spectral functions of typical semiconductors (Si, GaAs, SiC, and ZnO), insulators (C, BN, MgO, and LiF), and metals (Cu and $SrVO_3$). The results are compared with conventional *GW* calculations. It is found that the QP energies and spectral functions predicted by G_0W_0r are in good agreement with G_0W_0 but with a reduced scaling in the system size and number of *k* points, highlighting the strength of the present method. We believe that this method has great potential for applications, in particular for large unit cells.

We also apply this low-scaling G_0W_0r method to predict the ionization potentials and electron affinities of 100 closed shell molecules. For the ionization potential, the basis set extrapolated plane wave results agree very well with the Gaussian basis sets [84], often reaching better than 50 meV agreement. In order to achieve this agreement, we correct for finite basis set errors as well as errors introduced by periodically repeated images. For positive electron affinities differences between Gaussian basis sets and VASP are slightly larger. We attribute this to larger basis set extrapolation errors for the Gaussian basis sets. For quasi particle (QP) resonances above the vacuum level, differences between VASP and Gaussian basis sets are, however, found to be substantial. This is tentatively explained by insufficient basis set convergence of the Gaussian type orbital calculations as exemplified for selected test cases.

Moreover, we have coded and tested the self-consistent GW_0r method, where the screened Coulomb interaction *W* is fixed at the DFT level, while the interacting Green's function *G* are updated by solving the Dyson-equation with the updated self-energy. First results on the test material Si have been shown. It is found that after 5 iterations self-consistency in GW_0r is achieved, for example, the number of electrons is converged. It is also found that the band gap predicted by GW_0r method increases significantly compared to the single-shot G_0W_0r method.

Furthermore, we have extended the imaginary frequency scheme to the conventional GW implementation. Specifically, instead of evaluation of the two electron integral along the real frequency axis, we calculate it along the imaginary axis using the optimized imaginary time/frequency grids. We make full use of efficient discrete temporal Fourier transformations to obtain the self-energy along the imaginary frequency axis. Then, Thiele's reciprocal difference or least-squares methods are exploited to analytically continuing the self-energy to the real frequency axis. This method was successfully applied to typical semiconductors ZnO and CdTe. For CdTe, spin-orbit coupling was considered. It was found that the imaginary frequency version works equally well as the conventional G_0W_0 and low-scaling G_0W_0r implementations, with a modest computational effort and memory requirements that are between G_0W_0 and G_0W_0r. Since the spin-orbit coupling has not yet been implemented in the low-scaling G_0W_0r implementation and the conventional G_0W_0 implementation is often restricted to small systems, the imaginary frequency version might be a compromise for the moderately large systems where spin-orbit coupling is non-negligible.

Finally, we have formulated and discussed a feasible scheme to merge GW with DMFT. First, our low-scaling GW self-energies are obtained in the imaginary frequency domain, which will facilitate an elegant combination of GW with DMFT and thus enhance the predictive abilities of GW+DMFT for large correlated systems. Second, the on-site imaginary-frequency-dependent partially screened intra-orbital interactions $U(\mathrm{i}\omega)$, inter-orbital interactions $U'(\mathrm{i}\omega)$ and Hund's coupling $J(\mathrm{i}\omega)$, which are required in the dynamical impurity solver of DMFT, can be calculated by the cRPA in the same framework as the GW approximation. Exhaustive derivations are given and tests have been done on $\mathrm{SrVO_3}$ and other systems. The calculated results (U, U' and J) are in good agreement with the ones obtained from the conventional cRPA calculations. Finally, the so-called double counting in GW+DMFT has been formulated and successfully tested for the molecule Be and $\mathrm{SrVO_3}$. The preliminary GW+DMFT results on $\mathrm{SrVO_3}$ show the local quasi-particle weight of $Z = 0.7$, in qualitative agreement with published results. The merger of GW and DMFT is still under development by collaborating with Karsten Held's group at the Technical University of Vienna.

Part III.

Appendix

Appendix A Fourier transformations

In this appendix, Fourier transformations and some useful equations used in the main text of the thesis will be shown.

A.1 Continuous functions in a finite system

Considering a rectangular box in 3-dimension with side lengths L_x, L_y, L_z, any well-behaved function $f(\mathbf{r})$ fulfilling the periodic boundary conditions

$$f(\mathbf{r}+L_x\mathbf{e}_x) = f(\mathbf{r}+L_y\mathbf{e}_y) = f(\mathbf{r}+L_z\mathbf{e}_z) = f(\mathbf{r}), \tag{388}$$

can be expressed as a Fourier series

$$f(\mathbf{r}) = \frac{1}{\Omega}\sum_{\mathbf{k}} F(\mathbf{k})\mathrm{e}^{\mathrm{i}\mathbf{kr}}, \tag{389}$$

where $\mathbf{k}$ is a wave vector in the reciprocal space of the system with a volume $\Omega = L_xL_yL_z$

$$\mathbf{k} = n_x\frac{2\pi}{L_x}\mathbf{e}_x + n_y\frac{2\pi}{L_y}\mathbf{e}_y + n_z\frac{2\pi}{L_z}\mathbf{e}_y, \;\; \{n_x, n_y, n_z\} \in \text{ integer}. \tag{390}$$

Then, the Fourier coefficients $F(\mathbf{k})$ can be calculated by

$$F(\mathbf{k}) = \int_\Omega d\mathbf{r} f(\mathbf{r})\mathrm{e}^{-\mathrm{i}\mathbf{kr}}. \tag{391}$$

Useful formulas that are often used for simplifying equations are

$$\frac{1}{\Omega}\sum_{\mathbf{k}} \mathbf{e}^{\pm\mathrm{i}\mathbf{kr}} = \delta(\mathbf{r}), \tag{392}$$

$$\int_\Omega d\mathbf{r}\mathbf{e}^{\pm\mathrm{i}\mathbf{kr}} = \Omega\delta(\mathbf{k}). \tag{393}$$

A.2 Continuous functions in an infinite system

If the volume considered approaches infinity, the $\mathbf{k}$ vectors become quasi-continuous variables, and thus the $\mathbf{k}$-sum is converted into an integral

$$f(\mathbf{r}) = \int \frac{d\mathbf{k}}{(2\pi)^3} F(\mathbf{k}) \mathbf{e}^{\mathrm{i}\mathbf{kr}}, \tag{394}$$

$$F(\mathbf{k}) = \int d\mathbf{r} f(\mathbf{r}) \mathbf{e}^{-\mathrm{i}\mathbf{kr}}. \tag{395}$$

Here and in the following, we used notation $\int d\mathbf{k} = \int dk_x dk_y dk_z$ and $\int d\mathbf{r} = \int dr_x dr_y dr_z$.

Useful formulas that are often used for simplifying equations are

$$\int \frac{d\mathbf{k}}{(2\pi)^3}(\ldots) = \frac{1}{\Omega}\sum_{\mathbf{k}}(\ldots), \tag{396}$$

$$\int d\mathbf{k}\mathbf{e}^{\pm\mathrm{i}\mathbf{kr}} = (2\pi)^3\delta(\mathbf{r}), \tag{397}$$

$$\int_{\Omega} d\mathbf{r}\mathbf{e}^{\pm\mathrm{i}\mathbf{kr}} = \Omega\delta(\mathbf{k}). \tag{398}$$

A.3 Time and frequency Fourier transformations

Analogous to the spatial Fourier transformations, the temporal Fourier transformations can be given by

$$f(\tau) = \int_{-\infty}^{+\infty} \frac{d\omega}{2\pi} F(\omega) \mathbf{e}^{-\mathrm{i}\omega\tau}, \tag{399}$$

$$F(\omega) = \int_{-\infty}^{+\infty} d\tau f(\tau) \mathbf{e}^{\mathrm{i}\omega\tau}. \tag{400}$$

Comparing Eq. (399) and Eq. (394), one obtains that τ plays the role of $\mathbf{r}$, while ω plays the role of $\mathbf{k}$ but with an opposite sign.

Again, useful formulas that are often used for simplifying equations are

$$\int_{-\infty}^{+\infty} \frac{d\omega}{2\pi} \mathbf{e}^{-\mathrm{i}\omega\tau} = \delta(\tau), \tag{401}$$

$$\int_{-\infty}^{+\infty} d\tau \mathbf{e}^{\mathrm{i}\omega\tau} = 2\pi\delta(\omega). \tag{402}$$

For the Fourier transforms of operator $\nabla_{\mathbf{r}}$, ∇^2, $\nabla\times$, and ∂_τ, one can use the following substitution rule:

$$
\begin{aligned}
\nabla_{\mathbf{r}} \quad &\longleftrightarrow \quad \mathrm{i}\mathbf{k}, &(403)\\
\nabla_{\mathbf{r}}^2 \quad &\longleftrightarrow \quad -\mathbf{k}^2, &(404)\\
\nabla\times \quad &\longleftrightarrow \quad \mathrm{i}\mathbf{k}\times, &(405)\\
\partial_\tau \quad &\longleftrightarrow \quad -\mathrm{i}\omega. &(406)
\end{aligned}
$$

As an example,

$$\nabla_{\mathbf{r}} f(\mathbf{r}) = \nabla_{\mathbf{r}} \frac{1}{\Omega} \sum_{\mathbf{k}} F(\mathbf{k}) \mathbf{e}^{\mathrm{i}\mathbf{k}\mathbf{r}} = \frac{1}{\Omega} \sum_{\mathbf{k}} F(\mathbf{k}) \nabla_{\mathbf{r}} \mathbf{e}^{\mathrm{i}\mathbf{k}\mathbf{r}} = \frac{1}{\Omega} \sum_{\mathbf{k}} \mathrm{i}\mathbf{k} F(\mathbf{k}) \mathbf{e}^{\mathrm{i}\mathbf{k}\mathbf{r}} \tag{407}$$

A.4 The convolution theorem

The convolution theorem states that the convolution h of two functions u and f can be expressed as a simple product using their corresponding Fourier spectra H, U, and F.

$$
\begin{aligned}
h(\tau) &= \int d\tau'\, u(\tau-\tau') f(\tau'), &(408)\\
H(\omega) &= U(\omega) F(\omega), &(409)
\end{aligned}
$$

or the other way around

$$
\begin{aligned}
H(\omega) &= \int d\omega' U(\omega-\omega') F(\omega'), &(410)\\
h(\tau) &= u(\tau) f(\tau). &(411)
\end{aligned}
$$

This can be extended to the case of multiple convolutions

$$
\begin{aligned}
h(\tau) &= \int d\tau' \int d\tau'' u_1(\tau-\tau') u_2(\tau'-\tau'') f(\tau'') &(412)\\
H(\omega) &= U_1(\omega) U_2(\omega) H(\omega) &(413)
\end{aligned}
$$

As an example, here we show the proof for Eq. (413) from Eq. (412) using the definitions of temporal Fourier transformations:

$$
\begin{aligned}
&\int \frac{d\omega'}{2\pi} \mathbf{e}^{-\mathrm{i}\omega'\tau} H(\omega')\\
&= \int d\tau' \int d\tau'' \left(\int \frac{d\omega'}{2\pi} \mathbf{e}^{-\mathrm{i}\omega'(\tau-\tau')} U_1(\omega') \right) \left(\int \frac{d\omega''}{2\pi} \mathbf{e}^{-\mathrm{i}\omega''(\tau'-\tau'')} U_2(\omega'') \right) \left(\int \frac{d\omega'''}{2\pi} \mathbf{e}^{-\mathrm{i}\omega'''\tau''} F(\omega''') \right)\\
&= \int \frac{d\omega'}{2\pi} \frac{d\omega''}{2\pi} \frac{d\omega'''}{2\pi} \mathbf{e}^{-\mathrm{i}\omega'\tau} U_1(\omega') U_2(\omega'') F(\omega''') \underbrace{\left(\int d\tau' \mathbf{e}^{\mathrm{i}\tau'(\omega'-\omega'')} \right)}_{2\pi\delta(\omega'-\omega'')} \underbrace{\left(\int d\tau'' \mathbf{e}^{\mathrm{i}\tau''(\omega''-\omega''')} \right)}_{2\pi\delta(\omega''-\omega''')}\\
&= \int \frac{d\omega'}{2\pi} \mathbf{e}^{-\mathrm{i}\omega'\tau} U_1(\omega') U_2(\omega') F(\omega').
\end{aligned}
\tag{414}
$$

Clearly, Eq. (413) is justified. This rule can be proved similarly for higher order convolutions.

A.5 Continuous functions in translation invariant systems

For a translation invariant system, any function $f(\mathbf{r}, \mathbf{r}')$ depends only on the difference between the coordinates $\mathbf{r} - \mathbf{r}'$

$$f(\mathbf{r}, \mathbf{r}') = f(\mathbf{r}' - \mathbf{r}). \tag{415}$$

The consequences in reciprocal space from this constraint are

$$\begin{aligned} f(\mathbf{r}, \mathbf{r}') =& \frac{1}{\Omega^2} \sum_{\mathbf{k},\mathbf{k}'} F(\mathbf{k}, \mathbf{k}') \mathbf{e}^{\mathbf{ikr}} \mathbf{e}^{\mathbf{ik'r'}} \\ =& \frac{1}{\Omega^2} \sum_{\mathbf{k},\mathbf{k}'} F(\mathbf{k}, \mathbf{k}') \mathbf{e}^{\mathbf{ik(r-r')}} \mathbf{e}^{\mathbf{i(k+k')r'}} \\ =& \frac{1}{\Omega} \sum_{\mathbf{k}} \tilde{F}(\mathbf{k}) \mathbf{e}^{\mathbf{ik(r-r')}} = f(\mathbf{r}' - \mathbf{r}). \end{aligned} \tag{416}$$

Using Eq. (392) , one obtains $\mathbf{k} + \mathbf{k}' \equiv 0$ and $F(\mathbf{k}, \mathbf{k}') = \tilde{F}(\mathbf{k})\delta(\mathbf{k} + \mathbf{k}')$. Thus, we obtains the Fourier transformations of translation invariant systems

$$f(\mathbf{r}' - \mathbf{r}) = \frac{1}{\Omega} \sum_{\mathbf{k}} \tilde{F}(\mathbf{k}) \mathbf{e}^{\mathbf{ik(r-r')}} \tag{417}$$

$$\tilde{F}(\mathbf{k}) = \int d(\mathbf{r} - \mathbf{r}') f(\mathbf{r}' - \mathbf{r}) \mathbf{e}^{-\mathbf{ik(r-r')}}. \tag{418}$$

As an example, we show below the Fourier transformation of the Coulomb kernel $v(\mathbf{r}, \mathbf{r}') = \frac{1}{|\mathbf{r}-\mathbf{r}'|}$. Replacing $\mathbf{r} - \mathbf{r}' \Rightarrow \mathbf{r}$ yields $v(\mathbf{r}) = \frac{1}{|\mathbf{r}|}$. The Fourier transformation can be performed by using spherical coordinates

$$V(\mathbf{k}) = \int d\mathbf{r} e^{-i\mathbf{kr}} v(\mathbf{r}) \tag{419}$$

$$= \int_0^\infty dr\, r^2 \int_0^{2\pi} d\varphi \int_0^\pi d\theta\, \sin(\theta) e^{-ikr\cos(\theta)} v(\mathbf{r}) \tag{420}$$

$$= 2\pi \int_0^\infty dr\, r^2 v(\mathbf{r}) \int_0^\pi d\theta\, \sin(\theta) e^{-ikr\cos(\theta)}. \tag{421}$$

$$\tag{422}$$

Using the variable transformation $u = \cos(\theta)$ and $du = -\sin(\theta)d\theta$, we can write

$$V(\mathbf{k}) = 2\pi \int_0^\infty dr\, r^2 v(\mathbf{r}) \int_1^{-1} (-1)\, du\, e^{-ikru} \tag{423}$$

$$= 2\pi \int_0^\infty dr\, r^2 v(\mathbf{r}) \frac{2\sin(kr)}{kr}. \tag{424}$$

Choosing the specific identity $v(\mathbf{r}) = 1/|\mathbf{r}| = \lim_{\eta\to 0} e^{-\eta r}/r$, we finally obtain the Fourier transformed Coulomb kernel

$$\begin{aligned} V(\mathbf{k}) &= \frac{4\pi}{k} \lim_{\eta\to 0} \int_0^\infty dr\, e^{-\eta r} \sin(kr) && (425) \\ &= \frac{4\pi}{k} \lim_{\eta\to 0} \operatorname{Im} \int_0^\infty dr\, e^{ikr-\eta r} && (426) \\ &= \lim_{\eta\to 0} \frac{4\pi}{k^2+\eta^2} = \frac{4\pi}{k^2}. && (427) \end{aligned}$$

A.6 One-index periodic functions in a crystal

Considering a periodic crystal (supercell) defined by $N_\mathbf{k}$ times of unit cells, the volume of the crystal is given by $\Omega = N_\mathbf{k}\Omega_0$ with $\Omega_0 = \mathbf{a}_1 \cdot (\mathbf{a}_2 \times \mathbf{a}_3)$ being the volume of the unit cell, which is defined by three basis vectors $\mathbf{a}_1$, $\mathbf{a}_2$ and $\mathbf{a}_3$. If a continuous function $f(\mathbf{r})$ which fulfils the periodic boundary conditions and is periodic in the lattice

$$f(\mathbf{r}+\mathbf{R}) = f(\mathbf{r}), \tag{428}$$

where $\mathbf{R}$ is a real-space lattice vector

$$\mathbf{R} = n_1\mathbf{a}_1 + n_2\mathbf{a}_2 + n_3\mathbf{a}_3, \quad \{n_1, n_2, n_3\} \in \text{ integer}, \tag{429}$$

its Fourier transformation can be expressed as

$$f(\mathbf{r}) = \frac{1}{\Omega_0} \sum_{\mathbf{G}} F(\mathbf{G}) \mathbf{e}^{\mathrm{i}\mathbf{G}\mathbf{r}}. \tag{430}$$

It should be noted that here, $\mathbf{G}$ is a reciprocal superlattice vector and the volume of the unit cell Ω_0 is used, in contrast to Eq. (389). In obtaining Eq. (430), we have used the following relationships

$$\begin{aligned} \sum_{\mathbf{R}} \mathbf{e}^{\pm\mathrm{i}(\mathbf{k}-\mathbf{k}')\mathbf{R}} &= N_\mathbf{k}\delta_{\mathbf{k},\mathbf{k}'}, && (431) \\ \sum_{\mathbf{k}\in\mathrm{BZ}} \mathbf{e}^{\pm\mathrm{i}\mathbf{k}(\mathbf{R}-\mathbf{R}')} &= N_\mathbf{k}\delta_{\mathbf{R},\mathbf{R}'}. && (432) \end{aligned}$$

Decomposing $\mathbf{G}$ into

$$\mathbf{G} = \mathbf{q} + \mathbf{g}, \tag{433}$$

with $\mathbf{q}$ being a k-point restricted within the Brillouin zone (BZ) of the unit cell and $\mathbf{g}$ a reciprocal lattice vector of the unit cell, Eq. (430) becomes

$$f(\mathbf{r}) = \frac{1}{\Omega_0} \sum_{\mathbf{q}}^{\mathrm{BZ}} \sum_{\mathbf{g}} F(\mathbf{q}+\mathbf{g}) \mathbf{e}^{\mathrm{i}(\mathbf{q}+\mathbf{g})\mathbf{r}}. \tag{434}$$

The inverse of Fourier transformation is then given by

$$F(\mathbf{q}+\mathbf{g}) = \int_{\Omega_0} d\mathbf{r} f(\mathbf{r}) \mathbf{e}^{-\mathrm{i}(\mathbf{q}+\mathbf{g})\mathbf{r}}. \tag{435}$$

With Eqs. (425) and (434), one obtains the Coulomb kernel $\frac{1}{|\mathbf{r}-\mathbf{r}'|}$ in Fourier space

$$\frac{1}{|\mathbf{r}-\mathbf{r}'|} = \frac{1}{\Omega_0} \sum_{\mathbf{q}}^{\mathrm{BZ}} \sum_{\mathbf{g}} \frac{4\pi}{|\mathbf{q}+\mathbf{g}|^2} \mathbf{e}^{\mathrm{i}(\mathbf{q}+\mathbf{g})(\mathbf{r}-\mathbf{r}')}. \tag{436}$$

A.7 Two-index periodic functions of a crystal

For a periodic two-index function $f(\mathbf{r},\mathbf{r}')$ of a crystal, such as the Green's function and response function, it is periodic in space

$$f(\mathbf{r},\mathbf{r}') = f(\mathbf{r}+\mathbf{R},\mathbf{r}'+\mathbf{R}), \tag{437}$$

where $\mathbf{R}$ is a real-space lattice vector. From the constraint in Eq. (437), one obtains

$$\begin{aligned} f(\mathbf{r},\mathbf{r}') =& \frac{1}{\Omega_0} \sum_{\mathbf{q},\mathbf{q}'}^{\mathrm{BZ}} \sum_{\mathbf{g},\mathbf{g}'} \mathbf{e}^{\mathrm{i}(\mathbf{q}+\mathbf{g})\mathbf{r}} F(\mathbf{q}+\mathbf{g},\mathbf{q}'+\mathbf{g}') \mathbf{e}^{-\mathrm{i}(\mathbf{q}'+\mathbf{g}')\mathbf{r}'} \\ =& \frac{1}{\Omega_0} \sum_{\mathbf{q},\mathbf{q}'}^{\mathrm{BZ}} \sum_{\mathbf{g},\mathbf{g}'} \mathbf{e}^{\mathrm{i}(\mathbf{q}+\mathbf{g})(\mathbf{r}+\mathbf{R})} F(\mathbf{q}+\mathbf{g},\mathbf{q}'+\mathbf{g}') \mathbf{e}^{-\mathrm{i}(\mathbf{q}'+\mathbf{g}')(\mathbf{r}'+\mathbf{R})} = f(\mathbf{r}+\mathbf{R},\mathbf{r}'+\mathbf{R}). \end{aligned} \tag{438}$$

Here, $\mathbf{q}$ and $\mathbf{q}'$ are the k-points restricted within the BZ of the unit cell and $\mathbf{g}$ and $\mathbf{g}'$ are the lattice vectors of the reciprocal unit cell. Ω_0 is the volume of the unit cell. From Eq. (438) one obtains

$$\sum_{\mathbf{q},\mathbf{q}'}^{\mathrm{BZ}} (\mathbf{e}^{\mathrm{i}(\mathbf{q}-\mathbf{q}')\mathbf{R}} - 1) \sum_{\mathbf{g},\mathbf{g}'} \mathbf{e}^{\mathrm{i}(\mathbf{q}+\mathbf{g})\mathbf{r}} F(\mathbf{q}+\mathbf{g},\mathbf{q}'+\mathbf{g}') \mathbf{e}^{-\mathrm{i}(\mathbf{q}'+\mathbf{g}')\mathbf{r}'} = 0. \tag{439}$$

In deriving Eq. (439), $\mathbf{e}^{\mathrm{i}\mathbf{g}\mathbf{R}} \equiv 1$ has been used. Since Eq. (439) holds for any $\mathbf{R}$, one obains

$$\mathbf{e}^{\mathrm{i}(\mathbf{q}-\mathbf{q}')\mathbf{R}} \equiv 1. \tag{440}$$

This indicates that the difference between $\mathbf{q}$ and $\mathbf{q}'$ has to be a reciprocal lattice vector. As $\mathbf{q}$ and $\mathbf{q}'$ are restricted to BZ, $\mathbf{q}-\mathbf{q}' \equiv 0$ holds. Finally, one obtains the Fourier transformation of the two-index periodic function $f(\mathbf{r},\mathbf{r}')$

$$f(\mathbf{r},\mathbf{r}') = \frac{1}{\Omega_0} \sum_{\mathbf{q}}^{\mathrm{BZ}} \sum_{\mathbf{g},\mathbf{g}'} \mathbf{e}^{\mathrm{i}(\mathbf{q}+\mathbf{g})\mathbf{r}} F_{\mathbf{q}}(\mathbf{g},\mathbf{g}') \mathbf{e}^{-\mathrm{i}(\mathbf{q}+\mathbf{g}')\mathbf{r}'}. \tag{441}$$

Here, $F_{\mathbf{q}}(\mathbf{g},\mathbf{g}') \equiv F(\mathbf{q}+\mathbf{g},\mathbf{q}+\mathbf{g}')$ is assumed. The inverse of the Fourier transformation is then given by

$$F_{\mathbf{q}}(\mathbf{g},\mathbf{g}') = \frac{1}{\Omega_0} \int_{\Omega_0} d\mathbf{r} \int_{\Omega_0} d\mathbf{r}' \mathbf{e}^{-\mathrm{i}(\mathbf{q}+\mathbf{g})\mathbf{r}} f(\mathbf{r},\mathbf{r}') \mathbf{e}^{\mathrm{i}(\mathbf{q}+\mathbf{g}')\mathbf{r}'}. \tag{442}$$

Appendix B Non-uniform grids and temporal discrete Fourier transformations

In this appendix, it will be exhaustively shown how the non-uniform imaginary time/frequency grids and temporal discrete Fourier transformations are derived following the work of Kaltak *et al.* [103], where the interested readers could find the original derivation. It is noted that this representation corrects for some inconsistencies in the original publication.

B.1 Non-uniform imaginary time/frequency grids

We start by the RPA correlation energy [278, 279]

$$E_c^{\mathrm{RPA}} = \frac{1}{4\pi}\int_{-\infty}^{\infty} \mathrm{d}\omega \mathrm{Tr}[\ln(1-\chi(\mathrm{i}\omega)V) + \chi(\mathrm{i}\omega)V], \tag{443}$$

where $\chi(\mathrm{i}\omega)$ is the independent-particle polarizability along the imaginary frequency axis and V is the bare Coulomb potential. For the seek of brevity, we drop the trace symbol in the following.

Doing a series expansion for the correlation energy in Eq. (443) by using the series expansion of $\ln(1-x) = -\sum_{i=1}^{\infty}\frac{x^n}{n}$ yields

$$E_c = E_c^{(2)} + E_c^{(3)} + \cdots \tag{444}$$

where $E_c^{(n)}$ are the direct Møller-Plesset (MP) correlation energies for order n

$$E_c^{(n)} = -\frac{1}{4\pi}\frac{1}{n}\int_{-\infty}^{\infty} \mathrm{d}\omega \{\chi(\mathrm{i}\omega)V\}^n, \quad n \geq 2. \tag{445}$$

The lowest order contribution $n = 2$ is the direct MP2 correlation energy, which reads

$$E_c^{(2)} = -\frac{1}{8\pi}\int_{-\infty}^{\infty} \mathrm{d}\omega \{\chi(\mathrm{i}\omega)V\}^2. \tag{446}$$

Fourier transforming of $\chi(\mathrm{i}\omega)$ to the imaginary time domain, we obtain the corresponding imaginary time representation of $E_c^{(2)}$

$$\begin{aligned} E_c^{(2)} &= -\frac{1}{8\pi}\int_{-\infty}^{\infty} \mathrm{d}\omega [\int_{-\infty}^{\infty} \mathrm{d}\tau \hat{\chi}(\mathrm{i}\tau)\mathrm{e}^{\mathrm{i}\omega\tau} V \int_{-\infty}^{\infty} \mathrm{d}\tau' \hat{\chi}(\mathrm{i}\tau')\mathrm{e}^{\mathrm{i}\omega\tau'} V] \\ &= -\frac{1}{8\pi}\int_{-\infty}^{\infty} \mathrm{d}\tau \int_{-\infty}^{\infty} \mathrm{d}\tau' \underbrace{\int_{-\infty}^{\infty} \mathrm{d}\omega \mathrm{e}^{\mathrm{i}\omega(\tau+\tau')}}_{2\pi\delta(\tau+\tau')} \hat{\chi}(\mathrm{i}\tau)V\hat{\chi}(\mathrm{i}\tau')V \\ &= -\frac{1}{4}\int_{-\infty}^{\infty} \mathrm{d}\tau \{\hat{\chi}(\mathrm{i}\tau)V\}^2. \end{aligned} \tag{447}$$

In deriving Eq. (447), Eq. (401) and the fact that χ is an even function with respect to imaginary time/frequency have been used.

Due to the even symmetry of χ, the Fourier transformation becomes a cosine transformation

$$\chi(\mathrm{i}\omega) \;=\; = \int_{-\infty}^{\infty} \mathrm{d}\tau \hat{\chi}(\mathrm{i}\tau)\cos(\tau\omega) = 2\int_{0}^{\infty} \mathrm{d}\tau \hat{\chi}(\mathrm{i}\tau)\cos(\tau\omega), \tag{448}$$

$$\hat{\chi}(\mathrm{i}\tau) \;=\; = \frac{1}{2\pi}\int_{-\infty}^{\infty} \mathrm{d}\omega \chi(\mathrm{i}\omega)\cos(\tau\omega) = \frac{1}{\pi}\int_{0}^{\infty} \mathrm{d}\omega \chi(\mathrm{i}\omega)\cos(\tau\omega). \tag{449}$$

The independent-particle polarizability reads [73, 86]

$$\chi(\mathrm{i}\omega) = \sum_{\mu} \chi_{\mu}\phi(\omega, x_{\mu}), \tag{450}$$

$$\hat{\chi}(\mathrm{i}\tau) = \sum_{\mu} \chi_{\mu}\hat{\phi}(\tau, x_{\mu}), \tag{451}$$

where the auxiliary functions

$$\phi(\omega, x) = \frac{2x}{x^2 + \omega^2}, \tag{452}$$

$$\hat{\phi}(\tau, x) = \mathrm{e}^{-x|\tau|}, \tag{453}$$

are introduced, which describe the frequency and time dependence, respectively. To keep consistency, here, we have adopted the same notations as in Ref. [103].

- μ stands for the compound index (i, a), where i goes over occupied and a over unoccupied states and $\sum_{\mu}(\cdots) = \sum_{i}^{\mathrm{occ}}\sum_{a}^{\mathrm{unocc}}(\cdots)$.
- $x_{\mu} = \epsilon_a - \epsilon_i > 0$ is the transition energy between unoccupied a and occupied states i, which meets $\epsilon_{\min} \leq x_{\mu} \leq \epsilon_{\max}$ with $\epsilon_{\min}$ being the band gap and $\epsilon_{\max}$ the maximally considered transition energy.
- $\chi_{\mu} = -\langle\psi_i|e^{-\mathrm{i}(\mathbf{k}+\mathbf{g})\mathbf{r}}|\psi_a\rangle\langle\psi_a|e^{\mathrm{i}(\mathbf{k}+\mathbf{g}')\mathbf{r}'}|\psi_i\rangle$ stands for a matrix with the dimension given by the number of reciprocal lattice vectors, satisfying $|\mathbf{g}|^2\hbar/(2m) \leq$ ENCUTGW with ENCUTGW being the energy cutoff for the basis.

Inserting either Eq. (451) into Eq. (447), or Eq. (450) into Eq. (446), the resulting integrals can be carried out analytically, giving rise to an exact expression for the direct MP2 energy

$$E_c^{(2)} = -\frac{1}{2}\sum_{\mu\mu'} \chi_{\mu} V \chi_{\mu'} V \frac{1}{x_{\mu} + x_{\mu'}}. \tag{454}$$

One can avoid the computationally expensive summation over pairs (μ,μ') in Eq. (454) by evaluating the integrals in Eqs. (446) and (447) numerically using an appropriate quadrature

$$E_c^{(2)} \approx -\frac{1}{8\pi}\sum_{k=1}^{N}\gamma_k\{\chi(\mathrm{i}\omega_k)V\}^2, \tag{455}$$

$$E_c^{(2)} \approx -\frac{1}{4}\sum_{i=1}^{N}\sigma_i\{\hat{\chi}(\mathrm{i}\tau_i)V\}^2. \tag{456}$$

To keep the necessary quadrature points N as small as possible, one needs to minimize the discretization error between the exact and approximate direct MP2 energy. To this end, we subtract Eq. (454) from Eq. (455) and substitute $\chi(\mathrm{i}\omega)$ by Eq. (450) obtaining

$$\frac{1}{2}\sum_{\mu\mu'}\chi_\mu V\chi_{\mu'}V\left\{\frac{1}{x_\mu+x_{\mu'}}-\frac{1}{4\pi}\sum_{k=1}^{N}\gamma_k\phi(\omega_k,x_\mu)\phi(\omega_k,x_{\mu'})\right\}. \tag{457}$$

Clearly, we have obtained an error function to be minimized in order to determine the optimal quadrature $(\{\omega_k\}_{k=1}^N,\{\gamma_k\}_{k=1}^N)$ for the frequency domain

$$\mathcal{H}(\vec{\gamma},\vec{\omega},x,x') = \frac{1}{x+x'}-\frac{1}{4\pi}\sum_{k=1}^{N}\gamma_k\phi(\omega_k,x)\phi(\omega_k,x'), \tag{458}$$

with $(x,x')\in[\epsilon_{\mathrm{min}},\epsilon_{\mathrm{max}}]\times[\epsilon_{\mathrm{min}},\epsilon_{\mathrm{max}}]$.

Analogously, subtracting Eq. (454) from Eq. (456), one obtains the error function to be minimized to obtain the optimal quadrature $(\{\tau_i\}_{i=1}^N,\{\sigma_i\}_{i=1}^N)$ for the time domain

$$\hat{\mathcal{H}}(\vec{\sigma},\vec{\tau},x+x') = \frac{1}{x+x'}-\frac{1}{2}\sum_{i=1}^{N}\sigma_i\underbrace{\hat{\phi}(\tau_i,x)\hat{\phi}(\tau_i,x')}_{\mathrm{e}^{-(x+x')\tau_i}}. \tag{459}$$

One can see that in Eq. (459) the error function depends on $x+x'$ only and is essentially one-dimensional. However, the error function in the frequency domain shown in Eq. (458) depends on two linearly independent variables x and x'. Fortunately, the largest errors of $\mathcal{H}$ are on the diagonal $x = x'$ [103]. Therefore, it is a good approximation to consider the one-dimensional problems with the following error functions:

$$\eta(\vec{\gamma},\vec{\omega},x) = \frac{1}{x}-\frac{1}{2\pi}\sum_{k=1}^{N}\gamma_k\phi^2(\omega_k,x) = \frac{1}{x}-\frac{1}{2\pi}\sum_{k=1}^{N}\gamma_k\left(\frac{2x}{x^2+\omega_k^2}\right)^2 \tag{460}$$

$$\hat{\eta}(\vec{\sigma},\vec{\tau},x) = \frac{1}{x}-\sum_{i=1}^{N}\sigma_i\hat{\phi}^2(\tau_i,x) = \frac{1}{x}-\sum_{i=1}^{N}\sigma_i\mathrm{e}^{-2x\tau_i}. \tag{461}$$

By minimizing the error functions $\eta(\vec{\gamma},\vec{\omega},x)$ and $\hat{\eta}(\vec{\sigma},\vec{\tau},x)$ with respect to either $||\cdot||_2$ or $||\cdot||_\infty$ norm, one obtains the least square or Minimax solutions of the quadratures for the frequency and time domain. Actually, it should be noted that VASP first evaluates the numerically more convenient non-scaled optimal quadratures $(\{\omega_k\}_{k=1}^N, \{\gamma_k\}_{k=1}^N)$ and $(\{\tau_i\}_{i=1}^N, \{\sigma_i\}_{i=1}^N)$ for $x \in I = [1, R]$ with $R = \epsilon_{\max}/\epsilon_{\min}$. Scaled optimal quadratures $(\{\omega'_k\}_{k=1}^N, \{\gamma'_k\}_{k=1}^N)$ and $(\{\tau'_i\}_{i=1}^N, \{\sigma'_i\}_{i=1}^N)$ for $x \in [\epsilon_{\min}, \epsilon_{\max}]$ are then obtained straightforwardly by

$$\gamma'_k = \gamma_k \epsilon_{\min}, \quad \omega'_k = \omega_k \epsilon_{\min} \tag{462}$$

$$\sigma'_i = \sigma_i/\epsilon_{\min}, \quad \tau'_i = \tau_i/\epsilon_{\min}. \tag{463}$$

Since the MP2 energy $E_c^{(2)}$ is dominant in the RPA correlation energy E_c^{RPA}, that is $|E_c^{(n)}| < |E_c^{(2)}|$ for $n > 2$, the above resulting quadratures $(\{\omega'_k\}_1^N, \{\gamma'_k\}_1^N)$ and $(\{\tau'_i\}_1^N, \{\sigma'_i\}_1^N)$ obtained from the second order diagram should be applicable for any other higher order diagrams. It has also been found that the two grids are dual to each other. That is, given $\{\mathrm{i}\tau_j\}_{j=1}^N$, the discretization error function is minimal at the grid points $\{\mathrm{i}\omega_k\}_{k=1}^N$, and vice versa [103].

B.2 Temporal discrete Fourier transformations

For an even function F with respect to imaginary time/frequency, such as the polarizability χ, the forward Fourier transformation is given by

$$F(\mathrm{i}\omega) = 2\int_0^\infty \mathrm{d}\tau \cos(\omega\tau) F(\mathrm{i}\tau). \tag{464}$$

A natural question is whether one can obtain a discrete transformation matrix γ_{ki} from the imaginary time to the frequency or the other way around if the optimized quadrature points $(\{\omega_k\}_{k=1}^N, \{\gamma_k\}_{k=1}^N)$ and $(\{\tau_i\}_{i=1}^N, \{\sigma_i\}_{i=1}^N)$ are known and fixed, such that

$$F(\mathrm{i}\omega_k) - \sum_{i=1}^N \gamma_{ki} \cos(\omega_k \tau_i) F(\mathrm{i}\tau_i)$$

is minimized with respect to either $\|\cdot\|_2$ or $\|\cdot\|_\infty$ norm. The answer is yes. This can be done analogous to Appendix (B.1). The coefficients γ_{ki} can be determined by minimizing the error function between the exact and approximate polarizability

$$\begin{aligned}\Omega^c(\boldsymbol{\gamma}, \omega_k, x) &= \chi(\mathrm{i}\omega_k)^{\text{Exact}} - \chi(\mathrm{i}\omega_k)^{\text{Approx.}} \\ &= \sum_\mu \chi_\mu \phi(\omega_k, x_\mu) - \sum_{i=1}^N \gamma_{ki} \cos(\omega_k \tau_i) \sum_\mu \chi_\mu \hat{\phi}(\tau_i, x_\mu) \\ &= \sum_\mu \chi_\mu \Big[\frac{2x_\mu}{x_\mu^2 + \omega_k^2} - \sum_{i=1}^N \gamma_{ki} \cos(\omega_k \tau_i) \mathrm{e}^{-x_\mu \tau_i}\Big].\end{aligned} \tag{465}$$

Finally, we end up with the following error function at each frequency point ω_k for a specific energy difference $x \in [\epsilon_{\min}, \epsilon_{\max}]$:

$$\eta^c(\boldsymbol{\gamma}, \omega_k, x) = \frac{2x}{x^2 + \omega_k^2} - \sum_{i=1}^{N} \gamma_{ki} \cos(\omega_k \tau_i) \mathrm{e}^{-x\tau_i}. \tag{466}$$

Here, the imaginary time $\{\mathrm{i}\tau_i\}_{i=1}^N$ and frequency $\{\mathrm{i}\omega_k\}_{k=1}^N$ grids are precalculated. Specifically, for one frequency point ω_k, one obtains a vector $\{\gamma_{ki}\}$, $\forall i = 1, \cdots, N$. Repeating this for all frequency points $\omega_k, \forall k = 1, \cdots, N$, then one obtains the transformation matrix $[\gamma_{ki}]$, $\forall i, k = 1, \cdots, N$. It should be noted that here the error function $\eta^c(\boldsymbol{\gamma}, \omega_k, x)$, actually, is the quadrature error of integral of $2\int_0^\infty \mathrm{d}\tau \cos(\omega_k \tau) \mathrm{e}^{-x\tau}$

$$\eta^c(\boldsymbol{\gamma}, \omega_k, x) = \underbrace{2\int_0^\infty \mathrm{d}\tau \cos(\omega_k \tau) \mathrm{e}^{-x\tau}}_{\frac{2x}{x^2+\omega_k^2}} - \sum_{i=1}^{N} \gamma_{ki} \cos(\omega_k \tau_i) \mathrm{e}^{-x\tau_i} \tag{467}$$

for the chosen frequency ω_k.

Similarly, the transformation matrix from the imaginary frequency to time domain can be determined by minimizing the error function

$$\begin{aligned} \eta^c(\boldsymbol{\xi}, \tau_i, x) =& \hat{\phi}(\tau_i, x) - \sum_{k=1}^{N} \xi_{ik} \cos(\tau_i \omega_k) \hat{\phi}(\omega_k, x) \\ =& \mathrm{e}^{-x|\tau|_i} - \sum_{k=1}^{N} \xi_{ik} \cos(\tau_i \omega_k) \frac{2x}{x^2 + \omega_k^2}. \end{aligned} \tag{468}$$

Again, the imaginary time $\{\mathrm{i}\tau_i\}_{i=1}^N$ and frequency $\{\mathrm{i}\omega_k\}_{k=1}^N$ grids are precalculated. For one frequency point τ_i, one obtains a vector $\{\xi_{ik}\}$, $\forall k = 1, \cdots, N$. Repeating this for all frequency points $\tau_i, \forall i = 1, \cdots, N$, then one obtains the transformation matrix $[\xi_{ik}]$, $\forall k, i = 1, \cdots, N$. Note that here the error function $\eta^c(\boldsymbol{\xi}, \tau_i, x)$, actually, is the quadrature error of integral $2\int_0^\infty \frac{\mathrm{d}\omega}{2\pi} \cos(\tau_i \omega) \frac{2x}{x^2+\omega^2}$

$$\eta^c(\boldsymbol{\xi}, \tau_i, x) = \underbrace{2\int_0^\infty \frac{\mathrm{d}\omega}{2\pi} \cos(\tau_i \omega) \frac{2x}{x^2 + \omega^2}}_{\mathrm{e}^{-x|\tau|_i}} - \sum_{k=1}^{N} \xi_{ik} \cos(\tau_i \omega_k) \frac{2x}{x^2 + \omega_k^2} \tag{469}$$

In contrast, for an odd function F with respect to imaginary time/frequency, the forward Fourier transformation is described by

$$F(\mathrm{i}\omega) = 2\mathrm{i} \int_0^\infty \mathrm{d}\tau \sin(\omega\tau) F(\mathrm{i}\tau), \tag{470}$$

which is approximated by a discrete sine transformation (ST)

$$F(\mathrm{i}\omega_k) = \mathrm{i}\sum_{j=1}^{N} \lambda_{kj}\sin(\omega_k\tau_j)F(\mathrm{i}\tau_j). \tag{471}$$

Again, $\{\mathrm{i}\tau_j\}_{j=1}^{N}$ and $\{\mathrm{i}\omega_k\}_{k=1}^{N}$ are precalculated and chosen to be identical to the cosine grid. However, the coefficients λ_{kj} are determined by minimizing the error function

$$\eta^s(\boldsymbol{\lambda}, \omega_k, x) = \underbrace{\frac{2\omega_k}{x^2 + \omega_k^2}}_{2\int_0^\infty \mathrm{d}\tau\,\sin(\omega_k\tau)\mathrm{e}^{-x\tau}} - \sum_{j=1}^{N} \lambda_{kj}\sin(\omega_k\tau_j)\mathrm{e}^{-x\tau_j}. \tag{472}$$

The inverse ST is then obtained by

$$F(\mathrm{i}\tau_j) = -\mathrm{i}\sum_{k=1}^{N} \zeta_{jk}\sin(\tau_j\omega_k)F(\mathrm{i}\omega_k), \tag{473}$$

where the matrix $\boldsymbol{\zeta}\,\mathbf{sin}\,(\boldsymbol{\tau\omega})$ is the inverse of the matrix $\boldsymbol{\lambda}\,\mathbf{sin}\,(\boldsymbol{\omega\tau})$ in Eq. (471).

Appendix C Analytic continuation

The generalized mathematical problem of an analytic continuation can be stated as follows: find an analytic function $f(z)$ in the upper complex plane that coincides with calculated values on a discrete set of points

$$f(z_j) = f_j, \quad j = 1, 2....N \tag{474}$$

where (z_j,f_j) are the known point-value pairs of the function. To this end, there are several methods available, for example, the maximum entropy method (MEM) [280], statistical sampling method (SSM) [281], and Padé approximate method (PAM) [109]. In the following, we will recapitulate MEM and PAM methods, but put particular focus on the latter. We refer the readers to those original papers or book for more details.

C.1 Maximum entropy method

MEM is widely used for determining the spectral function $A(\omega)$ given the Green function data sets $G(\mathrm{i}\tau)$ obtained from a quantum Monte-Carlo (QMC) calculation. The starting point is the Fourier transform of the spectral representation of the finite-temperature Green's function

$$G(\mathrm{i}\tau) = \int_{-\infty}^{+\infty} d\omega \frac{e^{\tau(\mu-\omega)}}{1 + e^{\beta(\mu-\omega)}} A(\omega). \tag{475}$$

Here, $\beta = \frac{1}{k_\mathrm{B}T}$ with T being the temperature. From Eq. (475) one can see that the analytical continuation is an ill-conditioned problem: the kernel of Eq. (475) is very small for large frequencies $|\omega|$ so that large changes in $A(\omega)$ have only a small impact on $G(\mathrm{i}\tau)$. This indicates that there might be several possible $A(\omega)$ giving similar solutions for $G(\mathrm{i}\tau)$. Which one is the most accurate one becomes an elusive issue. To address this problem, M. Jarrella and J.E. Gubernatisb [280] proposed the maximum entropy method that is based on the Bayesian theorem. The essence of the MEM is that the most likely spectral function $A(\omega)$ is the one that maximizes *a posteriori* probability [280]

$$P(A|G) = P(G|A)P(A)/P(G), \tag{476}$$

where $P(G)$ is a constant for a given Green function, and the conditional probability $P(G|A)$ and *a priori* probability $P(A)$, respectively, can be obtained by [280]

$$P(G|A) = e^{-\frac{\chi^2}{2}} \tag{477}$$

$$P(A) \sim e^{\alpha S}, \tag{478}$$

where χ^2 is the quadratic difference between given $G(\mathrm{i}\tau)$ and that obtained from $A(\omega)$ by Eq. (475), α is a constant that should be chosen very carefully (see Ref. [280]) and S is the entropy, which is calculated by [280]

$$S = \int_{-\omega_0/2}^{+\omega_0/2} d\omega A(\omega) \ln[A(\omega)\omega_0]. \tag{479}$$

Generally speaking, the MEM is a good method in particular for the cases where the data sets have large noise, e.g., the data obtained from quantum Monte-Carlo (QMC), for which MEM provides an efficient way to make the statistical errors as small as possible. In addition, it can provide reliable features at small frequencies, such as the height and width of the central peak, and the overall weight and position of the Hubbard bands. However, it has disadvantages in the sense that it requires a reasonable default model. Besides, because of the statistical errors in the QMC calculations and because Eq. (475) is ill-conditioned for large $|\omega|$, MEM thus cannot resolve fine details at large frequencies. Statistical sampling method (SSM) improves the analytic continuation in the sense that it does not require a default model and can resolve the structure on a very small energy scale [281]. However, both MEM and SSM can not predict accurate poles of the function to be fitted. In our low-scaling GW method, the self-energy is exact without any noise and we are mainly concerned with the calculation of the quasiparticle energies. Therefore, MEM and SSM are not desirable methods for our case. Instead, the Padé approximate method tends to represent well the position and weight of low-energy features in the spectral functions, which are exactly what we desire. In the following we will focus on the Padé approximate method.

C.2 Padé approximate method

A Padé approximant can be expressed as a $[k/r]$ rational polynomial [282]:

$$f(z) = \frac{\sum_{i=1}^{k+1} p_i z^{i-1}}{\sum_{i=1}^{r} q_i z^{i-1} + z^r}, \tag{480}$$

where p_i and q_i are the unknown complex coefficients to be determined given the known data sets (z_j, f_j). Since the correlated self-energy $\Sigma^c(\mathrm{i}\omega)$ has asymptotes $A/\mathrm{i}\omega$, it is suitably fitted using a $[(r-1)/r]$ Padé approximant [282]

$$f(z) = \frac{\sum_{i=1}^{r} p_i z^{i-1}}{\sum_{i=1}^{r} q_i z^{i-1} + z^r} = \frac{p_1 + p_2 z + \ldots\ldots + p_r z^{r-1}}{q_1 + q_2 z + \ldots\ldots + q_r z^{r-1} + z^r}. \tag{481}$$

To solve this Padé fitting, there are three methods that are commonly used: Mutipole expansion (ME), least-squares (LS) method and Thiele's reciprocal difference (TRD) method.

C.2.1 Multipole expansion method

Multipole expansion method is first explored by Godby *et al.* [96,102] in analytically continuing the self-energy to the real frequency axis by taking into account the pole structure of the self-energy

$$\Sigma(i\omega) = a_0 + \sum_{k=1}^{n} \frac{a_k}{i\omega - z_k}, \tag{482}$$

where a_0, a_k and z_k are complex numbers. n is the number of poles. This is easily implemented by calling the Levenberg-Marquardt routine [283]. In the following, we will give more details as to how ME is implemented.

In our case, instead of fitting the self-energy Σ directly, we apply the model to the Green's function G since it has a more favorable structure than the self-energy. G is calculated from the self-energy by the Dyson equation

$$G(i\omega) = \frac{1}{i\omega + E_F - \Sigma(i\omega)}. \tag{483}$$

In order to avoid dealing with complex numbers, a block vector $\vec{y}$ is created that contains both the real and imaginary parts of $G(i\omega)$

$$\vec{y} = [(\mathrm{Re}[G(i\omega_j)], j = 0, ...N-1), (\mathrm{Im}[G(i\omega_j)], j = 0, ...N-1)]. \tag{484}$$

To avoid branch cuts, only positive frequency points are used. To use the Levenberg-Marquardt routine, the function and its derivative at each frequency point should be provided. To this aim, we introduce

$$a_k = b_k + ic_k \tag{485}$$

$$z_k = x_k + iy_k. \tag{486}$$

Then, the real and imaginary parts of Green's functions read

$$\mathrm{Re}[G(i\omega)] = b_0 + \sum_{k=1}^{n} \frac{c_k(\omega - y_k) - b_k x_k}{x_k^2 + (\omega - y_k)^2} \tag{487}$$

$$\mathrm{Im}[G(i\omega)] = c_0 + \sum_{k=1}^{n} \frac{-b_k(\omega - y_k) - c_k y_k}{x_k^2 + (\omega - y_k)^2}. \tag{488}$$

The derivatives with respect to the parameters are given by

$$\frac{\partial \mathrm{Re}[G(i\omega)]}{\partial b_0} = 1 \tag{489}$$

$$\frac{\partial \mathrm{Re}[G(i\omega)]}{\partial c_0} = 0 \tag{490}$$

$$\frac{\partial \mathrm{Re}[G(i\omega)]}{\partial b_k} = \frac{-x_k}{x_k^2 + (\omega - y_k)^2} \tag{491}$$

$$\frac{\partial \mathrm{Re}[G(i\omega)]}{\partial c_k} = \frac{\omega - y_k}{x_k^2 + (\omega - y_k)^2} \tag{492}$$

$$\frac{\partial \mathrm{Re}[G(i\omega)]}{\partial x_k} = \frac{-b_k(x_k^2 + (\omega - y_k)^2) - (c_k(\omega - y_k) - b_k x_k)2x_k}{(x_k^2 + (\omega - y_k)^2)^2} \tag{493}$$

$$\frac{\partial \mathrm{Re}[G(i\omega)]}{\partial y_k} = \frac{-c_k(x_k^2 + (\omega - y_k)^2) + (c_k(\omega - y_k) - b_k x_k)2(\omega - y_k)}{(x_k^2 + (\omega - y_k)^2)^2} \tag{494}$$

$$\frac{\partial \mathrm{Im}[G(i\omega)]}{\partial b_0} = 0 \tag{495}$$

$$\frac{\partial \mathrm{Im}[G(i\omega)]}{\partial c_0} = 1 \tag{496}$$

$$\frac{\partial \mathrm{Im}[G(i\omega)]}{\partial b_k} = \frac{-(\omega - y_k)}{x_k^2 + (\omega - y_k)^2} \tag{497}$$

$$\frac{\partial \mathrm{Im}[G(i\omega)]}{\partial c_k} = \frac{-x_k}{x_k^2 + (\omega - y_k)^2} \tag{498}$$

$$\frac{\partial \mathrm{Im}[G(i\omega)]}{\partial x_k} = \frac{-c_k(x_k^2 + (\omega - y_k)^2) + (b_k(\omega - y_k) + c_k x_k)2x_k}{(x_k^2 + (\omega - y_k)^2)^2} \tag{499}$$

$$\frac{\partial \mathrm{Im}[G(i\omega)]}{\partial y_k} = \frac{b_k(x_k^2 + (\omega - y_k)^2) - (b_k(\omega - y_k) - c_k x_k)2(\omega - y_k)}{(x_k^2 + (\omega - y_k)^2)^2}. \tag{500}$$

Once the parameters have been obtained, one can perform the analytic continuation to the real frequency axis by

$$G(\omega) = a_0 + \sum_{k=1}^{n} \frac{a_k}{\omega - E_F - z_k}. \tag{501}$$

However, it turns out that it is rather unstable when the number of poles exceeds three. The fitted parameters are too sensitive to the initial parameters. The 2-pole model is always robust, but it results in a poor fit. This also holds for the 3-pole model, though it is physically sound. The 4-pole model yields the best fit, but it is rather unstable, even though we started from the parameters of the 2-pole or 3-pole models. The models beyond 4 poles are generally unstable.

C.2.2 Least-squares (LS) method

Inserting Eq. (474) into Eq. (481) for each known points (z_j,f_j) and defining a vector of unknowns [110, 282]

$$\mathbf{x} = [p_1, p_2, ..., p_r, q_1, q_2, ..., q_r]^{\mathbf{T}}, \tag{502}$$

one could easily obtain the following linear system of equations [110, 282]

$$\mathbf{Ax{=}b}, \tag{503}$$

where the matrix **A** and right-hand-side vector **b**, respectively, are expressed as [110, 282]

$$\mathbf{A} = \begin{pmatrix} 1 & z_1 & z_1^2 & ... & z_1^{r-1} & -f_1 & -f_1 z_1 & ... & -f_1 z_1^{r-1} \\ 1 & z_2 & z_2^2 & ... & z_2^{r-1} & -f_2 & -f_2 z_2 & ... & -f_2 z_2^{r-1} \\ 1 & z_3 & z_3^2 & ... & z_3^{r-1} & -f_3 & -f_3 z_3 & ... & -f_3 z_3^{r-1} \\ ... & ... & ... & ... & ... & ... & ... & ... & ... \\ ... & ... & ... & ... & ... & ... & ... & ... & ... \\ 1 & z_M & z_M^2 & ... & z_M^{r-1} & -f_M & -f_M z_M & ... & -f_M z_M^{r-1} \end{pmatrix} \tag{504}$$

$$\mathbf{b} = [f_1 z_1^r, f_2 z_2^r, ..., f_M z_M^r]^{\mathbf{T}}. \tag{505}$$

It is found that the precision of input points plays an important role in how good the Padé fit is. In addition, as the number of frequencies N increases to a large number, the condition number of the matrix **A**, however, rapidly increases, which makes the LS ill-defined. For our low-scaling GW implementation, the GW self-energies can be obtained with a high precision and the optimized grids used yield linear equations that are remarkably linearly independent. From our tests, it is, however, found that the LS method works almost equally well with the Thiele's reciprocal difference method, as will be introduced below, except for few cases. In order to improve the condition number of the matrix **A**, one possible solution is to use bound Lagrange polynomials instead of the rational polynomials.

C.2.3 Thiele's reciprocal difference (TRD) method

In the TRD method, the Padé approximate $P_N(z)$ is expressed by a continued fraction expansion [109]

$$
\begin{aligned}
P_N(z) &= \frac{a_1}{1+}\,\frac{a_2(z-z_1)}{1+}\cdots\frac{a_N(z-z_{N-1})}{1+(z-z_N)g_{N+1}(z)} &(506)\\
&= \cfrac{a_1}{1+\cfrac{a_2(z-z_1)}{1+\cfrac{a_3(z-z_2)}{1+\cfrac{\cdots}{1+\cfrac{a_N(z-z_{N-1})}{1+(z-z_N)g_{N+1}(z)}}}}}, &(507)
\end{aligned}
$$

where the complex coefficients a_n are given by the following recursion relations:

$$
\begin{aligned}
a_n = g_n(z_n), \quad g_1(z_n) = f_n, \quad n = 1, ..., N &\qquad (508)\\
g_n(z) = \frac{g_{n-1}(z_{n-1}) - g_{n-1}(z)}{(z-z_{n-1})g_{n-1}(z)}. &\qquad (509)
\end{aligned}
$$

It is straightforward to prove from the above recursion relations that [109]

$$P_N(z_j) = f_j, \quad j = 1, ..., N \qquad (510)$$

holds for the known point-value pairs $\{z_i, f_j\}_{j=1}^{N}$ of the function $f(z)$ (the diagonal elements of the self-energy in the G_0W_0r case).

This method is very simple and not difficult to implement and it has been successfully applied to the analytic continuation of dynamic response functions [284]. It is also found that the TRD method is rather efficient and robust except for few cases where there are poles close to the DFT eigenvalues. In general, the TRD and LS methods work equally well for most cases. In our practical implementation, however, we combine the TRD and LS methods and choose a more reasonable value from one of them.

Appendix D Derivation of the head of intra-band dielectric functions

We start from the independent polarizability in the reciprocal space and imaginary frequency domain, which has been derived in Appendix (G)

$$\begin{aligned}\chi_{\mathbf{G},\mathbf{G}'}(\mathbf{q},\mathrm{i}\omega) &= -\frac{1}{\Omega_0}\sum_{\mathbf{k}}^{\mathrm{BZ}}\sum_{i}^{\mathrm{occ}}\sum_{a}^{\mathrm{unocc}}\frac{2(\epsilon_{a\mathbf{k}+\mathbf{q}}-\epsilon_{i\mathbf{k}})}{(\epsilon_{a\mathbf{k}+\mathbf{q}}-\epsilon_{i\mathbf{k}})^2+\omega^2}\langle\phi_{i\mathbf{k}}|\mathrm{e}^{-\mathrm{i}(\mathbf{q}+\mathbf{G})\mathbf{r}}|\phi_{a\mathbf{k}+\mathbf{q}}\rangle\langle\phi_{a\mathbf{k}+\mathbf{q}}|\mathrm{e}^{\mathrm{i}(\mathbf{q}+\mathbf{G}')\mathbf{r}'}|\phi_{i\mathbf{k}}\rangle\\ &= -\frac{1}{\Omega_0}\sum_{\mathbf{k}}^{\mathrm{BZ}}\sum_{i}^{\mathrm{occ}}\sum_{a}^{\mathrm{unocc}}\frac{2(\epsilon_{a\mathbf{k}+\mathbf{q}}-\epsilon_{i\mathbf{k}})}{(\epsilon_{a\mathbf{k}+\mathbf{q}}-\epsilon_{i\mathbf{k}})^2+\omega^2}\langle u_{i\mathbf{k}}|\mathrm{e}^{-\mathrm{i}\mathbf{G}\mathbf{r}}|u_{a\mathbf{k}+\mathbf{q}}\rangle\langle u_{a\mathbf{k}+\mathbf{q}}|\mathrm{e}^{\mathrm{i}\mathbf{G}'\mathbf{r}'}|u_{i\mathbf{k}}\rangle,\end{aligned} \tag{511}$$

where $\epsilon_{i\mathbf{k}}$ is the eigenvalue of state $(i,\mathbf{k})$ and $u_{i\mathbf{k}}(\mathbf{r})$ is the cell periodic part of a one-electron orbital $\phi_{i\mathbf{k}}(\mathbf{r})$. Ω_0 is the volume of the unit cell. The intra-band polarizability ($i = a = n \in p.f.$, where $p.f.$ indicates the partially filled bands) can be calculated as

$$\chi^{\mathrm{intra}}_{\mathbf{G},\mathbf{G}'}(\mathbf{q},\mathrm{i}\omega) = -\frac{1}{\Omega_0}\sum_{\mathbf{k}}^{\mathrm{BZ}}\sum_{n}^{p.f.}\frac{2(\epsilon_{n\mathbf{k}+\mathbf{q}}-\epsilon_{n\mathbf{k}})}{(\epsilon_{n\mathbf{k}+\mathbf{q}}-\epsilon_{n\mathbf{k}})^2+\omega^2}\langle u_{n\mathbf{k}}|e^{-\mathrm{i}\mathbf{G}\mathbf{r}}|u_{n\mathbf{k}+\mathbf{q}}\rangle\langle u_{n\mathbf{k}+\mathbf{q}}|e^{\mathrm{i}\mathbf{G}'\mathbf{r}'}|u_{n\mathbf{k}}\rangle. \tag{512}$$

The intra-band dielectric function can then be calculated by

$$\begin{aligned}\varepsilon^{\mathrm{intra}}_{\mathbf{G},\mathbf{G}'}(\mathbf{q},\mathrm{i}\omega) &= -\frac{4\pi e^2}{|\mathbf{q}+\mathbf{G}||\mathbf{q}+\mathbf{G}'|}\chi^{\mathrm{intra}}_{\mathbf{G},\mathbf{G}'}(\mathbf{q},\mathrm{i}\omega)\\ &= \frac{4\pi e^2}{|\mathbf{q}+\mathbf{G}||\mathbf{q}+\mathbf{G}'|}\frac{1}{\Omega_0}\sum_{\mathbf{k}}\sum_{n}^{p.f.}\frac{2(\epsilon_{n\mathbf{k}+\mathbf{q}}-\epsilon_{n\mathbf{k}})}{(\epsilon_{n\mathbf{k}+\mathbf{q}}-\epsilon_{n\mathbf{k}})^2+\omega^2}\\ &\quad\times\langle u_{n\mathbf{k}+\mathbf{q}}|e^{\mathrm{i}\mathbf{G}\mathbf{r}}|u_{n\mathbf{k}}\rangle\langle u_{n\mathbf{k}}|e^{-\mathrm{i}\mathbf{G}'\mathbf{r}'}|u_{n\mathbf{k}+\mathbf{q}}\rangle.\end{aligned} \tag{513}$$

In the long-wave ($\mathbf{q} \to 0$) limit, the head ($\mathbf{G} = \mathbf{G}' = 0$) of the intra-band dielectric function diverges because it is divided by ($|\mathbf{q}|^2 \to 0$). Thus, special considerations should be taken. Now we explicitly write down the head of the intra-band dielectric function

$$\varepsilon^{\mathrm{intra}}_{0,0}(\mathbf{q}\to 0,\mathrm{i}\omega) = \lim_{\mathbf{q}\to 0}\frac{1}{\Omega_0}\frac{4\pi e^2}{|\mathbf{q}|^2}\sum_{\mathbf{k}}^{\mathrm{BZ}}\sum_{n}^{p.f.}\frac{2(\epsilon_{n\mathbf{k}+\mathbf{q}}-\epsilon_{n\mathbf{k}})}{(\epsilon_{n\mathbf{k}+\mathbf{q}}-\epsilon_{n\mathbf{k}})^2+\omega^2}|\langle u_{n\mathbf{k}+\mathbf{q}}\mid u_{n\mathbf{k}}\rangle|^2. \tag{514}$$

By Taylor expansion of $u_{n\mathbf{k}+\mathbf{q}}$ around $\mathbf{q} \to 0$, we obtain

$$\begin{aligned}\langle u_{n\mathbf{k}+\mathbf{q}}\mid u_{n\mathbf{k}}\rangle =&\langle u_{n\mathbf{k}}\mid u_{n\mathbf{k}}\rangle + \mathbf{q}\langle\nabla_{\mathbf{k}}u_{n\mathbf{k}}\mid u_{n\mathbf{k}}\rangle + O(\mathbf{q}^2)\\ \approx&1 + O(\mathbf{q}^2).\end{aligned} \tag{515}$$

In deriving Eq. (515), we have used the fact that $\langle u_{n\mathbf{k}}|u_{n\mathbf{k}}\rangle = 1$ and $\nabla_{\mathbf{k}}u_{n\mathbf{k}}$ is nearly orthogonal to $u_{n\mathbf{k}}$ so that the second term $\mathbf{q}\langle\nabla_{\mathbf{k}}u_{n\mathbf{k}}\mid u_{n\mathbf{k}}\rangle$ is negligible. By Taylor expansion of transition energy $\epsilon_{n\mathbf{k}+\mathbf{q}} - \epsilon_{n\mathbf{k}}$ around $\mathbf{q} \to 0$, we obtain

$$\begin{aligned}\epsilon_{n\mathbf{k}+\mathbf{q}} - \epsilon_{n\mathbf{k}} =& \mathbf{q} \nabla_{\mathbf{k}} \epsilon_{n\mathbf{k}} + \frac{1}{2}\mathbf{q}^2 \nabla_{\mathbf{k}}^2 \epsilon_{n\mathbf{k}} + O(\mathbf{q}^3) \\ =& \frac{1}{2}\mathbf{q}^2 \nabla_{\mathbf{k}}^2 \epsilon_{n\mathbf{k}} + O(\mathbf{q}^3).\end{aligned} \tag{516}$$

In deriving Eq. (516), we have used the fact that $\mathbf{q} \nabla_{\mathbf{k}} \epsilon_{n\mathbf{k}}$ is an odd function in $\mathbf{k}$ and thus its summation over $\mathbf{k}$ is vanishing. Considering $\epsilon_{n\mathbf{k}+\mathbf{q}} - \epsilon_{n\mathbf{k}} \ll \omega$, we obtain

$$\begin{aligned}\frac{2(\epsilon_{n\mathbf{k}+\mathbf{q}} - \epsilon_{n\mathbf{k}})}{(\epsilon_{n\mathbf{k}+\mathbf{q}} - \epsilon_{n\mathbf{k}})^2 + \omega^2} =& \frac{2(\epsilon_{n\mathbf{k}+\mathbf{q}} - \epsilon_{n\mathbf{k}})}{\omega^2} \frac{1}{1 + (\frac{\epsilon_{n\mathbf{k}+\mathbf{q}} - \epsilon_{n\mathbf{k}}}{\omega})^2} \\ =& \frac{2(\epsilon_{n\mathbf{k}+\mathbf{q}} - \epsilon_{n\mathbf{k}})}{\omega^2} \left\{1 - (\frac{\epsilon_{n\mathbf{k}+\mathbf{q}} - \epsilon_{n\mathbf{k}}}{\omega})^2 + O[(\frac{\epsilon_{n\mathbf{k}+\mathbf{q}} - \epsilon_{n\mathbf{k}}}{\omega})^4]\right\} \\ =& \frac{\mathbf{q}^2 \nabla_{\mathbf{k}}^2 \epsilon_{n\mathbf{k}}}{\omega^2} + O(\mathbf{q}^6)\end{aligned} \tag{517}$$

Inserting Eq. (517) and Eq. (515) into Eq. (514), we finally obtain

$$\varepsilon_{0,0}^{\text{intra}}(\mathbf{q} \to 0, \mathrm{i}\omega) = \frac{1}{\omega^2} \frac{4\pi e^2}{\Omega_0} \sum_{\mathbf{k}}^{\text{BZ}} \sum_{n}^{p.f.} \nabla_{\mathbf{k}}^2 \epsilon_{n\mathbf{k}}. \tag{518}$$

Using the squared plasma frequency

$$\omega_{\text{plasma}}^2 = \frac{4\pi e^2}{\Omega_0} \sum_{\mathbf{k}}^{\text{BZ}} \sum_{n}^{p.f.} \nabla_{\mathbf{k}}^2 \epsilon_{n\mathbf{k}}, \tag{519}$$

we obtain a simple expression for the head of intra-band dielectric function

$$\varepsilon_{0,0}^{\text{intra}}(\mathbf{q} \to 0, \mathrm{i}\omega) = \frac{\omega_{\text{plasma}}^2}{\omega^2}. \tag{520}$$

It should be noted that for the wings ($\mathbf{G} = 0$ or $\mathbf{G}' = 0$) and body ($\mathbf{G} \neq 0$ and $\mathbf{G}' \neq 0$) of the intra-band dielectric function, it can be proved that they are both zero [wings=$O(\mathbf{q})$, body=$O(\mathbf{q}^2)$].

Appendix E Derivation of the self-energy within PAW

In this appendix, I will show in more details how the self-energy is derived within the framework of the PAW. To this end, there are two alternatives: one starts with the direct Møller-Plesset (MP2) energy using the relationship between MP2 energy and self-energy, and the other is directly obtained from the definitions of the Green's functions and self-energy.

E.1 Indirect motivation from the direct MP2 energy

To derive the one-electron self-energy in second order

$$\Sigma(\mathbf{r},\mathbf{R}',\mathrm{i}\tau) = -G(\mathbf{r},\mathbf{R}',\mathrm{i}\tau)W(\mathbf{r},\mathbf{R}',\mathrm{i}\tau) \tag{521}$$

within the PAW, it is advantageous to start from the equation for the Laplace transformed direct MP2 energy (LT-dMP2)

$$E^{\mathrm{MP2}} = -2\mathrm{Tr}\left[\overline{G}(\mathbf{R}',\mathbf{r},\mathrm{i}\tau)\underline{G}(\mathbf{r},\mathbf{R}',-\mathrm{i}\tau)W(\mathbf{r},\mathbf{R}',\mathrm{i}\tau)\right]. \tag{522}$$

Here, $\underline{G}(\mathbf{r},\mathbf{R}',-\mathrm{i}\tau)$ and $\overline{G}(\mathbf{r},\mathbf{R}',\mathrm{i}\tau)$ are the Green's functions for occupied and unoccupied states, respectively. $W(\mathbf{r},\mathbf{R}',\mathrm{i}\tau)$ is the screened Coulomb interaction in second order $W = V\chi V$ with V and $\chi = GG$ being the bare Coulomb interaction and independent-particle polarizability, respectively. With the definition of the self-energy in Eq. (521), Eq. (522) can be rewritten as

$$E^{\mathrm{MP2}} = 2\mathrm{Tr}\left[\overline{G}(\mathbf{R}',\mathbf{r},\mathrm{i}\tau)\underline{\Sigma}(\mathbf{r},\mathbf{R}',-\mathrm{i}\tau)\right], \tag{523}$$

where $\underline{\Sigma}(\mathbf{r},\mathbf{R}',-\mathrm{i}\tau)$ is the self-energy for the occupied states. In the following, we just show the derivation for the occupied self-energy $\underline{\Sigma}(\mathbf{r},\mathbf{R}',-\mathrm{i}\tau)$ only, while the derivation for the unoccupied self-energy $\overline{\Sigma}(\mathbf{r},\mathbf{R}',\mathrm{i}\tau)$ is similar and straightforward.

We are now going to rewrite the formula for LT-dMP2 using the representations of the Green's functions within the PAW method. This will help us to distil the structure required to represent the self-energy within the PAW method. We first concentrate on the object inside of the trace in Eq. (522), i.e., on

$$\overline{G}(\mathbf{R}',\mathbf{r},\mathrm{i}\tau)\underline{G}(\mathbf{r},\mathbf{R}',-\mathrm{i}\tau)W(\mathbf{r},\mathbf{R}',\mathrm{i}\tau). \tag{524}$$

Using the definitions for the unoccupied Green's functions in Eqs. (228–231) and the occupied Green's functions in Eqs. (232–235) the object inside of the trace operator then reads

$$\begin{aligned}
&\overline{G}(\mathbf{R}',\mathbf{r},\mathrm{i}\tau)\underline{G}(\mathbf{r},\mathbf{R}',-\mathrm{i}\tau)W(\mathbf{r},\mathbf{R}',\mathrm{i}\tau)\\
&=\overline{G}^{(1)}(\mathbf{R}',\mathbf{r},\mathrm{i}\tau)\underline{G}^{(1)}(\mathbf{r},\mathbf{R}',-\mathrm{i}\tau)W(\mathbf{r},\mathbf{R}',\mathrm{i}\tau)\\
&+\sum_{\mu\nu}\overline{G}^{(2)}(\mathbf{R}',\mu,\mathrm{i}\tau)\underline{G}^{(2)}(\nu,\mathbf{R}',-\mathrm{i}\tau)Q_{\mu\nu}(\mathbf{r})W(\mathbf{r},\mathbf{R}',\mathrm{i}\tau),\\
&+\sum_{\alpha\beta}\overline{G}^{(3)}(\beta,\mathbf{r},\mathrm{i}\tau)\underline{G}^{(3)}(\mathbf{r},\alpha,-\mathrm{i}\tau)W(\mathbf{r},\mathbf{R}',\mathrm{i}\tau)Q_{\alpha\beta}(\mathbf{R}'),\\
&+\sum_{\mu\nu\alpha\beta}\overline{G}^{(4)}(\beta,\mu,\mathrm{i}\tau)\underline{G}^{(4)}(\nu,\alpha,-\mathrm{i}\tau)Q_{\mu\nu}(\mathbf{r})W(\mathbf{r},\mathbf{R}',\mathrm{i}\tau)Q_{\alpha\beta}(\mathbf{R}').
\end{aligned}\tag{525}$$

With this, the direct MP2 energy can be expressed by

$$\begin{aligned}
\frac{1}{2}E^{\mathrm{MP2}}=&-\sum_{\mathbf{r}\in C}\sum_{\mathbf{R}'\in S}\overline{G}^{(1)}(\mathbf{R}',\mathbf{r},\mathrm{i}\tau)\underline{G}^{(1)}(\mathbf{r},\mathbf{R}',-\mathrm{i}\tau)W(\mathbf{r},\mathbf{R}',\mathrm{i}\tau)\\
&-\sum_{\mathbf{r}\in C}\sum_{\mathbf{R}'\in S}\sum_{\mu\nu}\overline{G}^{(2)}(\mathbf{R}',\mu,\mathrm{i}\tau)\underline{G}^{(2)}(\nu,\mathbf{R}',-\mathrm{i}\tau)Q_{\mu\nu}(\mathbf{r})W(\mathbf{r},\mathbf{R}',\mathrm{i}\tau),\\
&-\sum_{\mathbf{r}\in C}\sum_{\mathbf{R}'\in S}\sum_{\alpha\beta}\overline{G}^{(3)}(\beta,\mathbf{r},\mathrm{i}\tau)\underline{G}^{(3)}(\mathbf{r},\alpha,-\mathrm{i}\tau)W(\mathbf{r},\mathbf{R}',\mathrm{i}\tau)Q_{\alpha\beta}(\mathbf{R}'),\\
&-\sum_{\mathbf{r}\in C}\sum_{\mathbf{R}'\in S}\sum_{\mu\nu\alpha\beta}\overline{G}^{(4)}(\beta,\mu,\mathrm{i}\tau)\underline{G}^{(4)}(\nu,\alpha,-\mathrm{i}\tau)Q_{\mu\nu}(\mathbf{r})W(\mathbf{r},\mathbf{R}',\mathrm{i}\tau)Q_{\alpha\beta}(\mathbf{R}').
\end{aligned}\tag{526}$$

We now define quantities $D^{(2)}$, $D^{(3)}$ and $D^{(4)}$

$$D^{(2)}(\mu\nu,\mathbf{R}',\mathrm{i}\tau) = \sum_{\mathbf{r}\in C}Q_{\mu\nu}(\mathbf{r})W(\mathbf{r},\mathbf{R}',\mathrm{i}\tau),\tag{527}$$

$$D^{(3)}(\mathbf{r},\alpha\beta,\mathrm{i}\tau) = \sum_{\mathbf{R}'\in S}W(\mathbf{r},\mathbf{R}',\mathrm{i}\tau)Q_{\alpha\beta}(\mathbf{R}'),\tag{528}$$

$$D^{(4)}(\mu\nu,\alpha\beta,\mathrm{i}\tau) = \sum_{\mathbf{r}\in C}\sum_{\mathbf{R}'\in S}Q_{\mu\nu}(\mathbf{r})W(\mathbf{r},\mathbf{R}',\mathrm{i}\tau)Q_{\alpha\beta}(\mathbf{R}').\tag{529}$$

Then Eq. (526) reduces to

$$\begin{aligned}
\frac{1}{2}E^{\mathrm{MP2}}=&-\sum_{\mathbf{r}\in C}\sum_{\mathbf{R}'\in S}\overline{G}^{(1)}(\mathbf{R}',\mathbf{r},\mathrm{i}\tau)\underline{G}^{(1)}(\mathbf{r},\mathbf{R}',-\mathrm{i}\tau)W(\mathbf{r},\mathbf{R}',\mathrm{i}\tau)\\
&-\sum_{\mathbf{R}'\in S}\sum_{\mu\nu}\overline{G}^{(2)}(\mathbf{R}',\mu,\mathrm{i}\tau)\underline{G}^{(2)}(\nu,\mathbf{R}',-\mathrm{i}\tau)D^{(2)}(\mu\nu,\mathbf{R}',\mathrm{i}\tau),\\
&-\sum_{\mathbf{r}\in C}\sum_{\alpha\beta}\overline{G}^{(3)}(\beta,\mathbf{r},\mathrm{i}\tau)\underline{G}^{(3)}(\mathbf{r},\alpha,-\mathrm{i}\tau)D^{(3)}(\mathbf{r},\alpha\beta,\mathrm{i}\tau),\\
&-\sum_{\mu\nu\alpha\beta}\overline{G}^{(4)}(\beta,\mu,\mathrm{i}\tau)\underline{G}^{(4)}(\nu,\alpha,-\mathrm{i}\tau)D^{(4)}(\mu\nu,\alpha\beta,\mathrm{i}\tau).
\end{aligned}\tag{530}$$

By comparing Eq. (530) with Eq. (523), we finally obtain a useful definition of the self-energy within the PAW scheme

$$\begin{aligned}
\underline{\Sigma}^{(1)}(\mathbf{r},\mathbf{R}',-\mathrm{i}\tau) &= -\underline{G}^{(1)}(\mathbf{r},\mathbf{R}',-\mathrm{i}\tau)W(\mathbf{r},\mathbf{R}',\mathrm{i}\tau), && (531)\\
\underline{\Sigma}^{(2)}(\mu,\mathbf{R}',-\mathrm{i}\tau) &= -\sum_{\nu}\underline{G}^{(2)}(\nu,\mathbf{R}',-\mathrm{i}\tau)D^{(2)}(\mu\nu,\mathbf{R}',\mathrm{i}\tau), && (532)\\
\underline{\Sigma}^{(3)}(\mathbf{r},\beta,-\mathrm{i}\tau) &= -\sum_{\alpha}\underline{G}^{(3)}(\mathbf{r},\alpha,-\mathrm{i}\tau)D^{(3)}(\mathbf{r},\alpha\beta,\mathrm{i}\tau), && (533)\\
\underline{\Sigma}^{(4)}(\mu,\beta,-\mathrm{i}\tau) &= -\sum_{\nu\alpha}\underline{G}^{(4)}(\nu,\alpha,-\mathrm{i}\tau)D^{(4)}(\mu\nu,\alpha\beta,\mathrm{i}\tau). && (534)
\end{aligned}$$

The derivation of the unoccupied self-energy $\overline{\Sigma}$ is simply done by replacing $\underline{G}$ with $\overline{G}$

$$\begin{aligned}
\overline{\Sigma}^{(1)}(\mathbf{r},\mathbf{R}',\mathrm{i}\tau) &= -\overline{G}^{(1)}(\mathbf{r},\mathbf{R}',\mathrm{i}\tau)W(\mathbf{r},\mathbf{R}',\mathrm{i}\tau), && (535)\\
\overline{\Sigma}^{(2)}(\mu,\mathbf{R}',\mathrm{i}\tau) &= -\sum_{\nu}\overline{G}^{(2)}(\nu,\mathbf{R}',\mathrm{i}\tau)D^{(2)}(\mu\nu,\mathbf{R}',\mathrm{i}\tau), && (536)\\
\overline{\Sigma}^{(3)}(\mathbf{r},\beta,\mathrm{i}\tau) &= -\sum_{\alpha}\overline{G}^{(3)}(\mathbf{r},\alpha,\mathrm{i}\tau)D^{(3)}(\mathbf{r},\alpha\beta,\mathrm{i}\tau), && (537)\\
\overline{\Sigma}^{(4)}(\mu,\beta,\mathrm{i}\tau) &= -\sum_{\nu\alpha}\overline{G}^{(4)}(\nu,\alpha,\mathrm{i}\tau)D^{(4)}(\mu\nu,\alpha\beta,\mathrm{i}\tau). && (538)
\end{aligned}$$

In the second step, the matrix elements of the self-energy in the orbital basis are then obtained by

$$\begin{aligned}
\underline{\Sigma}^{(\mathbf{k})}_{\mathrm{nn}}(-\mathrm{i}\tau) = &\sum_{\mathbf{r}\in C}\sum_{\mathbf{R}'\in S}\tilde{\psi}^{*}_{n\mathbf{k}}(\mathbf{r})\underline{\Sigma}^{(1)}(\mathbf{r},\mathbf{R}',-\mathrm{i}\tau)\tilde{\psi}_{n\mathbf{k}}(\mathbf{R}')\\
&+\sum_{\mu}\sum_{\mathbf{R}'\in S}\langle\tilde{\psi}_{n\mathbf{k}}|\tilde{p}_{\mu}\rangle\underline{\Sigma}^{(2)}(\mu,\mathbf{R}',-\mathrm{i}\tau)\tilde{\psi}_{n\mathbf{k}}(\mathbf{R}')\\
&+\sum_{\mathbf{r}\in C}\sum_{\beta}\tilde{\psi}^{*}_{n\mathbf{k}}(\mathbf{r})\underline{\Sigma}^{(3)}(\mathbf{r},\beta,-\mathrm{i}\tau)\langle\tilde{p}_{\beta}|\tilde{\psi}_{n\mathbf{k}}\rangle\\
&+\sum_{\mu}\sum_{\beta}\langle\tilde{\psi}_{n\mathbf{k}}|\tilde{p}_{\mu}\rangle\underline{\Sigma}^{(4)}(\mu,\beta,-\mathrm{i}\tau)\langle\tilde{p}_{\beta}|\tilde{\psi}_{n\mathbf{k}}\rangle.
\end{aligned}\tag{539}$$

$$\begin{aligned}
\overline{\Sigma}^{(\mathbf{k})}_{\mathrm{nn}}(\mathrm{i}\tau) = &\sum_{\mathbf{r}\in C}\sum_{\mathbf{R}'\in S}\tilde{\psi}^{*}_{n\mathbf{k}}(\mathbf{r})\overline{\Sigma}^{(1)}(\mathbf{r},\mathbf{R}',\mathrm{i}\tau)\tilde{\psi}_{n\mathbf{k}}(\mathbf{R}')\\
&+\sum_{\mu}\sum_{\mathbf{R}'\in S}\langle\tilde{\psi}_{n\mathbf{k}}|\tilde{p}_{\mu}\rangle\overline{\Sigma}^{(2)}(\mu,\mathbf{R}',\mathrm{i}\tau)\tilde{\psi}_{n\mathbf{k}}(\mathbf{R}')\\
&+\sum_{\mathbf{r}\in C}\sum_{\beta}\tilde{\psi}^{*}_{n\mathbf{k}}(\mathbf{r})\overline{\Sigma}^{(3)}(\mathbf{r},\beta,\mathrm{i}\tau)\langle\tilde{p}_{\beta}|\tilde{\psi}_{n\mathbf{k}}\rangle\\
&+\sum_{\mu}\sum_{\beta}\langle\tilde{\psi}_{n\mathbf{k}}|\tilde{p}_{\mu}\rangle\overline{\Sigma}^{(4)}(\mu,\beta,\mathrm{i}\tau)\langle\tilde{p}_{\beta}|\tilde{\psi}_{n\mathbf{k}}\rangle.
\end{aligned}\tag{540}$$

It should be mentioned that although the above derivation has been done on the second-order self-energy only, it is applicable to other higher orders as well. This gives rise to a general formulation of the correlated self-energy as long as the second-order screened Coulomb interaction is replaced by the correlated screened Coulomb interaction $V\chi V + V\chi V\chi V + \ldots$.

E.2 Direct derivation from the definitions

In contrast to the above Section (E.1), here we show the derivation of the matrix elements of the self-energy within the PAW method directly from the definitions of the Green's functions and self-energy. Now we concentrate on the unoccupied self-energy only, while the occupied self-energy are obtained by replacing $\overline{G}$ with $\underline{G}$.

$$\begin{aligned}
\overline{\Sigma}^{\mathbf{k}}_{nm}(\mathrm{i}\tau) &= \langle\psi_{n\mathbf{k}}|\hat{\overline{\Sigma}}(\mathrm{i}\tau)|\psi_{m\mathbf{k}}\rangle = -\langle\psi_{n\mathbf{k}}|\hat{\overline{G}}(\mathrm{i}\tau)\hat{W}(\mathrm{i}\tau)|\psi_{m\mathbf{k}}\rangle \\
&= \langle\psi_{n\mathbf{k}}|\sum_{a}^{\mathrm{unocc}}|\psi_a\rangle\langle\psi_a|\mathbf{e}^{-\mathrm{i}\epsilon_a\tau}\hat{W}(\mathrm{i}\tau)|\psi_{m\mathbf{k}}\rangle \\
&= \sum_{a}^{\mathrm{unocc}}\sum_{\mathbf{r}\in C}\sum_{\mathbf{R}'\in S}\langle\psi_{n\mathbf{k}}|\mathbf{r}\rangle\langle\mathbf{r}|\left\{|\psi_a\rangle\langle\psi_a|\mathbf{e}^{-\mathrm{i}\epsilon_a\tau}\hat{W}(\mathrm{i}\tau)\right\}|\mathbf{R}'\rangle\langle\mathbf{R}'|\psi_{m\mathbf{k}}\rangle \\
&= \sum_{a}^{\mathrm{unocc}}\sum_{\mathbf{r}\in C}\sum_{\mathbf{R}'\in S}\mathbf{e}^{-\mathrm{i}\epsilon_a\tau}W(\mathbf{r},\mathbf{R}',\mathrm{i}\tau)\langle\psi_{n\mathbf{k}}|\mathbf{r}\rangle\langle\mathbf{r}|\psi_a\rangle\langle\psi_a|\mathbf{R}'\rangle\langle\mathbf{R}'|\psi_{m\mathbf{k}}\rangle.
\end{aligned} \tag{541}$$

Note that in deriving Eq. (541) the completeness relationships

$$\sum_{\mathbf{r}\in C}|\mathbf{r}\rangle\langle\mathbf{r}| = \hat{\mathbf{1}} \tag{542}$$

$$\sum_{\mathbf{R}'\in S}|\mathbf{R}'\rangle\langle\mathbf{R}'| = \hat{\mathbf{1}}, \tag{543}$$

and the "space-time" representation of the self-energy

$$\langle\mathbf{r}|\hat{\overline{\Sigma}}(\mathrm{i}\tau)\rangle|\mathbf{R}'\rangle = -\langle\mathbf{r}|\hat{\overline{G}}(\mathrm{i}\tau)\hat{W}(\mathrm{i}\tau)\rangle|\mathbf{R}'\rangle = -\langle\mathbf{r}|\hat{\overline{G}}(\mathrm{i}\tau)|\mathbf{R}'\rangle\langle\mathbf{r}|\hat{W}(\mathrm{i}\tau)|\mathbf{R}'\rangle \tag{544}$$

have been used. Also, we have used a composite index $a = (n', \mathbf{k})$ with $n' \in$ unocc for brevity.

According to the PAW method [Eq. (222)], we obtain

$$\begin{aligned}
\langle\psi_{n\mathbf{k}}|\mathbf{r}\rangle\langle\mathbf{r}|\psi_a\rangle &= \langle\tilde{\psi}_{n\mathbf{k}}|\mathbf{r}\rangle\langle\mathbf{r}|\tilde{\psi}_a\rangle + \sum_{\mu\nu}\langle\tilde{\psi}_{n\mathbf{k}}|\tilde{p}_\mu\rangle\langle\tilde{p}_\nu|\tilde{\psi}_a\rangle\left\{\langle\phi_\mu|\mathbf{r}\rangle\langle\mathbf{r}|\phi_\nu\rangle - \langle\tilde{\phi}_\mu|\mathbf{r}\rangle\langle\mathbf{r}|\tilde{\phi}_\nu\rangle\right\} \\
&= \langle\tilde{\psi}_{n\mathbf{k}}|\mathbf{r}\rangle\langle\mathbf{r}|\tilde{\psi}_a\rangle + \sum_{\mu\nu}\langle\tilde{\psi}_{n\mathbf{k}}|\tilde{p}_\mu\rangle\langle\tilde{p}_\nu|\tilde{\psi}_a\rangle Q_{\mu\nu}(\mathbf{r}),
\end{aligned} \tag{545}$$

and

$$\begin{aligned}\langle\psi_a|\mathbf{R}'\rangle\langle\mathbf{R}'|\psi_{m\mathbf{k}}\rangle &= \langle\tilde{\psi}_a|\mathbf{R}'\rangle\langle\mathbf{R}'|\tilde{\psi}_{m\mathbf{k}}\rangle + \sum_{\alpha\beta}\langle\tilde{\psi}_a|\tilde{p}_\alpha\rangle\langle\tilde{p}_\beta|\tilde{\psi}_{m\mathbf{k}}\rangle\left\{\langle\phi_\alpha|\mathbf{R}'\rangle\langle\mathbf{R}'|\phi_\beta\rangle - \langle\tilde{\phi}_\alpha|\mathbf{R}'\rangle\langle\mathbf{R}'|\tilde{\phi}_\beta\rangle\right\}\\ &= \langle\tilde{\psi}_a|\mathbf{R}'\rangle\langle\mathbf{R}'|\tilde{\psi}_{m\mathbf{k}}\rangle + \sum_{\alpha\beta}\langle\tilde{\psi}_a|\tilde{p}_\alpha\rangle\langle\tilde{p}_\beta|\tilde{\psi}_{m\mathbf{k}}\rangle Q_{\alpha\beta}(\mathbf{R}').\end{aligned} \tag{546}$$

To summarize, there are four terms in the self-energy:

$$\overline{\Sigma}^{\mathbf{k}}_{nm}(\mathrm{i}\tau) = \overline{\Sigma}^{\mathbf{k}(1)}_{nm}(\mathrm{i}\tau) + \overline{\Sigma}^{\mathbf{k}(2)}_{nm}(\mathrm{i}\tau) + \overline{\Sigma}^{\mathbf{k}(3)}_{nm}(\mathrm{i}\tau) + \overline{\Sigma}^{\mathbf{k}(4)}_{nm}(\mathrm{i}\tau), \tag{547}$$

where each term is given by

$$\begin{aligned}\overline{\Sigma}^{\mathbf{k}(1)}_{nm}(\mathrm{i}\tau) &= \sum_{a}^{\mathrm{unocc}}\sum_{\mathbf{r}\in C}\sum_{\mathbf{R}'\in S}\mathbf{e}^{-\mathrm{i}\epsilon_a\tau}W(\mathbf{r},\mathbf{R}',\mathrm{i}\tau)\langle\tilde{\psi}_{n\mathbf{k}}|\mathbf{r}\rangle\langle\mathbf{r}|\tilde{\psi}_a\rangle\langle\tilde{\psi}_a|\mathbf{R}'\rangle\langle\mathbf{R}'|\tilde{\psi}_{m\mathbf{k}}\rangle\\ &= \sum_{\mathbf{r}\in C}\sum_{\mathbf{R}'\in S}\tilde{\psi}^*_{n\mathbf{k}}(\mathbf{r})\left\{\sum_{a}^{\mathrm{unocc}}\tilde{\psi}_a(\mathbf{r})\tilde{\psi}^*_i(\mathbf{R}')\mathbf{e}^{-\mathrm{i}\epsilon_a\tau}\right\}W(\mathbf{r},\mathbf{R}',\mathrm{i}\tau)\tilde{\psi}_{m\mathbf{k}}(\mathbf{R}')\\ &= \sum_{\mathbf{r}\in C}\sum_{\mathbf{R}'\in S}\tilde{\psi}^*_{n\mathbf{k}}(\mathbf{r})\overline{G}^{(1)}(\mathbf{r},\mathbf{R}',\mathrm{i}\tau)W(\mathbf{r},\mathbf{R}',\mathrm{i}\tau)\tilde{\psi}_{m\mathbf{k}}(\mathbf{R}')\\ &= \sum_{\mathbf{r}\in C}\sum_{\mathbf{R}'\in S}\tilde{\psi}^*_{n\mathbf{k}}(\mathbf{r})\overline{\Sigma}^{(1)}(\mathbf{r},\mathbf{R}',\mathrm{i}\tau)\tilde{\psi}_{n\mathbf{k}}(\mathbf{R}'),\end{aligned} \tag{548}$$

$$\begin{aligned}\overline{\Sigma}^{\mathbf{k}(2)}_{nm}(\mathrm{i}\tau) &= \sum_{a}^{\mathrm{unocc}}\sum_{\mathbf{r}\in C}\sum_{\mathbf{R}'\in S}\mathbf{e}^{-\mathrm{i}\epsilon_a\tau}W(\mathbf{r},\mathbf{R}',\mathrm{i}\tau)\langle\tilde{\psi}_a|\mathbf{R}'\rangle\langle\mathbf{R}'|\tilde{\psi}_{m\mathbf{k}}\rangle\sum_{\mu\nu}\langle\tilde{\psi}_{n\mathbf{k}}|\tilde{p}_\mu\rangle\langle\tilde{p}_\nu|\tilde{\psi}_a\rangle Q_{\mu\nu}(\mathbf{r})\\ &= \sum_{\mathbf{r}\in C}\sum_{\mathbf{R}'\in S}\sum_{\mu\nu}\langle\tilde{\psi}_{n\mathbf{k}}|\tilde{p}_\mu\rangle\left\{\sum_{a}^{\mathrm{unocc}}\langle\tilde{p}_\nu|\tilde{\psi}_a\rangle\tilde{\psi}^*_i(\mathbf{R}')\mathbf{e}^{-\mathrm{i}\epsilon_a\tau}\right\}Q_{\mu\nu}(\mathbf{r})W(\mathbf{r},\mathbf{R}',\mathrm{i}\tau)\tilde{\psi}_{m\mathbf{k}}(\mathbf{R}')\\ &= \sum_{\mathbf{r}\in C}\sum_{\mathbf{R}'\in S}\sum_{\mu\nu}\langle\tilde{\psi}_{n\mathbf{k}}|\tilde{p}_\mu\rangle\overline{G}^{(2)}(\nu,\mathbf{R}',\mathrm{i}\tau)Q_{\mu\nu}(\mathbf{r})W(\mathbf{r},\mathbf{R}',\mathrm{i}\tau)\tilde{\psi}_{m\mathbf{k}}(\mathbf{R}')\\ &= \sum_{\mu}\sum_{\mathbf{R}'\in S}\langle\tilde{\psi}_{n\mathbf{k}}|\tilde{p}_\mu\rangle\overline{\Sigma}^{(2)}(\mu,\mathbf{R}',\mathrm{i}\tau)\tilde{\psi}_{n\mathbf{k}}(\mathbf{R}'),\end{aligned} \tag{549}$$

$$\begin{aligned}\overline{\Sigma}^{\mathbf{k}(3)}_{nm}(\mathrm{i}\tau) &= \sum_{a}^{\mathrm{unocc}}\sum_{\mathbf{r}\in C}\sum_{\mathbf{R}'\in S}\mathbf{e}^{-\mathrm{i}\epsilon_a\tau}W(\mathbf{r},\mathbf{R}',\mathrm{i}\tau)\langle\tilde{\psi}_{n\mathbf{k}}|\mathbf{r}\rangle\langle\mathbf{r}|\tilde{\psi}_a\rangle\sum_{\alpha\beta}\langle\tilde{\psi}_a|\tilde{p}_\alpha\rangle\langle\tilde{p}_\beta|\tilde{\psi}_{m\mathbf{k}}\rangle Q_{\alpha\beta}(\mathbf{R}')\\ &= \sum_{\mathbf{r}\in C}\sum_{\mathbf{R}'\in S}\sum_{\alpha\beta}\tilde{\psi}^*_{n\mathbf{k}}(\mathbf{r})\left\{\sum_{a}^{\mathrm{unocc}}\tilde{\psi}_a(\mathbf{r})\langle\tilde{\psi}_a|\tilde{p}_\alpha\rangle\mathbf{e}^{-\mathrm{i}\epsilon_a\tau}\right\}W(\mathbf{r},\mathbf{R}',\mathrm{i}\tau)Q_{\alpha\beta}(\mathbf{R}')\langle\tilde{p}_\beta|\tilde{\psi}_{m\mathbf{k}}\rangle\\ &= \sum_{\mathbf{r}\in C}\sum_{\mathbf{R}'\in S}\sum_{\alpha\beta}\tilde{\psi}^*_{n\mathbf{k}}(\mathbf{r})\overline{G}^{(3)}(\mathbf{r},\alpha,\mathrm{i}\tau)W(\mathbf{r},\mathbf{R}',\mathrm{i}\tau)Q_{\alpha\beta}(\mathbf{R}')\langle\tilde{p}_\beta|\tilde{\psi}_{m\mathbf{k}}\rangle\\ &= \sum_{\mathbf{r}\in C}\sum_{\beta}\tilde{\psi}^*_{n\mathbf{k}}(\mathbf{r})\overline{\Sigma}^{(3)}(\mathbf{r},\beta,\mathrm{i}\tau)\langle\tilde{p}_\beta|\tilde{\psi}_{n\mathbf{k}}\rangle,\end{aligned} \tag{550}$$

$$\begin{aligned}
\overline{\Sigma}_{nm}^{\mathbf{k}(4)}(\mathrm{i}\tau) &= \sum_{a}^{\mathrm{unocc}} \sum_{\mathbf{r}\in C} \sum_{\mathbf{R}'\in S} \mathbf{e}^{-\mathrm{i}\epsilon_a\tau} W(\mathbf{r},\mathbf{R}',\mathrm{i}\tau) \sum_{\mu\nu} \langle\tilde{\psi}_{n\mathbf{k}}|\tilde{p}_\mu\rangle\langle\tilde{p}_\nu|\tilde{\psi}_a\rangle Q_{\mu\nu}(\mathbf{r}) \sum_{\alpha\beta} \langle\tilde{\psi}_a|\tilde{p}_\alpha\rangle\langle\tilde{p}_\beta|\tilde{\psi}_{m\mathbf{k}}\rangle Q_{\alpha\beta}(\mathbf{R}') \\
&= \sum_{\mathbf{r}\in C} \sum_{\mathbf{R}'\in S} \sum_{\mu\nu\alpha\beta} \langle\tilde{\psi}_{n\mathbf{k}}|\tilde{p}_\mu\rangle \left\{ \sum_{a}^{\mathrm{unocc}} \langle\tilde{p}_\nu|\tilde{\psi}_a\rangle\langle\tilde{\psi}_a|\tilde{p}_\alpha\rangle \mathbf{e}^{-\mathrm{i}\epsilon_a\tau} \right\} Q_{\mu\nu}(\mathbf{r}) W(\mathbf{r},\mathbf{R}',\mathrm{i}\tau) Q_{\alpha\beta}(\mathbf{R}') \langle\tilde{p}_\beta|\tilde{\psi}_{m\mathbf{k}}\rangle \\
&= \sum_{\mathbf{r}\in C} \sum_{\mathbf{R}'\in S} \sum_{\mu\nu\alpha\beta} \langle\tilde{\psi}_{n\mathbf{k}}|\tilde{p}_\mu\rangle \overline{G}^{(4)}(\nu,\alpha,\mathrm{i}\tau) Q_{\mu\nu}(\mathbf{r}) W(\mathbf{r},\mathbf{R}',\mathrm{i}\tau) Q_{\alpha\beta}(\mathbf{R}') \langle\tilde{p}_\beta|\tilde{\psi}_{m\mathbf{k}}\rangle \\
&= \sum_{\mu} \sum_{\beta} \langle\tilde{\psi}_{n\mathbf{k}}|\tilde{p}_\mu\rangle \overline{\Sigma}^{(4)}(\mu,\beta,\mathrm{i}\tau) \langle\tilde{p}_\beta|\tilde{\psi}_{n\mathbf{k}}\rangle.
\end{aligned} \tag{551}$$

Note that in deriving Eqs. (548–551), the definitions in Eqs. (527–529) and Eqs. (531–534) have been used. By comparing Eq. (540), one can see that we have obtained exactly the same expression of the matrix elements of self-energy in the orbital basis. Again, the occupied self-energy can be obtained by replacing $\overline{G}$ with $\underline{G}$.

Appendix F Relationship between $\Sigma_{n\mathbf{k},n'\mathbf{k}-\mathbf{q}}(\omega)$ and $W_{n\mathbf{k},n'\mathbf{k}-\mathbf{q}}(\omega)$

Proof:

$$\mathrm{Im}[\Sigma_{n\mathbf{k},n'\mathbf{k}-\mathbf{q}}(E)] = \begin{cases} -\mathrm{Im}[W_{n\mathbf{k},n'\mathbf{k}-\mathbf{q}}(\epsilon_{n'\mathbf{k}-\mathbf{q}} - E)\theta(\epsilon_{n'\mathbf{k}-\mathbf{q}} - E)\theta(\mu - \epsilon_{n'\mathbf{k}-\mathbf{q}})] \\ \quad \text{if } E < \epsilon_{n'\mathbf{k}-\mathbf{q}} < \mu,\ \epsilon_{n'\mathbf{k}-\mathbf{q}} \in \text{occ} \\ \\ +\mathrm{Im}[W_{n\mathbf{k},n'\mathbf{k}-\mathbf{q}}(E - \epsilon_{n'\mathbf{k}-\mathbf{q}})\theta(E - \epsilon_{n'\mathbf{k}-\mathbf{q}})\theta(\epsilon_{n'\mathbf{k}-\mathbf{q}} - \mu)] \\ \quad \text{if } E > \epsilon_{n'\mathbf{k}-\mathbf{q}} > \mu,\ \epsilon_{n'\mathbf{k}-\mathbf{q}} \in \text{unocc} \end{cases} \tag{552}$$

We start from the definition of the self-energy for each pair $(n\mathbf{k}, n'\mathbf{k}-\mathbf{q})$

$$\begin{aligned} \Sigma_{n\mathbf{k},n'\mathbf{k}-\mathbf{q}}(E) &= \frac{\mathrm{i}}{2\pi}\int_{-\infty}^{+\infty} d\omega G_{n\mathbf{k},n'\mathbf{k}-\mathbf{q}}(E+\omega)W_{n\mathbf{k},n'\mathbf{k}-\mathbf{q}}(\omega) \\ &= \frac{\mathrm{i}}{2\pi}\int_{-\infty}^{+\infty} d\omega \left\{ \int_{-\infty}^{\mu} d\omega_1 \frac{A_{n\mathbf{k},n'\mathbf{k}-\mathbf{q}}(\omega_1)}{E+\omega-\omega_1-\mathrm{i}\delta} + \int_{\mu}^{+\infty} d\omega_1 \frac{A_{n\mathbf{k},n'\mathbf{k}-\mathbf{q}}(\omega_1)}{E+\omega-\omega_1+\mathrm{i}\delta} \right\} \\ &\times \left\{ \int_{-\infty}^{0} d\omega_2 \frac{D_{n\mathbf{k},n'\mathbf{k}-\mathbf{q}}(\omega_2)}{\omega-\omega_2-\mathrm{i}\eta} + \int_{0}^{+\infty} d\omega_2 \frac{D_{n\mathbf{k},n'\mathbf{k}-\mathbf{q}}(\omega_2)}{\omega-\omega_2-\mathrm{i}\eta} \right\}. \end{aligned} \tag{553}$$

Here, δ and η are both positive infinitesimal. Note that in deriving Eq. (553) we have used spectral representation of the Green's function

$$G_{n\mathbf{k},n'\mathbf{k}-\mathbf{q}}(\omega) = \int_{-\infty}^{\mu} d\omega' \frac{A_{n\mathbf{k},n'\mathbf{k}-\mathbf{q}}(\omega')}{\omega-\omega'-\mathrm{i}\delta} + \int_{\mu}^{+\infty} d\omega' \frac{A_{n\mathbf{k},n'\mathbf{k}-\mathbf{q}}(\omega')}{\omega-\omega'+\mathrm{i}\delta}, \tag{554}$$

and spectral representation of screened coulomb interaction

$$W_{n\mathbf{k},n'\mathbf{k}-\mathbf{q}}(\omega) = \int_{-\infty}^{0} d\omega' \frac{D_{n\mathbf{k},n'\mathbf{k}-\mathbf{q}}(\omega')}{\omega-\omega'-\mathrm{i}\delta} + \int_{0}^{+\infty} d\omega' \frac{D_{n\mathbf{k},n'\mathbf{k}-\mathbf{q}}(\omega')}{\omega-\omega'+\mathrm{i}\delta}, \tag{555}$$

where $A_{n\mathbf{k},n'\mathbf{k}-\mathbf{q}}(\omega)$ is the spectral function of Green's function, which is proportional to the imaginary part of $G_{n\mathbf{k},n'\mathbf{k}-\mathbf{q}}(\omega)$

$$A_{n\mathbf{k},n'\mathbf{k}-\mathbf{q}}(\omega) = -\frac{1}{\pi}\mathrm{Im}[G_{n\mathbf{k},n'\mathbf{k}-\mathbf{q}}(\omega)]\,\mathrm{sgn}(\omega-\mu). \tag{556}$$

Here, $D_{n\mathbf{k},n'\mathbf{k}-\mathbf{q}}(\omega)$ is the spectral function of screened coulomb interaction, which is proportional to the imaginary part of $W_{n\mathbf{k},n'\mathbf{k}-\mathbf{q}}(\omega)$

$$D_{n\mathbf{k},n'\mathbf{k}-\mathbf{q}}(\omega) = -\frac{1}{\pi}\mathrm{Im}[W_{n\mathbf{k},n'\mathbf{k}-\mathbf{q}}(\omega)]\,\mathrm{sgn}(\omega). \tag{557}$$

Note that $D_{n\mathbf{k},n'\mathbf{k}-\mathbf{q}}(-\omega) = -D_{n\mathbf{k},n'\mathbf{k}-\mathbf{q}}(\omega)$, i.e., $D_{n\mathbf{k},n'\mathbf{k}-\mathbf{q}}(\omega)$ is an odd function with respect to ω. With this, the following equation holds

$$W_{n\mathbf{k},n'\mathbf{k}-\mathbf{q}}(\omega) = \int_0^{+\infty} d\omega' D_{n\mathbf{k},n'\mathbf{k}-\mathbf{q}}(\omega') \left\{ \frac{1}{\omega - \omega' + \mathrm{i}\delta} + \frac{-1}{\omega + \omega' - \mathrm{i}\delta} \right\}. \tag{558}$$

Therefore, Eq. (553) reduces to

$$\begin{aligned} \Sigma_{n\mathbf{k},n'\mathbf{k}-\mathbf{q}}(E) = \frac{\mathrm{i}}{2\pi} \int_{-\infty}^{+\infty} d\omega & \left\{ \int_{-\infty}^{\mu} d\omega_1 \frac{A_{n\mathbf{k},n'\mathbf{k}-\mathbf{q}}(\omega_1)}{E + \omega - \omega_1 - \mathrm{i}\delta} + \int_{\mu}^{+\infty} d\omega_1 \frac{A_{n\mathbf{k},n'\mathbf{k}-\mathbf{q}}(\omega_1)}{E + \omega - \omega_1 + \mathrm{i}\delta} \right\} \\ & \times \left\{ \int_0^{+\infty} d\omega_2 D_{n\mathbf{k},n'\mathbf{k}-\mathbf{q}}(\omega_2) [\frac{1}{\omega - \omega_2 + \mathrm{i}\eta} + \frac{-1}{\omega + \omega_2 - \mathrm{i}\eta}] \right\}. \end{aligned} \tag{559}$$

Performing the contour integration in the ω-plane yields

$$\begin{aligned} \Sigma_{n\mathbf{k},n'\mathbf{k}-\mathbf{q}}(E) = & \int_{-\infty}^{\mu} d\omega_1 \int_0^{+\infty} d\omega_2 \frac{A_{n\mathbf{k},n'\mathbf{k}-\mathbf{q}}(\omega_1) D_{n\mathbf{k},n'\mathbf{k}-\mathbf{q}}(\omega_2)}{E + \omega_2 - \omega_1 - \mathrm{i}\delta} \\ & + \int_{\mu}^{+\infty} d\omega_1 \int_0^{+\infty} d\omega_2 \frac{A_{n\mathbf{k},n'\mathbf{k}-\mathbf{q}}(\omega_1) D_{n\mathbf{k},n'\mathbf{k}-\mathbf{q}}(\omega_2)}{E - \omega_2 - \omega_1 + \mathrm{i}\delta}. \end{aligned} \tag{560}$$

Now we employ the spectral representation of self-energy $\Sigma_{n\mathbf{k},n'\mathbf{k}-\mathbf{q}}(\omega)$

$$\Sigma_{n\mathbf{k},n'\mathbf{k}-\mathbf{q}}(\omega) = \int_{-\infty}^{\mu} d\omega' \frac{\Gamma_{n\mathbf{k},n'\mathbf{k}-\mathbf{q}}(\omega')}{\omega - \omega' - \mathrm{i}\delta} + \int_{\mu}^{+\infty} d\omega' \frac{\Gamma_{n\mathbf{k},n'\mathbf{k}-\mathbf{q}}(\omega')}{\omega - \omega' + \mathrm{i}\delta}, \tag{561}$$

where $\Gamma_{n\mathbf{k},n'\mathbf{k}-\mathbf{q}}(\omega)$ is the spectral function of self-energy, which is proportional to the imaginary part of $\Sigma_{n\mathbf{k},n'\mathbf{k}-\mathbf{q}}(\omega)$

$$\Gamma_{n\mathbf{k},n'\mathbf{k}-\mathbf{q}}(\omega) = -\frac{1}{\pi} \mathrm{Im}[\Sigma_{n\mathbf{k},n'\mathbf{k}-\mathbf{q}}(\omega)] \, \mathrm{sgn}(\omega - \mu). \tag{562}$$

Using the following well-known theorem from complex function theory

$$\mathrm{Im}[\frac{1}{x \pm \mathrm{i}\delta}] = \mp \pi \delta(x), \tag{563}$$

we obtain from Eq. (560)

$$\begin{aligned} \Gamma_{n\mathbf{k},n'\mathbf{k}-\mathbf{q}}(E) = & - \mathrm{sgn}(E - \mu) \int_{-\infty}^{\mu} d\omega_1 \int_0^{+\infty} d\omega_2 A_{n\mathbf{k},n'\mathbf{k}-\mathbf{q}}(\omega_1) D_{n\mathbf{k},n'\mathbf{k}-\mathbf{q}}(\omega_2) \delta(E + \omega_2 - \omega_1) \\ & + \mathrm{sgn}(E - \mu) \int_{\mu}^{+\infty} d\omega_1 \int_0^{+\infty} d\omega_2 A_{n\mathbf{k},n'\mathbf{k}-\mathbf{q}}(\omega_1) D_{n\mathbf{k},n'\mathbf{k}-\mathbf{q}}(\omega_2) \delta(E - \omega_2 - \omega_1) \\ \overset{\omega_1 = E + \omega_2 < \mu}{\underset{\omega_1 = E - \omega_2 > \mu}{=\!=\!=\!=}} & - \mathrm{sgn}(E - \mu) \int_0^{+\infty} d\omega_2 A_{n\mathbf{k},n'\mathbf{k}-\mathbf{q}}(E + \omega_2) D_{n\mathbf{k},n'\mathbf{k}-\mathbf{q}}(\omega_2) \theta(\mu - E - \omega_2) \\ & + \mathrm{sgn}(E - \mu) \int_0^{+\infty} d\omega_2 A_{n\mathbf{k},n'\mathbf{k}-\mathbf{q}}(E - \omega_2) D_{n\mathbf{k},n'\mathbf{k}-\mathbf{q}}(\omega_2) \theta(E - \omega_2 - \mu). \end{aligned} \tag{564}$$

For non-interacting case, the spectral function of Green's function reduces to δ function

$$A_{n\mathbf{k},n'\mathbf{k-q}}(\omega) = \delta(\omega - \epsilon_{n'\mathbf{k-q}}). \tag{565}$$

Inserting Eq. (565) into Eq. (564) finally yields

$$\begin{aligned}
\Gamma_{n\mathbf{k},n'\mathbf{k-q}}(E) =& - \mathrm{sgn}(E-\mu)\int_0^{+\infty} d\omega_2 \delta(E+\omega_2-\epsilon_{n'\mathbf{k-q}}) D_{n\mathbf{k},n'\mathbf{k-q}}(\omega_2)\theta(\mu - E - \omega_2) \\
&+ \mathrm{sgn}(E-\mu)\int_0^{+\infty} d\omega_2 \delta(E-\omega_2-\epsilon_{n'\mathbf{k-q}}) D_{n\mathbf{k},n'\mathbf{k-q}}(\omega_2)\theta(E - \omega_2 - \mu) \\
\underset{\omega_2=E-\epsilon_{n'\mathbf{k-q}}>0}{\overset{\omega_2=\epsilon_{n'\mathbf{k-q}}-E>0}{=\!=\!=\!=}} & - \mathrm{sgn}(E-\mu) D_{n\mathbf{k},n'\mathbf{k-q}}(\epsilon_{n'\mathbf{k-q}} - E)\theta(\epsilon_{n'\mathbf{k-q}} - E)\theta(\mu - \epsilon_{n'\mathbf{k-q}}) \\
&+ \mathrm{sgn}(E-\mu) D_{n\mathbf{k},n'\mathbf{k-q}}(E - \epsilon_{n'\mathbf{k-q}})\theta(E - \epsilon_{n'\mathbf{k-q}})\theta(\epsilon_{n'\mathbf{k-q}} - \mu) \\
=& + D_{n\mathbf{k},n'\mathbf{k-q}}(\epsilon_{n'\mathbf{k-q}} - E)\theta(\epsilon_{n'\mathbf{k-q}} - E)\theta(\mu - \epsilon_{n'\mathbf{k-q}}) \\
&+ D_{n\mathbf{k},n'\mathbf{k-q}}(E - \epsilon_{n'\mathbf{k-q}})\theta(E - \epsilon_{n'\mathbf{k-q}})\theta(\epsilon_{n'\mathbf{k-q}} - \mu).
\end{aligned} \tag{566}$$

Combining Eqs. (557) and (562) with Eq. (566), we finally obtain

$$\begin{aligned}
\mathrm{Im}[\Sigma_{n\mathbf{k},n'\mathbf{k-q}}(E)]\,\mathrm{sgn}(E-\mu) =& \mathrm{Im}[W_{n\mathbf{k},n'\mathbf{k-q}}(\epsilon_{n'\mathbf{k-q}} - E)]\theta(\epsilon_{n'\mathbf{k-q}} - E)\theta(\mu - \epsilon_{n'\mathbf{k-q}}) \\
&+ \mathrm{Im}[W_{n\mathbf{k},n'\mathbf{k-q}}(E - \epsilon_{n'\mathbf{k-q}})]\theta(E - \epsilon_{n'\mathbf{k-q}})\theta(\epsilon_{n'\mathbf{k-q}} - \mu),
\end{aligned} \tag{567}$$

i.e., Eq. (552) is justified.

Appendix G Derivation of the correlated polarizability χ^c from formula of Kubo and Nakano

In this appendix, I will show a more exhaustive derivation for the correlated polarizability χ^c from the Kubo and Nakano formula following the Merzuk Kaltak's derivation. For the original derivation, please refer to his PhD thesis [267].

According to the Kubo and Nakano, the correlated polarizability χ^c can be expressed as the density-density fluctuation response in the correlated subspace [285]

$$\chi^c(\mathbf{r}, \mathbf{r}', \mathrm{i}\tau) = -\langle \Psi_0 | \hat{T}\left[\delta\hat{n}_c(\mathbf{r}, \mathrm{i}\tau)\delta\hat{n}_c(\mathbf{r}')\right] | \Psi_0 \rangle, \tag{568}$$

where $|\Psi_0\rangle$ denotes the non-interacting ground state of a M-particle system, $\hat{n}_c(\mathbf{r})$ represents the correlated particle number operator accounting for states in the correlated subspace C of interest located at $\mathbf{r}$, and $\hat{n}_r$ represents the remaining states, satisfying $\hat{n}(\mathbf{r}) = \hat{n}_c(\mathbf{r}) + \hat{n}_r(\mathbf{r})$. $\hat{T}$ is the time-ordering operator. The density fluctuation operator $\delta\hat{n}_c(\mathbf{r}, \mathrm{i}\tau)$ is given by

$$\delta\hat{n}_c(\mathbf{r}, \mathrm{i}\tau) = \hat{n}_c(\mathbf{r}, \mathrm{i}\tau) - \langle \Psi_0 | \hat{n}_c(\mathbf{r}, \mathrm{i}\tau) | \Psi_0 \rangle. \tag{569}$$

Inserting a complete eigenset of the non-interacting many-body system

$$\sum_{s=0}^{\infty} |\Psi_s\rangle\langle\Psi_s| = \mathbf{1} \tag{570}$$

into the Kubo-Nakano formula in Eq. (568), one obtains

$$\begin{aligned}\chi^c(\mathbf{r}, \mathbf{r}', \mathrm{i}\tau) = &-\sum_{s=1}^{\infty} \Theta(\tau)\mathbf{e}^{(E_0-E_s)\tau}\langle\Psi_0|\hat{n}_c(\mathbf{r})|\Psi_s\rangle\langle\Psi_s|\hat{n}_c(\mathbf{r}')|\Psi_0\rangle \\ &-\sum_{s=1}^{\infty} \Theta(-\tau)\mathbf{e}^{(E_s-E_0)\tau}\langle\Psi_0|\hat{n}_c(\mathbf{r}')|\Psi_s\rangle\langle\Psi_s|\hat{n}_c(\mathbf{r})|\Psi_0\rangle.\end{aligned} \tag{571}$$

Here, we have used the interaction picture relation $\hat{n}_c(\mathbf{r}, \mathrm{i}\tau) = \mathbf{e}^{H_0\tau}\hat{n}_c(\mathbf{r})\mathbf{e}^{-H_0\tau}$ where H_0 is the Hamiltonian a system of M non-interacting electrons

$$\hat{H}_0 = \sum_{l=1}^{M} \hat{h}_l, \tag{572}$$

with h_l being the one-electron Hamiltonian of a free electron at position $\mathbf{r}_l$, and the fact that $|\Psi_s\rangle$ is an eigenvector of the Hamiltonian H_0, with corresponding eigenenergy E_s. The $s = 0$ term is dropped due to the second term of right-hand side of Eq. (569). Θ is the Heaviside step function.

Next, we calculate the expectation value

$$\langle\Psi_0|\hat{n}_c(\mathbf{r})|\Psi_s\rangle. \tag{573}$$

We start by the definition of the many-body basis set. Adopting the Einstein convention, the corresponding complete eigenset of H_0 is given by the set of all Slater-determinants Ψ_s

$$\Psi_s(\mathbf{x_1},\cdots,\mathbf{x}_M) = [\varepsilon_{(s)}]^{\bar{n}_1,\cdots,\bar{n}_M}\,\phi_{\bar{n}_1}(\mathbf{r}_1)\cdots\phi_{\bar{n}_M}(\mathbf{r}_M) \tag{574}$$

with corresponding eigenenergies

$$E_s = \sum_{\bar{n}\in I_s}\epsilon_{\bar{n}}. \tag{575}$$

Here, $\phi_{\bar{n}}(\mathbf{r})$ and $\epsilon_{\bar{n}}$ are the one-electron eigenfunction and eigenenergy of the one-electron Hamiltonian h_l, respectively. Thus, each determinant Ψ_s contains a specific set of occupied and unoccupied states indicated by the index set I_s and the Levi-Civita tensor is defined as [286]

$$[\varepsilon_{(s)}]^{\bar{n}_1,\cdots,\bar{n}_M} = \frac{1}{\sqrt{M!}}\begin{vmatrix}\delta_{1\bar{n}_1} & \ldots & \delta_{1\bar{n}_M}\\ \vdots & \ddots & \vdots\\ \delta_{M\bar{n}_1} & \ldots & \delta_{M\bar{n}_M}\end{vmatrix},\ \bar{n}_1,\cdots,\bar{n}_M\in I_s. \tag{576}$$

Because the relation of Bloch states and Wannier functions

$$\begin{aligned}|\phi_{\bar{n}}\rangle = |\phi_{n\mathbf{k}}\rangle &= \sum_{\alpha\mathbf{R}_\alpha}\mathbf{e}^{\mathbf{ikR}_\alpha}T^{\dagger(\mathbf{k})}_{\alpha n}|w_{\alpha\mathbf{R}_\alpha}\rangle\\ &= \sum_{\bar{\alpha}}T^*_{\bar{n}\bar{\alpha}}|w_{\bar{\alpha}}\rangle.\end{aligned} \tag{577}$$

Here and in the following we use super indices $\bar{\alpha}_i = (\alpha_i,\mathbf{R}_{\alpha_i})$ for Wannier states, $\bar{n}_i = (n_i,\mathbf{k}_i)$ for Bloch states and the shorthand $T^\dagger_{\bar{\alpha}_i\bar{n}_i} = T^*_{\bar{n}_i\bar{\alpha}_i} = \mathbf{e}^{\mathbf{i}\mathbf{k}_i\cdot\mathbf{R}_{\alpha_i}}T^{*(\mathbf{k}_i)}_{n_i\alpha_i}$ indicates the transformation matrix from the Wannier basis to Bloch basis. A transformation to the Wannier basis is easily performed by a replacement of $\varepsilon\rightarrow\tau$, where the weighted Levi-Civita tensor $\tau_{(s)}$ is defined by

$$\begin{aligned}[\tau_{(s)}]^{\bar{\alpha}_1,\cdots,\bar{\alpha}_M} &= [\varepsilon_{(s)}]^{\bar{n}_1,\cdots,\bar{n}_M}\,T^\dagger_{\bar{\alpha}_1\bar{n}_1}\cdots T^\dagger_{\bar{\alpha}_M\bar{n}_M}\\ &= [\varepsilon_{(s)}]^{\bar{n}_1,\cdots,\bar{n}_M}\,T^*_{\bar{n}_1\bar{\alpha}_1}\cdots T^*_{\bar{n}_M\bar{\alpha}_M}\end{aligned} \tag{578}$$

The Fock space of the M particle Hamiltonian (572) is spanned by single, double and higher excited Slater determinants Ψ_s. For instance, singly excited states are obtained by replacing one occupied state ϕ_i in the ground state Ψ_0 with an unoccupied state ϕ_a and defining the index set I_s appropriately.

Next, we focus on the quantization of the Schrödinger field $\hat{\psi}(\mathbf{r})$. Here, the concept of a field operator $\hat{\psi}(\mathbf{r})$, which acts on the Fock space, is very convenient, since it allows us to express the possibility of creation and annihilation of electrons intrinsically in its notation. For instance, the action of the field operator $\hat{\psi}(\mathbf{r})$ onto an arbitrary M particle state Ψ_s can be written as [287]

$$\begin{aligned}\langle \mathbf{r}_2, \mathbf{r}_3, \cdots, \mathbf{r}_M | \hat{\psi}(\mathbf{r}) \Psi_s^M \rangle &= \sqrt{M} \int \mathrm{d}\mathbf{r}_1 \delta(\mathbf{r} - \mathbf{r}_1) \times \Psi_s(\mathbf{r}_1, \cdots, \mathbf{r}_M) \\ &= \sqrt{M} \Psi_s(\mathbf{r}, \mathbf{r}_2, \cdots, \mathbf{r}_M),\end{aligned} \tag{579}$$

giving an $(M-1)$ particle state $\left[\hat{\psi}(\mathbf{r})\Psi_s\right]$ with a missing electron at $\mathbf{r}$. The action of $\hat{\psi}^\dagger(\mathbf{r})$ is obtained by complex conjugation of Eq. (579). The product of the latter with $\hat{\psi}(\mathbf{r})$ gives the well-known density operator $\hat{n}(\mathbf{r})$

$$\hat{n}(\mathbf{r}) = \hat{\psi}^\dagger(\mathbf{r})\hat{\psi}(\mathbf{r}) \tag{580}$$

counting the number of electrons at position $\mathbf{r}$. Bloch and Wannier representations of the field operators are given by

$$\hat{\psi}(\mathbf{r}) = \sum_{\bar{n}} \phi_{\bar{n}}(\mathbf{r}) \hat{a}_{\bar{n}} \tag{581}$$

$$\hat{\psi}(\mathbf{r}) = \sum_{\bar{\alpha}} w_{\bar{\alpha}}(\mathbf{r}) \hat{c}_{\bar{\alpha}} \tag{582}$$

with the corresponding inverses

$$\hat{a}_{\bar{n}} = \int \mathrm{d}\mathbf{r} \phi^*_{\bar{n}}(\mathbf{r}) \hat{\psi}(\mathbf{r}) \tag{583}$$

$$\hat{c}_{\bar{\alpha}} = \int \mathrm{d}\mathbf{r} w^*_{\bar{\alpha}}(\mathbf{r}) \hat{\psi}(\mathbf{r}). \tag{584}$$

Inserting of Eqs. (581) and (582) into Eq. (580) yields the particle operator $\hat{n}$ in the Bloch and Wannier representation

$$\hat{n}(\mathbf{r}) = \sum_{\bar{n}_1 \bar{n}_2} \phi^*_{\bar{n}_1}(\mathbf{r}) \phi_{\bar{n}_2}(\mathbf{r}) a^\dagger_{\bar{n}_1} a_{\bar{n}_2} \tag{585}$$

$$\hat{n}(\mathbf{r}) = \sum_{\bar{\alpha}\bar{\beta}} w^*_{\bar{\alpha}}(\mathbf{r}) w_{\bar{\beta}}(\mathbf{r}) c^\dagger_{\bar{\alpha}} c_{\bar{\beta}}. \tag{586}$$

Restricting the sums in Eqs. (582) and (586) to correlated states only, i.e., the subspace C, we obtain the correlated field operator

$$\hat{\psi}_c(\mathbf{r}) = \sum_{\bar{\alpha} \in C} w_{\bar{\alpha}}(\mathbf{r}) \hat{c}_{\bar{\alpha}}, \tag{587}$$

and the corresponding correlated density operator

$$\begin{aligned}\hat{n}_c(\mathbf{r}) = \hat{\psi}^\dagger_c(\mathbf{r}) \hat{\psi}_c(\mathbf{r}) &= \sum_{\bar{\alpha}\bar{\beta} \in C} w^*_{\bar{\alpha}}(\mathbf{r}) w_{\bar{\beta}}(\mathbf{r}) c^\dagger_{\bar{\alpha}} c_{\bar{\beta}} \\ = \sum_{\bar{\alpha}\bar{\beta} \in C} w^*_{\bar{\alpha}}(\mathbf{r}) w_{\bar{\beta}}(\mathbf{r}) &\int \mathrm{d}\mathbf{r}_1 w_{\bar{\alpha}}(\mathbf{r}_1) \hat{\psi}^\dagger(\mathbf{r}_1) \int \mathrm{d}\mathbf{r}_2 w^*_{\bar{\beta}}(\mathbf{r}_2) \hat{\psi}(\mathbf{r}_2).\end{aligned} \tag{588}$$

Expectation values of the correlated density operator $\hat{n}_c$ can thus be evaluated by inserting Eq. (588) into Eq. (573)

$$\langle\Psi_0|\hat{n}_c(\mathbf{r})|\Psi_s\rangle = \sum_{\bar{\alpha}\bar{\beta}\in C} w^*_{\bar{\alpha}}(\mathbf{r})w_{\bar{\beta}}(\mathbf{r})\int \mathrm{d}\mathbf{r}_1\mathrm{d}\mathbf{r}_2 w_{\bar{\alpha}}(\mathbf{r}_1)w^*_{\bar{\beta}}(\mathbf{r}_2)\langle\Psi_0|\hat{\psi}^\dagger(\mathbf{r}_1)\hat{\psi}(\mathbf{r}_2)|\Psi_s\rangle. \tag{589}$$

Now we focus on the evaluation of the expectation value on the right-hand side of this expression. For a Slater determinant $|\Psi_s\rangle$ the action of the field operator $\hat{\psi}(\mathbf{r}_2)$ onto the M electron state $\Psi_s(\mathbf{r}'_1, \cdots, \mathbf{r}'_M)$ is given by Eq. (579). Together with the adjoint relation, one obtains

$$\begin{aligned}
&\langle\Psi_0|\hat{\psi}^\dagger(\mathbf{r}_1)\hat{\psi}(\mathbf{r}_2)|\Psi_s\rangle\\
=&M\int \mathrm{d}\mathbf{r}'_2\cdots\mathrm{d}\mathbf{r}'_M\Psi^*_0(\mathbf{r}_1,\mathbf{r}'_2,\cdots,\mathbf{r}'_M)\Psi_s(\mathbf{r}_2,\mathbf{r}'_2,\cdots,\mathbf{r}'_M)\\
=&M\int \mathrm{d}\mathbf{r}'_2\cdots\mathrm{d}\mathbf{r}'_M\left[\tau^*_{(0)}\right]^{\bar{\alpha}_1\bar{\alpha}_2\cdots\bar{\alpha}_M} w^*_{\bar{\alpha}_1}(\mathbf{r}_1)w^*_{\bar{\alpha}_2}(\mathbf{r}_2)\cdots w^*_{\bar{\alpha}_M}(\mathbf{r}_M)\left[\tau_{(s)}\right]^{\bar{\beta}_1\bar{\alpha}_2\cdots\bar{\alpha}_M} w_{\bar{\beta}_1}(\mathbf{r}_2)w_{\bar{\alpha}_2}(\mathbf{r}_2)\cdots w_{\bar{\alpha}_M}(\mathbf{r}_M)\\
=&Mw^*_{\bar{\alpha}_1}(\mathbf{r}_1)w_{\bar{\beta}_1}(\mathbf{r}_2)\left[\tau^*_{(0)}\right]^{\bar{\alpha}_1\bar{\alpha}_2\cdots\bar{\alpha}_M}\left[\tau_{(s)}\right]^{\bar{\beta}_1\bar{\alpha}_2\cdots\bar{\alpha}_M}\int \mathrm{d}\mathbf{r}'_2\cdots\mathrm{d}\mathbf{r}'_M w^*_{\bar{\alpha}_2}(\mathbf{r}_2)w_{\bar{\alpha}_2}(\mathbf{r}_2)\cdots w^*_{\bar{\alpha}_M}(\mathbf{r}_M)\cdots w_{\bar{\alpha}_M}(\mathbf{r}_M)\\
=&Mw^*_{\bar{\alpha}_1}(\mathbf{r}_1)w_{\bar{\beta}_1}(\mathbf{r}_2)\left[\tau^*_{(0)}\right]^{\bar{\alpha}_1\bar{\alpha}_2\cdots\bar{\alpha}_M}\left[\tau_{(s)}\right]^{\bar{\beta}_1\bar{\alpha}_2\cdots\bar{\alpha}_M}.
\end{aligned} \tag{590}$$

The contraction of the τ tensors in the last line can be evaluated using the identity [288]

$$\left[\varepsilon^*_{(0)}\right]^{\bar{n}_1\bar{n}_2\cdots\bar{n}_M}\left[\varepsilon_{(s)}\right]^{\bar{j}_1\bar{n}_2\cdots\bar{n}_M} = \frac{(M-1)!}{M!}\delta_{\bar{n}_1\bar{i}(s)}\delta_{\bar{j}_1\bar{a}(s)}. \tag{591}$$

Therefore, one could obtain

$$\begin{aligned}
\left[\tau^*_{(0)}\right]^{\bar{\alpha}_1\bar{\alpha}_2\cdots\bar{\alpha}_M}\left[\tau_{(s)}\right]^{\bar{\beta}_1\bar{\alpha}_2\cdots\bar{\alpha}_M} =&\left[\varepsilon^*_{(0)}\right]^{\bar{n}_1\bar{n}_2\cdots\bar{n}_M} T_{\bar{n}_1\bar{\alpha}_1}\cdots T_{\bar{n}_M\bar{\alpha}_M}\times\left[\varepsilon_{(s)}\right]^{\bar{j}_1\bar{n}'_2\cdots\bar{n}'_M} T^*_{\bar{j}_1\bar{\beta}_1}\cdots T^*_{\bar{n}'_M\bar{\beta}_M}\\
=&\left[\varepsilon^*_{(0)}\right]^{\bar{n}_1\bar{n}_2\cdots\bar{n}_M}\left[\varepsilon_{(s)}\right]^{\bar{j}_1\bar{n}'_2\cdots\bar{n}'_M}\times T_{\bar{n}_1\bar{\alpha}_1}\cdots T_{\bar{n}_M\bar{\alpha}_M}\times T^*_{\bar{j}_1\bar{\beta}_1}\cdots T^*_{\bar{n}'_M\bar{\beta}_M}\\
=&\frac{(M-1)!}{M!}\delta_{\bar{n}_1\bar{i}(s)}\delta_{\bar{j}_1\bar{a}(s)}\times T_{\bar{n}_1\bar{\alpha}_1}\cdots T_{\bar{n}_M\bar{\alpha}_M}\times T^*_{\bar{j}_1\bar{\beta}_1}\cdots T^*_{\bar{n}'_M\bar{\beta}_M}\\
=&\frac{(M-1)!}{M!}T_{\bar{i}(s)\bar{\alpha}_1}T^*_{\bar{a}(s)\bar{\beta}_1}.
\end{aligned} \tag{592}$$

Here, $\bar{i}(s)$ is the occupied state (contained in I_0) and is replaced by the unoccupied state $\bar{a}(s)$ in the index set I_s. This implies that only singly excited Slater determinants Ψ_s contribute and the matrix elements in Eq.(590) read

$$\langle\Psi_0|\hat{n}_c(\mathbf{r})|\Psi_s\rangle = \sum_{\bar{\alpha}\bar{\beta}\in C} T_{\bar{i}(s)\bar{\alpha}}T^*_{\bar{a}(s)\bar{\beta}}w^*_{\bar{\alpha}}(\mathbf{r})w_{\bar{\beta}}(\mathbf{r}). \tag{593}$$

After inserting Eq. (593) into Eq. (571) and then Fourier transformation to frequency domain using the fact

$$\begin{aligned}
\int_{-\infty}^{+\infty}\Theta(\tau)\mathbf{e}^{(E_0-E_s)\tau}e^{\mathrm{i}\omega\tau}d\tau &= \frac{-1}{\mathrm{i}\omega+E_0-E_s}\\
\int_{-\infty}^{+\infty}\Theta(-\tau)\mathbf{e}^{(E_s-E_0)\tau}e^{\mathrm{i}\omega\tau}d\tau &= \frac{1}{\mathrm{i}\omega+E_s-E_0},
\end{aligned} \tag{594}$$

one obtains

$$\chi^c(\mathbf{r},\mathbf{r}',\mathrm{i}\omega) = \sum_{s=1}^{\infty}\sum_{\bar\alpha\bar\beta\bar\gamma\bar\delta\in C} \Xi^{(s)}_{\bar\alpha\bar\beta\bar\gamma\bar\delta}(\mathrm{i}\omega) w^*_{\bar\alpha}(\mathbf{r}) w_{\bar\beta}(\mathbf{r}) w^*_{\bar\gamma}(\mathbf{r}') w_{\bar\delta}(\mathbf{r}'), \tag{595}$$

with the four-point polarizability tensor [289]

$$\Xi^{(s)}_{\bar\alpha\bar\beta\bar\gamma\bar\delta}(\mathrm{i}\omega) = \frac{T_{\bar i(s)\bar\alpha} T^*_{\bar a(s)\bar\beta} T_{\bar a(s)\bar\gamma} T^*_{\bar i(s)\bar\delta}}{\mathrm{i}\omega + E_0 - E_s} - \frac{T_{\bar a(s)\bar\alpha} T^*_{\bar i(s)\bar\beta} T_{\bar i(s)\bar\gamma} T^*_{\bar a(s)\bar\delta}}{\mathrm{i}\omega + E_s - E_0}. \tag{596}$$

The sum over singly excited Slater determinants $\sum_{s=1}^{\infty}$ can be rewritten into a double Bloch sum $\sum_{\bar n\bar n'} f_{\bar n}(1 - f_{\bar n'})$ using the one-electron occupancies $f_{\bar n}, f_{\bar n'}$ and the replacements

$$E_0 - E_s \to \epsilon_{\bar n} - \epsilon_{\bar n'}, \quad \bar i \to \bar n, \quad \bar a \to \bar n'. \tag{597}$$

Exchanging $\bar n \leftrightarrow \bar n'$ in the second term of Eq. (596), one obtains the Wannier representation for the correlated independent-particle polarizability

$$\begin{aligned}\chi^c(\mathbf{r},\mathbf{r}',\mathrm{i}\omega) =& \sum_{\bar n\bar n'}^{\text{all}} \sum_{\bar\alpha\bar\beta\bar\gamma\bar\delta\in C} \frac{f_{\bar n}(1 - f_{\bar n'}) - f_{\bar n'}(1 - f_{\bar n})}{\mathrm{i}\omega + \epsilon_{\bar n} - \epsilon_{\bar n'}} \times T_{\bar n\bar\alpha} T^*_{\bar n'\bar\beta} T_{\bar n'\bar\gamma} T^*_{\bar n\bar\delta} w^*_{\bar\alpha}(\mathbf{r}) w_{\bar\beta}(\mathbf{r}) w^*_{\bar\gamma}(\mathbf{r}') w_{\bar\delta}(\mathbf{r}'),\\ =& \sum_{\bar n\bar n'}^{\text{all}} \sum_{\bar\alpha\bar\beta\bar\gamma\bar\delta\in C} \frac{f_{\bar n} - f_{\bar n'}}{\mathrm{i}\omega + \epsilon_{\bar n} - \epsilon_{\bar n'}} \times T_{\bar n\bar\alpha} T^*_{\bar n'\bar\beta} T_{\bar n'\bar\gamma} T^*_{\bar n\bar\delta} w^*_{\bar\alpha}(\mathbf{r}) w_{\bar\beta}(\mathbf{r}) w^*_{\bar\gamma}(\mathbf{r}') w_{\bar\delta}(\mathbf{r}').\end{aligned} \tag{598}$$

Now we Fourier transform Eq. (598) to reciprocal space using the definition in Eq. (442)

$$\chi^c_{\mathbf{GG}'}(\mathbf{q},\mathrm{i}\omega) = \frac{1}{\Omega_0}\int_{\Omega_0} d\mathbf{r} \int_{\Omega_0} d\mathbf{r}' \mathbf{e}^{-\mathrm{i}(\mathbf{q}+\mathbf{G})\mathbf{r}} \chi^c(\mathbf{r},\mathbf{r}',\mathrm{i}\omega) \mathbf{e}^{\mathrm{i}(\mathbf{q}+\mathbf{G}')\mathbf{r}'}, \tag{599}$$

where Ω_0 is the volume of the unit cell. Decomposing the Wannier functions into Bloch functions via

$$|w_{\bar\alpha}\rangle = |w_{\alpha\mathbf{R}_\alpha}\rangle = \frac{1}{N_{\mathbf{k}}} \sum_{n\mathbf{k}} \mathbf{e}^{-\mathrm{i}\mathbf{k}\mathbf{R}_\alpha} T^{(\mathbf{k})}_{n\alpha} |\phi_{n\mathbf{k}}\rangle, \tag{600}$$

where $N_{\mathbf{k}}$ is the number of k-points within the BZ, and using the following notations

$$\bar\alpha = (\alpha, \mathbf{R}_\alpha), \quad \sum_{\bar\alpha} = \sum_{\alpha,\mathbf{R}_\alpha}, \quad \bar n = (n, \mathbf{k}), \quad \sum_{\bar n} = \sum_{n\mathbf{k}}, \tag{601}$$

$$T_{\bar n\bar\alpha} = \mathbf{e}^{-\mathrm{i}\mathbf{k}\mathbf{R}_\alpha} T^{(\mathbf{k})}_{n\alpha}. \tag{602}$$

Finally, one obtains

$$\begin{aligned}\chi^c_{\mathbf{GG}'}(\mathbf{q},\mathrm{i}\omega) =& \frac{1}{\Omega_0} \sum_{\bar n\bar n'}^{\text{all}} \frac{1}{N^4_{\mathbf{k}}} \sum_{\bar n_1\bar n_2\bar n_3\bar n_4} \sum_{\alpha\beta\gamma\delta\in C} \frac{f_{\bar n} - f_{\bar n'}}{\mathrm{i}\omega + \epsilon_{\bar n} - \epsilon_{\bar n'}}\\ &\times\langle\phi_{\bar n_1}|\mathbf{e}^{-\mathrm{i}(\mathbf{q}+\mathbf{G})\mathbf{r}}|\phi_{\bar n_2}\rangle\langle\phi_{\bar n_3}|\mathbf{e}^{\mathrm{i}(\mathbf{q}+\mathbf{G}')\mathbf{r}'}|\phi_{\bar n_4}\rangle\\ &\times T^{(\mathbf{k})}_{n\alpha} T^{*(\mathbf{k}_1)}_{n_1\alpha} T^{(\mathbf{k}_2)}_{n_2\beta} T^{*(\mathbf{k}')}_{n'\beta} T^{(\mathbf{k}')}_{n'\gamma} T^{*(\mathbf{k}_3)}_{n_3\gamma} T^{(\mathbf{k}_4)}_{n_4\delta} T^{*(\mathbf{k})}_{n\delta}\\ &\times \sum_{\mathbf{R}_\alpha} \mathbf{e}^{\mathrm{i}\mathbf{R}_\alpha(\mathbf{k}_1-\mathbf{k})} \sum_{\mathbf{R}_\beta} \mathbf{e}^{-\mathrm{i}\mathbf{R}_\beta(\mathbf{k}_2-\mathbf{k}')} \sum_{\mathbf{R}_\gamma} \mathbf{e}^{\mathrm{i}\mathbf{R}_\gamma(\mathbf{k}_3-\mathbf{k}')} \sum_{\mathbf{R}_\delta} \mathbf{e}^{-\mathrm{i}\mathbf{R}_\delta(\mathbf{k}_4-\mathbf{k})}.\end{aligned} \tag{603}$$

The sum over lattice vectors **R** can be carried out using the identity

$$\sum_{\mathbf{R}_\beta} \mathbf{e}^{-\mathrm{i}\mathbf{R}_\beta(\mathbf{k}_2-\mathbf{k}')} = N_k \delta_{\mathbf{k}_2,\mathbf{k}'+\mathbf{G}}, \tag{604}$$

and because the periodicity condition, $T^{(\mathbf{k}'+\mathbf{G})}_{n_2\beta} = T^{(\mathbf{k}')}_{n_2\beta}$ holds and the Bloch functions obey $|\phi_{nk+\mathbf{G}}\rangle = |\phi_{nk}\rangle$ [290], so that we obtain

$$\begin{aligned}
&\frac{1}{N_\mathbf{k}} \sum_{\bar{n}_2} [\sum_{\beta\in C} T^{(\mathbf{k}_2)}_{n_2\beta} T^{*(\mathbf{k}')}_{n'\beta}] |\phi_{\bar{n}_2}\rangle \sum_{\mathbf{R}_\beta} \mathbf{e}^{-\mathrm{i}\mathbf{R}_\beta(\mathbf{k}_2-\mathbf{k}')} \\
=&\frac{1}{N_\mathbf{k}} \sum_{n_2\mathbf{k}_2} [\sum_{\beta\in C} T^{(\mathbf{k}_2)}_{n_2\beta} T^{*(\mathbf{k}')}_{n'\beta}] |\phi_{n_2\mathbf{k}_2}\rangle N_\mathbf{k} \delta_{\mathbf{k}_2,\mathbf{k}'+\mathbf{G}} \\
=&\sum_{n_2} [\sum_{\beta\in C} T^{(\mathbf{k}'+\mathbf{G})}_{n_2\beta} T^{*(\mathbf{k}')}_{n'\beta}] |\phi_{n_2\mathbf{k}'+\mathbf{G}}\rangle \\
=&\sum_{n_2} [\sum_{\beta\in C} T^{(\mathbf{k}')}_{n_2\beta} T^{*(\mathbf{k}')}_{n'\beta}] |\phi_{n_2\mathbf{k}'}\rangle.
\end{aligned} \tag{605}$$

Now we define a correlated projector

$$P^{(\mathbf{k}')}_{n_2n'} = \sum_{\beta\in C} T^{(\mathbf{k}')}_{n_2\beta} T^{*(\mathbf{k}')}_{n'\beta}, \tag{606}$$

and a correlated Bloch state

$$|\bar{\phi}_{\bar{n}'}\rangle = |\bar{\phi}_{n'\mathbf{k}'}\rangle = \sum_{n_2} P^{(\mathbf{k}')}_{n_2n'} |\phi_{n_2\mathbf{k}'}\rangle. \tag{607}$$

Finally, Eq. (603) can be rewritten into

$$\chi^c_{\mathbf{GG}'}(\mathbf{q}, \mathrm{i}\omega) = \frac{1}{\Omega_0} \sum_{\bar{n}\bar{n}'}^{\text{all}} \frac{f_{\bar{n}} - f_{\bar{n}'}}{\mathrm{i}\omega + \epsilon_{\bar{n}} - \epsilon_{\bar{n}'}} \langle\bar{\phi}_{\bar{n}}|\mathbf{e}^{-\mathrm{i}(\mathbf{q}+\mathbf{G})\mathbf{r}}|\bar{\phi}_{\bar{n}'}\rangle_{\Omega_0} \langle\bar{\phi}_{\bar{n}'}|\mathbf{e}^{\mathrm{i}(\mathbf{q}+\mathbf{G}')\mathbf{r}'}|\bar{\phi}_{\bar{n}}\rangle_{\Omega_0}. \tag{608}$$

Note that the matrix elements on the right-hand side of Eq. (608) are invariant under the transformations

$$\mathbf{r} \to \mathbf{r} + \mathbf{R} \text{ and } \mathbf{r}' \to \mathbf{r}' - \mathbf{R}.$$

For $\mathbf{r} \to \mathbf{r} + \mathbf{R}$, one obtains

$$\begin{aligned}
&\langle\bar{\phi}_{n\mathbf{k}}(\mathbf{r}+\mathbf{R})|\mathbf{e}^{-\mathrm{i}(\mathbf{q}+\mathbf{G})(\mathbf{r}+\mathbf{R})}|\bar{\phi}_{n\mathbf{k}'}(\mathbf{r}+\mathbf{R})\rangle \\
=&\int d\mathbf{r} \bar{\phi}^*_{n\mathbf{k}}(\mathbf{r}+\mathbf{R}) \mathbf{e}^{-\mathrm{i}(\mathbf{q}+\mathbf{G})(\mathbf{r}+\mathbf{R})} \bar{\phi}_{n\mathbf{k}'}(\mathbf{r}+\mathbf{R}) \\
=&\int d\mathbf{r} \bar{\phi}^*_{n\mathbf{k}}(\mathbf{r}) \mathbf{e}^{-\mathrm{i}\mathbf{k}\mathbf{R}} \mathbf{e}^{-\mathrm{i}(\mathbf{q}+\mathbf{G})\mathbf{r}} \mathbf{e}^{-\mathrm{i}\mathbf{q}\mathbf{R}} \bar{\phi}_{n\mathbf{k}'}(\mathbf{r}) \mathbf{e}^{\mathrm{i}\mathbf{k}'\mathbf{R}} \\
=&\int d\mathbf{r} \bar{\phi}^*_{n\mathbf{k}}(\mathbf{r}) \mathbf{e}^{-\mathrm{i}(\mathbf{q}+\mathbf{G})\mathbf{r}} \bar{\phi}_{n\mathbf{k}'}(\mathbf{r}) \mathbf{e}^{\mathrm{i}\mathbf{R}(-\mathbf{k}-\mathbf{q}+\mathbf{k}')} \\
\equiv&\langle\bar{\phi}_{n\mathbf{k}}(\mathbf{r})|\mathbf{e}^{-\mathrm{i}(\mathbf{q}+\mathbf{G})\mathbf{r}}|\bar{\phi}_{n\mathbf{k}'}(\mathbf{r})\rangle
\end{aligned} \tag{609}$$

The above derivation has used the Bloch theorem and the fact that $\mathbf{e}^{\pm\mathrm{i}\mathbf{GR}} \equiv 1$, yielding $\mathbf{e}^{\mathrm{i}\mathbf{R}(-\mathbf{k}-\mathbf{q}+\mathbf{k}')} \equiv 1$, i.e, $\mathbf{k}' = \mathbf{k} + \mathbf{q}$. Similarly, $\mathbf{k}' = \mathbf{k} + \mathbf{q}$ holds for $\mathbf{r} \rightarrow \mathbf{r} - \mathbf{R}$ as well. We finally end up with

$$\begin{aligned}
\chi^{c}_{\mathbf{GG}'}(\mathbf{q}, \mathrm{i}\omega) =& \frac{1}{\Omega_0} \sum_{\mathbf{k}}^{\mathrm{BZ}} \sum_{n,n'}^{\mathrm{all}} \frac{f_{n\mathbf{k}} - f_{n'\mathbf{k}+\mathbf{q}}}{\mathrm{i}\omega + \epsilon_{n\mathbf{k}} - \epsilon_{n'\mathbf{k}+\mathbf{q}}} \langle \bar{\phi}_{n\mathbf{k}} | \mathbf{e}^{-\mathrm{i}(\mathbf{q}+\mathbf{G})\mathbf{r}} | \bar{\phi}_{n'\mathbf{k}+\mathbf{q}} \rangle_{\Omega_0} \langle \bar{\phi}_{n'\mathbf{k}+\mathbf{q}} | \mathbf{e}^{\mathrm{i}(\mathbf{q}+\mathbf{G}')\mathbf{r}'} | \bar{\phi}_{n\mathbf{k}} \rangle_{\Omega_0} \\
=& -\frac{1}{\Omega_0} \sum_{\mathbf{k}}^{\mathrm{BZ}} \sum_{i}^{\mathrm{occ}} \sum_{a}^{\mathrm{unocc}} \frac{2(\epsilon_{a\mathbf{k}+\mathbf{q}} - \epsilon_{i\mathbf{k}})}{(\epsilon_{a\mathbf{k}+\mathbf{q}} - \epsilon_{i\mathbf{k}})^2 + \omega^2} \langle \bar{\phi}_{i\mathbf{k}} | \mathbf{e}^{-\mathrm{i}(\mathbf{q}+\mathbf{G})\mathbf{r}} | \bar{\phi}_{a\mathbf{k}+\mathbf{q}} \rangle_{\Omega_0} \langle \bar{\phi}_{a\mathbf{k}+\mathbf{q}} | \mathbf{e}^{\mathrm{i}(\mathbf{q}+\mathbf{G}')\mathbf{r}'} | \bar{\phi}_{i\mathbf{k}} \rangle_{\Omega_0},
\end{aligned} \tag{610}$$

where $|\bar{\phi}_{i\mathbf{k}}\rangle$ is defined in Eq. (607). Note that in deriving Eq. (610) the term including $\sum_{n,n'}^{\mathrm{all}} \frac{\mathrm{i}\omega(f_{n\mathbf{k}} - f_{n'\mathbf{k}+\mathbf{q}})}{(\epsilon_{n'\mathbf{k}+\mathbf{q}} - \epsilon_{n\mathbf{k}})^2 + \omega^2}(\cdots)$ is vanishing because $\frac{\mathrm{i}\omega(f_{n\mathbf{k}} - f_{n'\mathbf{k}+\mathbf{q}})}{(\epsilon_{n'\mathbf{k}+\mathbf{q}} - \epsilon_{n\mathbf{k}})^2 + \omega^2}$ is an odd tensor with respect to n and n'.

Taking a closer look at Eq. (610), one would obtain that the correlated independent-particle polarizability χ^c has exactly the same expression as the independent-particle polarizability χ as long as $|\bar{\phi}_{i\mathbf{k}}\rangle$ is replaced by $|\phi_{i\mathbf{k}}\rangle$

$$\chi_{\mathbf{GG}'}(\mathbf{q}, \mathrm{i}\omega) = -\frac{1}{\Omega_0} \sum_{\mathbf{k}}^{\mathrm{BZ}} \sum_{i}^{\mathrm{occ}} \sum_{a}^{\mathrm{unocc}} \frac{2(\epsilon_{a\mathbf{k}+\mathbf{q}} - \epsilon_{i\mathbf{k}})}{(\epsilon_{a\mathbf{k}+\mathbf{q}} - \epsilon_{i\mathbf{k}})^2 + \omega^2} \langle \phi_{i\mathbf{k}} | \mathbf{e}^{-\mathrm{i}(\mathbf{q}+\mathbf{G})\mathbf{r}} | \phi_{a\mathbf{k}+\mathbf{q}} \rangle_{\Omega_0} \langle \phi_{a\mathbf{k}+\mathbf{q}} | \mathbf{e}^{\mathrm{i}(\mathbf{q}+\mathbf{G}')\mathbf{r}'} | \phi_{i\mathbf{k}} \rangle_{\Omega_0}. \tag{611}$$

Fourier transformation of Eq. (611) to imaginary time yields

$$\chi_{\mathbf{GG}'}(\mathbf{q}, \mathrm{i}\tau) = -\frac{1}{\Omega_0} \sum_{\mathbf{k}}^{\mathrm{BZ}} \sum_{i}^{\mathrm{occ}} \sum_{a}^{\mathrm{unocc}} \mathbf{e}^{-(\epsilon_{a\mathbf{k}+\mathbf{q}} - \epsilon_{i\mathbf{k}})\tau} \langle \phi_{i\mathbf{k}} | \mathbf{e}^{-\mathrm{i}(\mathbf{q}+\mathbf{G})\mathbf{r}} | \phi_{a\mathbf{k}+\mathbf{q}} \rangle_{\Omega_0} \langle \phi_{a\mathbf{k}+\mathbf{q}} | \mathbf{e}^{\mathrm{i}(\mathbf{q}+\mathbf{G}')\mathbf{r}'} | \phi_{i\mathbf{k}} \rangle_{\Omega_0}. \tag{612}$$

Fourier transformation of Eq. (612) further to the real space yields a simple expression for the polarizability

$$\begin{aligned}
\chi(\mathbf{r}, \mathbf{r}', \mathrm{i}\tau) =& -\sum_{\mathbf{k},\mathbf{q}}^{\mathrm{BZ}} \sum_{i}^{\mathrm{occ}} \sum_{a}^{\mathrm{unocc}} \mathbf{e}^{-(\epsilon_{a\mathbf{k}+\mathbf{q}} - \epsilon_{i\mathbf{k}})\tau} \phi^{*}_{i\mathbf{k}}(\mathbf{r}) \phi_{a\mathbf{k}+\mathbf{q}}(\mathbf{r}) \phi^{*}_{a\mathbf{k}+\mathbf{q}}(\mathbf{r}') \phi_{i\mathbf{k}}(\mathbf{r}') \\
=& -\sum_{\mathbf{k},\mathbf{q}}^{\mathrm{BZ}} \sum_{a}^{\mathrm{unocc}} \phi_{a\mathbf{k}+\mathbf{q}}(\mathbf{r}) \phi^{*}_{a\mathbf{k}+\mathbf{q}}(\mathbf{r}') \mathbf{e}^{-\epsilon_{a\mathbf{k}+\mathbf{q}}\tau} \sum_{i}^{\mathrm{occ}} \phi_{i\mathbf{k}}(\mathbf{r}') \phi^{*}_{i\mathbf{k}}(\mathbf{r}) \mathbf{e}^{\epsilon_{i\mathbf{k}}\tau},
\end{aligned} \tag{613}$$

which is consistent with the space-time method [96, 102].

References

References

[1] C. Cohen-Tannoudji, B. Diu, and F. Laloe. *Quantum mechanics: volume 1*. John Wiley and Sons, 1977.

[2] R.G. Parr and Y. Weitao. *Density functional theory of atoms and molecules*. Oxford University Press, 1989.

[3] J. Thijssen. *Computational physics*. Cambridge University Press, 2007.

[4] J.C. Slater. The theory of complex spectra. *Phys. Rev.*, 34:1293–1322, 1929.

[5] A. Szabo and N. S. Ostlund. *Modern quantum chemistry*. Dover, Mineola, New York, 1996.

[6] J. Kohanoff. *Electronic structure calculations for solids and molecules*. Cambridge University Press, 2006.

[7] C. David Sherrill, F. Henry, and III Schaefer. The configuration interaction method: Advances in highly correlated approaches. *Advances in Quantum Chemistry*, 34:143–269, 1999.

[8] P. Hohenberg and W. Kohn. Inhomogeneous electron gas. *Phys. Rev.*, 136:B864–B871, 1964.

[9] W. Kohn and L.J. Sham. Self-consistent equations including exchange and correlation effects. *Phys. Rev.*, 140:A1133–A1138, 1965.

[10] J.P. Perdew, R.G. Parr, M. Levy, and J.L. Balduz. Density-functional theory for fractional particle number: derivative discontinuities of the energy. *Phys. Rev. Lett.*, 49:1691–1694, 1982.

[11] J.P. Perdew and M. Levy. Physical content of the exact Kohn-Sham orbital energies: band gaps and derivative discontinuities. *Phys. Rev. Lett.*, 51:1884–1887, 1983.

[12] J.P. Perdew and M. Levy. Comment on “Significance of the highest occupied Kohn-Sham eigenvalue”. *Phys. Rev. B*, 56:16021–16028, 1997.

[13] W.G. Aulbur and L. Jönsson and J.W. Wilkins. *Quasiparticle calculations in solids*, volume 54 of *Solid State Phys.* Academic Press, 1999.

[14] L.J. Sham and M. Schlüter. Density functional theory of the energy gap. *Phys. Rev. Lett.*, 51:1888–1891, 1983.

[15] Christoph Freysoldt, Blazej Grabowski, Tilmann Hickel, Jörg Neugebauer, Georg Kresse, Anderson Janotti, and Chris G. Van de Walle. First-principles calculations for point defects in solids. *Rev. Mod. Phys.*, 86:253–305, 2014.

[16] P.A.M. Dirac. Note on exchange phenomena in the thomas atom. *Math. Proc. Cambridge*, 26:376–385, 1930.

[17] D.M. Ceperley and B.J. Alder. Ground state of the electron gas by a stochastic method. *Phys. Rev. Lett.*, 45:566–569, 1980.

[18] S.H. Vosko, L. Wilk, and M. Nusair. Accurate spin-dependent electron liquid correlation energies for local spin density calculations: a critical analysis. *Can. J. Phys.*, 58(8):1200–1211, 1980.

[19] J. P. Perdew and A. Zunger. Self-interaction correction to density-functional approximations for many-electron systems. *Phys. Rev. B*, 23:5048–5079, 1981.

[20] J.P. Perdew, K. Burke, and Y. Wang. Generalized gradient approximation for the exchange-

correlation hole of a many-electron system. *Phys. Rev. B*, 54:16533–16539, 1996.

[21] Perdew J. P., Burke K., and Ernzerhof M. Generalized gradient approximation made simple. *Phys. Rev. Lett.*, 77:3865, 1996.

[22] J.P. Perdew, A. Ruzsinszky, G.I. Csonka, O.A. Vydrov, G.E. Scuseria, L.A. Constantin, X. Zhou, and K. Burke. Restoring the density-gradient expansion for exchange in solids and surfaces. *Phys. Rev. Lett.*, 100:136406, 2008.

[23] M.P. Allen and D.J. Tildesley. *Computer simulation of liquids*. Oxford University Press, 1989.

[24] M.C. Payne, M.P. Teter, D.C. Allan, T.A. Arias, and J.D. Joannopoulos. Iterative minimization techniques for ab initio total-energy calculations: molecular dynamics and conjugate gradients. *Rev. Mod. Phys.*, 64:1045–1097, 1992.

[25] M. Marsman. *Periodic systems, plane waves, the PAW method, and hybrid functionals*, pages 61–76. Wiley-VCH Verlag GmbH and Co. KGaA, 2009.

[26] N.W. Ashcroft and N.D. Mermin. *Solid state physics*. Brooks Cole, 1976.

[27] H.J. Monkhorst and J.D. Pack. Special points for Brillouin zone integrations. *Phys. Rev. B*, 13:5188–5192, 1976.

[28] Leif E. H. *Ab initio study of defects in amorphous silicon nitride*. PhD thesis, University of Vienna, 2015.

[29] J Ihm and A Zunger and M L Cohen. Momentum-space formalism for the total energy of solids. *Journal of Physics C: Solid State Physics*, 12(21):4409, 1979.

[30] G. Kresse and D. Joubert. From ultrasoft pseudopotentials to the projector augmented-wave method. *Phys. Rev. B*, 59:1758–1775, 1999.

[31] D. Vanderbilt. Soft self-consistent pseudopotentials in a generalized eigenvalue formalism. *Phys. Rev. B*, 41:7892–7895, 1990.

[32] P.E. Blöchl. Projector augmented-wave method. *Phys. Rev. B*, 50:17953–17979, 1994.

[33] M. Shishkin and G. Kresse. Implementation and performance of the frequency-dependent *GW* method within the PAW framework. *Phys. Rev. B*, 74:035101, 2006.

[34] I.G. Austin and N.F. Mott. Metallic and nonmetallic behavior in transition metal oxides. *Science*, 168:71–77, 1970.

[35] G. Kotliar, S. Y. Savrasov, K. Haule, V. S. Oudovenko, O. Parcollet, and C. A. Marianetti. Electronic structure calculations with dynamical mean-field theory. *Rev. Mod. Phys.*, 78:865–951, 2006.

[36] V.I. Anisimov and O. Gunnarsson. Density-functional calculation of effective coulomb interactions in metals. *Phys. Rev. B*, 43:7570–7574, 1991.

[37] V.I. Anisimov, J. Zaanen, and O.K. Andersen. Band theory and mott insulators: Hubbard u instead of stoner i. *Phys. Rev. B*, 44:943–954, 1991.

[38] V.I. Anisimov, I.V. Solovyev, M.A. Korotin, M.T. Czyżyk, and G.A. Sawatzky. Density-functional theory and NiO photoemission spectra. *Phys. Rev. B*, 48:16929–16934, 1993.

[39] I.V. Solovyev, P.H. Dederichs, and V.I. Anisimov. Corrected atomic limit in the local-density approximation and the electronic structure of d impurities in Rb. *Phys. Rev. B*, 50:16861–16871, 1994.

[40] V.I. Anisimov, F. Aryasetiawan, and A.I. Lichtenstein. First-principles calculations of the electronic structure and spectra of strongly correlated

systems: the LDA+U method . *J. Phys.: Condens. Matter*, 9:767–808, 1997.

[41] Eva Pavarini, Erik Koch, Frithjof Anders, and Mark Jarrell (Eds.). *Correlated Electrons: From Models to Materials: lecture notes of the Autumn school 2012, Correlated Electrons 2012; Autumn School organized by the Forschungszentrum Jülich and the German Research School for Simulation Sciences at Forschungszentrum Jülich 3-7 September 2012*. Forschungszentrum Jülich GmbH, Institute for Advanced Simulation, 2011.

[42] N. Marzari and D. Vanderbilt. Maximally localized generalized wannier functions for composite energy bands. *Phys. Rev. B*, 56:12847, 1997.

[43] I. Souza, N. Marzari, and D. Vanderbilt. Maximally localized generalized wannier functions for composite energy bands. *Phys. Rev. B*, 65:035109, 2001.

[44] A.I. Liechtenstein, V.I. Anisimov, and J. Zaanen. Density-functional theory and strong interactions: Orbital ordering in Mott-Hubbard insulators. *Phys. Rev. B*, 52:R5467–R5470, 1995.

[45] Gunnarsson, O. and Andersen, O. K. and Jepsen, O. and Zaanen, J. Density-functional calculation of the parameters in the Anderson model: Application to Mn in CdTe. *Phys. Rev. B*, 39:1708–1722, 1989.

[46] Aryasetiawan, F. and Imada, M. and Georges, A. and Kotliar, G. and Biermann, S. and Lichtenstein, A. I. Frequency-dependent local interactions and low-energy effective models from electronic structure calculations. *Phys. Rev. B*, 70:195104, 2004.

[47] Aryasetiawan, F. and Karlsson, K. and Jepsen, O. and Schönberger, U. Calculations of Hubbard U from first-principles. *Phys. Rev. B*, 74:125106, 2006.

[48] S.L. Dudarev, G.A. Botton, S.Y. Savrasov, C.J. Humphreys, and A.P. Sutton. Electron-energy-loss spectra and the structural stability of nickel oxide: An LSDA+U study. *Phys. Rev. B*, 57:1505–1509, 1998.

[49] Weitao Yang, Yingkai Zhang, and Paul W. Ayers. Degenerate ground states and a fractional number of electrons in density and reduced density matrix functional theory. *Phys. Rev. Lett.*, 84:5172–5175, 2000.

[50] Paula Mori-Sánchez, Aron J. Cohen, and Weitao Yang. Localization and delocalization errors in density functional theory and implications for band-gap prediction. *Phys. Rev. Lett.*, 100:146401, 2008.

[51] Aron J. Cohen, Paula Mori-Sánchez, and Weitao Yang. Insights into current limitations of density functional theory. *Science*, 321(5890):792–794, 2008.

[52] J. Paier, R. Hirschl, M. Marsman, and G. Kresse. The Perdew-Burke-Ernzerhof exchange-correlation functional applied to the G2-1 test set using a plane-wave basis set. *J Chem Phys*, 122:234102, 2005.

[53] Aliaksandr V. Krukau and Oleg A. Vydrov and Artur F. Izmaylov and Gustavo E. Scuseria. Influence of the exchange screening parameter on the performance of screened hybrid functionals. *The Journal of Chemical Physics*, 125(22):224106, 2006.

[54] Benjamin G. Janesko, Thomas M. Henderson, and Gustavo E. Scuseria. Screened hybrid density functionals for solid-state chemistry and physics. *Physical Chemistry Chemical Physics*, 11:443–454, 2009.

[55] Cesare Franchini. Hybrid functionals applied to perovskites. *J. Phys.: Condens. Matter*, 26:253202, 2014.

[56] Eva Pavarini, Erik Koch, , and Piers Coleman (Eds.). *Many-Body Physics: From Kondo to Hubbard, lecture notes of the Autumn school 2015; Autumn School organized by the Forschungszentrum Jülich and the German Research School for Simulation Sciences at Forschungszentrum Jülich 21-25 September 2015*. Forschungszentrum Jülich GmbH, Institute for Advanced Simulation, 2015.

[57] M. Marsman, J. Paier, A. Stroppa, and G. Kresse. Hybrid functionals applied to extended systems. *Journal of Physics: Condensed Matter*, 20:064201, 2008.

[58] A. D. Becke. Density funnctional thermochemistry. III. The role of exact exchange. *J. Chem. Phys.*, 98:5648–5652, 1993.

[59] A. D. Becke. A new mixing of hartree-fock and local density functional theories. *J. Chem. Phys.*, 98(2):1372–1377, 1993.

[60] P.J. Stephens, F.J. Devlin, C.F. Chabalowski, and M.J. Frisch. Ab initio calculation of vibrational absorption and circular dichroism spectra using density functional force fields. *J. Chem. Phys.*, 98:11623–11627, 1994.

[61] J.P. Perdew, M. Ernzerhof, and K. Burke. Rationale for mixing exact exchange with density functional approximations. *J. Chem. Phys.*, 105:9982–9985, 1996.

[62] J. Paier, M. Marsman, and G. Kresse. Why does the B3LYP hybrid functional fail for metals? *J. Chem. Phys.*, 127:024103, 1–10, 2007.

[63] J. Paier, M. Marsman, K. Hummer, and G. Kresse. Screened hybrid density functionals applied to solids. *J. Chem. Phys.*, 124:154709, 2006.

[64] J. Heyd, G.E. Scuseria, and M. Ernzerhof. Hybrid functionals based on a screened Coulomb potential. *J. Chem. Phys.*, 118:8207, 2003.

[65] R.D. Adamson, J.P. Dombroski, and P.M.W. Gill. Chemistry without Coulomb tails. *Chem. Phys. Lett.*, 254:329 – 336, 1996.

[66] P.M.W. Gill and R.D. Adamson. A family of attenuated Coulomb operators. *Chem. Phys. Lett.*, 261:105 – 110, 1996.

[67] T. Leininger, H. Stoll, H.J. Werner, and A. Savin. Combining long-range configuration interaction with short-range density functionals. *Chem. Phys. Lett.*, 275:151 – 160, 1997.

[68] Weiwei Xing, Peitao Liu, Xiyue Cheng, Haiyang Niu, Dianzhong Li Hui Ma, Yiyi Li, and Xing-Qiu Chen. Vacancy formation enthalpy of filled d-band noble metals by hybrid functionals. *Phys. Rev. B*, 90:144105, 2014.

[69] Kerstin Hummer, Judith Harl, and Georg Kresse. Heyd-Scuseria-Ernzerhof hybrid functional for calculating the lattice dynamics of semiconductors. *Phys. Rev. B*, 80:115205, 2009.

[70] L. Hedin. New method for calculating the one-particle Green's function with application to the electron-gas problem. *Phys. Rev.*, 139:A796–A823, 1965.

[71] L. Hedin and S. Lundqvist. *Solid State Physics*. Academic, New York, 1969.

[72] F. Aryasetiawan. *Advances in Condensed Matter Science*. Gordon and Breach, New York, 2000.

[73] Giovanni Onida, Lucia Reining, and Angel Rubio. Electronic excitations: density-functional versus many-body green's-function approaches. *Rev. Mod. Phys.*, 74:601–659, 2002.

[74] Volodymyr Dzhagan. https://www.tu-chemnitz.de/physik/HLPH/elec_spec.html.

[75] D.N. Zubarev. Double-time Green functions in statistical physics. *Sov. Phys. Usp.*, 3(3):320, 1960.

[76] F. Aryasetiawan and O. Gunnarsson. The *GW* method. *Rep. Prog. Phys.*, 61(3):237, 1998.

[77] V. M. Galitskii and A. B. Migdal. Total energy from one-paticle green's function. *Sov. Phys. JETP*, 7:96, 1958.

[78] Richard D. Mattuck. *A Guide to Feynman Diagrams in the Many-Body Problem: Second Edition*. Dover publications, inc., New York, 1992.

[79] J.W. Negele and H. Orland. *Quantum many particle systems*. Westview Press, 1998.

[80] Gian-Marco Rignanese. Many-Body Perturbation Theory: the *GW* method. Lecture notes of International summer school on New trends in computational approaches for many-body systems, Sherbrooke, Québec, Canada . 2012.

[81] L. Hedin, B.I. Lundqvist, and S. Lundqvist. Beyond the one-electron approximation: density of states for interacting electrons. *J. Res. Nat. Bur. Stand. Sec. A: Phys. Ch.*, 74A(3):417, 1970.

[82] L. Hedin. On correlation effects in electron spectroscopies and the *GW* approximation. *J. Phys.: Condens. Matter*, 11(42):R489, 1999.

[83] Mark S Hybertsen and Steven G. Louie. Electron correlation in semiconductors and insulators: Band gaps and quasiparticle energies. *Phys. Rev. B*, 34(8):5390–5413, 1986.

[84] Michiel J. van Setten, Fabio Caruso, Sahar Sharifzadeh, Xinguo Ren, Matthias Scheffler, Fang Liu, Johannes Lischner, Lin Lin, Jack R. Deslippe, Steven G. Louie, Chao Yang, Florian Weigend, Jeffrey B. Neaton, Ferdinand Evers, and Patrick Rinke. GW100: Benchmarking G0W0 for Molecular Systems. *J. Chem. Theory Comput.*, 11(12):5665–5687, 2015. PMID: 26642984.

[85] M. van Schilfgaarde, Takao Kotani, and S. Faleev. Quasiparticle self-consistent *GW* theory. *Phys. Rev. Lett.*, 96:226402, 2006.

[86] M. Shishkin and G. Kresse. Self-consistent *GW* calculations for semiconductors and insulators. *Phys. Rev. B*, 75:235102, 2007.

[87] Mark van Schilfgaarde, Takao Kotani, and Sergey V. Faleev. Adequacy of approximations in *GW* theory. *Phys. Rev. B*, 74:245125, 2006.

[88] F. Fuchs, J. Furthmüller, F. Bechstedt, M. Shishkin, and G. Kresse. Quasiparticle band structure based on a generalized kohn-sham scheme. *Phys. Rev. B*, 76:115109, 2007.

[89] M. Shishkin, M. Marsman, and G. Kresse. Accurate quasiparticle spectra from self-consistent *GW* calculations with vertex corrections. *Phys. Rev. Lett.*, 99:246403, 2007.

[90] B. Holm and U. von Barth. Fully self-consistent *GW* self-energy of the electron gas. *Phys. Rev. B*, 57:2108–2117, 1998.

[91] Wei Ku and Adolfo G. Eguiluz. Band-gap problem in semiconductors revisited: Effects of core states and many-body self-consistency. *Phys. Rev. Lett.*, 89:126401, 2002.

[92] A. Grüneis, G. Kresse, Y. Hinuma, and F. Oba. Ionization potentials of solids: The importance of vertex corrections. *Phys. Rev. Lett.*, 112:096401, 2014.

[93] Lebègue, S. and Arnaud, B. and Alouani, M. and Bloechl, P. E. Implementation of an all-electron

GW approximation based on the projector augmented wave method without plasmon pole approximation: Application to Si, SiC, AlAs, InAs, NaH, and KH. *Phys. Rev. B*, 67:155208, 2003.

[94] Kotani, Takao and van Schilfgaarde, Mark and Faleev, Sergey V. Quasiparticle self-consistent *GW* method: A basis for the independent-particle approximation. *Phys. Rev. B*, 76:165106, 2007.

[95] Friedrich, Christoph and Blügel, Stefan and Schindlmayr, Arno. Efficient implementation of the *GW* approximation within the all-electron FLAPW method. *Phys. Rev. B*, 81:125102, 2010.

[96] H. N. Rojas, R. W. Godby, and R. J. Needs. Space-time method for ab initio calculations of self-energies and dielectric response functions of solids. *Phys. Rev. Lett.*, 74:1827, 1995.

[97] Kutepov, Andrey and Haule, Kristjan and Savrasov, Sergey Y. and Kotliar, Gabriel. Electronic structure of Pu and Am metals by self-consistent relativistic *GW* method. *Phys. Rev. B*, 85:155129, 2012.

[98] Chu, Iek-Heng and Trinastic, Jonathan P. and Wang, Yun-Peng and Eguiluz, Adolfo G. and Kozhevnikov, Anton and Schulthess, Thomas C. and Cheng, Hai-Ping. All-electron self-consistent *GW* in the Matsubara-time domain: Implementation and benchmarks of semiconductors and insulators. *Phys. Rev. B*, 93:125210, 2016.

[99] S. Adler. Quantum theory of the dielectric constant in real solids. *Phys. Rev.*, 126:413–420, 1962.

[100] N. Wiser. Dielectric constant with local field effects included. *Phys. Rev.*, 129:62–69, 1963.

[101] T. Miyake and F. Aryasetiawan. Efficient algorithm for calculating noninteracting frequency-dependent linear response functions. *Phys. Rev. B*, 61:7172–7175, 2000.

[102] L. Steinbeck, A. Rubio, L. Reining, M. Torrent, I. White, and W. Godby. Enhancements to the *GW* space-time method. *Comput. Phys. Commun.*, 125:105, 2000.

[103] M. Kaltak, J. Klimeš, and G. Kresse. Low scaling algorithms for the random phase approximation: Imaginary time and laplace transformations. *J. Chem. Theory Comput.*, 10:2498, 2014.

[104] M. Kaltak, J. Klimeš, and G. Kresse. Cubic scaling algorithm for the random phase approximation: Self-interstitials and vacancies in Si. *Phys. Rev. B*, 90:054115, 2014.

[105] A. Georges, G. Kotliar, W. Krauth, and M. J. Rozenberg. Dynamical mean-field theory of strongly correlated fermion systems and the limit of infinite dimensions. *Rev. Mod. Phys.*, 68:13, 1996.

[106] G. Kotliar, S. Y. Savrasov, K. Haule, V. S. Oudovenko, O. Parcollet, and C. A. Marianetti. Electronic structure calculations with dynamical mean-field theory. *Rev. Mod. Phys.*, 78:865, 2006.

[107] Liu, Peitao and Kaltak, Merzuk and Jiří, Klimeš and Kresse, Georg. Cubic scaling *GW*: Towards fast quasiparticle calculations. *Phys. Rev. B*, 94:165109, 2016.

[108] note that the auxiliary green's functions in eqs. (39–41) of ref. [104] represent eqs. (243–245).

[109] G. A. Jr. Baker. *Essentials of Padé Approximants*. Academic Press, New York, 1975.

[110] Ž. Osolin and R. Žitko. Pade approximant approach for obtaining finite-temperature spectral functions of quantum impurity models using

the numerical renormalization group technique. *Phys. Rev. B*, 87:245135, 2013.

[111] T. Miyake, C. Martins, R. Sakuma, and F. Aryasetiawan. Effects of momentum-dependent self-energy in the electronic structure of correlated materials. *Phys. Rev. B*, 87:115110, 2013.

[112] G. Kresse and J. Hafner. Ab initio molecular dynamics for liquid metals. *Phys. Rev. B*, 47:558, 1993.

[113] G. Kresse and J. Furthmüller. Efficient iterative schemes for ab initio total-energy calculations using a plane-wave basis set. *Phys. Rev. B*, 54:11169, 1996.

[114] B.-C. Shih, Y. Xue, P. Zhang, M. L. Cohen, and S. G. Louie. Quasiparticle Band Gap of ZnO: High Accuracy from the Conventional G0W0 Approach. *Phys. Rev. Lett.*, 105:146401, 2010.

[115] J. Klimeš, M. Kaltak, and G. Kresse. Predictive *GW* calculations using plane waves and pseudopotentials. *Phys. Rev. B*, 90:075125, 2014.

[116] M. Gajdoš, K. Hummer, G. Kresse, J. Furthmüller, and F. Bechstedt. Linear optical properties in the projector-augmented wave methodology. *Phys. Rev. B*, 73:045112, 2006.

[117] Claudia Ambrosch-Draxl and Jorge O. Sofo. Linear optical properties of solids within the full-potential linearized augmented plane wave method. *Computer Physics Communications*, 175:1–14, 2006.

[118] J. M. Tomczak, M. Casula, T. Miyake, and S. Biermann. Asymmetry in band widening and quasiparticle lifetimes in $SrVO_3$: Competition between screened exchange and local correlations from combined *GW* and dynamical mean-field theory *GW*+DMFT. *Phys. Rev. B*, 90:165138, 2014.

[119] Jan M. Tomczak and Michele Casula and Takashi Miyake and Ferdi Aryasetiawan and Silke Biermann. Combined GW and dynamical mean-field theory: Dynamical screening effects in transition metal oxides. *EPL (Europhysics Letters)*, 100(6):67001, 2012.

[120] Boehnke, L. and Nilsson, F. and Aryasetiawan, F. and Werner, P. When strong correlations become weak: Consistent merging of *GW* and DMFT. *Phys. Rev. B*, 94:201106, 2016.

[121] Guzzo, Matteo and Lani, Giovanna and Sottile, Francesco and Romaniello, Pina and Gatti, Matteo and Kas, Joshua J. and Rehr, John J. and Silly, Mathieu G. and Sirotti, Fausto and Reining, Lucia. Valence Electron Photoemission Spectrum of Semiconductors: Ab Initio Description of Multiple Satellites. *Phys. Rev. Lett.*, 107:166401, 2011.

[122] A. Marini, G. Onida, and R. D. Sole. Quasiparticle electronic structure of copper in the *GW* approximation. *Phys. Rev. Lett.*, 88:016403, 2002.

[123] V.P. Zhukov, E.V. Chulkov, and P.M. Echenique. Lifetimes of d holes in Cu and Au: Full-potential LMTO approach. *Phys. Rev. B*, 68:045102, 2003.

[124] R. Courths and S. Hüfner. Photoemission experiments on copper. *Phys. Rep.*, 112:53, 1984.

[125] Maggio, Emanuele and Liu, Peitao and van Setten, Michiel J. and Kresse, Georg. GW100: A Plane Wave Perspective for Small Molecules. *Journal of Chemical Theory and Computation*, 13(2):635–648, 2017.

[126] W Hanke and L J Sham. Many-Particle Effects in the Optical Excitations of a Semiconductor. *Phys. Rev. Lett.*, 43(5):387–390, 1979.

[127] G. Strinati, H. J. Mattausch, and W. Hanke. Dynamical correlation effects on the quasiparticle bloch states of a covalent crystal. *Phys. Rev. Lett.*, 45:290, 1980.

[128] G. Strinati, H. J. Mattausch, and W. Hanke. Dynamical aspects of correlation corrections in a covalent crystal. *Phys. Rev. B*, 25:2867, 1982.

[129] Sergey V. Faleev, Mark van Schilfgaarde, and Takao Kotani. All-Electron Self-Consistent *GW* Approximation: Application to Si, MnO, and NiO. *Phys. Rev. Lett.*, 93:126406, 2004.

[130] F. Caruso, P. Rinke, X. Ren, M. Scheffler, and A. Rubio. Unified description of ground and excited states of finite systems: The self-consistent *GW* approach. *Phys. Rev. B*, 86:081102, 2012.

[131] Fabio Caruso, Patrick Rinke, Xinguo Ren, Angel Rubio, and Matthias Scheffler. Self-consistent *GW*: All-electron implementation with localized basis functions. *Phys. Rev. B*, 88(7):075105, 2013.

[132] Ferdinand Kaplan, Florian Weigend, Ferdinand Evers, and Michiel Jan van Setten. Off-Diagonal Self-Energy Terms and Partially Self-Consistency in GW Calculations for Single Molecules: Efficient Implementation and Quantitative Effects on Ionization Potentials. *J. Chem. Theory Comput.*, 11(11):5152–5160, 2015.

[133] Ferdinand Kaplan, Michael E. Harding, Christian Seiler, Florian Weigend, Ferdinand Evers, and Michiel Jan van Setten. Quasi-Particle Self-Consistent *GW* for Molecules. *J. Chem. Theory Comput.*, 12(6):2528–2541, 2016.

[134] Johannes Lischner, Sahar Sharifzadeh, Jack R. Deslippe, Jeffrey B. Neaton, and Steven G. Louie. Effects of self-consistency and plasmon-pole models on *GW* calculations for closed-shell molecules. *Phys. Rev. B*, 90(11):115130, 2014.

[135] P. Koval, D. Foerster, and D. Sánchez-Portal. Fully self-consistent *GW* and quasiparticle self-consistent *GW* for molecules. *Phys. Rev. B*, 89:155417, 2014.

[136] X. Ren, P. Rinke, V. Blum, J. Wieferink, A. Tkatchenko, A. Sanfilippo, K. Reuter, and M. Scheffler. Resolution-of-identity approach to hartree-fock, hybrid density functionals, RPA, MP2 and *GW* with numeric atom-centered orbital basis functions. *New J. Phys.*, 14:053020, 2012.

[137] X. Blase, C. Attaccalite, and V. Olevano. First-principles GW calculations for fullerenes, porphyrins, phtalocyanine, and other molecules of interest for organic photovoltaic applications. *Phys. Rev. B*, 83:115103, 2011.

[138] Fabien Bruneval. Ionization energy of atoms obtained from GW self-energy or from random phase approximation total energies. *J. Chem. Phys.*, 136(19):194107, 2012.

[139] Michiel J. van Setten, Florian Weigend, and Ferdinand Evers. *J. Chem. Theory Comput.*, 9:232–246, 2013.

[140] Jan Wilhelm, Mauro Del Ben, and Jürg Hutter. GW in the Gaussian and Plane Waves Scheme with Application to Linear Acenes. *J. Chem. Theory Comput.*, 12(8):3623–3635, 2016.

[141] D Foerster, P. Koval, and Daniel Sánchez-Portal. An O(N3) implementation of Hedin's *GW* approximation for molecules. *J. Chem. Phys.*, 135(7):074105, 2011.

[142] San Huang Ke. All-electron *GW* methods implemented in molecular orbital space: Ionization energy and electron affinity of conjugated molecules. *Phys. Rev. B*, 84(20):205415, 2011.

[143] J. Laflamme Janssen, B. Rousseau, and M. Cote. Efficient dielectric matrix calculations using the Lanczos algorithm for fast many-body G0W0 implementations. *Phys. Rev. B*, 91:125120, 2015.

[144] Marco Govoni and Giulia Galli. Large scale *GW* calculations. *J. Chem. Theory Comput.*, 11(6):2680–2696, 2015.

[145] Fabien Bruneval and Miguel A L Marques. Benchmarking the Starting Points of the *GW* Approximation for Molecules. *J. Chem. Theory Comput.*, 9(1):324–329, 2013.

[146] Jack Deslippe, Georgy Samsonidze, David a. Strubbe, Manish Jain, Marvin L. Cohen, and Steven G. Louie. Berkeley*GW*: A massively parallel computer package for the calculation of the quasiparticle and optical properties of materials and nanostructures. *Comput. Phys. Commun.*, 183(6):1269–1289, 2012.

[147] Arno Schindlmayr. Analytic evaluation of the electronic self-energy in the *GW* approximation for two electrons on a sphere. *Phys. Rev. B*, 87(7):075104, 2013.

[148] Christoph Friedrich, Mathias C. Müller, and Stefan Blügel. Band convergence and linearization error correction of all-electron *GW* calculations: The extreme case of zinc oxide. *Phys. Rev. B*, 83:081101, 2011. *ibid* **84**, 039906(E) (2011).

[149] Fabien Bruneval and Xavier Gonze. Accurate *GW* self-energies in a plane-wave basis using only a few empty states: Towards large systems. *Phys. Rev. B*, 78:1–9, 2008.

[150] J. Harl and G. Kresse. Cohesive energy curves for noble gas solids calculated by adiabatic connection fluctuation-dissipation theory. *Phys. Rev. B*, 77:045136, 2008.

[151] James J. Shepherd, Andreas Grüneis, George H. Booth, Georg Kresse, and Ali Alavi. Convergence of many-body wave-function expansions using a plane-wave basis: From homogeneous electron gas to solid state systems. *Phys. Rev. B*, 86:035111, 2012.

[152] T. Björkman, A. Gulans, A. V. Krasheninnikov, and R. M. Nieminen. van der waals bonding in layered compounds from advanced density-functional first-principles calculations. *Phys. Rev. Lett.*, 108:235502, 2012.

[153] Carlo A. Rozzi, Daniele Varsano, Andrea Marini, Eberhard K. U. Gross, and Angel Rubio. Exact coulomb cutoff technique for supercell calculations. *Phys. Rev. B*, 73:205119, 2006.

[154] A. Baldereschi and E. Tosatti. Mean-value point and dielectric properties of semiconductors and insulators. *Phys. Rev. B*, 17:4710–4717, 1978.

[155] G. Makov and M. C. Payne. Periodic boundary conditions in ab initio calculations. *Phys. Rev. B*, 51:4014–4022, 1995.

[156] R. L. Kelly. Atomic and Ionic Spectrum Lines below 2000 Angstroms: Hydrogen through Krypton. *J. Phys. Chem. Ref. Data*, 16:Supplement 1, 1987.

[157] Karl-Michael Weitzel, Joachim Mähnert, and Martin Penno. ZEKE-PEPICO investigations of dissociation energies in ionic reactions. *Chem. Phys. Lett.*, 224(3):371–380, 1994.

[158] Robert C Wetzel, Frank A Baiocchi, Todd R Hayes, and Robert S Freund. Absolute cross sections for electron-impact ionization of the rare-gas atoms by the fast-neutral-beam method. *Phys. Rev. A*, 35(2):559–577, 1987.

[159] Harald Schäfer and Helmut Rabeneck. Massenspektroskopische Untersuchung der Borfluorid-

Komplexe ABF4. *Zeitschrift für Anorg. und Allg. Chemie*, 545(2):224–226, 1987.

[160] E McCormack, J M Gilligan, C Cornaggia, and E E Eyler. Measurement of high Rydberg states and the ionization potential of H2. *Phys. Rev. A*, 39(4):2260–2263, 1989.

[161] Ph. Dugourd, D Rayane, P Labastie, B Vezin, J Chevaleyre, and M Broyer. Measurements of lithium cluster ionization potentials. *Chem. Phys. Lett.*, 197(4–5):433–437, 1992.

[162] Manfred M Kappes, Peter Radi, Martin Schär, and Ernst Schumacher. Photoionization measurements on dialkali monohalides generated in supersonic nozzle beams. *Chem. Phys. Lett.*, 113(3):243–248, 1985.

[163] André Herrmann, Samuel Leutwyler, Ernst Schumacher, and Ludger Wöste. On Metal-Atom Clusters IV. Photoionization thresholds and multiphoton ionization spectra of alkali-metal molecules. *Helv. Chim. Acta*, 61(1):453–487, 1978.

[164] T Trickl, E F Cromwell, Y T Lee, and A H Kung. State-selective ionization of nitrogen in the X 2Σ+gv+=0 and v+=1 states by twocolor (1+ 1) photon excitation near threshold. *J. Chem. Phys.*, 91(10), 1989.

[165] Denis K Bulgin, John M Dyke, and Alan Morris. HeI photoelectron spectrum of the P2(X 1 Σ + g) molecule. *J. Chem. Soc. Faraday Trans. 2*, 72:2225, 1976.

[166] K H Lau, R D Brittain, and D L Hildenbrand. Vaporization of arsenic trisulfide and the dissociation energy of arsenic monosulfide. *J. Phys. Chem.*, 86(22):4429–4432, 1982.

[167] H Van Lonkhuyzen and C A De Lange. High-resolution UV photoelectron spectroscopy of diatomic halogens. *Chem. Phys.*, 89(2):313–322, 1984.

[168] John M Dyke, G D Josland, J G Snijders, and P M Boerrigter. Ionization energies of the diatomic halogens and interhalogens studied with relativistic hartree-fock-slater calculations. *Chem. Phys.*, 91(3):419–424, 1984.

[169] K. Kimura, S. Katsumata, Y. Achiba, T. Yamazaki, and S. Iwata. Ionization energies, Ab initio assignments, and valence electronic structure for 200 molecules. In *Handb. HeI Photoelectron Spectra Fundam. Org. Compd.* Japan Scientific Soc. Press, Tokyo, 1981.

[170] Gerhard Bieri and Leif Åsbrink. 30.4-nm He(II) photoelectron spectra of organic molecules. *J. Electron Spectros. Relat. Phenomena*, 20(1):149–167, 1980.

[171] Ragulan Ramanathan, Jeffrey A Zimmerman, and John R Eyler. Ionization potentials of small carbon clusters. *J. Chem. Phys.*, 98(10):7838, 1993.

[172] V.V. Plemenkov, Y.Y. Villem, N.V. Villem, I.G. Bolesov, L.S. Surmina, N.I. Yakushkina, and A.A. Formanovskii. Photoelectron spectra of polyalkylcyclopropenes and polyalkylcyclopropanes. *Zh. Obs. Khim.*, 51:2076, 1981.

[173] J O Howell, J M Goncalves, C Amatore, L Klasinc, R M Wightman, and J K Kochi. Electron transfer from aromatic hydrocarbons and their .pi.-complexes with metals. Comparison of the standard oxidation potentials and vertical ionization potentials. *J. Am. Chem. Soc.*, 106(14):3968–3976, 1984.

[174] Emil W Fu and Robert C Dunbar. Photodissociation spectroscopy and structural rearrangements in ions of cyclooctatetraene, styrene, and related

molecules. *J. Am. Chem. Soc.*, 100(8):2283–2288, 1978.

[175] V.D. Kiselev, A.G. Sakhabutdinov, I.M. Shakirov, V.V. Zverev, and A.I. Konovalov. Bis reactants in Diels-Alder reactions. VII. Preparation and properties of polyadducts of reactions of bis(polymethylcyclopentadienes) and bis(maleimides). *Zh. Org. Khim.*, 28:2244, 1992.

[176] Gerhard Bieri, Wolfgang von Niessen, Leif Åsbrink, and Agneta Svensson. The He(II) photoelectron spectra of the fluorosubstituted ethylenes and their analysis by the Green's function method. *Chem. Phys.*, 60(1):61–79, 1981.

[177] R Cambi, G Ciullo, A Sgamellotti, F Tarantelli, R Fantoni, A Giardini-guidoni, I E McCarthy, and V di Martino. An (e, 2e) spectroscopic invistigation and a green's function study of the ionization of chloro- and bromo-ethylene. *Chem. Phys. Lett.*, 101(4–5):477–484, 1983.

[178] K Wittel, H Bock, and R Manne. Photoelectron spectra of iodo ethylenes. *Tetrahedron*, 30(5):651–658, 1974.

[179] Gerhard Bieri, Leif Åsbrink, and Wolfgang Von Niessen. 30.4-nm He(II) Photoelectron spectra of organic molecules: Part IV. Fluoro-compounds (C, H, F). *J. Electron Spectros. Relat. Phenomena*, 23(2):281–322, 1981.

[180] R N Dixon, J N Murrell, and B Narayan. The photoelectron spectra of the halomethanes. *Mol. Phys.*, 20(4):611–623, 1971.

[181] G Jonkers, C.A.de Lange, and J G Snijders. Effects of relativity in the He(I) Photoelecron Spectrum of CI4. *Chem. Phys.*, 69(1):109–114, 1982.

[182] R Roberge, C Sandorfy, J I Matthews, and O P Strausz. The far ultraviolet and HeI photoelectron spectra of alkyl and fluorine substituted silane derivatives. *J. Chem. Phys.*, 69(11):5105, 1978.

[183] A W Potts and W C Price. The Photoelectron Spectra of Methane, Silane, Germane and Stannane. *Proc. R. Soc. London A Math. Phys. Eng. Sci.*, 326(1565):165–179, 1972.

[184] H Bock, W Ensslin, F Feher, and R Freund. Photoelectron spectra and molecular properties. LI. Ionization potentials of silanes Si_nH_{2n+2}. *J. Am. Chem. Soc.*, 98(3):668–674, 1976.

[185] NIST Chemistry WebBook, 2015.

[186] M Farber, R D Srivastava, and James W Moyer. Mass-spectrometric determination of the thermodynamics of potassium hydroxide and minor potassiumcontaining species required in magnetohydrodynamic power systems. *J. Chem. Thermodyn.*, 14(12):1103–1113, 1982.

[187] B. Ruscic, C A Mayhew, and J Berkowitz. Photoionization studies of (BH3)n (n=1,2). *J. Chem. Phys.*, 88(9):5580, 1988.

[188] Leif Åsbrink, Agneta Svensson, Wolfgang von Niessen, and Gerhard Bieri. 30.4-nm He(II) photoelectron spectra of organic molecules: Part V. Hetero-compounds containing first-row elements (C, H, B, N, O, F). *J. Electron Spectros. Relat. Phenomena*, 24(2):293–314, 1981.

[189] H Baumgaertel, H W Jochims, E Ruehl, H Bock, R Dammel, J Minkwitz, and R Nass. Photoelectron spectra and molecular properties. 112. Photoelectron and photoionization mass spectra of the fluoroamines NH3-nFn. *Inorg. Chem.*, 28(5):943–949, 1989.

[190] Tomislav Cvitaš and Leo Klasinc. High resolution photoelectron spectrum of hydrazoic acid. *J. Chem. Soc. Faraday Trans. 2*, 72:1240, 1976.

[191] A H Cowley, R A Kemp, M Lattman, and M L McKee. Lewis base behavior of methylated and fluorinated phosphines. Photoelectron spectroscopic investigation. *Inorg. Chem.*, 21(1):85–88, 1982.

[192] Reinhard Demuth. Photoelektronenspektren von einigen Trihalogensilylphosphanen und -arsanen X3SiER2 (X =F, Cl; E = N, P, As; R = H, CH3) / Photoelectron Spectra of Some Trihalogensilyl Phosphines and Arsines X3SiER2 (X = F, Cl; E = N, P, As; R = H, CH3). *Zeitschrift für Naturforsch. B*, 32(11):1252, 1977.

[193] Gerhard Bieri, Leif Åsbrink, and Wolfgang von Niessen. 30.4-nm He (II) photoelectron spectra of organic molecules: Part VII. Miscellaneous compounds. *J. Electron Spectros. Relat. Phenomena*, 27(2):129–178, 1982.

[194] M S Banna and D A Shirley. Molecular photoelectron spectroscopy at 132.3 eV. The second-row hydrides. *J. Chem. Phys.*, 63(11):4759, 1975.

[195] R.G. Wang, M A Dillon, and David Spence. Electron spectroscopy of hydrogen chloride from 5 to 19 eVa). *J. Chem. Phys.*, 80(1):63, 1984.

[196] J Berkowitz, H A Tasman, and W A Chupka. Double-Oven Experiments with Lithium Halide Vapors. *J. Chem. Phys.*, 36(8):2170, 1962.

[197] D L Hildenbrand. Mass-Spectrometric Studies of Bonding in the Group IIA Fluorides. *J. Chem. Phys.*, 48(8):3657, 1968.

[198] John M Dyke, D Haggerston, A.E Wright, A Morris, E van Lenthe, and J.C Snijders. A study of the transition metal tetrafluorides (TiF4, ZrF4, HfF4) using high temperature ultraviolet photoelectron spectroscopy. *J. Electron Spectros. Relat. Phenomena*, 85(1-2):23–33, 1997.

[199] John M Dyke, C Kirby, A Morris, B.W.J. Gravenor, R Klein, and P Rosmus. A study of aluminium monofluoride and aluminium trifluoride by high-temperature photoelectron spectroscopy. *Chem. Phys.*, 88(2):289–298, 1984.

[200] M Farber and R D Srivastava. Electron and thermal dissociation of BF3(g). *J. Chem. Phys.*, 81(1):241, 1984.

[201] Ellen R Fisher, Bernice L Kickel, and P.B. Armentrout. Collision-induced dissociation and charge transfer reactions of SF+x (x=1-4): Thermochemistry of sulfur fluoride ions and neutrals. *J. Chem. Phys.*, 97(7):4859, 1992.

[202] A W Potts and W C Price. Photoelectron Studies of Ionic Materials using Molecular Beam Techniques. *Phys. Scr.*, 16(5-6):191, 1977.

[203] O Grabandt, R Mooyman, and C.A. De Lange. He(I) Photoelectron spectroscopy of the gallium monohalides. *Chem. Phys.*, 143(2):227–238, 1990.

[204] E P F Lee and A W Potts. An Investigation of the Valence Shell Electronic Structure of Alkaline Earth Halides by Using ab initio s.c.f. Calculations and Photoelectron Spectroscopy. *Proc. R. Soc. A Math. Phys. Eng. Sci.*, 365(1722):395–411, 1979.

[205] Geoffrey K Barker, Michael F Lappert, J Brian Pedley, Graham J Sharp, and Nicholas P C Westwood. Bonding studies of boron and the Group 3-5 elements. Part XV. He(I) photoelectron spectra of monomeric Group 3 trihalide, trimethyl, and mixed halogenomethyl species. *J. Chem. Soc. Dalt. Trans.*, (18):1765, 1975.

[206] JÅrgen Kreile, Armin Schweig, and Walter Theil. Experimental and theoretical investigation of the photoionization of hydrogen cyanide. *Chem. Phys. Lett.*, 87(5):473–476, 1982.

[207] Denis K Bulgin, John M Dyke, and Alan Morris. Vacuum ultraviolet photoelectron spectrum of the PN(X 1 Σ +) molecule. *J. Chem. Soc., Faraday Trans. 2*, 73(7):983–990, 1977.

[208] V.I. Vovna, F.I. Vilesov, and S.N. Lopatin. Photoelectron spectra of hydrazine and some alkyl derivatives. *Opt. Spectrosc.*, 38:143, 1975.

[209] Koichi Ohno, Kohji Okamura, Hideo Yamakado, Shigeo Hoshino, Tomohide Takami, and Masayo Yamauchi. Penning Ionization of HCHO, CH2CH2, and CH2CHCHO by Collision with He(23S) Metastable Atoms. *J. Phys. Chem.*, 99(39):14247–14253, 1995.

[210] A S Vorob'ev, I I Furlei, A Sh. Sultanov, V I Khvostenko, G V Leplyanin, A R Derzhinskii, and G A Tolstikov. Mass spectrometry of resonance capture of electrons and photo-electron spectroscopy of molecules of ethylene oxide, ethylene sulfide, and their derivatives. *Bull. Acad. Sci. USSR Div. Chem. Sci.*, 38(7):1388–1394, 1989.

[211] Koichi Ohno, Keitaro Imai, and Yoshiya Harada. Variations in reactivity of lone-pair electrons due to intramolecular hydrogen bonding as observed by Penning ionization electron spectroscopy. *J. Am. Chem. Soc.*, 107(26):8078–8082, 1985.

[212] Keith Johnson, I Powis, and C.J. Danby. A photoelectron-photoion coincidence study of acetaldehyde and ethylene oxide molecular ions. *Chem. Phys.*, 70(3):329–343, 1982.

[213] Wolfgang von Niessen, Gerhard Bieri, and Leif Åsbrink. 30.4-nm He (II) photoelectron spectra of organic molecules. *J. Electron Spectros. Relat. Phenomena*, 21(2):175–191, 1980.

[214] F S Ashmore and A R Burgess. Study of some medium size alcohols and hydroperoxides by photoelectron spectroscopy. *J. Chem. Soc. Faraday Trans. 2*, 73(7):1247, 1977.

[215] J H D Eland and J Berkowitz. Photoionization mass spectrometry of HI and DI at high resolution. *J. Chem. Phys.*, 67(11):5034, 1977.

[216] A Schweig and W Thiel. Photoionization cross sections: He I- and He II-photoelectron spectra of homologous oxygen and sulphur compounds. *Mol. Phys.*, 27(1):265–268, 1974.

[217] A.W. Potts and T.A. Williams. The observation of forbidden transitions in He II photoelectron spectra. *J. Electron Spectros. Relat. Phenomena*, 3(1):3–17, 1974.

[218] Stephen Cradock and William Duncan. Photoelectron spectra of OCSe and SCSe. *J. Chem. Soc. Faraday Trans. 2*, 71(0):1262, 1975.

[219] Shunji Katsumata, Haruo Shiromaru, and Toshiaki Kimura. Photoelectron Angular Distribution and Assignment of Photoelectron Spectrum of Ozone. *Bull. Chem. Soc. Jpn.*, 57(7):1784–1788, 1984.

[220] Lowell P Theard and Donald L Hildenbrand. Heat of Formation of Be2O(g) by Mass Spectrometry. *J. Chem. Phys.*, 41(11):3416, 1964.

[221] N.F. Dalleska and P.B. Armentrout. Guided ion beam studies of reactions of alkaline earth ions with O2. *Int. J. Mass Spectrom. Ion Process.*, 134(2-3):203–212, 1994.

[222] R.E. Ballard, Jimmy Jones, Derek Read, Andrew Inchley, and Martin Cranmer. He(I) photoelectron studies of liquids and gases. *Chem. Phys. Lett.*, 137(2):125–129, 1987.

[223] G.G. Furin, A.S. Sultanov, and I I Furlei. Photoelectronic spectra of fluorine-containing aromatic amines. *Dokl. Phys. Chem.*, 3:530, 1987.

[224] Tsunetoshi Kobayashi and Saburo Nagakura. Photoelectron spectra of aminopyridines and cyanopyridines. *J. Electron Spectros. Relat. Phenomena*, 4(3):207–212, 1974.

[225] N.S. Hush and Agnes S Cheung. Ionization potentials and donor properties of nucleic acid bases and related compounds. *Chem. Phys. Lett.*, 34(1):11–13, 1975.

[226] J Lin, C Yu, S Peng, I Akiyama, K Li, Li Kao Lee, and P R LeBreton. Ultraviolet photoelectron studies of the ground-state electronic structure and gas-phase tautomerism of purine and adenine. *J. Am. Chem. Soc.*, 102(14):4627–4631, 1980.

[227] D Dougherty, K Wittel, J Meeks, and S P McGlynn. Photoelectron spectroscopy of carbonyls. Ureas, uracils, and thymine. *J. Am. Chem. Soc.*, 98(13):3815–3820, 1976.

[228] Michael H Palmer, Isobel Simpson, and Roelof J Platenkamp. The electronic structure of flavin derivatives. *J. Mol. Struct.*, 66:243–263, 1980.

[229] V Beutel, H.-G. Kramer, G L Bhale, M Kuhn, K Weyers, and W. Demtroder. High-resolution isotope selective laser spectroscopy of Ag_2 molecules. *J. Chem. Phys.*, 98(4):2699, 1993.

[230] K Franzreb, A Wucher, and H Oechsner. Electron impact ionization of small silver and copper clusters. *Zeitschrift fr Phys. D Atoms, Mol. Clust.*, 17(1):51–56, 1990.

[231] Tosio Kato. On the eigenfunctions of many-particle systems in quantum mechanics. *Comm. Pure Appl. Math.*, 10(2):151–177, 1957.

[232] Peter Scherpelz, Marco Govoni, Ikutaro Hamada, and Giulia Galli. Implementation and Validation of Fully Relativistic *GW* Calculations: SpinOrbit Coupling in Molecules, Nanocrystals, and Solids. *J. Chem. Theory Comput.*, 12(8):3523–3544, 2016.

[233] R. C. Weast and M. J. Astle. *CRC Handbook of Chemistry and Physics, 92nd ed.* CRC Press, New York, 2011.

[234] Larry a. Curtiss, Paul C. Redfern, and Krishnan Raghavachari. Gaussian-4 theory. *J. Chem. Phys.*, 126(8):084108, 2007.

[235] Joseph T. Golab, Brenda S. Thies, Danny L. Yeager, and Jeffrey a. Nichols. The ionization potentials of F2: A comparison of multiconfigurational electron propagator (MCEP) with other large scale methods using the same basis set. *J. Chem. Phys.*, 84(1):284, 1986.

[236] Sierra Rayne and Kaya Forest. Survey of main group compounds (HBr) at the Gaussian-4 level of theory: Adiabatic ionization energies and enthalpies of formation. *Comput. Theor. Chem.*, 974(1-3):163–179, 2011.

[237] K M McHugh, J G Eaton, G H Lee, H W Sarkas, L H Kidder, J T Snodgrass, M R Manaa, and K H Bowen. Photoelectron spectra of the alkali metal cluster anions: $Na^-_{n=2-5}$, $K^-_{n=2-7}$, $Rb^-_{n=2-3}$, and $Cs^-_{n=2-3}$. *J. Chem. Phys.*, 91(6), 1989.

[238] R O Jones, G Ganteför, S Hunsicker, and P Pieperhoff. Structure and spectroscopy of phosphorus cluster anions: Theory (simulated annealing) and experiment (photoelectron detachment). *J. Chem. Phys.*, 103:9549, 1995.

[239] T P Lippa, S.-J. Xu, S A Lyapustina, J M Nilles, and K H Bowen. Photoelectron spectroscopy of As^-, As_2^-, As_3^-, As_4^- and As_5^-. *J. Chem. Phys.*, 109(24), 1998.

[240] J A Ayala, W E Wentworth, and E C M Chen. Electron attachment to halogens. *J. Phys. Chem.*, 85(7):768–777, 1981.

[241] Don W Arnold, S E Bradforth, T N Kitsopoulos, and Daniel M Neumark. Vibrationally resolved spectra of C2-C11 by anion photoelectron spectroscopy. *J. Chem. Phys.*, 95(12):8753, 1991.

[242] Thomas M. Miller, A. A. Viggiano, and Amy E Stevens Miller. Electron Attachment and Detachment: Cyclooctatetraene. *J. Phys. Chem. A*, 106(43):10200–10204, 2002.

[243] Harry W Sarkas, Jay H Hendricks, Susan T Arnold, and K H Bowen. Photoelectron spectroscopy of lithium hydride anion. *J. Chem. Phys.*, 100(3):1884, 1994.

[244] C. Tom Wickham-Jones, Sean Moran, and G Barney Ellison. Photoelectron spectroscopy of BH_3^-. *J. Chem. Phys.*, 90(2):795, 1989.

[245] O.V. Boltalina, A.Y. Borshchevskii, L.N. Sidorov, and V.N. Chepurnykh. Enthalpy of the Formation of TiF5- Anion in a Gas Phase. *Zh. Fiz. Khim. SSSR*, 65:928, 1991.

[246] Amy E Stevens Miller, Thomas M Miller, A A Viggiano, Robert A Morris, Jane M Van Doren, Susan T Arnold, and John F Paulson. Negative ion chemistry of SF4. *J. Chem. Phys.*, 102(22):8865, 1995.

[247] Thomas M Miller, Doreen G Leopold, Kermit K Murray, and W C Lineberger. Electron affinities of the alkali halides and the structure of their negative ions. *J. Chem. Phys.*, 85(5):2368, 1986.

[248] S J Cavanagh, S T Gibson, and B R Lewis. High-resolution photoelectron spectroscopy of linear←bent polyatomic photodetachment transitions: The electron affinity of CS2. *J. Chem. Phys.*, 137(14):144304, 2012.

[249] Don W Arnold, Cangshan Xu, Eun H Kim, and Daniel M Neumark. Study of low-lying electronic states of ozone by anion photoelectron spectroscopy of O_3^-. *J. Chem. Phys.*, 101(2):912, 1994.

[250] Mark R Nimlos and G Barney Ellison. Photoelectron spectroscopy of sulfur-containing anions (SO2-, S3-, and S2O-). *J. Phys. Chem.*, 90(12):2574–2580, 1986.

[251] Soren N Eustis, Di Wang, Kit H Bowen, and G Naresh Patwari. Photoelectron spectroscopy of hydrated hexafluorobenzene anions. *J. Chem. Phys.*, 127(11):114312, 2007.

[252] J Schiedt, R Weinkauf, Daniel M Neumark, and E.W. Schlag. Anion spectroscopy of uracil, thymine and the amino-oxo and amino-hydroxy tautomers of cytosine and their water clusters. *Chem. Phys.*, 239(1-3):511–524, 1998.

[253] K. Aflatooni, G. A. Gallup, and P. D. Burrow. Electron Attachment Energies of the DNA Bases. *J. Phys. Chem. A*, 102(31):6205–6207, 1998.

[254] H Handschuh, Chiaen Cha, P S Bechthold, G. Gantefor, and W Eberhardt. Electronic shells or molecular orbitals: Photoelectron spectra of Ag_n^- clusters. *J. Chem. Phys.*, 102(16):6406, 1995.

[255] K J Taylor, C. L. Pettiette-Hall, O Cheshnovsky, and R E Smalley. Ultraviolet photoelectron spectra of coinage metal clusters. *J. Chem. Phys.*, 96(4):3319, 1992.

[256] Xiaohu Wu, Zhengbo Qin, Hua Xie, Ran Cong, Xiaohu Wu, Zichao Tang, and Hongjun Fan. Photoelectron Imaging and Theoretical Studies of Group 11 Cyanides MCN (M = Cu, Ag, Au). *J. Phys. Chem. A*, 114(49):12839–12844, 2010.

[257] M.G. Williams, R.D. Tomlinson, and M.J. Hampshire. X-ray determination of the lattice parameters and thermal expansion of cadmium tel-

luride in the temperature range 20-420°C. *Solid State Communications*, 7(24):1831 – 1832, 1969.

[258] Adrian Stan, Nils Erik Dahlen, and Robert van Leeuwen. Levels of self-consistency in the *GW* approximation. *The Journal of Chemical Physics*, 130(11):1–10, 2009.

[259] P. García-González and R. W. Godby. Self-consistent calculation of total energies of the electron gas using many-body perturbation theory. *Phys. Rev. B*, 63:075112, 2001.

[260] Wolf-Dieter Schöne and Adolfo G. Eguiluz. Self-consistent calculations of quasiparticle states in metals and semiconductors. *Phys. Rev. Lett.*, 81:1662–1665, 1998.

[261] C. Kittel. *Introduction to Solid State Physics, 6th ed.* Wiley, New York, 1986.

[262] Biermann, S. and Aryasetiawan, F. and Georges, A. First-Principles Approach to the Electronic Structure of Strongly Correlated Systems: Combining the *GW* Approximation and Dynamical Mean-Field Theory. *Phys. Rev. Lett.*, 90:086402, 2003.

[263] K. Held. Electronic structure calculations using dynamical mean field theory. *Advances in Physics*, 56:829, 2007.

[264] Eva Pavarini, Erik Koch, Dieter Vollhardt, and Alexander (Eds.) Lichtenstein. *The LDA+DMFT approach to strongly correlated materials: lecture notes of the autumn school 2011, hands-on LDA+DMFT; autumn school organized by the DFG research unit 1346 dynamical mean-field approach with predictive power for strongly correlated materials at Forschungszentrum Jülich 4-7 October 2011*. Forschungszentrum, Zentralbibliothek, 2011.

[265] Huang, Li and Ayral, Thomas and Biermann, Silke and Werner, Philipp. Extended dynamical mean-field study of the Hubbard model with long-range interactions. *Phys. Rev. B*, 90:195114, 2014.

[266] Ayral, Thomas and Biermann, Silke and Werner, Philipp. Screening and nonlocal correlations in the extended Hubbard model from self-consistent combined *GW* and dynamical mean field theory. *Phys. Rev. B*, 87:125149, 2013.

[267] Merzuk Kaltak. *Merging GW with DMFT*. PhD thesis, University of Vienna, 2015.

[268] Masatoshi Imada and Takashi Miyake. Electronic Structure Calculation by First Principles for Strongly Correlated Electron Systems. *Journal of the Physical Society of Japan*, 79(11):112001, 2010.

[269] Gull, Emanuel and Millis, Andrew J. and Lichtenstein, Alexander I. and Rubtsov, Alexey N. and Troyer, Matthias and Werner, Philipp. Continuous-time Monte Carlo methods for quantum impurity models. *Rev. Mod. Phys.*, 83:349–404, 2011.

[270] Nekrasov, I. A. and Held, K. and Keller, G. and Kondakov, D. E. and Pruschke, Th. and Kollar, M. and Andersen, O. K. and Anisimov, V. I. and Vollhardt, D. Momentum-resolved spectral functions of $SrVO_3$ calculated by LDA + DMFT. *Phys. Rev. B*, 73:155112, 2006.

[271] Vaugier, Loïg and Jiang, Hong and Biermann, Silke. Hubbard U and Hund exchange J in transition metal oxides: Screening versus localization trends from constrained random phase approximation. *Phys. Rev. B*, 86:165105, 2012.

[272] Sakuma, R. and Werner, Ph. and Aryasetiawan, F. Electronic structure of $SrVO_3$ within *GW*+DMFT. *Phys. Rev. B*, 88:235110, 2013.

[273] Choi, Sangkook and Kutepov, Andrey and Haule, Kristjan and van Schilfgaarde, Mark and Kotliar, Gabriel. First-principles treatment of Mott insulators: linearized QSGW+DMFT approach. *Npj Quantum Materials*, 1:16001, 2016.

[274] Parragh, N. and Toschi, A. and Held, K. and Sangiovanni, G. Conserved quantities of $SU(2)$-invariant interactions for correlated fermions and the advantages for quantum Monte Carlo simulations. *Phys. Rev. B*, 86:155158, 2012.

[275] M. Wallerberger. *w2dynamics: Continuous time quantum Monte Carlo calculations of one- and two-particle propagators*. PhD thesis, 2016.

[276] Casula, Michele and Rubtsov, Alexey and Biermann, Silke. Dynamical screening effects in correlated materials: Plasmon satellites and spectral weight transfers from a Green's function ansatz to extended dynamical mean field theory. *Phys. Rev. B*, 85:035115, 2012.

[277] Werner, Philipp and Millis, Andrew J. Dynamical Screening in Correlated Electron Materials. *Phys. Rev. Lett.*, 104:146401, Apr 2010.

[278] Murray Gell-Mann and Keith A. Brueckner. Correlation energy of an electron gas at high density. *Phys. Rev.*, 106:364–368, 1957.

[279] David C. Langreth and John P. Perdew. Exchange-correlation energy of a metallic surface: Wave-vector analysis. *Phys. Rev. B*, 15:2884–2901, 1977.

[280] M. Jarrella and J.E. Gubernatisb. Bayesian inference and the analytic continuation of imaginary-time quantum monte carlo data. *Physics Reports*, 269:133, 1996.

[281] K. Vafayi and O. Gunnarsson. Analytical continuation of spectral data from imaginary time axis to real frequency axis using statistical sampling. *Phys. Rev. B*, 76:035115, 2007.

[282] Schött, Johan and Locht, Inka L. M. and Lundin, Elin and Grånäs, Oscar and Eriksson, Olle and Di Marco, Igor. Analytic continuation by averaging Padé approximants. *Phys. Rev. B*, 93:075104, 2016.

[283] W. H. Press, S. A. Teukolsky, W. T. Vetterling, and B. P. Flannery. *Numerical Recipes 3rd Edition: The Art of Scientific Computing*. Cambridge University Press, 1975.

[284] K.-H. Lee and K. J. Chang. Analytic continuation of the dynamic response function using an n-point padé approximant. *Phys. Rev. B*, 54:R8285, 1996.

[285] E. Aasioglu, C. Friedrich, and S. Blügel. Effective coulomb interaction in transition metals from constrained random-phase approximation. *Phys. Rev. B*, 83:121101, 2011.

[286] C.B. Lang and N. Pucker. *Mathematische Methoden in der Physik*. Spektrum Akademischer Verlag, 2005.

[287] Klaus Fredenhagen. *Quantum field theory*. Lecture Notes, 2009.

[288] R.A. Bertlmann. *Anomalies in Quantum Field Theory*. Clarendon Press, 2000.

[289] Y. Nomura, M. Kaltak, K. Nakamura, C. Taranto, S. Sakai, A. Toschi, R. Arita, K. Held, G. Kresse, and M. Imada. Effective on-site interaction for dynamical mean-field theory. *Phys. Rev. B*, 86:085117, 2012.

[290] Nicola Marzari, Arash A. Mostofi, Jonathan R. Yates, Ivo Souza, and David Vanderbilt. Maximally localized wannier functions: Theory and applications. *Rev. Mod. Phys.*, 84:1419–1475, 2012.

Acknowledgments

First of all, I should appreciate my family who are always supporting my studies on physics. In particular, I would like to thank my wife, He Song, who always encourages and helps me whenever I have troubles. Without her support and help, this dissertation would not be finished in time.

Special thanks I owe to Georg Kresse and Cesare Franchini who help me a lot in all aspects as my supervisors. They always give me enough patience with my not good oral English in our regular discussions. From each discussion, I benefited a lot from their expertise and experience in the DFT and *GW* methods. Their feedback were always clear, constructive and motivating. These prevented me from doing many mistakes and definitely contributed greatly to the success of this dissertation.

Likewise, I would like to thank my friendly and cooperative group members, who built a very pleasant and professional working atmosphere. It was Xianfeng Hao that helped me familiarize the group when I joined the group, which made me easier to get started in my study. Bongjae Kim is a so kind person. Whenever I discussed with him, he always would like to share his expertise and experience in strongly correlated materials. Michele Reticcioli is a very humorous Italy guy. I thank him for any discussions with him and help in providing the technical support in the unfolding method. I should give my special appreciation to Merzuk Kaltak. It was he that taught me a lot in developing the VASP code, which helped me faster familiarize the VASP code and advanced my work. Furthermore, I would like to thank Michael Pöltl, who helps me solve the technical questions. Also, I would like to thank Doris Hecht-Aichholzer and Katharina Simma, who both helped me a lot in dealing with the things associated with the university. I should thank Rene Moser as well. Whenever I have difficulties in understanding the German language, he is always so kind to help me. Also, I should thank Benjamin Ramberger for his helpful discussions and careful translations in the German abstract of my thesis. For these and many other reasons, I thank all of my colleges, Zeynep, Menno, Emanuele, Tobias, Manuel, and so on, for the great and exciting time we had together.

In addition, I would like to thank Xingqiu Chen, my supervisor when I was at Institute of Metal research (IMR). Without his recommendations, I would not have this opportunity to study in the University of Vienna. Also, I should thank Yikun Luan and Dianzhong Li, who always

give me a hand when I need it. Besides, I would like to thank all of my colleges at IMR. It was HaiYang Niu that helped me start my first DFT calculation and showed me how to obtain the useful information. Whenever I talked with him, he always gave me constructive suggestions in my career. Xiyue Chen is a very smart girl, who helped me figure out how to install the Linux system in the virtual machine. Yan Sun is a great guy, who always likes to share his expertise in the topological calculations when we discuss. Furthermore, I should show my gratitude to Pengyue Wei. It was she that helped me deal with the stuff at IMR, which saved me a lot of time.

Last but not least, I would like to thank my collaborators, Jiří Klimeš, Karsten Held, Alessandro Toschi, Jan Tomczak, and Daniel Springer, from whom I have benefited a lot in each fruitful discussion, which facilitates my work. In particular, I would like to thank Karsten Held and Alessandro Toschi for their fascinating and motivating courses about the quantum field theory, which helped me a lot in understanding the many body physics and definitely made me easier in developing the VASP code. Besides, I enjoyed the lectures given by Jan Kuneš and discussions with Zhicheng Zhong, who helped me understand the Model Hamiltonian. Also, I thank Liang Si for his helpful discussion on DMFT.

This work was supported by the Austrian Science Fund (FWF) within the SFB ViCoM (Grant No. F 41) and I597-N16 (research unit FOR 1346 of the Deutsche Forschungsgemeinschaft and FWF). Computing time at our local cluster and the Vienna Scientific Cluster is greatly acknowledged. Finally, I would like to thank everyone who helped me in any sense.

Publications:

- Jan M. Tomczak, Peitao Liu, Alessandro Toschi, Georg Kresse and Karsten Held, Merging *GW* with DMFT and non-local correlations beyond, The European Physical Journal (2017) (submitted).

- Bongjae Kim, Peitao Liu, and Cesare Franchini, Dimensionality-strain phase diagram of strontium iridates, Physical Review B 95 115111(2017).

- Emanuele Maggio, Peitao Liu, Michiel J. van Setten, and Georg Kresse, *GW*100: a plane wave perspective for small molecules, Journal of Chemical Theory and Computation 13, 635 (2017).

- Bongjae Kim, Peitao Liu, and Cesare Franchini, Magnetic properties of bilayer $Sr_3Ir_2O_7$: role of epitaxial strain and oxygen vacancies, Physical Review B 95, 024406 (2017).

- Bongjae Kim, Peitao Liu, Zeynep Ergonenc, Alessandro Toschi, Sergii Khmelevskyi, and Cesare Franchini, A new route to relativistic insulators: The Lifshitz transition of $NaOsO_3$ driven by spin fluctuations and spin-orbit coupling renormalization, Physical Review B 94, 241113(R) (2016).
  (Rapid Communications).

- Peitao Liu, Michele Reticcioli, Bongjae Kim, Alessandra Continenza, Georg Kresse, D.D. Sarma, Xing-Qiu Chen, and Cesare Franchini, Electron and hole doping in the relativistic Mott insulator Sr_2IrO_4: a first-principles study using band unfolding technique, Physical Review B 94, 195145 (2016).

- Peitao Liu, Merzuk Kaltak, Jiri Klimes, and Georg Kresse, Cubic scaling *GW*: towards fast quasiparticle calculations, Physical Review B 94, 165109 (2016). (PRB Editors' Suggestions).

- Peitao Liu, Shoulong Wang, Dianzhong Li, Yiyi Li, and Xing-Qiu Chen, Fast and Huge Anisotropic Diffusion of Cu (Ag) and their Resistance on the Self-diffusivity in β-Sn, Journal of Materials Science & Technology 32, 121 (2016).

- Peitao Liu, Sergii Khmelevskyi, Bongjae Kim, Martijn Marsman, Dianzhong Li, Xing-Qiu Chen, D. D. Sarma, Georg Kresse, and Cesare Franchini, Anisotropic magnetic couplings and structure-driven canted to collinear transitions in Sr_2IrO_4 by magnetically constrained noncollinear DFT, Physical Review B 92, 054428 (2015).

- Weiwei Xing, Peitao Liu, Xiyue Cheng, Haiyang Niu, Hui Ma, Dianzhong Li, Yiyi Li, and Xing-Qiu Chen, Vacancy Formation Enthalpy of Filled d-band Nobel Metals by hybrid Functional, Physical Review B 90, 144105 (2014).

- Weiwei Xing, Xing-Qiu Chen, Peitao Liu, Xin Wang, Pengcheng Zhang, Dianzhong Li, and Yiyi Li. First-principles studies of hydrogen behavior interacting with oxygen-enriched nanostructured particles in the ODS steels, Journal of Hydrogen Energy 39, 18506 (2014).

- Peitao Liu, Weiwei Xing, Xiyue Cheng, Dianzhong Li, Yiyi Li, and Xing-Qiu Chen, Effects of dilute substitutional solutes on interstitial carbon in α-Fe: Interactions and associated carbon diffusion from first-principles calculations, Physical Review B 90, 024103 (2014).

- Xiyue Cheng, Wei Zhang, Xing-Qiu Chen, Haiyang Niu, Peitao Liu, Kui Du, Gang Liu, Dianzhong Li, Hui-Ming Cheng, Hengqiang Ye, and Yiyi Li, Interstitial-boron solution strengthened WB_{3+x}, Applied Physics Letters 103, 171903 (2013).

- Haiyang Niu, Xing-Qiu Chen, Peitao Liu, Weriwei Xing, Xiyue Cheng, Dianzhong Li, and Yiyi Li, Extra-electron induced covalent strengthening and generalization of intrinsic ductile-to-brittle criterion, Scientific reports 2, 718 (2012).

Presentations:

- Peitao Liu, Xing-Qiu Chen, Dianzhong Li and Yiyi Li, First-principles investigations of phase stabilities, dynamical, electronic and thermal properties of intermetallic compound Al_3Fe_2Si. 14th International IUPAC Conference on High Temperature Materials Chemistry (HTMC-XIV), Beijing, China, Sept. 2012 (Poster).

- Peitao Liu, Xiyue Cheng, Haiyang Niu, Xingqiu Chen, Dianzhong Li and Yiyi Li, Structure, Phonon, Bonding, and Hardness of a series of TMB_4 , TMB_6 and TMB_{12} (TM = transition metal), 37th International Conference and Exposition on Advanced Ceramics and Composites, Daytona Beach, FL, America, January, 2013 (Oral).

- Peitao Liu, Xing-Qiu Chen, Dianzhong Li, and Cesare Franchini, Metal-Insulator Transition in 5d Transition Metal Oxides $Sr_{n+1}Ir_nO_{3n+1}$ ($n = 1, 2$, and ∞): Effects of Spin-Orbit Coupling and Electronic Interactions, the Autumn School on Correlated Electrons: DMFT at 25: Infinite Dimensions, Forschungszentrum Jülich, Germany, Sept. 2014 (Poster).

- Peitao Liu, Xing-Qiu Chen, Dianzhong Li, and Cesare Franchini, Metal-Insulator

Transition in 5d Transition Metal Oxides $Sr_{n+1}Ir_nO_{3n+1}$ (n = 1, 2, and ∞): Effects of Spin-Orbit Coupling and Electronic Interactions, International Conference of Young Researchers on Advanced Materials, Haikou (China), Oct. 2014 (oral).

- Peitao Liu, Sergii Khmelevskyi, Bongjae Kim, Xing-Qiu Chen, Dianzhong Li, and Cesare Franchini. Electronic, magnetic and optical properties of $Sr_{n+1}Ir_nO_{3n+1}$ (n = 1, 2, and ∞), APS meeting, San Antonio, Texas (USA), March, 2015 (oral).

- Peitao Liu, Sergii Khmelevskyi, Bongjae Kim, Xing-Qiu Chen, Dianzhong Li, and Cesare Franchini. Electronic, magnetic and optical properties of $Sr_{n+1}Ir_nO_{3n+1}$ (n = 1, 2, and ∞), PSK-conference, San Sebastian, Spain, Sept., 2015 (oral).

- Peitao Liu, Sergii Khmelevskyi, Bongjae Kim, Xing-Qiu Chen, Dianzhong Li, and Cesare Franchini. Electronic, magnetic and optical properties of $Sr_{n+1}Ir_nO_{3n+1}$ (n = 1, 2, and ∞), 2nd international workshop on dynamical mean-field approach for strongly correlated materials, Dresden, Germany, Sept., 2015 (oral).

- Peitao Liu, Merzuk Kaltak, Jiri Klimes, and Georg Kresse, Cubic scaling *GW*: towards fast quasiparticle calculations, DPG-conference, Regensburg, Germany, March., 2016 (oral).

- Peitao Liu, Merzuk Kaltak, Jiri Klimes, and Georg Kresse, Cubic scaling *GW*: towards fast quasiparticle calculations, ViCoM Young Researchers Meeting 2016, Vienna, Austria, Sept., 2016 (poster). (Best Poster Award (Jury Prize)).

- Peitao Liu, Merzuk Kaltak, Jiri Klimes, and Georg Kresse, Constrained random phase approximation and Cubic scaling *GW*, Conference: What about U?-Effects of Hubbard Interactions and Hund's Coupling in Solids, Trieste, Italy, Oct., 2016 (poster).